TECHNISCHE UNIVERSITÄT MÜNCHEN

Max-Planck-Institut für Plasmaphysik

Linear and nonlinear analysis of plasma edge instabilities

Tobias Breu

Vollständiger Abdruck der von der Fakultät für Physik der Technischen Universität München zur Erlangung des akademischen Grades eines

Doktors der Naturwissenschaften (Dr. rer. nat.)

genehmigten Dissertation.

Vorsitzender: Univ.-Prof. Dr. Rudolf Gross

Prüfer der Dissertation:

1. Hon.-Prof. Dr. Sibylle Günter
2. Univ.-Prof. Dr. Harald Friedrich

Die Dissertation wurde am 12.09.2011 bei der Technischen Universität München eingereicht und durch die Fakultät für Physik am 12.12.2011 angenommen.

Contents

1 Introduction

1.1 Nuclear fusion

The energy source of stars is the nuclear fusion of light atoms, as first proposed by Atkinson and Houtermans [1] in 1929. For stars with a mass equal to or lighter than our sun, the primary reaction mechanism is the proton-proton chain reaction, while for heavier stars it is mainly the Bethe-Weizsäcker cycle [2] [3] [4]. The basic concept is that two nuclei have to come close enough to each other so that the short-ranged attracting strong force can act and cause a fusion reaction. This requires that at first the long-range repelling electric force has to be overcome (Coulomb barrier).

To employ nuclear fusion as a means to generate electricity in terrestrial power plants, those stellar processes unfortunately cannot simply be copied and downscaled, as the probability of fusion reactions actually happening, i.e. the cross section σ of the reaction is much too low. From today's view, the only realistic fusion reaction is between deuterium (D) and tritium (T)

$$^{2}_{1}\mathrm{D} + ^{3}_{1}\mathrm{T} \rightarrow ^{4}_{2}\mathrm{He} + ^{1}_{0}\mathrm{n} + 17.59\ \mathrm{MeV}$$

where the energy of 17.59 MeV is split to 3.5 MeV for the α particle $^{4}_{2}He$ and 14.1 MeV for the neutron. At temperatures of 100 million degree Kelvin, the reaction rate for the D-T fusion reaction is $\approx 10^{-22}\frac{\mathrm{m}^3}{\mathrm{s}}$ [5]. Deuterium is easily available from sea water and supply is practically unlimited. The neutron from the fusion reaction can be used to breed tritium by a reaction with lithium

$$^{1}_{0}n + ^{6}_{3}\mathrm{Li} \rightarrow ^{3}_{1}\mathrm{T} + ^{4}_{2}\mathrm{He} + 4.78\ \mathrm{MeV}$$

The most advanced concept of a fusion reactor today is based on the magnetic confinement of a D-T fuel mix heated up to temperatures of 100 - 200 million degree Kelvin. Higher temperatures are connected with higher average velocities of the particles, making it possible for them to overcome the Coulomb barrier. At these temperatures, the fuel is in the state of a plasma, where D and T are fully ionized along with unbound electrons.

To confine the plasma within a reactor, magnetic fields are applied. The basic confinement mechanism can be understood as follows: a single electrically charged particle is forced to a circular motion perpendicular to the direction of a magnetic field line (gyration), providing confinement in this perpendicular direction. Parallel to the magnetic field however, it feels no Lorentz force and is still free. Early experiments used a cylindrical setup, i.e. straight magnetic field lines inside the cylinder, with magnetic mirrors on both ends[1] to minimize

[1] increasing magnetic field strength at the ends of the cylinder, causing a repelling force

losses. This however proved to be ineffective for particles with high energies, as their parallel velocity is high enough to overcome the mirror force, and particle collisions lead to a refilling of the phase space. The solution is to close both parallel ends to a torus, providing confinement in the direction parallel to the magnetic field (toroidal direction). This is however still not sufficient, as the hoop force would cause the torus to expand radially with time. The magnetic field has to be given a poloidal component, causing a helical magnetic configuration. This can be realized in two ways, the first one being the tokamak concept, see. fig. 1.1. As a plasma at high temperatures is a good electrical conductor, a toroidal current can be induced in the plasma through a transformer, causing a poloidal magnetic field. This can be also used as a heating mechanism for the plasma, but as the conductivity of the plasma increases with increasing temperature[2], this is limited to temperatures up to a few 10 million degree Kelvin. Additional heating is applied in the form of electromagnetic waves or neutral beam injection. Unfortunately, to drive the toroidal current, the poloidal magnetic flux through the plasma has to change continuously, requiring a constant ramp-up of the current in the transformer coil. This cannot be done indefinitely and thus without any additional current drive mechanisms, the tokamak can intrinsically only be operated in pulses. The strength of the toroidal magnetic field decreases with an $\frac{1}{R}$ dependence from the location of the transformer coil to the outside of the tokamak, hence the inner side is termed high-field side (HFS) and the outer one low-field side (LFS). The second concept is the stellarator shown in fig. 1.2,

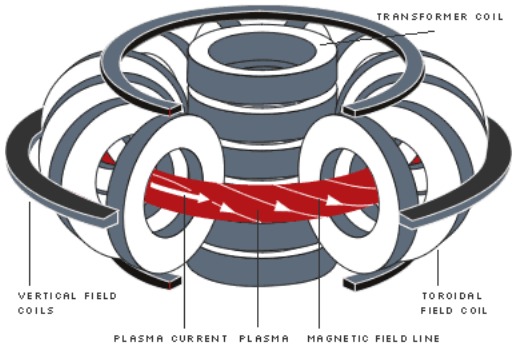

Figure 1.1: Basic tokamak configuration. Source: [7]

where the necessary magnetic field is generated purely by shaped coils and no plasma current is required. Therefore the stellarator can in principle be continuously operated without additional external means.
The plasma naturally loses energy and consequently temperature, e.g. by radiation of only partially ionized impurities[3] in the plasma. The goal is to achieve a self-sustained fusion reaction, where all energy / temperature losses are compensated by the energy of the reactions themselves. This is called ignition and described by the Lawson criterion

$$nT\tau_E \geq \frac{12k_B}{Q_\alpha}\frac{T^2}{<\sigma v>}, \tag{1.1}$$

with the plasma density n, plasma temperature T confinement time τ_E, thermal velocity v, cross section σ for the fusion reaction partners, $< ... >$ denotes the average over the particle

[2] approximately proportional to $T^{\frac{3}{2}}$ [6]
[3] e.g. particles from the wall material

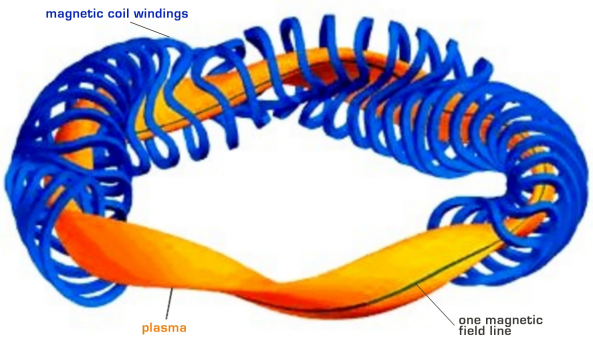

Figure 1.2: Basic stellarator configuration. Source: [7]

velocity distribution and k_B is the Boltzmann constant. In case of a DT plasma, the quantity Q_α is the energy of the α particle, $Q_\alpha = 3.5$ MeV. The confinement time is defined as $\frac{W}{P_{loss}}$, where W is the energy content of the plasma and and P_{loss} is the energy loss rate[4]. Defining the plasma β as the ratio of plasma thermal pressure to magnetic pressure

$$\beta = \frac{2\mu_0 n k_B T}{B^2}, \tag{1.2}$$

where B is the magnetic field and μ_0 the vacuum permeability, we can express the Lawson criterion as

$$\beta\tau_E \geq \frac{24\mu_0 k_B^2}{Q_\alpha B^2} \frac{T^2}{<\sigma v>}. \tag{1.3}$$

The confinement time is limited by transport processes, whereas higher β is desirable because the fusion power increases $\sim \beta^2$, but the occurrence of instabilities put upper bounds on the value of β. Furthermore, one wants the magnetic field B to be as small as possible, as it has to be generated by external means and thus consumes energy.

1.2 Thesis motivation and outline

Modern tokamaks show high pressure gradients and a peak in the current density at the edge region of the plasma, i.e. at the low-field side. This often results in instabilities in this region, where exceeding a pressure gradient threshold causes ballooning modes and the current density can drive peeling modes / external kinks. In the framework of the linear ideal magnetohydrodynamics (MHD) model of the plasma, ballooning and peeling modes show coupling. This coupling provides a theoretical model for the type I edge localized mode (ELM) instability, which for larger Tokamaks like ITER [8] can cause unacceptable heat loads on crucial parts of the device, the divertor plates. Coupled peeling-ballooning modes yield threshold values for the maximum pressure gradient and current density which are comparable to experimentally observed values for type I ELMs. For the edge region, however,

[4] energy losses are e.g. heat conduction and radiation

fundamental assumptions of the ideal MHD model may break down. Therefore, we compare the linear ideal MHD stability predictions with a more sophisticated 3D gyrofluid turbulence model of the plasma, which has larger regions of validity on both temporal and spatial scales and moreover features additional types of instabilities. A comparison of both fluid models can be done numerically in terms of growth rates of modes and their mode numbers, which characterize the structure of the instabilities.

This thesis is structured as follows:
In chapters 2 and 3, we give an overview of the theoretical framework of both models necessary for this thesis. This is concluded with a theoretical discussion of their differences concerning regions of validity and physical mechanisms in chapter 4.
In chapter 5, we describe characteristics of the plasma edge region from experimental observations along with theoretical interpretations.
Chapter 6 is dedicated to the investigation the influence of the distance of a perfectly conducting wall from the plasma boundary on two specific instabilities, the edge ballooning mode and the external kink. This is done in the framework of ideal linear MHD and necessary for appropriate comparisons with the gyrofluid model.
In chapter 7, we perform simulations for the numerical comparison of ideal linear MHD and the gyrofluid model. We prepare suitable equilibria based on the observations in chapter 5 and then simulate their characteristics with codes for both fluid descriptions. Focusing on the pressure gradient driven ballooning mode, we compare the initial linear phase of instabilities along with separate discussion of the characteristics of the ideal linear MHD and gyrofluid simulations.
The first part of the comparison is concerned with the influence of the pressure gradient on the stability of plasma equilibria. This is studied by varying the maximum pressure gradient, but leaving the width of the edge region constant, and changing the width at constant maximum pressure gradient.
Second, the toroidicity of tokamaks has an influence on several plasma instabilities and can be quantified by the aspect ratio ϵ. The effect of ϵ can both be stabilizing and destabilizing, depending on the type of instability.
Shaping the poloidal plasma cross section can have strong stabilizing effects as observed in experiments. We use a κ-δ model to describe the shaping analytically, with plasma elongation κ and triangularity δ, while the maximum pressure gradient is held fixed.
The last, briefly investigated case features a large pressure gradient in the core of the plasma, yielding a prominent ballooning mode. It is otherwise specifically designed to dimish all other instabilities occurring exclusively in only one of the fluid model simulations.
The final chapter 8 summarizes the main results of this thesis and gives a brief outlook on possible future topics based on our work.

2 Ideal MHD theoretical background

In this chapter, we present the linear ideal MHD model. We give the necessary equations for plasma equilibria in tokamaks and introduce methods to test those equilibria for their linear stability. For the purpose of this thesis, two main instabilities are investigated in detail: the ballooning mode and the external kink / peeling mode. While giving the basic assumptions and approximations, the question of their validity regime is described in 4, where we contrast both fluid models (ideal MHD and gyrofluid) with each other.
We conclude with a summary of the important characteristics of ideal MHD; a comprehensive review of ideal MHD can further be found in [9], [10].

2.1 From the kinetic equations to the ideal MHD model

2.1.1 The Boltzmann equation

The ideal MHD model describes the plasma as a perfectly conductive fluid composed of only a single species, assumed to be quasi-neutral but able to carry a current. The starting point for the derivation of the ideal MHD equations is a kinetic model for an arbitrary number α of particle species. It describes the plasma in terms of a microscopic distribution function $\hat{f}_\alpha(\vec{x}, \vec{v}, t)$ instead of $3N\alpha$ equations of motion for $N\alpha$ particles in the system. The quantity

$$\hat{f}_\alpha(\vec{x}, \vec{v}, t) d\vec{x} d\vec{v} \tag{2.1}$$

gives the number of particles of species α having position and velocity within the interval $[\vec{x} + d\vec{x}, \vec{v} + d\vec{v}]$ at a certain time t. Assuming the motion in the six-dimensional phase space to be incompressible, i.e. the particle number is conserved along a phase space trajectory, we have the Liouville equation

$$\frac{d\hat{f}_\alpha}{dt} = 0 \tag{2.2}$$

This has the form of a continuity equation and can be written as

$$\begin{aligned} \frac{d\hat{f}_\alpha}{dt} &= \frac{\partial \hat{f}_\alpha}{\partial t} + \frac{\partial \vec{x}}{\partial t} \cdot \nabla \hat{f}_\alpha + \frac{\partial \vec{v}}{\partial t} \cdot \nabla_{\vec{v}} \hat{f}_\alpha \\ &= \frac{\partial \hat{f}_\alpha}{\partial t} + \vec{v} \cdot \nabla \hat{f}_\alpha + \vec{a} \cdot \nabla_{\vec{v}} \hat{f}_\alpha = 0, \end{aligned} \tag{2.3}$$

called the Klimontovich equation.
The only forces $\vec{F}$ considered here are electromagnetic, and any relativistic effects are neglected, so

$$\vec{a} = \frac{\vec{F}}{m_\alpha} = \frac{q_\alpha}{m_\alpha}(\vec{E} + \vec{v} \times \vec{B}). \tag{2.4}$$

At this point, the distribution function could in principle still be written as a sum over delta distributions

$$\hat{f}_\alpha(\vec{x}, \vec{v}, t) = \sum_{i=1}^{N} \delta_\alpha(\vec{x}_i, \vec{v}_i, t) \tag{2.5}$$

with $\vec{x}_i$ and $\vec{v}_i$ being the position and velocity of particle i at the time t. We now switch over to a smooth distribution function $f_\alpha(\vec{x}, \vec{v}, t)$ through averaging $\hat{f}_\alpha$ over a macroscopically small, but microscopically large volume, compare [11] and [12]. Furthermore, we split the electromagnetic fields in a macroscopic part $\vec{E}$, $\vec{B}$ and a microscopic part $\delta_{E,B}$.
From $\hat{f}_\alpha(\vec{x}, \vec{v}, t)$, we can obtain the velocity-averaged current density $\vec{j}$ and charge density ρ, which are the source terms for the macroscopic part of the electromagnetic fields. The latter can be calculated from the Maxwell equations. The microscopic parts, however, determine the particle interactions within the Debye sphere.
Now writing eq. (2.3) with the macroscopic quantities on the left hand side and culminating all the microscopic quantities into a single term[1] $\left(\frac{\partial f_\alpha}{\partial t}\right)_c$ on the right hand side, we obtain the Boltzmann equation [11]:

$$\frac{\partial f_\alpha}{\partial t} + \vec{v} \cdot \nabla f_\alpha + \frac{q_\alpha}{m_\alpha}\left(\vec{E} + \vec{v} \times \vec{B}\right) \cdot \nabla_v f_\alpha \quad = \quad \left(\frac{\partial f_\alpha}{\partial t}\right)_c \tag{2.6}$$

2.1.2 Fluid moments

The first step of the derivation of the ideal MHD equations is to take the following velocity moments of eq. (2.6)

$$\int \left[\frac{df_\alpha}{dt} - \left(\frac{\partial f_\alpha}{\partial t}\right)_c\right] d\vec{v} \quad = \quad 0 \tag{2.7}$$

$$\int m\vec{u} \left[\frac{df_\alpha}{dt} - \left(\frac{\partial f_\alpha}{\partial t}\right)_c\right] d\vec{v} \quad = \quad 0 \tag{2.8}$$

$$\int \frac{1}{2} m\vec{u}^2 \left[\frac{df_\alpha}{dt} - \left(\frac{\partial f_\alpha}{\partial t}\right)_c\right] d\vec{v} \quad = \quad 0. \tag{2.9}$$

Integration of the collision term yields terms which describe momentum and energy transfer between different particle species, while the terms between particles of the same species vanish due to conservation of total momentum and energy [9].
With the following definitions

[1] This term is called collision term and can formally be written as $\left(\frac{\partial f_\alpha}{\partial t}\right)_c = \sum_\beta C_{\alpha\beta}$, where β denotes all plasma species

- particle density

$$n_\alpha = \int f_\alpha d\vec{v} \tag{2.10}$$

- center of mass velocity

$$\vec{u}_\alpha = \frac{1}{n_\alpha} \int \vec{v} f_\alpha d\vec{v}, \tag{2.11}$$

- thermal (random) particle velocity

$$\vec{w}_\alpha = \vec{v} - \vec{u}_\alpha, \tag{2.12}$$

we can further introduce the quantities [9]

- friction density

$$\vec{R}_{\alpha\beta} = m_\alpha \int \vec{w}_\alpha C_{\alpha\beta} d\vec{w}_\alpha \tag{2.13}$$

- pressure tensor

$$P_\alpha = m_\alpha \int \vec{w}_\alpha \vec{w}_\alpha^T f_\alpha d\vec{v} \tag{2.14}$$

- heat transfer between unlike particle species $\alpha \neq \beta$

$$Q_{\alpha\beta} = \frac{1}{2} \int w_\alpha^2 C_{\alpha\beta} d\vec{w}_\alpha \tag{2.15}$$

- heat flux

$$\vec{h}_\alpha = \frac{1}{2} m_\alpha \int w_\alpha^2 \cdot \vec{w}_\alpha f_\alpha d\vec{v}. \tag{2.16}$$

With this, performing the integrals in eqs. (2.7 - 2.9), we obtain the moment equations

- continuity equation

$$\frac{\partial n_\alpha}{\partial t} + \nabla \cdot (n_\alpha \vec{u}_\alpha) \quad = \quad 0 \tag{2.17}$$

- momentum equation

$$m_\alpha n_\alpha \left[\frac{\partial \vec{u}_\alpha}{\partial t} + (\vec{u}_\alpha \cdot \nabla) \vec{u}_\alpha \right] - q_\alpha n_\alpha (\vec{E} + \vec{u}_\alpha \times \vec{B}) + \nabla \cdot P_\alpha \quad = \quad R_{\alpha\beta} \tag{2.18}$$

- energy equation

$$\frac{3}{2}n_\alpha k_B \frac{dT_\alpha}{dt} + (P_\alpha \cdot \nabla)\vec{u}_\alpha + \nabla \cdot \vec{q}_\alpha = Q_{\alpha\beta}, \tag{2.19}$$

where k_B is the Boltzmann constant. This procedure never yields a closed equation system: every moment equation includes the moment of the next order. A common choice for a closure equation is the adiabacity condition and will be given later in the framework of the final, one-species ideal MHD equation. Together with the Maxwell equations

$$\nabla \times \vec{E} = -\frac{\partial \vec{B}}{\partial t} \tag{2.20}$$

$$\nabla \cdot \vec{B} = 0 \tag{2.21}$$

$$\nabla \times \vec{B} = \mu_0 \vec{j} + \frac{1}{c^2}\frac{\partial \vec{E}}{\partial t} \tag{2.22}$$

$$\nabla \cdot \vec{E} = \frac{\sigma}{\epsilon_0}, \tag{2.23}$$

where

$$\sigma = \sum_\alpha q_\alpha n_\alpha \tag{2.24}$$

$$\tag{2.25}$$

is the total charge density and

$$\vec{j} = \sum_\alpha q_\alpha n_\alpha \vec{u}_\alpha \tag{2.26}$$

the total current density, eqs. (2.17) - (2.19) give a general MHD description of a plasma for an arbitrary number of species.

2.1.3 Single fluid equations

For our purpose, the plasma is further considered to consist of only 2 species, electrons and ions[2]: $\alpha = \{\mathrm{e}, \mathrm{i}\}$. The single fluid ideal MHD equations are now obtained eliminating phenomena happening on a fast time scale, having short wavelength.
The first assumption is that all velocities are assumed to be small against the speed of light. This is formally achieved by

$$c \to \infty \tag{2.27}$$

or equivalently for the vacuum permittivity

$$\epsilon_0 = \frac{1}{\mu_0 c^2} \to 0. \tag{2.28}$$

This has two consequences concerning the Maxwell equations:

[2] e.g. deuterium ions

- in eq. (2.22), the displacement current can be neglected

$$\nabla \times \vec{B} \approx \mu_0 \vec{j} \tag{2.29}$$

- eq. (2.23) implies quasi-neutrality of the plasma

$$n := n_i - n_e = \frac{\epsilon_0}{e} \nabla \cdot \vec{E} \approx 0. \tag{2.30}$$

In a second assumption we neglect the electron mass, as it is very small in comparison to the ion mass. All electron responses to forces are thus instantaneous. With this, the momentum equation (2.18) for $\alpha = e$ now reads

$$-en(\vec{E} + \vec{u}_e \times \vec{B}) + \nabla \cdot P_e = \vec{R}_{e\beta}. \tag{2.31}$$

Considering only a scalar, isotropic pressure p_α instead of a pressure tensor P_α and introducing the single fluid variables

$$\begin{aligned} \vec{v} &= \vec{u}_i && (2.32)\\ p &= p_e + p_i && (2.33)\\ \rho &= m_i n && (2.34)\\ \vec{j} &= en(\vec{u}_i - \vec{u}_e) && (2.35) \end{aligned}$$

then gives us the final single fluid ideal MHD equations

$$\begin{aligned} \frac{\partial \rho}{\partial t} + \nabla \cdot (\rho \vec{v}) &= 0 && (2.36)\\ \rho \frac{d\vec{v}}{dt} &= \vec{j} \times \vec{B} - \nabla p && (2.37)\\ \vec{E} + \vec{v} \times \vec{B} &= 0 && (2.38)\\ \nabla \times \vec{E} &= -\frac{\partial \vec{B}}{\partial t} && (2.39)\\ \nabla \times \vec{B} &= \mu_0 \vec{j} && (2.40)\\ \nabla \cdot \vec{B} &= 0. && (2.41) \end{aligned}$$

As closure condition, we choose the adiabatic law of state

$$\frac{d}{dt}\left(\frac{p}{\rho^\gamma}\right) = 0, \tag{2.42}$$

where γ is the adiabatic index. The friction term $R_{\alpha\beta} = 0$ in eq. (2.37) because $\vec{R}_{ei} = -\vec{R}_{ie}$, and eq. (2.37) is obtained by adding the corresponding momentum equations for ions and electrons.

2.2 The Grad Shafranov equation

The Grad Shafranov equation [13], [14] determines the equilibrium for an axisymmetric plasma (no dependence in toroidal direction) within the framework of ideal MHD. Under the condition of a static (time-independent) equilibrium, the basic equation (2.37) is the force balance

$$\nabla p = \vec{j} \times \vec{B}. \tag{2.43}$$

We now rewrite this equation in a suitable way for the tokamak.

Using cylindrical coordinates (R, ϕ, Z), for axisymmetric plasmas the basic assumption is $\frac{\partial}{\partial \phi} = 0$ for any scalar quantity. With the vector potential $\vec{A}$, we can then write

$$\begin{aligned} \vec{B} &= \nabla \times \vec{A} \\ &= -\frac{\partial A_\Phi}{\partial z}\vec{e}_R + \frac{1}{R}\frac{\partial (RA_\Phi)}{\partial R}\vec{e}_Z + \left(\frac{\partial A_R}{\partial Z} - \frac{\partial A_Z}{\partial R}\right)\vec{e}_\Phi \\ &= B_R\vec{e}_R + B_Z\vec{e}_Z + B_\Phi\vec{e}_\Phi \\ &= \vec{B}_p + B_\Phi\vec{e}_\Phi, \end{aligned} \tag{2.44}$$

i.e. a decomposition in poloidal and toroidal direction. Introducing the stream function ψ as

$$\psi = RA_\Phi, \tag{2.45}$$

the R and Z components of $\vec{B}$ read as

$$B_R = -\frac{1}{R}\frac{\partial \psi}{\partial Z} \tag{2.46}$$

$$B_Z = \frac{1}{R}\frac{\partial \psi}{\partial R} \tag{2.47}$$

and therefore

$$\vec{B}_p = \frac{1}{R}\nabla\psi \times \vec{e}_\Phi. \tag{2.48}$$

The stream function ψ is closely related to the poloidal flux ψ_p via

$$\psi_p = 2\pi\psi. \tag{2.49}$$

For the definition of poloidal and toroidal flux, compare fig. 2.1.

Using the decomposition from eq. (2.44) with Ampère's law gives

$$\mu_0\vec{j} = \nabla \times \left(\vec{B}_p + B_\Phi\vec{e}_\Phi\right). \tag{2.50}$$

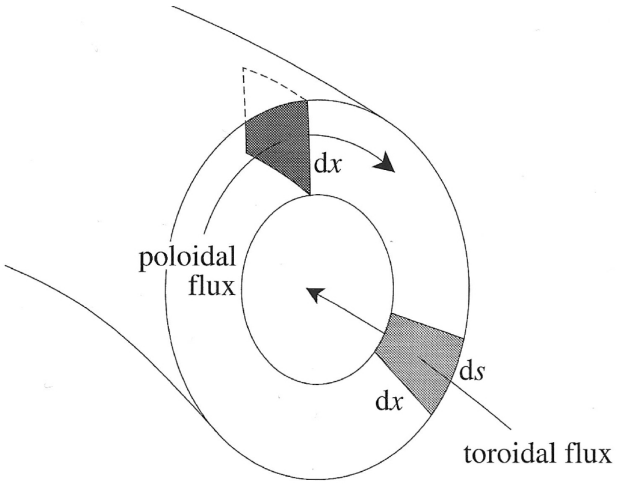

Figure 2.1: Poloidal and toroidal flux. Source: [15]

Evaluating the first term on the right hand side, we get

$$\nabla \times \vec{B}_p = \nabla \times \left(-\frac{1}{R}\frac{\partial \psi}{\partial Z}\vec{e}_R + \frac{1}{R}\frac{\partial \psi}{\partial R}\vec{e}_Z \right) \tag{2.51}$$

$$= -\left(\frac{\partial}{\partial R}\frac{1}{R}\frac{\partial \psi}{\partial R} + \frac{1}{R}\frac{\partial^2 \psi}{\partial Z^2} \right) \vec{e}_\Phi \tag{2.52}$$

$$= -\frac{1}{R}\Delta^* \psi \vec{e}_\Phi \tag{2.53}$$

with the elliptic differential operator

$$\Delta^* = R^2 \nabla \cdot \left(\frac{\nabla \psi}{R^2} \right). \tag{2.54}$$

The second term can be compactly written as

$$\nabla \times (B_\Phi \vec{e}_\Phi) = \frac{1}{R}\nabla (R B_\Phi) \times \vec{e}_\Phi. \tag{2.55}$$

Now multiplying the momentum equation with $\vec{B}$ yields

$$\vec{B} \cdot \nabla p = 0, \tag{2.56}$$

so there is no change in pressure along the magnetic field lines, i.e. the pressure is a function of the surface label only $p = p(\psi)$. In the same manner, multiplying with $\vec{j}$ and using eq. (2.50), we see that

$$R B_\Phi =: F \tag{2.57}$$

is also a surface quantity $F = F(\psi)$. It is related to the poloidal current via

$$I_p(\psi) = -2\pi F(\psi). \tag{2.58}$$

We can therefore write

$$\nabla p = \frac{\partial p}{\partial \psi}\nabla\psi \tag{2.59}$$

$$\nabla F = \frac{\partial F}{\partial \psi}\nabla\psi. \tag{2.60}$$

In the last step, we use the momentum equation eq. (2.43) together with eqs. (2.44), (2.50) and (2.59):

$$\begin{aligned}
\nabla p &= \frac{\partial p}{\partial \psi}\nabla\psi = \vec{j}\times\vec{B} \\
&= \left(\vec{j}_\Phi + \vec{j}_p\right)\times\left(\vec{B}_\Phi + \vec{B}_p\right) \\
&= \vec{j}_\Phi\times\vec{B}_p + \vec{j}_p\times\vec{B}_\Phi \\
&= -\frac{1}{\mu_0 R}\Delta^*\psi\cdot\vec{e}_\Phi\times\left(\frac{1}{R}\nabla\psi\times\vec{e}_\Phi\right) \\
&\quad + \left(\frac{1}{\mu_0 R}\nabla F\times\vec{e}_\Phi\right)\times B_\Phi\vec{e}_\Phi.
\end{aligned} \tag{2.61}$$

Calculating the first term on the right hand side gives

$$\begin{aligned}
-\frac{1}{\mu_0 R}\Delta^*\psi\cdot\vec{e}_\Phi\times\left(\frac{1}{R}\nabla\psi\times\vec{e}_\Phi\right) &= -\frac{1}{\mu_0 R^2}\Delta^*\psi\left[\vec{e}_\Phi\times(\nabla\psi\times\vec{e}_\Phi)\right] \\
&= -\frac{1}{\mu_0 R^2}\Delta^*\psi\nabla\psi,
\end{aligned} \tag{2.62}$$

because

$$\nabla\psi\cdot\vec{e}_\Phi = 0. \tag{2.63}$$

The second term on the right hand side is

$$\begin{aligned}
\left(\frac{1}{\mu_0 R}\nabla F\times\vec{e}_\Phi\right)\times B_\Phi\vec{e}_\Phi &= \left(\frac{1}{\mu_0 R}\frac{\partial F}{\partial\psi}\nabla\psi\times\vec{e}_\Phi\right)\times B_\Phi\vec{e}_\Phi \\
&= -\frac{B_\Phi}{R}\frac{\partial F}{\partial\psi}\nabla\psi + \left(\frac{1}{R}\frac{\partial F}{\partial\psi}\nabla\psi\cdot B_\Phi\vec{e}_\Phi\right)\vec{e}_\Phi \\
&= -\frac{1}{\mu_0 R^2}F\frac{\partial F}{\partial\psi}\nabla\psi.
\end{aligned} \tag{2.64}$$

Projecting eq. (2.61) on $\nabla\psi$, we obtain the Grad Shafranov equation

$$\Delta^*\psi = -\mu_0 R^2\frac{\partial p}{\partial\psi} - F\frac{\partial F}{\partial\psi}. \tag{2.65}$$

The functions p and F can be considered free functions and cannot be gained through MHD a priori. They must be taken from models, as input from experimental observations or other theories beyond the scope of MHD.

2.3 Extended energy principle

We present the two major methods to address the stability of equilibria within the framework of ideal MHD, formulated as initial value problem and eigenvalue problem. Correspondence between both formulations can be shown, see e.g. [9]. We assume that perturbations to the plasma are small and consequently linearize all relevant plasma quantities $\vec{C}(\vec{r},t)$ around their equilibrium values $\vec{C}_0(\vec{r})$:

$$\vec{C}(\vec{r},t) = \vec{C}_0(\vec{r}) + \vec{C}_1(\vec{r},t) \tag{2.66}$$

with pertubations $\left|\frac{\vec{C}_1}{\vec{C}_0}\right| \ll 1$.
We only consider static equilibria, i.e.

$$\vec{v}_0 = 0 \tag{2.67}$$
$$\vec{E}_0 = 0. \tag{2.68}$$

2.3.1 Initial value problem formulation

Using the above approach with the ideal MHD equations (2.36 - 2.42), the time evolution for the perturbed quantities read as [9]

$$\frac{\partial \rho_1}{\partial t} = -\nabla \cdot \rho_0 \vec{v}_1 \tag{2.69}$$
$$\rho_0 \frac{\partial \vec{v}_1}{\partial t} = -\nabla p_1 + \frac{1}{\mu_0}\left(\nabla \times \vec{B}_1\right) \times \vec{B}_0 + \frac{1}{\mu_0}\left(\nabla \times \vec{B}_0\right) \times \vec{B}_1 \tag{2.70}$$
$$\frac{\partial p_1}{\partial t} = -\vec{v}_1 \cdot \nabla p_0 - \gamma p_0 \nabla \cdot \vec{v}_1 \tag{2.71}$$
$$\frac{\partial \vec{B}_1}{\partial t} = \nabla \times \left(\vec{v}_1 \times \vec{B}_0\right) \tag{2.72}$$

together with

$$\nabla \cdot \vec{B}_1 = 0 \tag{2.73}$$
$$\mu_0 \vec{j}_1 = \nabla \times \vec{B}_1. \tag{2.74}$$

Introducing the displacement vector $\vec{\xi}$ by

$$\frac{\partial \vec{\xi}}{\partial t} = \vec{v}_1, \tag{2.75}$$

the perturbed quantities can be expressed in terms of $\vec{\xi}$:

$$\vec{B}_1 = \nabla \times \left(\vec{\xi} \times \vec{B}_0\right) \tag{2.76}$$
$$p_1 = -\vec{\xi} \cdot \nabla p_0 - \gamma p_0 \nabla \cdot \vec{\xi} \tag{2.77}$$
$$\rho_1 = -\nabla \cdot \left(\vec{\xi}\rho_0\right). \tag{2.78}$$

Inserting this into eq. (2.70) gives the equation of motion for a pertubation $\vec{\xi}$ applied at the time $t = 0$ [9]:

$$\rho_0 \frac{\partial^2}{\partial t^2}\vec{\xi} = \frac{1}{\mu_0}\left(\nabla \times \vec{B}_0\right) \times \left(\nabla \times \left(\vec{\xi} \times \vec{B}_0\right)\right) + \frac{1}{\mu_0}\left(\nabla \times \left(\nabla \times \left(\vec{\xi} \times \vec{B}_0\right)\right)\right) \times \vec{B}_0 + \nabla\left(\vec{\xi} \cdot \nabla p_0 + \gamma p_0 \nabla \cdot \vec{\xi}\right). \tag{2.79}$$

With initial values for $\vec{\xi}(\vec{r}, 0)$ and $\vec{v}_1(\vec{r}, 0)$, eq. (2.79) allows for the computation of the full time evolution of all plasma quantities considered.

2.3.2 Eigenvalue problem formulation

But often, one is just interested if the equilibrium is stable or unstable, together with a growth rate for the instability; this is the second formulation.
To this purpose, one rewrites eq. (2.79) as a normal mode problem, i.e. an eigenvalue problem. This can be achieved by Fourier analysis of the perturbed quantities

$$\vec{C}_1(\vec{r}, t) = \vec{C}_1(\vec{r}) \exp(-i\omega t). \tag{2.80}$$

For simplicity, we denote both $\vec{C}_1(\vec{r}, t)$ and $\vec{C}_1(\vec{r})$ with the same function symbol. Repeating the steps described above yields the time-independent eigenvalue equation

$$-\omega^2 \rho_0 \vec{\xi} = \vec{F}(\vec{\xi}) \tag{2.81}$$

with the force operator

$$\vec{F}(\vec{\xi}) = \frac{1}{\mu_0}\left(\nabla \times \vec{B}_1\right) \times \vec{B}_0 + \frac{1}{\mu_0}\left(\nabla \times \vec{B}_0\right) \times \vec{B}_1 \tag{2.82}$$

$$+\nabla\left(\vec{\xi} \cdot \nabla p_0 + \gamma p_0 \nabla \cdot \vec{\xi}\right). \tag{2.83}$$

As can be shown, see e.g. [6], $\vec{F}$ is self-adjoint and therefore the eigenvalues ω^2 are real in ideal MHD. The sign of ω^2 then determines oscillatory behavior or exponential instability of the physical quantities in question, which greatly simplifies calculations if one is only interested in tests for stability / instability, but not the actual values of growth rates. The spectrum of $\vec{F}$ involves discrete and continuous regions, but continuous values only appear in the stable part and thus analytical difficulties can be ignored when only investigating unstable modes.
From eq. (2.81), one can derive the extended energy principle for ideal MHD. This reformulates the stability problem as a criterion for the change in the potential energy δW of the plasma and explicitly shows the different driving terms for instabilities.
Multiplying eq. (2.81) with the complex conjugate $\vec{\xi}^*$ and integrating over the plasma volume yields

$$\omega^2 K(\vec{\xi}) = \delta W(\vec{\xi}) \tag{2.84}$$

with

$$\delta W = \frac{1}{2}\int dV \vec{\xi}^* \cdot \vec{F}(\vec{\xi}) \tag{2.85}$$

and the kinetic energy associated with the perturbation $\vec{\xi}$

$$\omega^2 K = \frac{1}{2}\int dV \rho \left|\vec{\xi}\right|^2, \tag{2.86}$$

which always satisfies $K > 0$. As the total energy is conserved in ideal MHD, the question of stability can be reduced to the sign of $\delta W(\vec{\xi})$: if $\delta W \geq 0$ for all physically allowed perturbations $\vec{\xi}$ of the plasma, the system is stable. If a $\vec{\xi}$ can be found for which $\delta W \leq 0$, the system is exponentially unstable. The authors of [16] gave an elementary proof of both the sufficiency and the necessity of this statement. Furthermore, they could show that for a perturbation $\eta(\vec{r})$ for which $\delta W(\eta) \leq 0$ with initial conditions

$$\vec{\xi}(\vec{r}, 0) = \eta(\vec{r}) \tag{2.87}$$

$$\frac{\partial \vec{\xi}}{\partial t}(\vec{r}, 0) = 0, \tag{2.88}$$

there exists a $\vec{\xi}(\vec{r}, t)$ that grows $\sim \exp(\lambda t)$, with a growth rate $\lambda \geq \sqrt{\frac{-\delta W(\eta)}{K(\eta)}}$.
In principle, this approach could be used to analyze a system consisting of plasma - vacuum region - wall. However, as the vacuum fields do not appear explicitly, one would have to deal with e.g. complicated pressure balance jump conditions at the interface plasma - vacuum region as an additional constraint. In [17] it was shown that these additional conditions can be incorporated into δW, and the latter quantity can furthermore be separated into three terms for the plasma (P), the plasma surface (S) and the vacuum (V):

$$\delta W = \delta W_P + \delta W_S + \delta W_V. \tag{2.89}$$

With the indices $\perp$ and $\parallel$ denoting the directions perpendicular and parallel to the magnetic field $\vec{B}$, the individual terms are:

$$\delta W_P = \frac{1}{2}\int_P dV \left[\frac{\left|\vec{Q}\right|^2}{\mu_0} - \vec{\xi}_\perp^* \cdot (\vec{j}_0 \times \vec{Q}) + \gamma p_0 \left|\nabla \cdot \vec{\xi}\right|^2 + (\vec{\xi}_\perp \cdot \nabla p_0)\nabla \cdot \vec{\xi}_\perp^*\right] \tag{2.90}$$

$$\delta W_S = \frac{1}{2}\int_S dS \left|\vec{n} \cdot \vec{\xi}_\perp\right|^2 \vec{n} \cdot [\![\nabla \left(p_0 + \frac{B_0^2}{2\mu_0}\right)]\!] \tag{2.91}$$

$$\delta W_V = \frac{1}{2}\int_V dV \frac{\left|\vec{B}_1^V\right|^2}{\mu_0} \tag{2.92}$$

where $\vec{B}_1^V$ is the perturbed part of the vacuum magnetic field, $[\![x]\!]$ denotes the jump of x at the boundary and we have defined

$$\vec{Q} = \vec{B}_1 = \nabla \times (\vec{\xi} \times \vec{B}_0). \tag{2.93}$$

$$\tag{2.94}$$

Eqs. (2.89) - (2.92) represent the standard form of the extended energy principle.
An intuitive form of the plasma term δW_P, originally proposed in [18] and [19], can be

obtained from the standard form in eq. (2.90) by the decomposition

$$\begin{aligned} \left|\vec{Q}\right|^2 &= \left|\vec{Q}_\perp\right|^2 + \left|Q_\parallel\right|^2 \\ &= \vec{b}\cdot\vec{Q} + \vec{b}\times\vec{Q}. \end{aligned} \tag{2.95}$$

With this, δW_P can now be written as [9]

$$\begin{aligned} \delta W_P = \frac{1}{2}\int_P dV\{&\frac{\left|\vec{Q}_\perp\right|^2}{\mu_0} + \frac{B_0^2}{\mu_0}\left|\nabla\cdot\vec{\xi}_\perp + 2\vec{\xi}_\perp\cdot\vec{\kappa}\right| + \gamma p_0\left|\nabla\cdot\vec{\xi}\right|^2 \\ &-2\left(\vec{\xi}_\perp\cdot\nabla p_0\right)\left(\vec{\kappa}\cdot\vec{\xi}_\perp^*\right) - j_{0\parallel}\left(\vec{\xi}_\perp^*\times\vec{B}_0\right)\cdot\vec{Q}_\perp\}, \end{aligned} \tag{2.96}$$

where the curvature $\vec{\kappa}$ is defined as

$$\vec{\kappa} = \vec{b}\cdot\nabla\vec{b}. \tag{2.97}$$

The first three terms in eq. (2.96) are always positive and thus are stabilizing. From left to right, they are associated with the energy required to:

- bend magnetic field lines (shear Alfvén wave)
- compress magnetic field lines (compressional Alfvén wave)
- compress the plasma (sound wave)

The last two terms can have positive or negative signs and are the driving terms for instabilities. The term $\sim \vec{\xi}_\perp\cdot\nabla p_0$ may cause pressure driven modes, e.g. ballooning modes. The dominant driving term is $\vec{\kappa}\cdot\nabla p_0$.
The term $\sim j_{0\parallel}$ can cause current driven modes generally called kink modes. At low β, the main drive is the current density and the current density gradient, while at high β also the pressure gradient contributes to the mode, c.f. chapter 2.5.1 below.

When there are no surface currents, the term δW_S is zero and has no influence on stability. The vacuum contribution δW_V is always positive and consequently stabilizing.

2.4 Ballooning modes

Ballooning modes are internal, pressure-driven modes. Internal modes are defined to cause no perturbations of the plasma-vacuum interface. They are usually localized in the direction perpendicular to the magnetic field, meaning $k_\perp \gg \frac{1}{a}$, but have longer parallel wavelength $\frac{k_\parallel}{k_\perp} \ll 1$, where a is the minor radius of the plasma and $k_\parallel$, $k_\perp$ are the wave numbers in the direction parallel and perpendicular to the magnetic field. As we have seen in eq. (2.96), the driving term is $\sim \vec{\kappa}\cdot\nabla p_0$. If the curvature $\vec{\kappa}$ and the pressure gradient ∇p_0 have same signs, this term is destabilizing. This is the case at the low field side of the torus and above a critical value $\nabla p_0 \sim \beta$, the plasma becomes unstable to ballooning modes.

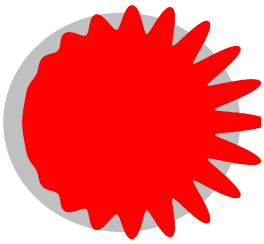

Figure 2.2: Schematic structure of a ballooning mode. Source: [20]

2.4.1 The ballooning transformation

Exploiting the wavelength characteristics for the parallel and perpendicular direction, we write $\vec{\xi}_\perp$ in an eikonal form

$$\vec{\xi}_\perp = \vec{\eta}_\perp \exp(iS) \tag{2.98}$$

with

$$\vec{k}_\perp = \nabla S \tag{2.99}$$
$$\vec{B} \cdot \nabla S = 0. \tag{2.100}$$

This representation includes a slowly varying quantity $\vec{\eta}_\perp$ and a rapidly varying quantity S, with regard to the typical equilibrium length scale a:

$$\frac{|a\nabla\vec{\eta}_\perp|}{|\vec{\eta}_\perp|} \sim 1 \tag{2.101}$$
$$|a\nabla S| \gg 1. \tag{2.102}$$

Inserting eq. (2.98) in the intuitive form of δW_F in eq. (2.96) gives

$$\begin{aligned}\delta W_P = \frac{1}{2\mu_0}\int dV \Bigg[&\left|\nabla\times(\vec{\eta}_\perp\times\vec{B}_0)\right|_\perp^2 + B_0^2\left|i\vec{k}_\perp\cdot\vec{\eta}_\perp + \nabla\cdot\vec{\eta}_\perp + 2\vec{\kappa}\cdot\vec{\eta}_\perp\right|^2 \\ &-2\mu_0\,(\vec{\eta}_\perp\cdot\nabla p_0)(\vec{\eta}_\perp^*\cdot\vec{\kappa}) - \mu_0 j_{0\parallel}(\vec{\eta}_\perp^*\times\vec{b}_0)\cdot\Big(\nabla\times(\vec{\eta}_\perp\times\vec{B}_0)\Big)_\perp\Bigg],\end{aligned} \tag{2.103}$$

where the term $\sim \left|\nabla\cdot\vec{\xi}\right|^2$ describing plasma compressibility has been dropped, because in an equilibrium with shear, a $\vec{\xi}_\parallel$ can always be found that makes this term vanish [9].
Eq. (2.103) can now be minimized order by order using the expansion

$$\vec{\eta}_\perp = \eta_{\perp 0} + \eta_{\perp 1} + \dots \tag{2.104}$$

with

$$\frac{|\eta_{\perp i+1}|}{|\eta_{\perp i}|} \sim \frac{1}{k_\perp a} \ll 1. \tag{2.105}$$

As we want to consider the limit $\vec{k}_\perp \to \infty$, only the expansion terms $\eta_{\perp 0}$ and $\eta_{\perp 1}$ are kept. Expanding δW_P accordingly, the first nonvanishing contribution occurs in the second order

term δW_{P2}.
To avoid confusion between equilibrium quantities and expansion indices, we drop any labels indicating equilibrium quantities. One can further express [9]

$$\eta_{\perp 0} = X \frac{\vec{b}}{B^2} \times \vec{k}_\perp, \tag{2.106}$$

where X is some scalar function, slowly varying on the equilibrium length scale. With that, the remaining expression for δW_{P2} describing potential instabilities reads as

$$\delta W_{P2} = \frac{1}{2\mu_0} \int dV \left[k_\perp \left| \vec{b} \cdot \nabla X \right|^2 - \frac{2\mu_0}{B^2} (\vec{b} \times \vec{k}_\perp \cdot \nabla p)(\vec{b} \times \vec{k}_\perp \cdot \vec{\kappa}) \left| X \right|^2 \right]. \tag{2.107}$$

Eq. (2.107) represents the change in the potential energy for localized instabilities for general multidimensional systems within the limits of ideal MHD.

We now use tokamak flux coordinates (ψ, θ, ϕ) (see e.g [9]) to rewrite the expression for δW_2 into an explicitly one-dimensional integral, i.e. rewrite the terms dV, $\vec{b} \cdot \nabla X$ and $\vec{b} \times \vec{k}_\perp$ in eq. (2.107).
The volume element in these coordinates is simply

$$dV = 2\pi J d\psi d\varphi \tag{2.108}$$

with J being the Jacobian for the transformation $(R, Z, \phi) \rightarrow (\psi, \theta, \phi)$. Defining a set of locally orthogonal unit vectors

$$\begin{aligned} \vec{n} &= \frac{\nabla \psi}{|\nabla \psi|} \\ \vec{t} &= \frac{B_\phi}{B} \vec{b}_p - \frac{B_p}{B} \vec{e}_\phi \\ \vec{b} &= \frac{B_p}{B} \vec{b}_p + \frac{B_\phi}{B} \vec{e}_\phi, \end{aligned} \tag{2.109}$$

we can decompose $\vec{k}$ as

$$\vec{k} = k_n \vec{n} + k_t \vec{t} \tag{2.110}$$

with components

$$k_n = \vec{n} \cdot \nabla S \tag{2.111}$$

$$k_t = \vec{t} \cdot \nabla S. \tag{2.112}$$

In flux coordinates, S reads as

$$\nabla S = \frac{\partial S}{\partial \psi} \nabla \psi + \frac{\partial S}{\partial \theta} \nabla \theta + \frac{\partial S}{\partial \phi} \nabla \phi \tag{2.113}$$

and therefore

$$k_n = (\vec{n} \cdot \nabla \psi) \frac{\partial S}{\partial \psi} \tag{2.114}$$

$$k_t = (\vec{t} \cdot \nabla \theta) \frac{\partial S}{\partial \theta} + (\vec{t} \cdot \vec{e}_\Phi) \frac{1}{R} \frac{\partial S}{\partial \phi} \tag{2.115}$$

Using this decomposition of $\vec{k}$, we can write the second term in question as

$$\vec{b} \cdot \nabla X = k_t \vec{n} - k_n \vec{t} \tag{2.116}$$

The last term $\vec{b} \times \vec{k}_\perp$ that needs rewriting can simply be expressed as

$$\vec{b} \times \vec{k}_\perp = \frac{1}{JB} \frac{\partial X}{\partial \theta} \tag{2.117}$$

There is no dependence of X on the toroidal angle ϕ, as this is completely accounted for in $S(\psi, \theta, \phi)$, as can be seen as follows: assuming axisymmetry, one can Fourier analyze $\vec{\xi}(\psi, \theta, \phi)$ with respect to the toroidal coordinate ϕ. This is possible because of the axisymmetry of the plasma, so we can assume decoupling of toroidal modes, which are labeled with the toroidal mode number n. Choosing a specific n, we have [9]

$$\vec{\xi}(\psi, \theta, \phi) = \vec{\xi}(\psi, \theta) \exp(-in\phi). \tag{2.118}$$

Comparing this with the eikonal representation eq. (2.98), we can write

$$\vec{\xi}(\psi, \theta) = \eta_\perp \exp\left(i\tilde{S}(\psi, \theta)\right) \tag{2.119}$$

and thus

$$\begin{aligned} \vec{\xi}(\psi, \theta, \phi) &= \vec{\xi}(\psi, \theta) \exp(-in\phi) \\ &= \eta_\perp \exp\left(i\tilde{S}(\psi, \theta)\right) \exp(-in\phi) \\ &= \eta_\perp \exp\left(i(\tilde{S}(\psi, \theta) - n\phi)\right). \end{aligned} \tag{2.120}$$

Therefore

$$S(\psi, \theta, \phi) = -n\phi + \tilde{S}(\psi, \theta). \tag{2.121}$$

For large n, this guarantees the desired rapid oscillation of the eikonal exponent. Combining the above gives the final one-dimensional expression of the change in potential energy for ballooning modes:

$$\delta W_{P2} = \frac{\pi}{\mu_0} \int d\psi W(\psi) \tag{2.122}$$

with

$$W(\psi) = \int_0^{2\pi} J d\theta \left[(k_n^2 + k_t^2) \left(\frac{1}{JB} \frac{\partial X}{\partial \theta} \right)^2 - \frac{2\mu_0 R B_p}{B^2} \frac{dp}{d\psi} (k_t^2 \kappa_n - k_t k_n \kappa_t) X^2 \right], \tag{2.123}$$

where the curvature κ has been decomposed as $\vec{k}$ in eq. (2.110).
However, there is a difficulty associated with configurations with shear $q' \neq 0$. Eq. (2.100) can be written as

$$\frac{B_\phi}{R} \frac{\partial S}{\partial \phi} + \frac{1}{J} \frac{\partial S}{\partial \theta} = 0, \tag{2.124}$$

and using this with the decomposition in eq. (2.121), we can write

$$\begin{aligned} & -\frac{B_\phi}{R}n + \frac{1}{J}\frac{\partial \tilde{S}}{\partial \theta} = 0 \\ \Longrightarrow \quad & \tilde{S} = n\int_{\varphi_0}^{\theta} d\theta' \frac{JB_\phi}{R} \\ \Longrightarrow \quad & S = n\left(-\phi + \int_{\theta_0}^{\varphi} d\theta' \frac{JB_\phi}{R}\right) \end{aligned} \tag{2.125}$$

The function S has to be periodic in the poloidal angle:

$$S(\phi, \psi, \theta + 2\pi) \equiv S(\phi, \psi, \theta) \tag{2.126}$$

But with the formulation so far, this cannot be matched with the original conditions [9], [21] for the eikonal representation in eq. (2.98): the quantity η should vary slowly, while $\exp(iS)$ should oscillate rapidly. This can be seen as follows:
Expanding S about a resonant surface ψ_0 gives

$$S \approx n\left(-\phi + \int_{\theta_0}^{\theta} \frac{JB_\phi}{R}\bigg|_{\psi_0} d\theta' + (\psi - \psi_0)\int_{\theta_0}^{\varphi} \frac{\partial}{\partial \psi}\frac{JB_\phi}{R}\bigg|_{\psi_0} d\theta'\right) \tag{2.127}$$

The third term on the right hand side of eq. (2.127) is related to the shear and only vanishes for $\psi = \psi_0$, i.e. a mode localized exactly at this flux surface. But even for a small radial extend $\psi - \psi_0$, the quantity $n(\psi - \psi_0)$ has to be considered for $n \gg 1$ and breaks the periodicity constraint.
This can be overcome by the ballooning transformation developed in [21]. For axisymmetric plasmas, performing a Fourier decomposition of the displacement $\vec{\xi}$ in the toroidal angle

$$\vec{\xi} = \exp(-in\phi)\vec{\xi}(\psi, \theta), \tag{2.128}$$

gives the normal mode formulation 2.81 in the form

$$\begin{aligned} \vec{F}(\vec{\xi})\vec{\xi}(\psi, \theta) &= \vec{F}(\psi, \theta)\vec{\xi}(\psi, \theta) \\ &= -\omega^2 \rho \vec{\xi}(\psi, \theta). \end{aligned} \tag{2.129}$$

The displacement $\vec{\xi}(\psi, \theta)$ can now be written as

$$\vec{\xi}(\psi, \theta) = \sum_m \exp(-im\theta)\int_{-\infty}^{+\infty} \exp(im\chi)\vec{\xi}_Q(\psi, \chi)d\chi \tag{2.130}$$

with the so-called quasimode $\vec{\xi}_Q$ and the ballooning angle χ. This formulation automatically ensures peroidicity of $\vec{\xi}$ in the poloidal angle φ if it satisfies the convergence property

$$\vec{\xi}_Q(\psi, \chi \to \pm\infty) \to 0. \tag{2.131}$$

The quasimode itself does not have to satisfy any periodicity restraints. By direct substitution of eq. (2.130) into eq. (2.129), one can see that the quasimode formally obeys the same eigenvalue equation as the original $\vec{\xi}(\psi, \varphi)$:

$$\vec{F}(\psi, \chi)\left(\vec{\xi}_Q(\psi, \chi)\right) = -\omega^2 \rho \vec{\xi}_Q(\psi, \chi). \tag{2.132}$$

The whole eikonal analysis for ballooning modes can now be repeated for a quasimode, with the only difference that the domain of integration for the poloidal angle now extends over $\pm\infty$. The actual displacement can then be constructed as in eq. (2.130. The quantity δW can be subsequently minimized by an expansion in $\frac{1}{\sqrt{n}}$ and to lowest order reads as in eqs. (2.122) and (2.123) with

$$k_n = n\left[RB_p\int_{\chi_0}^{\chi}\frac{\partial}{\partial\psi}\left(\frac{JB_\phi}{R}\right)d\chi'\right] \tag{2.133}$$

$$k_t = \frac{nB}{RB_p}. \tag{2.134}$$

Stability against ballooning modes can thus be tested separately on each flux surface, which requires a solution ψ of the Grad Shafranof equation.
The detailed calculation is done in [21] and shows that the most unstable ballooning modes occur in the limit $n\to\infty$. Furthermore, the higher order corrections depend only on terms of the lowest order approximation. Corrections to the leading order for $n\to\infty$ are of order $\mathcal{O}(\frac{1}{n})$ and are always stabilizing . For a ballooning mode with toroidal mode number n, the enveloping function of the poloidal harmonics of the radial displacement is a Gaussian and spans $\approx\sqrt{n}$ rational flux surfaces, i.e. has a width of $\approx\frac{a}{nqs}$.

However, the ballooning formalism requires corrections when applied to the plasma edge as described in [22]. In this case, integration over ψ extends to the plasma edge and thus renders the assumptions of the balloning formalism invalid. This can be understood in a simple physical picture: the ballooning transformation includes a quantity X slowly varying over plasma dimensions. This is always violated at the edge, where the pressure gradient drops from a finite value inside the separatrix to zero outside. This problem can be resolved by applying the ballooning transformation nevertheless, noting that only a few of the Fourier modes actually extend to the edge. The expansion is then done in powers of $\frac{1}{\sqrt[3]{n}}$ instead of $\frac{1}{\sqrt{n}}$. The derivations follow basically the same structure as in [21] and give the following modifications to the previously considered ballooning formalism:
The enveloping function is now an Airy function and spans only $\approx\sqrt[3]{n}$ rational surfaces resp. has a width of $\approx\frac{a}{\sqrt[3]{nqs}}$. The finite n correction to the leading order is of order $\mathcal{O}(\frac{1}{\sqrt[3]{n^2}})$ and thus larger for all n, while it remains stabilizing for all cases. When there is now coupling to peeling modes, the stability boundary at $n\to\infty$ is the same as for conventional ballooning theory.
Numerical calculations are presented in [22], which can also serve as a starting point for the development of the coupled peeling-ballooning model described in 5.3.1.

The simplest, least restrictive test for stability based on the energy principle for ballooning modes is the Mercier criterion. If it is fulfilled, the plasma is stable against interchange modes and the ballooning formalism is valid [9]. In that case, the plasma can of course still be unstable against ballooning modes. If it is violated, the ballooning formalism can no longer be applied; this however is irrelevant as the plasma equilibrium is already unstable. In case of a circular plasma with large aspect ratio and $\beta_p\approx 1$, this stability criterion simplifies

substantially to [9]

$$\left(\frac{r}{q}\frac{dq}{dr}\right)^2 + \frac{8r\mu_0}{B_0^2}\frac{dp}{dr}(1-q^2) > 0, \tag{2.135}$$

i.e. $q > 1$ has a stabilizing effect on the negative pressure gradient.

As shown in e.g. [23], shaping of the plasma modifies the stability criterion on the magnetic axis:

$$q_0^2 > 1 \rightarrow q_0^2\left\{1 - \frac{4}{1+3\kappa^2}\left[\frac{3}{4}\frac{\kappa^2-1}{\kappa^2+1}\left(\kappa^2 - \frac{2\delta}{\epsilon}\right) + \frac{\beta_{p0}(\kappa-1)^2}{\kappa^2+\kappa}\right]\right\} > 1 \tag{2.136}$$

The effects of the elongation κ, triangularity δ and poloidal β on axis β_{p0} can be summarized as follows (for the definitions see e.g. [9] and fig. 6.6):
For

$$\begin{array}{rcl} \kappa & > & 1 \\ \frac{\delta}{\epsilon} & > & \frac{\kappa^2}{2} \\ \beta_{p0} & = & 0, \end{array}$$

the shaping has stabilizing effects, for other combinations the effect is either zero ($\kappa = 1$) or destabilizing. Thus a desirable plasma shaping is that of suitable D-shape, compare [9] and the references therein.

2.4.2 The $s - \alpha$ model

Minimizing the ballooning mode energy equation (2.122) with respect to X leads to an Euler-Lagrange equation [9]

$$\frac{\partial}{\partial\theta}\left(f\frac{\partial X}{\partial\theta}\right) - gX = 0 \tag{2.137}$$

with

$$f = \frac{1}{JB^2}\left(k_n^2 + k_t^2\right) \tag{2.138}$$

$$g = -\frac{2\mu_0 JRB_p}{B^2}\frac{dp}{d\psi}\left(k_t^2\kappa_n - k_t k_n \kappa_t\right). \tag{2.139}$$

For a large aspect ratio, circular tokamak with low $\beta \approx \epsilon^2$, to leading order eq. (2.137) can be further written in cylindrical coordinates

$$\frac{\partial}{\partial\theta}\left[(1+\Lambda^2)\frac{\partial X}{\partial\theta}\right] + \alpha(\Lambda sin\theta + cos\theta)X = 0 \tag{2.140}$$

with

$$\Lambda = s(\theta - \theta_0) - \alpha(\sin\theta - \sin\theta_0), \tag{2.141}$$

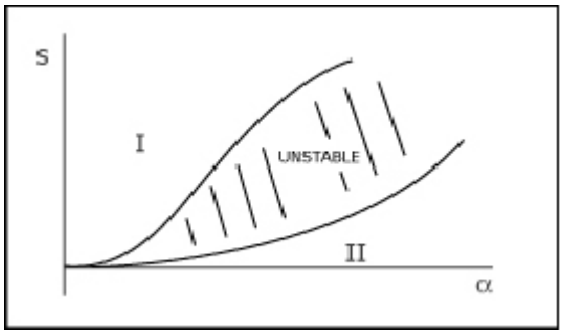

Figure 2.3: $s - \alpha$ diagram. Source: [25]

where θ_0 are integration constants, the normalized pressure gradient

$$a := -\frac{2\mu_0 r^2}{R_0 B_\theta^2}\frac{dp}{dr} = -q^2 R_0 \frac{d\beta}{dr} \tag{2.142}$$

and average shear

$$s := \frac{r}{q}\frac{dq}{dr}. \tag{2.143}$$

A numerical solution of eq.(2.140) is shown in fig. (2.3).
The stable upper left part is called first region of stability. The limiting curve for stability can roughly be approximated by a linear fit $s \approx 1.6\alpha$. The stable lower left part is accordingly called the second region of stability and is only present if the pressure modulation of the local shear [9]

$$\tilde{s} := \frac{r}{q}\frac{\partial}{\partial r}\left(\frac{JB_\theta}{R_0}\right) \tag{2.144}$$

is taken into account[3]:

$$\tilde{s} = s - \alpha\cos\theta. \tag{2.145}$$

2.5 External kinks

External kink modes are mainly driven by the current gradient and finite current density at the edge of the plasma. At high β, also the pressure can provide a drive of kink modes. An indirect drive through a pressure gradient at the edge is due to the bootstrap current 5.2. They have long parallel wavelength $\frac{k_\parallel}{k_\perp} \ll 1$, but usually[4] low $k_\perp \approx \frac{1}{a}$. In due course, we only

[3] For this plasma geometry, there is no path from the first region to the second region not traversing unstable operational regimes. Numerical studies [24] show that this can be overcome by a bean-shaped plasma
[4] For high β, the external kink develops a more ballooning-like structure

consider external kink modes, which cause a distorsion of the plasma boundary. The internal kink, characterized by the mode numbers $m = n = 1$, can be stabilized by the requirement $q > 1$ everywhere in the plasma, which is assured for all investigated cases in our numerical studies, but in general not realistic for experiments. In general, external kink modes show larger values of the poloidal mode number m [26], the observation often being

$$\frac{m}{n} \approx q_{edge}, \tag{2.146}$$

as this is the resonance condition. The drive for kink modes decreases with increasing n. An example visualization of a kink mode is shown in fig. 2.4.

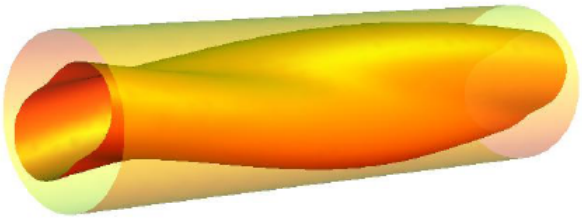

Figure 2.4: Pertubation structure of the plasma column for a kink mode. Adapted from: [26]

2.5.1 Stability

For a large aspect ratio, circular tokamak and low β it is possible [6] to derive δW for a perturbation $\vec{\xi}$: using cylindrical coordinates (r, θ, ϕ), we can use the ordering

$$\frac{\partial}{\partial r} \approx \frac{1}{r}\frac{\partial}{\partial \theta} \gg \frac{1}{R_0}\frac{\partial}{\partial \phi} \tag{2.147}$$

$$\xi_r \approx \xi_\theta \gg \xi_\phi, \tag{2.148}$$

assuming incompressibility

$$\nabla \cdot \vec{\xi} = 0. \tag{2.149}$$

Performing an expansion in ϵ, the perturbed parts of the magnetic field obey

$$B_{r1} \approx B_{\theta 1} \gg B_{\phi 1}. \tag{2.150}$$

With a the minor radius of the plasma and b the minor radius of a perfectly conducting wall, to leading order δW reads as

$$\begin{aligned} \delta W &= \pi R_0 \int_0^a \left(\frac{B_1^2}{\mu_0} - j_{z0}(B_{r1}\xi_\theta - B_{\theta 1}\vec{\xi_r} \right) d\theta r dr \\ &\quad + \pi R_0 \int_a^b \frac{B_{V1}^2}{\mu_0} d\theta r dr, \end{aligned} \tag{2.151}$$

with

$$B_1^2 = B_{r1}^2 + B_{\theta 1}^2 \tag{2.152}$$

and B_{V1} the magnetic field in the vacuum region between plasma and wall. Using a Fourier analysis of $\vec{\xi}$

$$\vec{\xi}(r,\theta,\phi) = \vec{\xi}(r)\exp(im\theta)\exp(-in\phi), \tag{2.153}$$

eq. (2.151) can be expressed as

$$\begin{aligned}\frac{\mu_0 R}{\pi^2 B_\phi^2}\delta W &= \int_0^a r\left[\left(r\frac{d\xi}{dr}\right)^2 + \left(m^2-1\right)\xi^2\right]\left(\frac{m}{n}-\frac{1}{q}\right)^2 dr \\ &+ \left[\frac{2}{q_a}\left(\frac{n}{m}-\frac{1}{q_a}\right) + (1+m\lambda)\left(\frac{n}{m}-\frac{1}{q_a}\right)^2\right] a^2\xi_a^2,\end{aligned} \tag{2.154}$$

with the definition

$$\lambda = \frac{1+\left(\frac{a}{b}\right)^2}{1-\left(\frac{a}{b}\right)^2}. \tag{2.155}$$

When $a \to b$, i.e. a vanishing vacuum region, the parameter λ becomes arbitrarily large and thus $\delta W > 0$ for all cases (also $\xi_a = 0$). If q is monotonically increasing with r, then inside the plasma $\frac{m}{n} < q_a$ for resonant surfaces and thus all modes will be stable, as the term $\frac{2}{q_a}\left(\frac{n}{m}-\frac{1}{q_a}\right)$ is the only possible destabilizing term. Outside the plasma $q \sim r^2$, and therefore resonant surfaces in the vacuum region close to the plasma can cause instabilites in the plasma.

A simple model can give estimates of the driving terms even for high β [9]. It assumes a circular plasma, constant pressure everywhere in the plasma and the whole current flowing on the plasma surface. Therefore the individual contributions to δW are

$$\delta W_P = \int_P \frac{B_1^2}{2\mu_0} dV \tag{2.156}$$

$$\delta W_V = \int_P \frac{B_{V1}^2}{2\mu_0} dV \tag{2.157}$$

$$\delta W_S = \frac{1}{2}\int_S \left|\vec{n}\cdot\vec{\xi}\right|^2 \vec{n}\cdot[\![\nabla\left(p+\frac{B^2}{2\mu_0}\right)]\!], \tag{2.158}$$

where the plasma and vacuum contributions are always positive. Performing the integral in eq. 2.158 gives

$$\delta W_S = -\epsilon^2 \frac{B_0^2 R_0}{\mu_0}\int_0^{2\pi} d\theta \left|\vec{n}\cdot\vec{\xi}\right|^2 \left[\left(\frac{B_\theta}{\epsilon B_0}\right)^2 + \frac{\beta_t}{\epsilon}\cos\theta\right], \tag{2.159}$$

with the torodial plasma β

$$\beta_t = \frac{2\mu_0 p}{B_0^2}. \tag{2.160}$$

The term $\sim B_\theta^2$ is connected with j_{tor} and thus is the current-driven part, while the second term $\sim \beta_t \cos\theta$ represents the pressure drive. On the high-field side, the latter is negative and thus stabilizing and vice versa, reflecting the ballooning structure. For low β, the second term is small compared to the current-driven first term, resulting in an almost purely current-driven kink mode.

3 Gyrofluid theory and the GEM model

We briefly outline the gyrokinetic formalism for the basic gyrokinetic equation underlying the gyrofluid model in toroidal geometry. The main points of the original gyrofluid model are presented, and the complete set of gyrofluid equations along with all corrections to the original model are given in the context of the GEM model.
For the basic gyrokinetic equation, we follow [27] and [28]. The references for the original gyrofluid model are [29] and [30]. The GEM model is summarized from [31] and [32].
For a comprehensive, modern overview of general gyrokinetics, see e.g. [33] and [34].

3.1 Basic gyrokinetics

The original gyrofluid equations in toroidal geometry [30] are based on the gyrokinetic Vlasov-Poisson equations in general geometry as derived in [27]. For a single particle with mass m and charge e, the Lagrangian L in canonical coordinates $\vec{p}, \vec{q}$ reads

$$L\vec{p}\dot{\vec{q}} - h(\vec{p}, \vec{q}, t), \tag{3.1}$$

where $h(\vec{p}, \vec{q}, t)$ is the canonical Hamiltonian. For a general coordinate transformation to the coordinates $\vec{z} = \vec{z}(\vec{p}, \vec{q}, t)$, the Lagrangian can be rewritten as

$$L = \sum_{i=1}^{6} \gamma_i \dot{z}^i - h + \vec{p} \cdot \dot{\vec{q}} \tag{3.2}$$

with

$$\gamma_i = \vec{p} \cdot \frac{\partial \vec{q}}{\partial z^i}. \tag{3.3}$$

This defines the fundamental one-form

$$\gamma = \sum_{i=1}^{6} \gamma_i \dot{z}^i - (h + \vec{p} \cdot \dot{\vec{q}})dt. \tag{3.4}$$

Including an electrostatic potential $\Phi(\vec{q}, t)$ and a magnetic vector potential $\vec{A}(\vec{q}, t)$, the Hamiltonian can be written as

$$h = \frac{1}{2m}\left[\vec{p} - \frac{e}{c}\vec{A}(\vec{q}, t)\right]^2 + e\Phi(\vec{q}, t). \tag{3.5}$$

Using noncanonical coordinates $\vec{z} = (\vec{x}, \vec{v})$ defined by

$$\begin{aligned} \vec{x} &= \vec{q} \\ \vec{v} &= \frac{1}{m}\left[\vec{p} - \frac{e}{c}\vec{A}\right], \end{aligned} \tag{3.6}$$

the fundamental one-form then is

$$\gamma = \left[\frac{e}{c}\vec{A}(\vec{x}) + m\vec{v}\right] \cdot d\vec{x} - \left[\frac{1}{2}mv^2 + e\Phi(\vec{x}, t)\right] dt. \tag{3.7}$$

From this, the gyrophase dependence can be removed by means of a Lie transformation, see e.g. [35]. The gyrophase θ is the angle of the fast, circular motion of the charged particle in the plane locally perpendicular to the magnetic field line. This is a transform from a coordinate system z to a coordinate system Z, formally

$$Z^\mu = Tz^\mu, \tag{3.8}$$

where

$$T = \ldots T_3 T_2 T_1 \tag{3.9}$$

with

$$T_n = \exp(\epsilon^n L_n). \tag{3.10}$$

The operators L_n are defined by

$$L_n f = g_n^\mu \frac{\partial f}{\partial z^\mu} \tag{3.11}$$

$$\frac{\partial Z^\mu}{\partial \epsilon^n} = g_n^\mu(Z), \tag{3.12}$$

where g_n^μ is the generator of the Lie transformation T_n.

The one-form γ in eq. (3.7) accordingly transforms as

$$\Gamma = T^{-1}\gamma + dS, \tag{3.13}$$

where dS represents a gauge transformation of all coordinates. A coordinate transformation to gyrocenter variables

$$\vec{x} = \vec{R} + \frac{v_\perp}{\Omega}\vec{a}(\vec{R}, \theta) \tag{3.14}$$

$$\mu = \frac{v_\perp^2}{2\Omega} \tag{3.15}$$

$$v_\parallel = \vec{v} \cdot \vec{b} \tag{3.16}$$

$$\theta = \tan^{-1}\left(\frac{\vec{v} \cdot \vec{e}_1}{\vec{v} \cdot \vec{e}_2}\right) \tag{3.17}$$

is introduced, where e_1, e_2 are arbitrary orthogonal unit vectors so that $e_1, e_2, \vec{b}$ form a local orthogonal system of unit vectors and we have defined

$$\vec{a} = \vec{e}_1 \cos\theta - \vec{e}_2 \sin\theta \tag{3.18}$$

$$\Omega = \frac{eB_0}{mc}. \tag{3.19}$$

Splitting γ in a equilibrium part γ_0 and a perturbed part $\tilde{\gamma}$. Lie transformations are applied order by order in ϵ to the one-form in gyrocenter coordinates. The gauge transformations dS_n are chosen so that all θ dependences vanish. Varying the resulting one-form with respect to the gyrocenter coordinates leads to the Euler-Langrange equations for these coordinates, which are[1]

$$\begin{aligned}
\frac{d\mu}{dt} &= 0 \\
\frac{d\theta}{dt} &= \Omega + e\frac{\partial \Psi}{\partial \mu} \\
\frac{d\vec{R}}{dt} &= v_\parallel \vec{b} + \frac{1}{B^*}\vec{b} \cdot \left(\frac{c}{e}\mu \nabla\Omega + \frac{1}{e} m c v_\parallel^2 \vec{b} \cdot \nabla \vec{b} + c\nabla\Psi \right) \\
m\frac{dv_\parallel}{dt} &= -\frac{\vec{B}^*}{B^*} \cdot (\mu\nabla\Omega + e\nabla\Psi)
\end{aligned} \tag{3.20}$$

with

$$\vec{B}^* = \left(B + \frac{mc}{e} v_\parallel \vec{b} \cdot \nabla \times \vec{b} \right) \cdot \vec{b} \tag{3.21}$$

$$\Psi = <\Phi> - \frac{e}{2\Omega}\left(\frac{\partial}{\partial\mu} <\tilde{\Phi}^2> + \frac{1}{\Omega} <\nabla\tilde{\Phi}_{av} \cdot \vec{b} \times \nabla\tilde{\Phi}> \right) \tag{3.22}$$

and

$$<\Phi> = \frac{1}{2\pi}\oint d\theta \Phi \tag{3.23}$$

$$\tilde{\Phi} = \Phi - <\Phi> \tag{3.24}$$

$$\tilde{\Phi}_{av} = \int_0^{2\pi} \tilde{\Phi} d\theta. \tag{3.25}$$

In the following, a tilde ˜ always denotes the fluctuating part of a quantity.
Eqs. (3.20) can be now inserted into the gyrokinetic Vlasov-Poisson equation for the distribution function $F = F_0 + \tilde{F}$ in gyrocenter coordinates, which reads

$$\frac{dF}{dt} = \frac{\partial F}{\partial t} + \frac{dv_\parallel}{dt}\frac{\partial F}{\partial v_\parallel} + \frac{d\vec{R}}{dt}\frac{\partial F}{\partial \vec{R}} = 0. \tag{3.26}$$

Using the usual gyrokinetic ordering

$$\frac{k_\parallel}{k_\perp} \approx \frac{\tilde{n}}{n} \approx \frac{e\tilde{\Phi}}{T_e} \approx \frac{\tilde{F}}{F_0} \approx \frac{\tilde{T}}{T} \approx \epsilon \ll 1 \tag{3.27}$$

$$k_\perp \rho \approx 1 \tag{3.28}$$

[1] for convenience, we do not indicate the gyroaveraged quantities by a special notation

with the small parameter

$$\epsilon = \frac{\rho}{L_\perp} \ll 1, \tag{3.29}$$

where $L_\perp$ is a typical length scale of the fluctuations and

$$\rho_s = \frac{\sqrt{M_i T_e} c}{eB}, \tag{3.30}$$

the above gives the basic gyrokinetic equation in general geometry correct to order ϵ as described in [30]

$$\begin{aligned} \frac{\partial}{\partial t} FB &+ \nabla \cdot \left[FB(v_\parallel \vec{b} + \vec{v}_E + \vec{v}_d) \right] \\ &+ \frac{\partial}{\partial v_\parallel} \left[FB \left(-\frac{e}{m} \vec{b} \cdot \nabla J_0 \Phi - \mu \vec{b} \cdot \nabla B + v_\parallel (\vec{b} \cdot \nabla \vec{b}) \cdot \vec{v}_E \right) \right] \\ &= 0, \end{aligned} \tag{3.31}$$

with

$$\vec{v}_E = \frac{c}{B} \vec{b} \times \nabla J_0 \Phi \tag{3.32}$$

$$\vec{v}_d = \frac{v_\perp^2 + \mu B}{\Omega B^2} \vec{B} \times \nabla B + \frac{4\pi v_\perp^2}{\Omega B^2} \vec{b} \times \nabla p. \tag{3.33}$$

The velocity v_E describes the gyro-averaged $\vec{E} \times \vec{B}$ drift, and v_d includes all drifts from ∇B and curvature. The linear operator J_0 carries out the gyroavering of the electrostatic potential Φ and is a Bessel function in Fourier space

$$J_0(b) = \sum_{n=0}^{\infty} \frac{1}{(n!)^2} \left(\frac{v_\perp}{2\Omega} \right)^{2n} \nabla_\perp^{2n}, \tag{3.34}$$

where

$$b = \frac{k_\perp v_\perp}{\Omega}. \tag{3.35}$$

The quasi-neutrality constraint is

$$n_e = \frac{n}{1 + \frac{b}{2}} - \frac{b T_\parallel}{2\left(1 + \frac{b}{2}\right)^2} + (\Gamma_0 - 1)\Phi, \tag{3.36}$$

where in general

$$\Gamma_n(b) = exp(-b) I_n(b), \tag{3.37}$$

and

$$I_n(b) = i^{-1} J_n(ib) \tag{3.38}$$

is the modified Bessel function.

3.2 The original gyrofluid model

The original gyrofluid equations were first derived for a sheared slab geometry [29] and later extended to toroidal geometry [30] as in eq. (3.31). Additionally a collision operator $C(F)$ is introduced to the right hand side of eq. (3.31), which for a single ion species is

$$C(F) = \nu_{ii}\left\{\tilde{F} - \left[\frac{\tilde{n}}{n} + \frac{u_\parallel v_\parallel}{v_T^2} + \frac{\tilde{T}_\parallel + 2\tilde{T}_\perp}{3T_0}\left(\frac{v_\parallel^2 + v_\perp^2}{2v_T^2} - \frac{3}{2}\right)\right]F_0\right\}. \tag{3.39}$$

Assuming low[2] β and a Maxwellian F_0

$$F_0 = \frac{n_0}{(2\pi v_T^2)^{\frac{3}{2}}}\exp\left(-\frac{v_\parallel^2}{2v_T^2} - \mu\frac{B}{v_T^2}\right), \tag{3.40}$$

eq. (3.31) can be rewritten as shown in [30], grouping all velocity dependent quantities on the same side of spatial gradients:

$$\begin{aligned}
\frac{\partial}{\partial t}FB \;&+\; B\nabla_\parallel\frac{FBv_\parallel}{B} + \vec{v}_\Phi\cdot\nabla(FBJ_0) + 2FBJ_0\frac{e}{T}i\omega_d\Phi \\
&+\; \frac{e}{T}i\omega_d\left(FBJ_1\Phi k_\perp\frac{v_\perp}{2\Omega}\right) + \frac{i\omega_d}{v_t^2}\left[FB(v_\perp^2 + \mu B)\right] \\
&-\; \frac{e}{m}\nabla_\parallel\left(J_0\Phi B\frac{\partial F_0}{\partial v_\perp}\right) + \frac{e}{m}J_0\Phi B \\
&\cdot\; \frac{\partial F_0}{\partial v_\perp}\left(\frac{\mu B}{v_t^2} - 1\right)\nabla_\parallel\ln B - \mu B\frac{\partial(FB)}{\partial v_\perp}\nabla_\parallel\ln B \\
&-\; \frac{\partial}{\partial v_\parallel}(FBJ_0v_\parallel)\frac{ie\omega_d\Phi}{T} = 0
\end{aligned} \tag{3.41}$$

with

$$v_T^2 = \frac{T_\perp}{m} \tag{3.42}$$

$$\omega_d = \frac{v_t^2}{i\Omega B^2}\vec{B}\times\nabla B\cdot\nabla. \tag{3.43}$$

[2] $\nabla B = 0$ and $\vec{j}$ is mostly toroidal

From eq. (3.41), one can now take fluid moments of the form $\int v_\parallel^j \mu^k dv_\parallel d\mu$, with the lowest moments defined as

$$
\begin{aligned}
n &= \int F d^3v && (3.44)\\
nu_\parallel &= \int F v_\parallel d^3v && (3.45)\\
p_\parallel &= \int F(v_\parallel - u_\parallel)^2 d^3v && (3.46)\\
p_\perp &= \frac{m}{2}\int F v_\perp^2 d^3v && (3.47)\\
q_\parallel &= m\int F(v_\parallel - u_\parallel)^3 d^3v && (3.48)\\
q_\perp &= \frac{m}{2}\int F v_\perp^2 (v_\parallel - u_\parallel) d^3v && (3.49)\\
r_{\parallel,\parallel} &= m\int F(v_\parallel - u_\parallel)^4 d^3v && (3.50)\\
r_{\parallel,\perp} &= \frac{m}{2}\int F v_\perp^2 (v_\parallel - u_\parallel)^2 d^3v && (3.51)\\
r_{\perp,\perp} &= \frac{m}{4}\int F v_\perp^4 d^3v && (3.52)\\
s_{\parallel,\parallel} &= m\int F(v_\parallel - u_\parallel)^5 d^3v && (3.53)\\
s_{\parallel,\perp} &= \frac{m}{2}\int F v_\perp^2 (v_\parallel - u_\parallel)^3 d^3v && (3.54)\\
s_{\perp,\perp} &= \frac{m}{2}\int F v_\perp^4 (v_\parallel - u_\parallel) d^3v. && (3.55)\\
& && (3.56)
\end{aligned}
$$

The temperatures can be obtained through

$$p_{\parallel,\perp} = nT_{\parallel,\perp}. \tag{3.57}$$

As with the ideal MHD model, the system of equations is not closed. The term $\nabla \cdot (FBv_\parallel \vec{b})$ in eq. (3.31) results in the usual moment hierarchy problem: the equation for moment n includes the moment $n+1$. For a model including moments up to the heat fluxes $q_{\parallel,\perp}$, one therefore needs closure conditions for the r and s moments. Furthermore, because of eq. (3.34), the gyroaveraging operator J_0 includes all even powers of $v_\parallel$ and thus can be regarded as a function of all fluid moments. Therefore, we need additional closure conditions for these finite Larmor radius (FLR) terms.

In this thesis, we only present the set of equations for GEM in the following section. We discuss the necessary closures and approximations, some of which are corrected in the GEM model.

We first give the closures for the FLR terms, which are of the form $< J_0 \ldots >$ and $< J_1 \ldots >$.

The average $< C >$ of the quantity C is defined as

$$< C >= \frac{1}{n} \int d^3 v FC = 2\pi \int dv_\parallel d\mu BFC \tag{3.58}$$

As is shown in [30], the fundamental approximation is

$$< J_0 > \approx \sqrt{\Gamma_0}. \tag{3.59}$$

This is the same approximation as for the sheared slab case [29], but was found to be reasonable also for the toroidal case. With this, we have the approximations

$$\begin{aligned}
< J_0 > &= \sqrt{\Gamma_0} && (3.60)\\
< J_0 v_\parallel > &= v_T \sqrt{\Gamma_0} && (3.61)\\
< J_0 v_\parallel^2 > &= v_T^2 \sqrt{\Gamma_0} && (3.62)\\
< J_0 v_\perp^2 > &= 2 v_T^2 \frac{\partial}{\partial b} \left(b \sqrt{\Gamma_0} \right) && (3.63)\\
< J_0 v_\parallel^3 > &= v_T^3 \sqrt{\Gamma_0} && (3.64)\\
< J_0 v_\perp^2 v_\parallel > &= 2 v_T^3 \frac{\partial}{\partial b} \left(b \sqrt{\Gamma_0} \right) && (3.65)\\
& && (3.66)
\end{aligned}$$

This introduces two modified Laplacian operators in the fluid moment equations

$$\begin{aligned}
\hat{\nabla}_\perp^2 \Phi &= 2b \frac{\partial \sqrt{\Gamma_0}}{\partial b} \Phi && (3.67)\\
\hat{\hat{\nabla}}_\perp^2 \Phi &= b \frac{\partial^2}{\partial b^2} \left(b \sqrt{\Gamma_0} \right) \Phi && (3.68)
\end{aligned}$$

Due to toroidicity, new terms occur which are not present in a slab model

$$\begin{aligned}
< J_1 \alpha > &= -\hat{\nabla}_\perp^2 && (3.69)\\
< J_1 v_\parallel^2 \alpha > &= -v_T^2 \hat{\nabla}_\perp^2 && (3.70)\\
< J_1 v_\perp^2 \alpha > &= -4 v_T^2 \hat{\hat{\nabla}}_\perp^2 && (3.71)\\
< J_0 v_\perp^4 > &= 4 v_T^4 \left(2\sqrt{\Gamma_0} + \hat{\nabla}_\perp^2 + \hat{\hat{\nabla}}_\perp^2 \right), && (3.72)
\end{aligned}$$

with

$$\alpha = \frac{k_\perp v_\perp}{\Omega} \tag{3.73}$$

For the 6 lowest fluid moments $n, n u_\parallel, p_\parallel, p_\perp, q_\parallel, q_\perp$, the moment hierarchy problem requires closures for $r_{\parallel,\parallel}, r_{\parallel,\perp}, r_{\perp,\perp}$ and $s_{\parallel,\parallel}, s_{\parallel,\perp}, s_{\perp,\perp}$. The closures are artificially broken into Maxwellian parts and dissipative pieces. The dissipative pieces are given by 10 coefficients

$$\nu_n = \nu_r + i \nu_i \frac{|\omega_d|}{\omega_d} = (\nu_r, \nu_i), \tag{3.74}$$

which were numerically optimized to give the best fit in order to model kinetic effects c.f. [30], but not consistently for all kinetic effects. The closures for the r and s moments are

$$r_{\parallel,\parallel} = 3(2p_\parallel - n) + \frac{32-9\pi}{3\pi-8}T_\parallel - 2i\frac{\sqrt{2\pi}}{3\pi-8}\frac{|k_\parallel|}{k_\parallel}q_\parallel \tag{3.75}$$

$$r_{\parallel,\perp} = p_\parallel + p_\perp - n - 2i\frac{\sqrt{2\pi}}{3\pi-8}\frac{|k_\parallel|}{k_\parallel}q_\parallel \tag{3.76}$$

$$r_{\parallel,\parallel} + r_{\parallel,\perp} = 7p_\parallel + p_\perp - 4n - 2i\frac{|w_d|}{w_d}(\nu_1 T_\parallel + \nu_2 T_\perp) \tag{3.77}$$

$$r_{\parallel,\perp} + r_{\perp,\perp} = p_\parallel + 5p_\perp - 3n - 2i\frac{|w_d|}{w_d}(\nu_3 T_\parallel + \nu_4 T_\perp) \tag{3.78}$$

$$s_{\parallel,\parallel} + s_{\parallel,\perp} = -i\frac{|w_d|}{w_d}(\nu_5 u_\parallel + \nu_6 q_\parallel + \nu_7 q_\perp \tag{3.79}$$

$$s_{\parallel,\perp} + s_{\perp,\perp} = -i\frac{|w_d|}{w_d}(\nu_8 u_\parallel + \nu_9 q_\parallel + \nu_{10} q_\perp \tag{3.80}$$

with the coefficients given in [30]. Finally, for the mirroring term $\mu\vec{b}\cdot\nabla B$, Maxwellian closures are used to give

$$r_{\parallel,\parallel} = 6p_\parallel - 3n \tag{3.81}$$

$$r_{\parallel,\perp} = p_\parallel + p_\perp - n \tag{3.82}$$

$$r_{\perp,\perp} = 4p_\perp - 2n. \tag{3.83}$$

3.3 GEM

The GEM (gyrofluid electromagnetic) model builds on the original gyrofluid model and includes six moments for each species z: density n, parallel velocity $u_\parallel$, temperatures $T_{\parallel,\perp}$ and heat fluxes $q_{\parallel,\perp}$. It ensures energetic consistency on all scales, especially at $k_\perp\rho_s \approx 1$, conserving the fluctuating free energy, which the original gyrofluid model did not. A proof of the energy theorem in physical units can be found in e.g. [36].

The fluctuating free energy results from the thermal free energy (origin: density fluctuations), $E \times B$ energy (origin: electrostatic potential), magnetic energy (parallel magnetic vector potential) and parallel free energy (parallel velocities and parallel heat fluxes) and should be conserved in a proper model. Neglecting free energy conservation gives only very small contributions to growth rate in a linear model, but is essential in the turbulent phase involving a saturated state. Energetic problems in the standard gyrofluid moments [29], [30] stem from finite FLR terms and an inconsistency in the treatment of the higher order moment terms: the original model treats parallel heat flux moments as dependent (dynamical) quantities in principle, but for simplicity uses a perturbed Maxwellian model for the moment closure in eqs. (3.81) - (3.83).

The starting point is the observation that there are 3 gyroavering operators in the moment equations

$$\tilde{\Phi}_G = \sqrt{\Gamma_0}\tilde{\Phi} \tag{3.84}$$

$$\frac{1}{2}\hat{\nabla}^2_\perp \tilde{\Phi}_G = b\frac{\partial\sqrt{\Gamma_0}}{\partial b}\tilde{\Phi} \tag{3.85}$$

$$\hat{\tilde{\nabla}}^2_\perp \tilde{\Phi}_G = b\frac{\partial^2}{\partial b^2}\left(b\sqrt{\Gamma_0}\right)\tilde{\Phi}, \tag{3.86}$$

giving three gyroaveraged and FLR corrected potentials

$$\tilde{\Phi}_G = \sqrt{\Gamma_0}\tilde{\Phi} \tag{3.87}$$

$$\tilde{\Omega}_G = b\frac{\partial\sqrt{\Gamma_0}}{\partial b}\tilde{\Phi} \tag{3.88}$$

$$\hat{\tilde{\Omega}}_G = \frac{b}{2}\frac{\partial^2\left(b\sqrt{\Gamma_0}\right)}{\partial b^2}\tilde{\Phi}, \tag{3.89}$$

but only the operators (3.84) and (3.85) appear in the polarisation equation (3.36) (linked to $\tilde{n}_e$ and $\tilde{T}_{i\perp}$). As shown in [31], this causes inconsistencies and non-conservation of FLR potential energy terms because of the occurrence of the potential (3.89). Specifically, this breaks the energy conservation in the transfer channel between potential and thermal energy. This has potential consequences for the parallel dynamics, magnetic pumping terms, curvature terms and the $E \times B$ advection terms, all of which are FLR effects. In the following, we use the definitions of the curvature operator

$$\mathcal{K} = \nabla \cdot \left[\frac{c}{B^2}(\vec{B} \times \nabla)\right] \tag{3.90}$$

the velocities

$$\vec{v}_E = \frac{c}{B^2}\vec{B} \times \nabla\tilde{\phi}_G \tag{3.91}$$

$$\vec{w}_E = \frac{c}{B^2}\vec{B} \times \nabla\tilde{\Omega}_G \tag{3.92}$$

and the identities

$$\frac{d}{dt} = \frac{\partial}{\partial t} + \vec{u}_E \cdot \nabla \tag{3.93}$$

$$\nabla_\parallel = \vec{b} \cdot \nabla + \vec{b}_\perp \cdot \nabla. \tag{3.94}$$

(i) Parallel dynamics (quasistatic compressible part of the drift dynamics)
For sound waves due to a parallel pressure gradient $\nabla_\parallel p$, the conservation of energy is expressed by the term $B\nabla_\parallel\left(\frac{\tilde{p}\tilde{u}_\parallel}{B}\right)$, which in the context of the original fluid model can be written as

$$B\nabla_\parallel\left(\frac{\tilde{p}\tilde{u}_\parallel}{B}\right) = B\nabla_\parallel\frac{\left[\tau_i\left(\tilde{n}_i + \tilde{T}_{i\parallel}\right) + \tilde{\Phi}_G\right]\tilde{u}_\parallel}{B} \tag{3.95}$$

with

$$\tau_i = \frac{T_i}{T_e}, \tag{3.96}$$

thus a modification required.
The same is true for the non-closure part of heat conduction dynamics. The part dealing with the energetics can be written as

$$\frac{1}{2}\tau_i \tilde{T}_{i\parallel} \frac{\partial \tilde{T}_{i\parallel}}{\partial t} = -B\nabla_\parallel \frac{\tau_i \tilde{T}_{i\parallel} \tilde{q}_{i\parallel}}{B} + \tilde{q}_{i\parallel} \nabla_\parallel \left[\tau_i \tilde{T}_{i\parallel}\right] \tag{3.97}$$

$$\frac{2}{3}\tilde{q}_{i\parallel} \frac{\partial \tilde{q}_{i\parallel}}{\partial t} = -\tilde{q}_{i\parallel} \nabla_\parallel \left[\tau_i \tilde{T}_{i\parallel}\right] \tag{3.98}$$

$$\tau_i \tilde{T}_{i\perp} \frac{\partial \tilde{T}_{i\perp}}{\partial t} = -B\nabla_\parallel \frac{\left[\tau_i \tilde{T}_{i\perp} + \tilde{\Omega}_G\right] \tilde{q}_{i\perp}}{B} + \tilde{q}_{i\perp} \nabla_\parallel \left[\tau_i \tilde{T}_{i\perp} + \tilde{\Omega}_G\right] \tag{3.99}$$

$$\tilde{q}_{i\perp} \frac{\partial \tilde{T}_{i\perp}}{\partial t} = -\tilde{q}_{i\perp} \nabla_\parallel \left[\tau_i \tilde{T}_{i\perp} + \tilde{\Omega}_G\right], \tag{3.100}$$

showing that there is no involvement of the potential 3.89.

(ii) Magnetic pumping terms
The equation for the fluctuating perpendicular ion heat flux $\tilde{q}_{i\perp}$ includes the potential 3.89

$$\frac{\partial \tilde{q}_{i\perp}}{\partial t} = -\left[\tau_i \left(\tilde{T}_{i\perp} - \tilde{T}_{i\parallel}\right) + 2\tilde{\tilde{\Omega}}_G - \tilde{\Omega}_G\right] \nabla_\parallel \log B, \tag{3.101}$$

which can be repaired by replacing $\tilde{\tilde{\Omega}}_G$ with $\tilde{\Omega}_G$, thus the modified equation reads

$$\frac{\partial \tilde{q}_{i\perp}}{\partial t} = -\left[\tau_i \left(\tilde{T}_{i\perp} - \tilde{T}_{i\parallel}\right) + \tilde{\Omega}_G\right] \nabla_\parallel \log B. \tag{3.102}$$

(iii) Curvature terms
The same problem shows up in the equations for the thermal state variables. The part for the perpendicular fluctuating ion temperature is

$$\frac{\partial \tilde{T}_{i\perp}}{\partial t} = \mathcal{K}\left(\frac{\tilde{\phi}_G + \tilde{\Omega}_G + \tau_i \tilde{p}_{i\perp}}{2} + \frac{3\tau_i \tilde{T}_{i\perp} + \tilde{\Omega}_G + 2\tilde{\tilde{\Omega}}_G}{2}\right). \tag{3.103}$$

Again, this can be repaired by $\tilde{\tilde{\Omega}}_G \to \tilde{\Omega}_G$, giving

$$\frac{\partial \tilde{T}_{i\perp}}{\partial t} = \mathcal{K}\left(\frac{\tilde{\phi}_G + \tilde{\Omega}_G + \tau_i \tilde{p}_{i\perp}}{2} + \frac{3(\tau_i \tilde{T}_{i\perp} + \tilde{\Omega}_G)}{2}\right). \tag{3.104}$$

(iv) FLR generalizations of the $E \times B$ advection
In these terms, the variables $\tilde{T}_{i\perp}$ and $\tilde{q}_{i\perp}$ are acted upon by the operator $\frac{2c}{B^2}\vec{B} \times \nabla\tilde{\tilde{\Omega}}_G \cdot \nabla$. This breaks the conservation of the FLR potential energy $\frac{1}{2}\tilde{\Omega}_G \tilde{T}_{i\perp}$, but can again be repaired

by the replacement of $\tilde{\hat{\Omega}}_G$ with $\tilde{\Omega}_G$.

The only non-FLR corrections are associated with the curvature terms in the fluid moment flux variables. Eqs. (3.81) - (3.83) affect the equations for $\tilde{u}_{\parallel}$, $\tilde{q}_{i\parallel}$ and $\tilde{q}_{i\perp}$ and arise from curvature drift terms in the gyrokinetic equation (3.31), but there are no curvature terms involving the potential in the equations for $\tilde{u}_{u\parallel}$, $\tilde{q}_{i\parallel}$ and $\tilde{q}_{i\perp}$. Furthermore, a perturbed Maxwellian closure was assumed, but the variables $\tilde{q}_{i\parallel}$ and $\tilde{q}_{i\perp}$ are still treated as dynamical. This means that the r moments should include terms of the form pressure $\times$ conductive heat fluxes. As described in [31], correcting this leads to the modified equations

$$\frac{\partial \tilde{u}_{\parallel}}{\partial t} = \frac{\tau_i}{2}\mathcal{K}(4\tilde{u}_{\parallel} + 2\tilde{q}_{i\parallel} + \tilde{q}_{i\perp}) \tag{3.105}$$

$$\frac{\partial \tilde{q}_{i\parallel}}{\partial t} = \frac{\tau_i}{2}\mathcal{K}(3\tilde{u}_{\parallel} + 8\tilde{q}_{i\parallel}) \tag{3.106}$$

$$\frac{\partial \tilde{q}_{i\perp}}{\partial t} = \frac{\tau_i}{2}\mathcal{K}(\tilde{u}_{\parallel} + 6\tilde{q}_{i\perp}), \tag{3.107}$$

ensuring free energy conservation.

3.3.1 The GEM equations

The complete set of equations for the 6-moment GEM model include the polarisation equation

$$\sum_i a_i \left[\Gamma_1 \tilde{n}_z + \Gamma_2 \tilde{T}_{z\perp} + \frac{\Gamma_0 - 1}{\tau_z}\tilde{\phi}\right] = \tilde{n}_e, \tag{3.108}$$

where z denotes the particle species, Ampere's law

$$-\nabla_{\perp}^2 \tilde{A}_{\parallel} = \sum_z a_z \tilde{u}_{z\parallel} = \tilde{j}_{\parallel}, \tag{3.109}$$

and the fluid moment equations.

The set of fluid moment equations without dissipation is

$$\frac{d[n_z+\tilde{n}_z]}{dt}+\vec{w}_E\cdot\nabla\left[T_z+\tilde{T}_z\right]+B\nabla_\parallel\frac{\tilde{u}_{z\parallel}}{B} = \mathcal{K}\left(\tilde{\phi}_G+\frac{\tau_z\tilde{p}_{z\parallel}+\tau_z\tilde{p}_{z\perp}+\tilde{\Omega}_G}{2}\right) \tag{3.110}$$

$$\beta_e\frac{\partial\tilde{A}_\parallel}{\partial t}+\mu_z\frac{d\tilde{u}_{z\parallel}}{dt}+\mu_z\vec{w}_E\cdot\nabla\tilde{q}_{z\perp} = -\nabla_\parallel\left(\tilde{\phi}_G+\tau_z\left[p_z+\tilde{p}_{z\parallel}\right]\right) +\mathcal{K}\left(\mu_z\tau_z\frac{4\tilde{u}_{z\parallel}+2\tilde{q}_{z\parallel}+\tilde{q}_{z\perp}}{2}\right) -\tau_z\left(\tilde{\Omega}_G+\tau_z\tilde{T}_{z\perp}-\tau_z\tilde{T}_{z\parallel}\right)\nabla_\parallel\log B \tag{3.111}$$

$$\frac{1}{2}\frac{d\left[T_z+\tilde{T}_{z\parallel}\right]}{dt}+B\nabla_\parallel\frac{\tilde{u}_{z\parallel}+\tilde{q}_{z\parallel}}{B} = \mathcal{K}\left(\frac{\tilde{\phi}_G+\tau_z\tilde{p}_{z\parallel}}{2}+\tau_z\tilde{T}_{z\parallel}\right)-(\tilde{u}_{z\parallel}+\tilde{q}_{z\perp})\nabla_\parallel\log B \tag{3.112}$$

$$\frac{d\left[T_z+\tilde{T}_{z\perp}\right]}{dt}+\vec{w}_E\cdot\nabla\left([n_z+\tilde{n}_z]+2\left[T_z+\tilde{T}_{z\perp}\right]\right)+B\nabla_\parallel\frac{\tilde{q}_{z\perp}}{B} = \mathcal{K}\left(\frac{\tilde{\phi}_G+\tilde{\Omega}_G+\tau_z\tilde{p}_{z\perp}}{2}+3\frac{\tilde{\phi}_G+\tau_z\tilde{T}_{z\perp}}{2}\right)+(\tilde{u}_{z\parallel}+\tilde{q}_{z\perp})\nabla_\parallel\log B \tag{3.113}$$

$$\mu_z\frac{d\tilde{q}_{z\parallel}}{dt}=-\frac{3}{2}\nabla_\parallel\left(\tau_z\left[T_z+\tilde{T}_{z\parallel}\right]\right)+\mathcal{K}\left(\mu_z\tau_z\frac{3\tilde{u}_{z\parallel}+8\tilde{q}_{z\parallel}}{2}\right) \tag{3.114}$$

$$\mu_z\frac{d\tilde{q}_{z\perp}}{dt}+\mu_z\vec{w}_E\cdot\nabla(\tilde{u}_{z\parallel}+2\tilde{q}_{z\perp})=-\nabla_\parallel\left(\tilde{\Omega}_G+\tau_z\left[T_z+\tilde{T}_{z\perp}\right]\right) +\mathcal{K}\left(\mu_z\tau_z\frac{\tilde{u}_{z\parallel}+6\tilde{q}_{z\perp}}{2}\right)-\tau_z\left(\tilde{\Omega}_G+\tau_z\tilde{T}_{z\perp}-\tau_z\tilde{T}_{z\parallel}\right)\nabla_\parallel\log B. \tag{3.115}$$

The treatment of dissipation in GEM involves three different mechanisms:

(i) Dissipation without collisions
This is due to phase mixing, i.e. Landau damping and is represented by a Landau damping operator

$$a_{Lz}:=a_{L0}\left(1-0.125VqR\nabla_\parallel^2\right) \tag{3.116}$$

directly applied to the parallel heat flux variables $\tilde{q}_{z\parallel}$ with

$$a_{L0}=1 \tag{3.117}$$

$$V=\frac{\tau_z}{\mu_z} \tag{3.118}$$

$$\nabla_\parallel^2=B\nabla_\parallel\left(\frac{1}{B}\right)\nabla_\parallel, \tag{3.119}$$

and qR and $\nabla_\parallel$ normalized to $L_\perp$.

(ii) Dissipation with collisions
This is done in a way that matches the collisional Braginskii fluid model [37] in the limit of large collision frequency and short mean free path. It includes dissipation through resistivity and thermal conduction with anisotropic temperatures. A drift kinetic Chapman-Enskog procedure is applied to a state with stationary state variables (c.f. [38]), generalized to a bi-Maxwellian distribution for the part without dissipation.
In contrast to the original gyrofluid model, a Lorentz collision operator is used and involved coefficients are chosen to capture the collisional limit as mentioned above. The modifications for the fluctuating quantities can then be written as

$$\beta_e \frac{\partial \tilde{A}_\parallel}{\partial t} + \mu_z \frac{d\tilde{u}_{z\parallel}}{dt} = ... + \mu_e \nu_e \left[\eta \tilde{j}_\parallel + \frac{\alpha_e}{\kappa_e} \left(\tilde{q}_{e\parallel} + \tilde{q}_{e\perp} + \alpha_e \tilde{j}_\parallel \right) \right] \tag{3.120}$$

$$\frac{1}{2} \frac{d\tilde{T}_{z\parallel}}{dt} = ... - \nu_z \left[\tau_z \left(\tilde{T}_{z\parallel} - \tilde{T}_{z\perp} \right) - \tilde{\Omega}_G \right] \tag{3.121}$$

$$\frac{d\tilde{T}_{z\perp}}{dt} = ... + \nu_z \left[\tau_z \left(\tilde{T}_{z\parallel} - \tilde{T}_{z\perp} \right) - \tilde{\Omega}_G \right] \tag{3.122}$$

$$\mu_z \frac{d\tilde{q}_{z\parallel}}{dt} = ... - \frac{5\mu_z \nu_z}{2\kappa_z} \left(\tilde{q}_{z\parallel} - 0.6\alpha_z \tilde{j}_\parallel \right) + 1.28\nu_z \left(\tilde{q}_{z\parallel} - 1.5\tilde{q}_{z\perp} \right) \tag{3.123}$$

$$\mu_z \frac{d\tilde{q}_{z\perp}}{dt} = ... - \frac{5\mu_z \nu_z}{2\kappa_z} \left(\tilde{q}_{z\perp} - 0.4\alpha_z \tilde{j}_\parallel \right) - 1.28\nu_z \left(\tilde{q}_{z\parallel} - 1.5\tilde{q}_{z\perp} \right). \tag{3.124}$$

For two particle species, deuterium ions i and electrons e, the parameters are

$$\eta = 0.51 \tag{3.125}$$

$$\alpha_e = 0.71 \tag{3.126}$$

$$\kappa_e = 3.2 \tag{3.127}$$

$$\kappa_i = 3.9, \tag{3.128}$$

and the collision frequencies ν_z for species z.

(iii) Nonlinear dissipation: cascading to arbitrarily small scales
This is implemented by artificial diffusion terms in the equations (3.115) and controlled by perpendicular and parallel dissipation coefficients $\nu_\perp$ and $\nu_\parallel$.
With eq. (3.93), the general form of the modifications to the moment equations can be formally written as

$$\frac{\partial F}{\partial t} = S + D(f), \tag{3.129}$$

with F being the functional of the time derivative of the dependent variables f , S the right hand side of eqs. (3.115) and D the artificial dissipation operator. For a constant magnetic field $\vec{B}$, the modeling of nonlinear dissipation in xy-plane [3] can be achieved by the substitutions

$$\vec{u}_E \cdot \nabla \to \vec{u}_E \cdot \nabla - \nu_\perp \nabla_\perp^2 - \nu_\parallel \nabla_\parallel^2 \tag{3.130}$$

[3] locally perpendicular to the magnetic field line, where x is a radial coordinate and y a poloidal coordinate

or as an alternative, hyperdiffusion

$$\vec{u}_E \cdot \nabla \to \vec{u}_E \cdot \nabla + \nabla_\perp^2 \nu_\perp \nabla_\perp^2 - \nu_\parallel \nabla_\parallel^2. \tag{3.131}$$

For variable $\vec{B}$, the substitutions are

$$\vec{u}_E \cdot \nabla \to \vec{u}_E \cdot \nabla - \nabla \cdot \nu_\perp \frac{1}{B^2} \nabla_\perp - \nabla \cdot (\vec{b} \nu_\parallel \vec{b}) \cdot \nabla \tag{3.132}$$

and for hyperdiffusion

$$\vec{u}_E \cdot \nabla \to \vec{u}_E \cdot \nabla + \nabla_\perp^2 \cdot \nu_\perp \frac{1}{B^4} \nabla_\perp^2 - \nabla \cdot (\vec{b} \nu_\parallel \vec{b}) \cdot \nabla. \tag{3.133}$$

4 Validity regimes

For the framework of ideal MHD presented in chapter 2, the following critical assumptions must be valid [9]

- high collisionality ν
- small gyroradius ρ_g
- small resistivity η
- slow timescales τ with plasma motion velocities $\ll$ the speed of light c.

High ν ensures an isotropic scalar pressure p, i.e. any anisotropic part Π of the total pressure P with

$$P = p\mathbb{1} + \Pi \tag{4.1}$$

can be neglected. As the electron mass m_e is considered arbitrarily small, the electrons have infinite small response time to any forces. This means that the MHD time scales must be large against the electron plasma frequency and the electron cyclotron frequency. Consequently, the spatial scales must also be large compared to the Debye length and the electron and ion gyroradii ρ_e and ρ_i. Small resistivity preserves the characteristic nested flux-surface topology. Finite resistivity breaks it and gives rise to new instabilities and phenomena like the tearing mode and the reconnection of magnetic field lines on a larger resistive time scale. The displacement current $\sim \frac{\partial \vec{E}}{\partial t}$ can be neglected because of the slow time scales resp. low velocities.

For typical tokamak plasma parameters[1], the last two assumptions are well satisfied, while the first one is violated by large margin. This violation enters the momentum and energy equation for ideal MHD, and therefore seems to render the ideal MHD theory invalid. Experimental observations nevertheless show ideal MHD to be applicable very well to a range of plasma phenomena. This is due to an essential difference between the directions parallel and perpendicular to the magnetic field lines. Generally speaking, the parallel direction is poorly treated in ideal MHD, because the mean free path along the field lines is of order 10^2m, i.e. the collisionality is low. In perpendicular direction however, the charged particles are confined to gyrating motion around the field lines with small gyroradius. So even with zero collisionality, the magnetic field ensures a short mean free path of the particles. Indeed

[1] $T \sim$ keV, $n \sim 10^{19} \frac{1}{\mathrm{m}^3}$

it could be shown in [39] that in the collisionless limit, the anisotropic part of the ion pressure is negligible

$$\frac{|\Pi_\perp i|}{p_i} \approx \frac{\rho_i}{a} \ll 1. \tag{4.2}$$

The parallel part of the ideal MHD equations mostly describe expansion and compression of the plasma. Most relevant ideal MHD plasma motions however are incompressible

$$\nabla \cdot \vec{v} = 0. \tag{4.3}$$

Therefore the parallel equations have little consequences for ideal MHD equilibrium and stability considerations. Furthermore, incompressible modes grow faster than compressible modes.

This motivates the introduction of collisionless MHD, satisfying all three assumptions. The derivation for the continuity equations remains unchanged, and is universally valid. Calculating the perpendicular part of the plasma current with the assumption of $\nu = 0$ results in modified momentum and energy equations. The set of equations for collisionless MHD is then given by [9]

$$\begin{aligned}
\frac{d\rho}{dt} &= 0 && (4.4)\\
\rho \left(\frac{d\vec{v}_\perp}{dt}\right)_\perp &= \vec{j} \times \vec{B} - \nabla_\perp p && (4.5)\\
\vec{B} \cdot \nabla \left(\frac{v_\parallel}{B}\right) &= -\nabla \cdot \vec{v}_\perp && (4.6)\\
\frac{dp}{dt} &= 0 && (4.7)\\
\vec{E} + \vec{v} \times \vec{B} &= 0 && (4.8)\\
\nabla \times \vec{E} &= -\frac{\partial \vec{B}}{\partial t} && (4.9)\\
\nabla \times \vec{B} &= \mu_0 \vec{j} && (4.10)\\
\nabla \cdot \vec{B} &= 0 && (4.11)
\end{aligned}$$

For incompressible motions, these equations basically give the same predictions as collision dominated ideal MHD [9].
The typical time scales τ_{MHD} of ideal MHD are

$$\tau_{MHD} = \frac{a}{V_{T_i}} \tag{4.12}$$

with the thermal ion velocity

$$V_{T_i} = \sqrt{\frac{2T_i}{M_i}}, \tag{4.13}$$

the latter also being the characteristic velocity of the ideal MHD regime. The length scale of ideal MHD instabilities is the dimension of the plasma $\sim a$. For common tokamaks like

ASDEX Upgrade, $\tau_{MHD} \approx 10^{-6}$s.

As gyrofluid models are a subset of gyrokinetic theory, they obey the same gyrokinetic ordering. This ordering is due to a large difference in frequencies between the gyration of particles around the magnetic field lines (fast) and the gyrocenter velocity (slow) and only the slow, low-frequency part is considered. The high-frequency part could simply be filtered out, but this would be nonconservative. Instead, the gyrokinetic equations are ordered as discussed in chapter 3, eq. (3.27). Generally speaking, the fluctuations of all plasma quantities have to be small and of the same order compared to the equilibrium quantities, and the difference in parallel/perpendicular dynamics is described by the ratio of typical wave numbers $\frac{k_\parallel}{k_\perp} \ll 1$. With the GEM modifications to the original gyrofluid theory, also free energy conservation is ensured [31] as discussed in chapter 3.

There are two defining perpendicular spatial scales of gyrofluid models, the drift scale

$$\rho_s = \frac{\sqrt{T_e M_i}}{eB} c \tag{4.14}$$

and the perpendicular gradient length $L_\perp$ of the background gradients. Gyrokinetic ordering requires the ratio to be small

$$\delta = \frac{\rho_s}{L_\perp}, \tag{4.15}$$

where δ is called drift parameter. For similar electron and ion temperatures $T_e \approx T_i$, we further have $\rho_s \approx \rho_i$ and

$$\delta \approx \frac{\rho_i}{a}, \tag{4.16}$$

i.e. the gyrofluid dynamics extends to the ion gyroradius scales, much smaller than the ideal MHD spatial scales.

As discussed before, ideal MHD neglects the electron mass[2] m_e, resulting in instantaneous response of the electrons parallel to the magnetic field lines. Therefore for MHD, we have

$$(\nabla p_e)_\parallel \ll (\nabla \phi)_\parallel. \tag{4.17}$$

The single fluid approximation of ideal MHD requires similar ion/electron moblitites, so the net current density j must satisfy

$$\frac{1}{ne} j \ll v_i, v_e \tag{4.18}$$

except for the Lorentz force, c.f. [40]. As outlined in [36], next to the characteristic MHD velocity V_{T_i}, the analysis of MHD waves in plasmas introduces two distinctive velocities: the Alfvén velocity

$$v_A^2 = \frac{B^2}{4\pi n M_i} \tag{4.19}$$

[2] As a consequence, the electron drift wave mechanism is not included in the ideal MHD dynamics

and the adiabatic sound velocity

$$v_s^2 = \frac{5}{3}\frac{p}{nM_i}. \tag{4.20}$$

Sound waves travel in parallel direction, and their velocity is small compared to the Alfvén velocity.
When comparing to the Alfvén velocity, the condition 4.18 is

$$j \ll nev_A. \tag{4.21}$$

Using the definition of v_A, this gives

$$j^2 \ll n^2e^2v_A^2 = n^2e^2\frac{B^2}{4\pi nM_i}, \tag{4.22}$$

representing the Alvén current as the current limit. Further using

$$\rho_i = \frac{c^2}{e^2B^2}M_iT_i \tag{4.23}$$

with Ampère's law

$$\vec{j} = \frac{c}{4\pi}\nabla \times \vec{B}, \tag{4.24}$$

gives

$$j^2 \approx \frac{c^2}{16\pi^2}\frac{B^2}{a^2}. \tag{4.25}$$

Combining eqs. (4.16) and (4.25) gives [36]

$$\frac{\rho_i^2}{a^2} \approx \delta^2 \ll \frac{2\pi p}{B^2} < \frac{8\pi p}{B^2} = \beta. \tag{4.26}$$

This is usually well satisfied everywhere in the fusion plasma. But when instead comparing to v_s, this gives the different criterion

$$\delta \ll \beta, \tag{4.27}$$

which is violated for the edge region of fusion plasmas. For the edge region with exemplary electron density $n_e = 2.5 \cdot 10^{19}\frac{1}{\mathrm{m}^3}$, electron temperature $T_e = 300$ eV and magnetic field strength $B_0 = 2.5\mathrm{T}$, we have

- $\beta \approx 10^{-4}$ - 10^{-3}
- $\delta^2 \approx 10^{-6} \ll \beta$
- $\delta \approx 10^{-3} \approx \beta$.

For the core region with e.g. $n_e = 5.0 \cdot 10^{19} \frac{1}{\mathrm{m}^3}$, $T_e = 2500$ eV and magnetic field strength $B_0 = 3.5\mathrm{T}$ it is

- $\beta \approx 10^{-2}$
- $\delta^2 \approx 10^{-6} \ll \beta$
- $\delta \approx 10^{-3} < \beta$.

This then means that the ideal MHD condition $(\nabla p_e)_\parallel \ll (\nabla \phi)_\parallel$ no longer holds. So the electron and ion species have to be treated separately, making two-/many-fluid models necessary.
The gyrofluid GEM model treats two species, ions and electrons, with valid descriptions of both the parallel and perpendicular direction. It also includes no assumptions on collisionality, giving rise to possible resistive effects. In contrast to the ideal linear MHD framework, temperature profile and temperature gradient effects for both species are present. A detailed description of the correlation of the plasma quantities along with the energy transfer channels and possible instabilities is given in [40].

The drives for instabilities in ideal MHD are the pressure gradient and the current density, giving rise to interchange/ballooning modes and kink modes. For the purpose of this thesis, we introduce the gyrofluid counterparts of the ballooning mode, the drift wave and the ion temperature gradient mode (ITG). The mode type can be identified by the parallel mode structure as discussed in [41].

The instabilities are characterized as follows:

- Drift wave:

$$\tilde{\Phi} \approx \tilde{p_e} \approx \tilde{p_i} \tag{4.28}$$

because for $\eta_i \approx 1$, we have $\tilde{T_e} < \tilde{n_e}$.

- ITG:

$$\tilde{T_i} \gg \text{all other quantities} \tag{4.29}$$
$$\tilde{Q_i} > \tilde{Q_e} \tag{4.30}$$
$$\tilde{p_i} > \tilde{p_e} \tag{4.31}$$

- Ballooning mode :

$$\tilde{h_e} \gtrsim \tilde{\Phi} \gg \text{all other quantities} \tag{4.32}$$
$$\tilde{p_e} \approx \tilde{T_i}, \tag{4.33}$$

with the nonadiabatic density

$$\tilde{h}_e = \tilde{n}_e - \tilde{\phi}, \tag{4.34}$$

mostly governing the free energy dynamics [41]. This represents the MHD regime for Φ

$$\nabla_\parallel \tilde{\Phi} \gg \nabla_\parallel \tilde{p_e} \rightarrow E_\parallel \approx 0 \tag{4.35}$$
$$\nabla_\perp \tilde{\Phi} \gg \nabla_\perp \tilde{p_e} \rightarrow E_\perp \gg \nabla_\perp \tilde{p}_e \tag{4.36}$$

It is further split in two regimes:
-resistive ballooning for $C\omega_{cv} \approx 1$

-ideal ballooning somewhat below $\alpha_M \lesssim 1$ with

$$\alpha_M = \hat{\beta}\omega_{cv}\omega_p \tag{4.37}$$
$$\omega_{cv} = \frac{2L_\perp}{R_0} \tag{4.38}$$
$$C = \frac{0.51\nu_e}{L_\perp c_s}\frac{m_e(qR_0)^2}{M_i} \tag{4.39}$$
$$\omega_p = (\omega_n + \omega_t) + \tau_i(\omega_n + \omega_i), \tag{4.40}$$

where

$$\omega_n = \frac{L_\perp}{L_n} \tag{4.41}$$
$$\omega_t = \frac{L_\perp}{L_{T_e}} \tag{4.42}$$
$$\omega_i = \frac{L_\perp}{L_{T_i}}. \tag{4.43}$$

5 The plasma edge

5.1 L- and H-mode

Experiments with increased neutral beam injection (NBI) heating at the ASDEX tokamak lead to the discovery of an operation regime of enhanced confinement [42] compared to previous discharges. This regime was termed H-mode (for high confinement mode) and occured abrubtly once a certain threshold in heating power was passed[1]. It manifested itself in steep edge gradients for temperatures (electron and ion), electron density and pressure and thus shows a pedestal, compare fig. 5.1. This forms because of a transport barrier in the plasma edge. Until today, the physical mechanism behind the transition from L- to H-mode remains unclear. No simulations at any level of theoretical sophistication were able to reproduce a stable H-mode or its dynamics. A possible mechanism is described in e.g. [43], while a comprehensive overview of H-mode theories can be found in [44].
The former operational regime with lower confiment is consequently named L-mode and the difference in confinement can be described by the H-factor

$$H = \frac{\tau_E^H}{\tau_E^L} \tag{5.1}$$

with the confinement times $\tau_E^{H,L}$ for the H- and L-mode. Typical values for H are around 2 for the regular H-mode[2].
The H-mode is in general accompanied by a variety of edge instabilities which will be described in detail below in chapter 5.3. These instabilities expel plasma and energy from the edge, lower the pedestal height and the profile gradients. After that the gradients get ramped up again and transit into the next instability interval because of continued heating and fueling, so the evolution is cyclic during the discharge.

For a plasma quantity C, the gradient length L_C associated with it is defined by

$$L_C^{-1} = \nabla \log(C) = \frac{\nabla L_C}{L_C} \tag{5.2}$$

and describes the characteristic distance over which the quantity changes. A typical deuterium H-mode discharge at ASDEX Upgrade[3] has electron density and temperature profiles in the edge region as shown in fig. 5.1.

[1] Before crossing this threshold however, the confiment was actually decreased with input of additional heating power
[2] The so-called improved H-mode achieves even higher values
[3] here: shot number 17151, see [45]

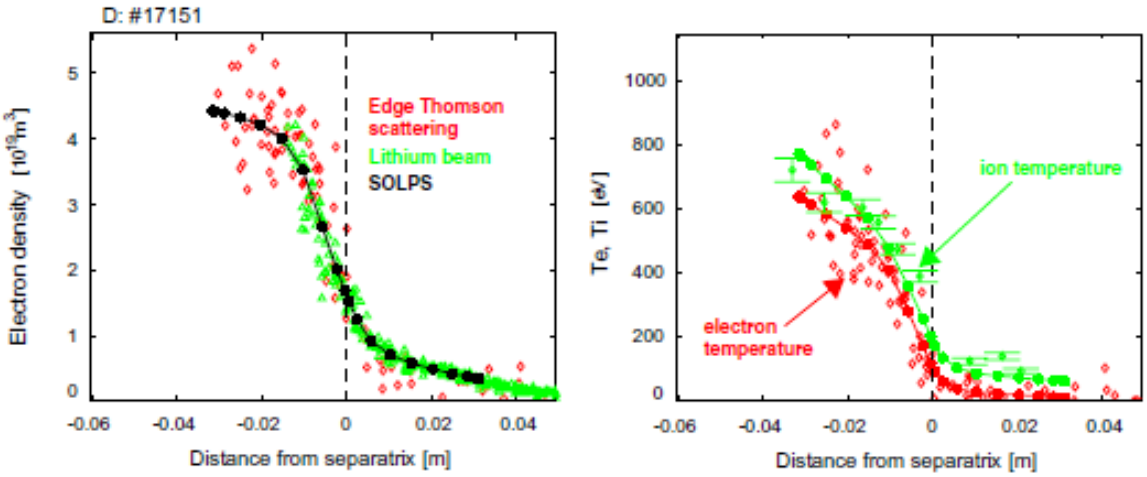

Figure 5.1: Electron density and temperatures in the edge region for ASDEX Upgrade shot 17151. Adapted from [45]

For this discharge, the ion temperature gradient length $L_{T_i} \approx 3.0$ cm - 4.0 cm, and the electron density gradient length is $L_{n_e} \approx 2L_{T_i}$, as can be taken from fig. 5.2. These gradient lengths, however, are in generall taken over different radial extents and should therefore only be considered as averaged quantitites, giving a simplified characteristic of the edge region.

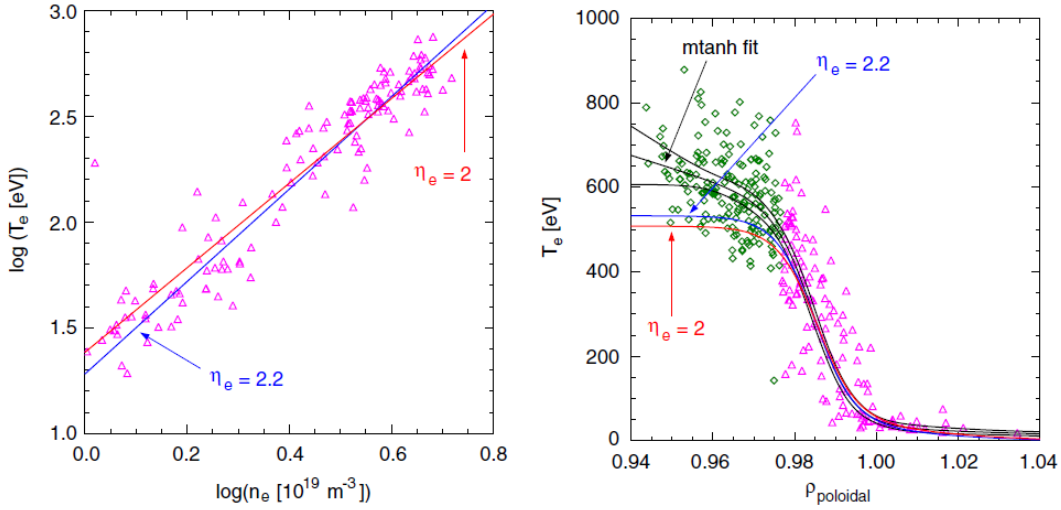

Figure 5.2: Left side: logarithmic plot for electron temperature and electron density. Their correlation gives the ratio η_e of L_{n_E} to L_{T_e}. Right side: modified tanh fit for the electron temperature measure points for different values of η_e. Adapted from [45]

In the edge, the ratio of of ion and electron temperatures is $\frac{T_i}{T_e} \approx 1.2$. Taking the mid-pedestal values, the electron density is about 2.5 - 3.0 in units of $10^{19}\mathrm{m}^3$ and the temperatures are 300 eV - 500 eV, corresponding to 3.5 - 5.8 million Kelvin.
For L-mode discharges, the gradient lengths for the temperatures do not differ much from

the H-mode values, with $L_{T_i} \approx 5$ - 6 cm. The density gradient length however is in the range of 3 - 4 times L_n, i.e. $\gtrsim 20$ cm.

5.2 Bootstrap current

The bootstrap current $\vec{j}_b$ is a toroidal current driven by the radial diffusion and the friction of particles in a tokamak plasma[4]. For large aspect ratios, the drive comes predominantly from a radial density gradient, while for small aspect ratios the current is rather driven by the radial pressure gradient. There are several model equations for realistic plasmas based on neoclassical models see e.g. [6] and [46]. In summary, the bootstrap current behaves like

$$< \vec{j}_b \cdot \vec{B} > \sim c_1 \frac{p_e'}{p_e} + c_2 \frac{p_i'}{p_i} + c_3 \frac{T_e'}{T_e} + c_4 \frac{T_i'}{T_i}, \tag{5.3}$$

where the coefficients $\{c_n\}$ are dependent on the collisionality, the ratio of trapped particles to circulating particles and the flux function $F(\psi) = RB_\phi$. The average $< x >$ is defined as [6]

$$< x >= \frac{\oint x \frac{dl_p}{B_p}}{\oint \frac{dl_p}{B_p}}, \tag{5.4}$$

where dl_p is a poloidal line element and B_p is the poloidal magnetic field.

Unlike the externally driven (ohmic) plasma current, $\vec{j}_b$ peaks off-axis and the magnitude as well as the peak position of the bootstrap current is very sensitive to the profile form, cf [6].
As the q profiles flattens with increased current density, the bootstrap current causes a decrease in shear. An experimental current density profile with a bootstrap current at the plasma edge is shown in fig. 5.3. For the purpose of this thesis however, we want to avoid a large bootstrap currents, especially at the plasma edge. This is because the bootstrap current may drive a large external kink instability, which is too close to the separatrix to be handled adequatly by gyrofluid or gyrokinetic codes. This is not a problem of the model itself, as the gyrofluid model GEM which is used in this thesis includes fully self-consistent fields. The issue is the q factor, which at the separatrix $\to \infty$. Consequently, in the vicinity of the separatrix the shear becomes very large. This causes a severe deformation of the computational grid cells, rendering simulations of that region inaccurate / impossible. For advancements in treating regions very close to the separatrix, see e.g. [47] on conformal coordinates.

5.3 Edge localised modes

Typical for H-mode operation are several types of edge instabilities termed edge localized modes (ELMs), which can be classified in type I - V and grassy ELMs [48]. All types have

[4]This is also true in reverse due to the Onsager symmetrie, see e.g. [6]

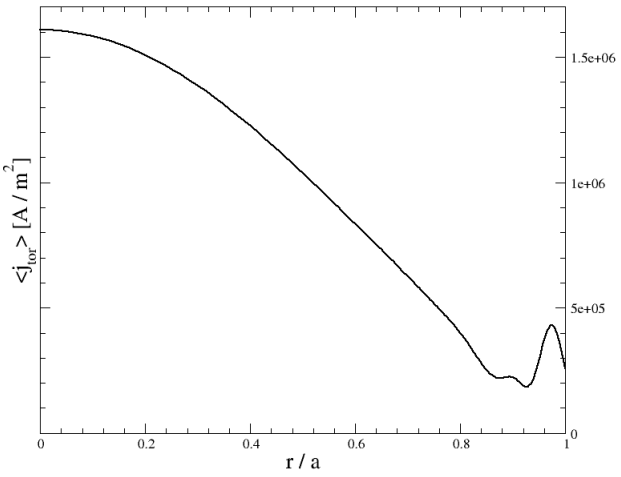

Figure 5.3: Typical current density profile with a bootstrap current at the edge

characteristics with regard to the parameter regime in which they appear, sometimes so narrow regimes that their occurrence is restricted to specific machines. For our purposes, we focus on type I ELMs with some notes on type III, as there exist predictive models in the framework of MHD. An overview of all known ELM types can be found in [48] and [49] .
The phenomenology of ELMs in general is a cyclic sequence of a bursty, fast time scale expulsion of plasma and energy from the edge accompanied with a degradation of ∇n_e, ∇T_e and the pedestal height, all of which then ramp up again on a slower timescale. ELM activity can be observed measuring the D_α activity, resulting from the plasma-wall interaction. A schematic picture of ELMs affecting the pressure profile is shown in fig. 5.4 Type I ELMs are less frequent than type III, with occurrence frequencies $f_{ELM} \approx 10$ Hz for type I[5] and $f_{ELM} \approx 100$ Hz for type III while the ELM itself takes a few 100 μs. Type I expels $\approx 10-20\%$ of the plasma edge energy and $\approx 5\%$ of the plasma edge particle inventory, while the smaller type III expels ≈ 1 - 5% of both. They lead to a decreased confinement factor ηH compared to eq. (5.1), with typically $\eta = 0.85$ [49].
For ITER-sized devices, the heat load to the divertor plates by type I ELMs may be too large, causing ablation of the plates and making it necessary to replace them in very short intervals, which is unacceptable for economic operation. Smaller ELMs however are desirable even though they lower the confinement, because they regularly flush out impurities and helium ash and limit plasma density.
Type III ELMs often show magnetic fluctuation precursors with poloidal mode number $m \geq 10$, while type I ELMs occur rather without any precursors and show a distinct crash in n_e only at the low field side. ELMs also show a filament-like structure, with pertubations of the plasma aligned with magnetic field lines with a radial extent of a few centimeters, see fig. 5.5. It is yet unclear if the filaments are a consequence of ELMs or a cause for them [48].

[5] These are example values, the device size plays an important role

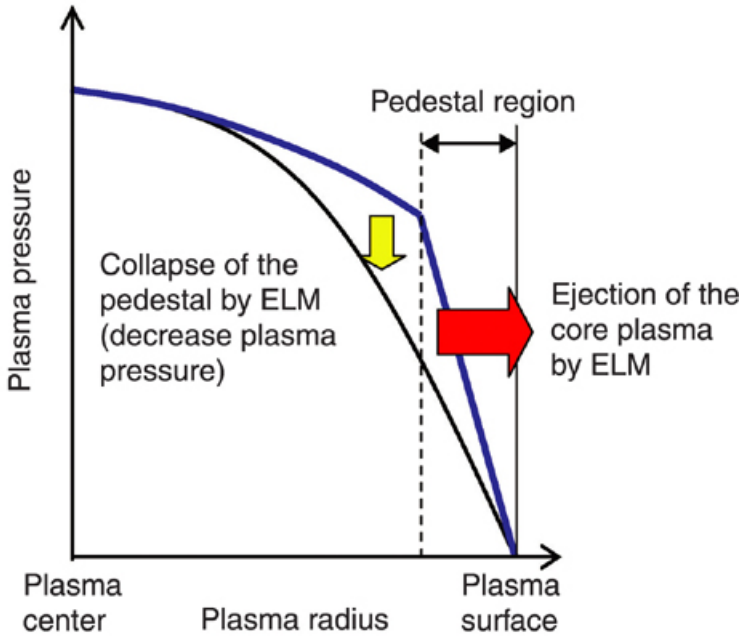

Figure 5.4: Schematic effect of ELMS on the pressure profile. Source: [50]

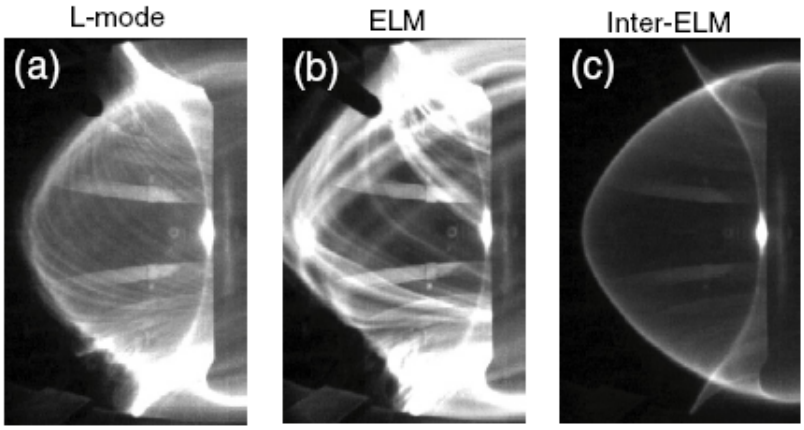

Figure 5.5: Filament structure before an ELM (a), during the ELM (b) and inbetween two ELMs (c). Source: [51]

5.3.1 Peeling-ballooning model

Like the H-mode, the physical mechanisms behind ELMs are still not understood. There is, however, a model for type I ELMs within the framework of ideal MHD[6], based on the coupling

[6]Type III ELMs are thought to be related to resistive effects and magnetic reconnection [48]

of peeling modes and ballooning modes [52]. Assuming a circular plasma cross section and a monotonically increasing q profile, the pertubation of the magnetic potential ψ for a given toroidal mode number n is written as a sum over poloidal harmonics

$$\psi = \exp(-in\varphi) \sum_{m=1}^{M+1} \exp(i\theta(m - m_0))C_m\psi_m(r - r_m), \tag{5.5}$$

where M denotes the number of rational surfaces in the plasma with toroidal mode number n, C_m is the amplitude of the mode labeled by m, ψ_m describes the normalized spatial structure of mode m and r_m is the radial position of the resonant surface with $q(r_m) = \frac{m}{n}$. The value of m_0 has to be chosen so that

$$m_0 < nq_0 < m_0 + 1, \tag{5.6}$$

where q_0 is the q value on the magnetic axis.
The sum in eq. (5.5) is over the M internal modes and one external Fourier mode[7] $C_{M+1}\psi_{M+1}$ with a resonant surface outside the plasma. With this approach the minimized change in potential energy δW for the magnetic pertubation ψ can formally be expressed as [52]

$$\delta W = C_{M+1}^2 \delta W_K + \frac{1}{2} \sum_{m=1}^{M} C_M C_{M+1} I_{M+1-m}, \tag{5.7}$$

where δW_K is the potential energy of an external kink in cylindrical geometry and the interaction term I_{M-m} describes the effect of the external mode $M+1$ on the internal modes. Under the assumption that the coupling between the last internal resonant harmonic and the external mode dominates[8], this can further be written as

$$\begin{aligned} \delta W &\approx C_{M+1}^2 \left(\delta W_K - \frac{1}{4} I_0^2 \frac{\det H_{M-1}}{\det H_M} \right) \\ &\approx C_M^2 \left(\frac{\det H_M}{\det H_{M-1}} - \frac{1}{4} I_0^2 \frac{1}{\delta W_K} \right), \end{aligned} \tag{5.8}$$

where

$$\frac{\det H_M}{\det H_{M-1}} = \delta W_B \tag{5.9}$$

describes the stability of the ballooning mode with toroidal mode number n and M resonant internal poloidal harmonics. The definitions of the matrices H_m are given in [52]. Equation 5.8 is an analytic expression for coupled ideal ballooning-kink instabilities, where the interaction term I_0 is always destabilizing in case of a circular cross section [52]. For $n \to \infty$, the conventional ballooning stability threshold is recovered [52], [53] and [54], but for finite n the above results in substantial modifications.

[7] This can be extended to several external modes, with ≈ 20 external modes a typical value for the linear ideal MHD stability computations in this thesis
[8] This is justified because the overlap of those two modes is generally the largest

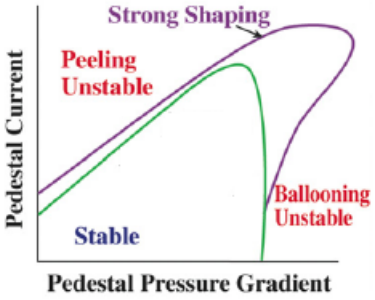

Figure 5.6: Schematic stability diagram for peeling-ballooning modes for different shapings. Adapted from:[54]

For an external mode whose resonant surface is just outside the plasma, i.e. a peeling mode, the kink contribution δW_K and the interaction term I_0 can be further simplified [52], giving

$$\begin{aligned} \delta W \quad \approx \quad & \frac{sd - q_a R \frac{j_\parallel}{B}}{M + 1 - nq_a} \\ & - \frac{\alpha(1+s^2)}{4s^4} \frac{\exp(-\frac{2}{s}\ln^2(M+1-nq_a)}{\delta W_B}, \end{aligned} \tag{5.10}$$

where q_a is the q value on the LCFS, $j_\parallel$ is the parallel current density at the edge of the plasma and s and α are defined as in the $s-\alpha$-model in chapter 2.4.2. This modifies the stability properties compared to treating peeling and ballooning instabilites separately and independently. Depending on the value of $M + 1 - nq_a$, the peeling or ballooning effect is more prominent, with the latter being maximal at $M + 1 - nq_a = \exp(-2)$ [52]. The onset of instability thus occurs at smaller values of the edge current density and pressure gradient as expected by conventional stability criteria, driving coupled peeling-ballooning modes at intermediate values of n, possibly preventing access to the 2nd region of stability.

Shaping the plasma cross section however can have a stabilizing effect, noticably increasing the maximum allowed pressure gradient and to a lesser extent the current density threshold, see fig. 5.6. For further numerical studies on the peeling-ballooning model, see e.g. [55] and [56].

The model for type I ELMs can now be envisaged as outlined in [54]. Additional heating increases the pressure gradient in the edge and forms an H-mode pedestal on a relatively fast timescale until the ballooning threshold is reached[9]. An increased pressure gradient in the edge can drive a large bootstrap current if the density is not too high. This happens on a resistive, slower timescale until the peeling mode treshold is crossed[10]. At this point, both the peeling and the ballooning criterion are violated and the type I ELM is triggered. The

[9] At this point, ballooning modes are triggered which might give rise to small ELMs. As ELMs decrease the pressure gradient, this would have a decreasing feedback on the ballooning mode growth, cf [54]

[10] Shaping effects may require a larger bootstrap current

plasma expulsion mechanism, however, is yet unclear and not included in the ideal MHD picture. The mechanism has to explain the very fast timescale of the crash and the plasma expulsion. However, lowering the pressure gradient has a self-enhancing effect on the peeling mode instability, which could explain the large amplitude of the type I ELM. Furthermore, a lesser pressure gradient drives a smaller bootstrap current, causing the plasma to drop below the peeling stability threshold again. After this, the plasma is at or near its original state with low pressure gradient and low current density.

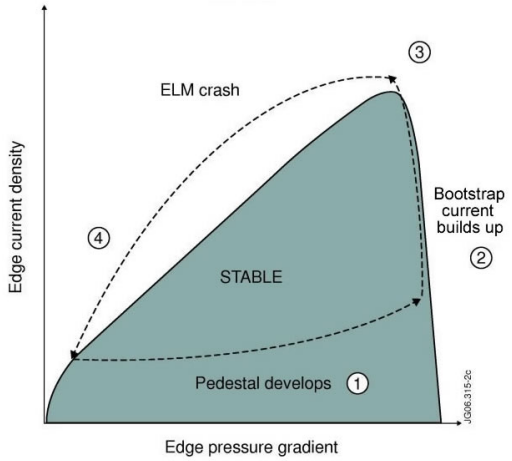

Figure 5.7: Schematic ELM cycle for the peeling-ballooning model. Source: [57]

Two possibilites for ELM control or mitigation are Pellet Pace Making (PPM) and the Resonant Magnetic Pertubation (RMP) method outlined in [58].
ELMs are triggered by injection of trigger pellets, where a higher ELM frequency in general leads to smaller ELMs. The idea behind PPM is then to trigger more, but smaller ELMs (type II or type III) instead of less frequent, but large type I ELMs. The trigger pellets are considerably smaller than the usual fuel pellets and are injected from the low-field side, preventing over-fuelling of the core plasma.
RMP coils generate non-axisymmetric magnetic pertubations on resonant flux surfaces at the edge region of the plasma, causing stochastic magnetic field lines and lowering the edge pressure gradient through increased radial transport. They do not have influence on the core region and thus cannot trigger any modes there.

6 Perfectly conducting wall: Influence on edge stability

The gyrofluid code GEM [31], numerically solving the GEM equations in chapter 3.3.1, run with local geometry uses a dampening layer for the edge of the radial computation box. All dependent fluctuating quantities are damped by a function shown in fig. 6.1. This function is an overlap of two Gaussians with a width[1] Δ, centered at $\pm\frac{1}{2}L_x$, where L_x is the length of the radial computation box and fixed $\Delta = 0.1L_x$. The fluxtube center is located at the origin of the computational box. The dampening ensures fixed background gradients with a smooth transition to zero amplitude of the fluctuating parts of the plasma quantities. While

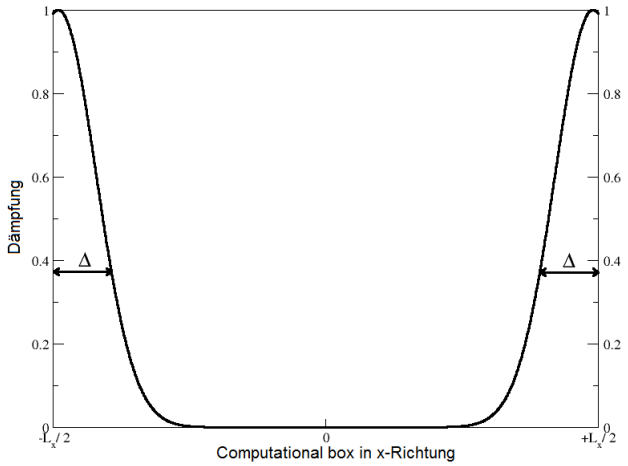

Figure 6.1: GEM edge dampening layer

this damping layer is not identical to a perfectly conducting wall close to the plasma, its effects are similar with respect to the plasma perturbations. For simplicity, we take the GEM quantity Δ to correspond to the distance between a perfectly conducting wall and the plasma. Note that the comparison of the GEM dampening layer and a perfectly conducting wall close to the plasma surface is only of meaning in the edge region of the plasma. The dampening layer always limits the radial computation box, regardless of the position of the latter, so only for flux tube positions in the edge of the plasma are the setups similar.
As discussed in 5, in the edge we have a typical length scale $L_\perp = L_{T_i} \approx 4$ cm. In our GEM simulations, we always chose[2] $L_x = L_\perp$, corresponding to $\Delta \approx 0.4$ cm. For a minor radius

[1] The Gaussian drops to $\frac{1}{e}$ at a distance Δ away from its center
[2] for the local geometry, flux tube model with fixed gradients, we always have to ensure $L_x < L_\perp$

$a = 50$ cm, this translates to a relative plasma-wall distance $d_{wp} := \frac{a+\Delta}{a} \approx 1.01$.
For realistic tokamaks, the distance between plasma and wall is much larger $d_{wp} > 1$. With regard to the comparison between the gyrofluid model and ideal MHD in chapter 7, in this chapter we thus study the influence of the distance between a perfectly conducting wall and a plasma with regard to ideal MHD instabilities.

We model 3 different equilibria with the high-resolution ideal MHD equilibrium solver HELENA [90] [59], all of which are designed to be unstable against both an edge ballooning mode and an external kink, but stable against internal kinks ($q > 1$). The profiles for each case, see figs. 6.2 - 6.5, were specifically chosen to yield these characteristics. The pressure gradients and current densities peak at $s \approx 0.96$ - 0.97, with the radial coordinate s defined as

$$s = \sqrt{\frac{\psi}{\psi_0}}. \tag{6.1}$$

The last closed flux surfaces are

- circular with large aspect ratio $\frac{R_0}{a} = 100$
- circular with small aspect ratio $\frac{R_0}{a} = 3.3$
- shaped with elongation and triangularity commensurate to experimental setups of ASDEX Upgrade.

For several values of d_{wp}, we then perform scans for the growth rates as a function of the toroidal mode number n and analyze the radial mode structures of the fastest growing mode with radial coordinate s with the linear MHD stability code ILSA [91] [92] [60] in MISHKA mode.

For up-down symmetric plasma cross sections, the geometric definitions of the elongation κ and the triangularity δ are

$$\begin{aligned} \kappa_G &= \frac{y_b}{x_d - x_0} \\ \delta_G &= \frac{x_b - x_0}{x_d - x_0}, \end{aligned} \tag{6.2}$$

compare fig. 6.6. For all cases investigated in this thesis, the last closed flux surface as used in HELENA is analytically prescribed by the equations

$$x(\theta) = x_0 + a\cos(\theta + \delta_H \sin(\theta) \tag{6.3}$$

$$y(\theta) = a\kappa_H \sin(\theta) \tag{6.4}$$

where x and y are cartesian coordinates and θ is the poloidal angle.
While these definitions ensure

$$\kappa_G = \kappa_H, \tag{6.5}$$

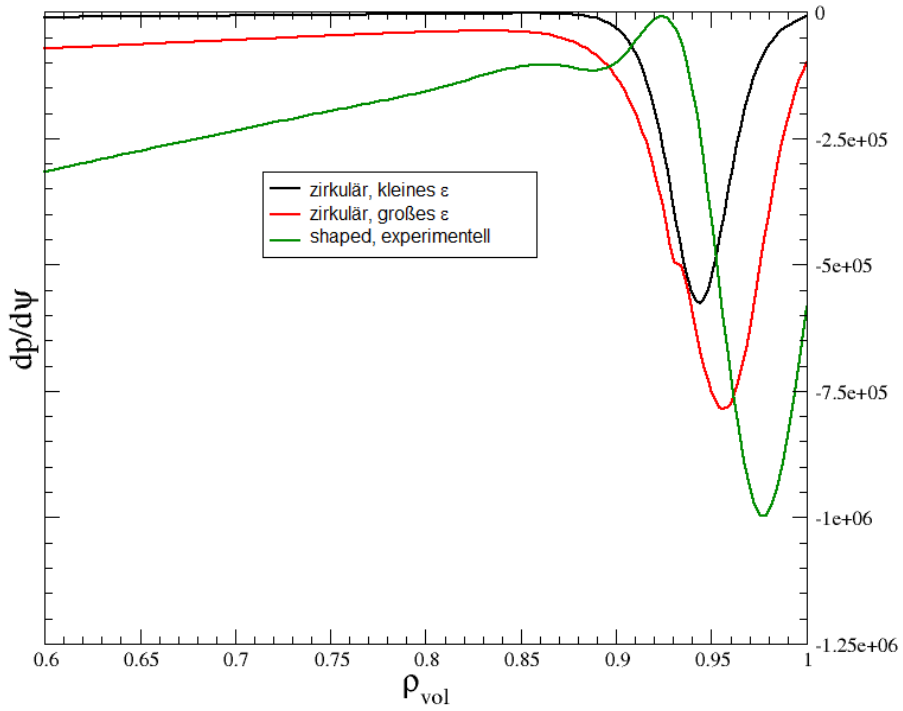

Figure 6.2: Pressure gradients

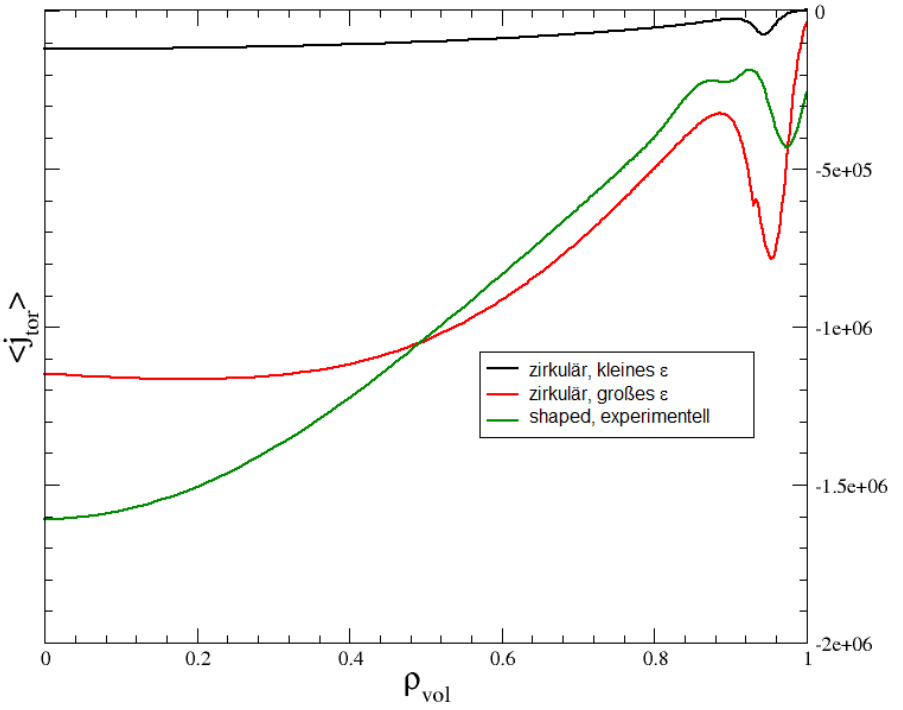

Figure 6.3: Current densities

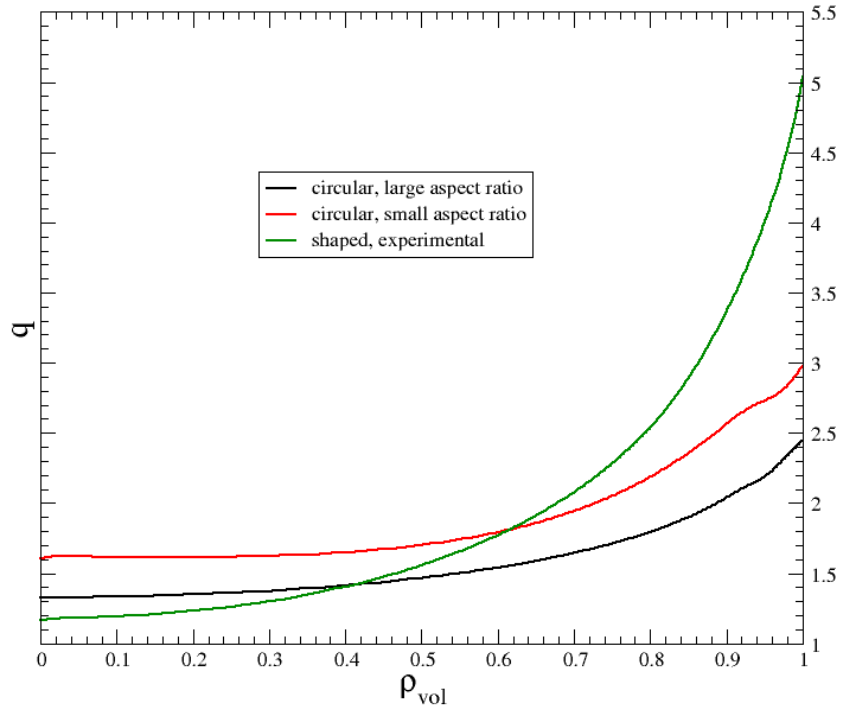

Figure 6.4: q profiles

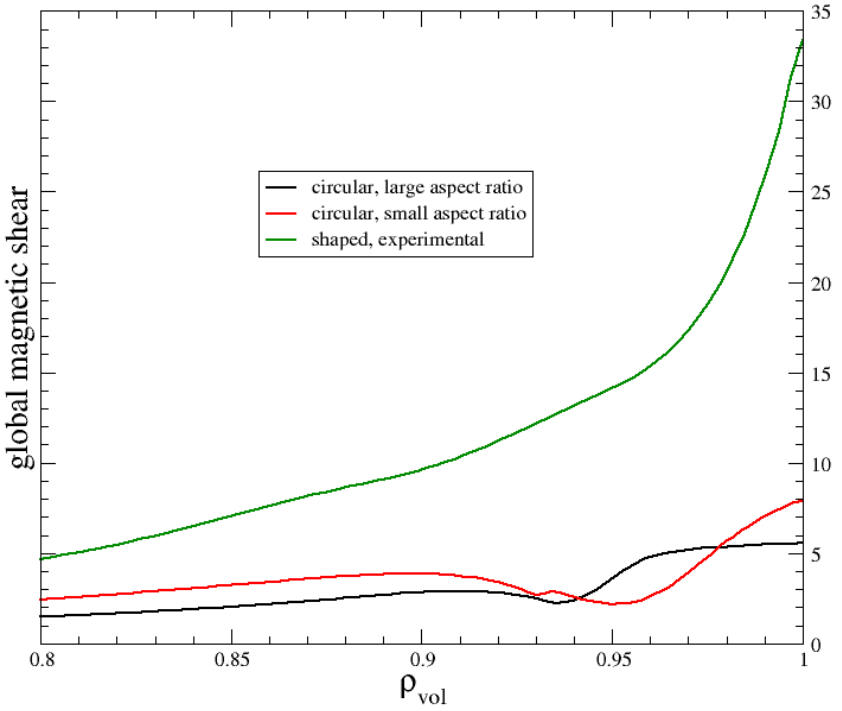

Figure 6.5: Global magnetic shear

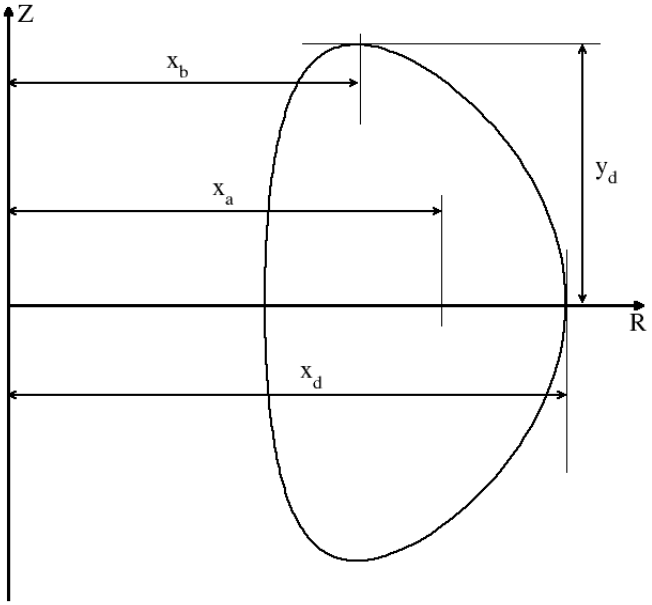

Figure 6.6: Geometric definitions for the plasma shape. The x position of the geometric center is x_0, the outermost point has x_d and the point with largest Z value has x position x_b.

the triangularity differs

$$\delta_G = \sin(\delta_H). \tag{6.6}$$

For small δ_H however, the difference is negligible.

6.1 Large aspect ratio limit

As a common theoretical approximation is to take the limit of a circular large aspect ratio plasma, we investigate the case with plasma parameters

- $R_0 = 20$ m
- $a = 0.2$ m
- $B_0 = 2.0$ T,

meaning $\epsilon = 0.01$. Much smaller values for ϵ resulted in problems for the computation of suitable equilibria. The spectra in fig. 6.7 show a significant influence of d_{wp} on modes with low to medium toroidal mode numbers $n \lesssim 16$, associated with external modes. The relatively higher instability of this part of the spectrum is due to an destabilizing effect of low inverse aspect ratio on low-n modes, compare e.g. the studies in [85].

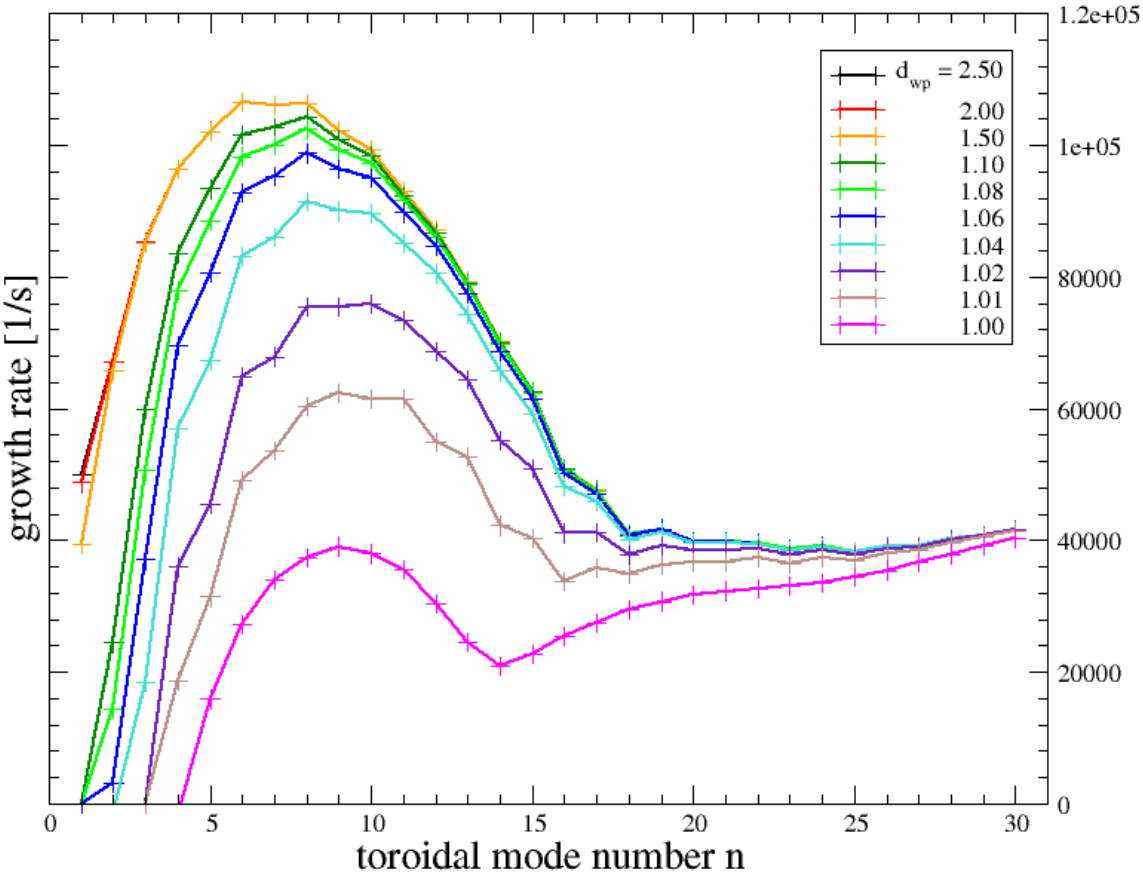

Figure 6.7: Growth rates vs. toroidal mode number n

For $d_{wp} \leq 1.10$, which corresponds to a distance of 2 cm between plasma surface and perfectly conducting wall, the effect of the wall becomes noticeable. The $n = 1$ mode gets fully stabilized, the maximum growth rates drop and the onset of instability is shifted to slightly higher n. This concurs with the theoretical expectations discussed in chapter 2.5 For the wall placed on the surface of the plasma, the maximum growth rate has dropped to $\approx \frac{1}{3}$ of its original value for $d_{wp} = 2.50$.

The high-n part of the spectra, associated with ballooning modes, is barely affected by d_{wp}. Only for $d_{wp} = 1.02$ (i.e. 0.4 cm between plasma and wall) and less, one can observe a slight drop in growth rates for this part. This reflects the weak ballooning drive $\sim \kappa \nabla p_0$ from a small curvature κ of the plasma and a small coupling between internal and external modes, which was presented in chapter 5.3.1.

The weak coupling can also be observed in the radial mode structures, see fig. 6.8 and 6.9 . When decreasing d_{wp}, the mode structure of the ballooning modes is mostly unaffected; slight changes become visible for $d_{wp} \leq 1.10$. The external part of the perturbation, however, decreases relative to the amplitude of the ballooning part with smaller d_{wp}. For $d_{wp} < 1.05$, i.e. the distance between plasma surface and wall < 1 cm, the ballooning amplitude becomes dominant. The position of maximum amplitude of the ballooning mode does not change with d_{wp}, and is located approximately at the position of maximum pressure gradient.

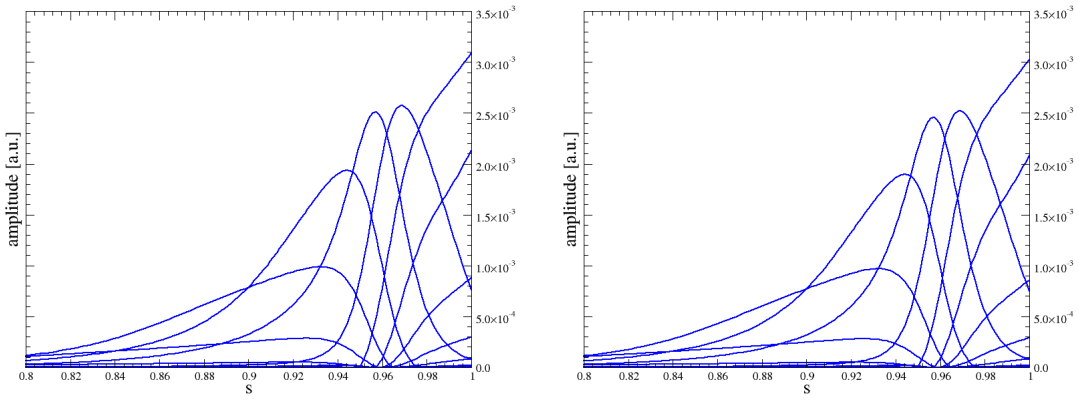

$d_{wp} = 2.50$ $d_{wp} = 1.25$

Figure 6.8: Radial mode structures for the fastest growing modes

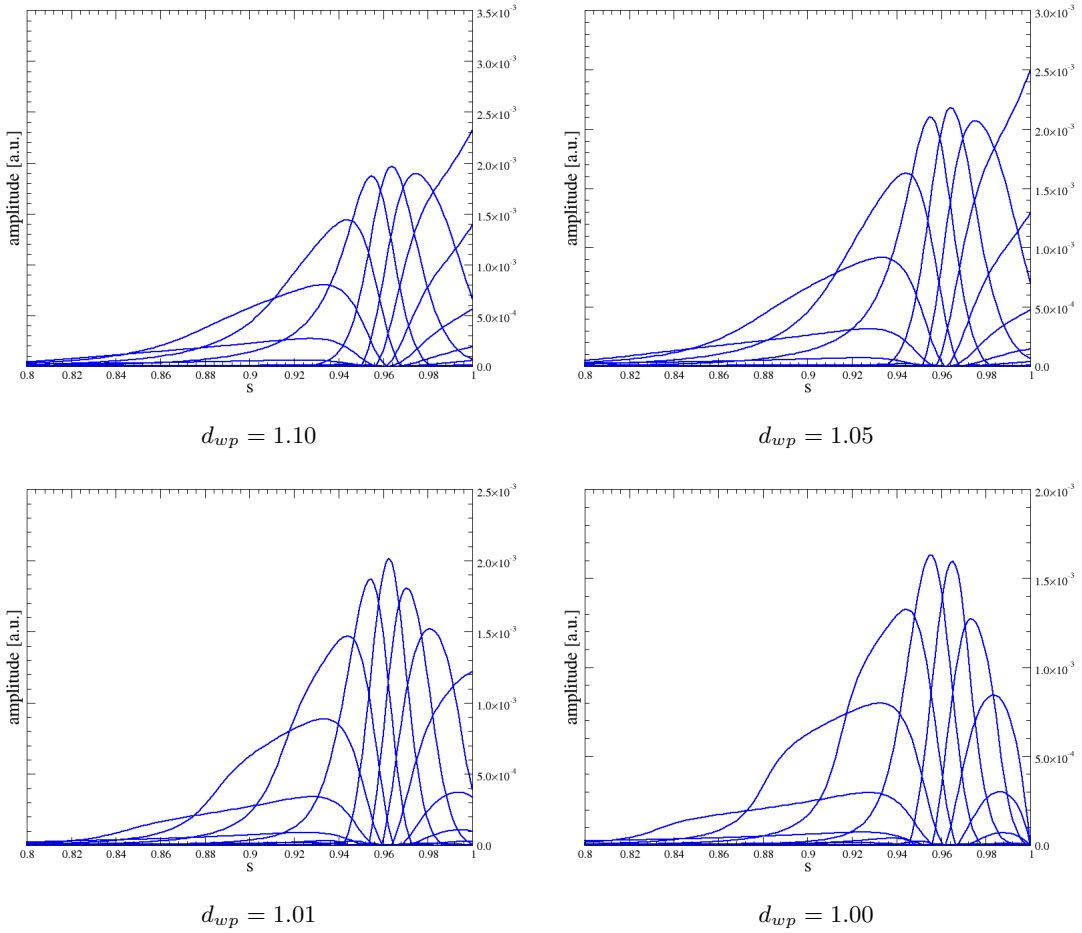

$d_{wp} = 1.10$ $d_{wp} = 1.05$

$d_{wp} = 1.01$ $d_{wp} = 1.00$

Figure 6.9: Radial mode structures for the fastest growing modes

6.2 Small aspect ratio

The plasma parameters for this circular equilibrium are

- $R_0 = 1.65$ m
- $a = 0.5$ m
- $B_0 = 2.0$ T,

giving $\epsilon = 0.303$. For the fastest growing modes, the spectra in fig. 6.10 show toroidal mode numbers of $n = 10$ - 18, typical for experimental equilibria with both an edge ballooning and external kink instability, and higher compared to the previous case with a large aspect ratio.

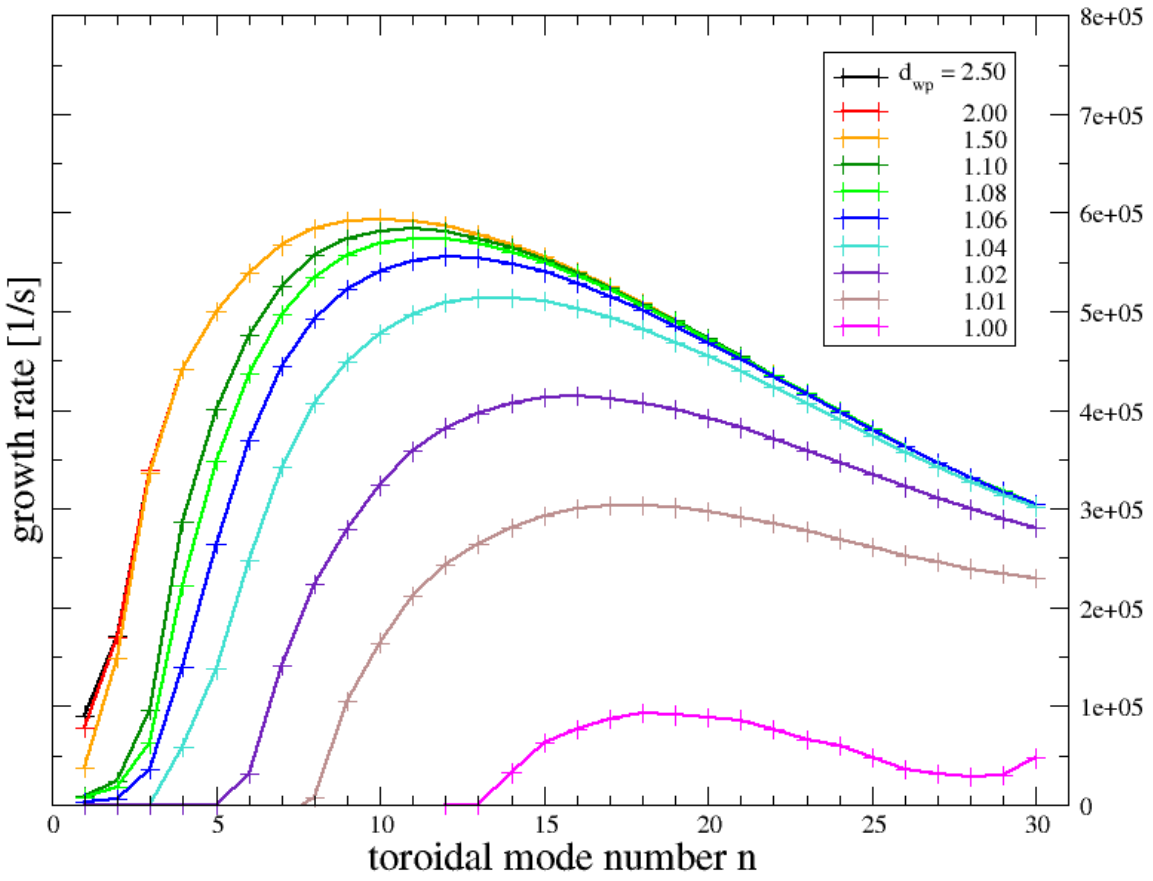

Figure 6.10: Growth rates vs. toroidal mode number n

Except for the case with $d_{wp} = 1.00$, the overall growth rates are much higher compared to the large aspect ratio equilibrium, although the maximum pressure gradient $\frac{dp}{d\psi}$ is only larger by $\approx 40\%$. For $d_{wp} = 2.50$, the highest growth for the small aspect ratio is ≈ 6 times the corresponding growth rate for the large aspect ratio case. This behavior reflects the increased ballooning drive by a substantially higher curvature κ, which is ≈ 12 times larger compared to the large aspect ratio. The increased curvature drive for ballooning modes therefore dominates the stabilizing effect from magnetic field line bending, recall the intuitive form of the energy principle in eq. 2.96.

For smaller d_{wp}, the mode numbers corresponding to the maximum growth rates as well as the onset of instability are shifted towards larger values of n. The shift, however, is much more pronounced than in the large aspect ratio case. The low-n and medium-n part of the spectra show similiar decreasing growth rates as the previous case with small ϵ, but the drop of the maximum growth rates is noticeably larger. For $d_{wp} = 2.50 \rightarrow 1.00$, the relative decrease is $\approx \frac{1}{6}$, twice the value as for the case with $\epsilon = 0.01$.

The high-n, ballooning part of the spectra equally shows a larger impact of d_{wp}, especially for $d_{wp} = 1.00$. As for small ϵ, the effect of the wall becomes visible at $d_{wp} = 1.10$ and lower. For above plasma parameters, this means a plasma-wall distance of 5cm.

The evolution of the radial mode structures with d_{wp} in figs. 6.11 and 6.12 show the edge ballooning mode, with a maximum approximately at the position where the pressure gradient. The amplitude of the external kink at the boundary of the computational domain is initially larger than the one corresponding to the ballooning mode, but drops below for $d_{wp} < 1.05$. The overall picture of the radial mode structures is similar compared to the large aspect ratio case, despite the differences for the high-n part of the spectra for both setups.

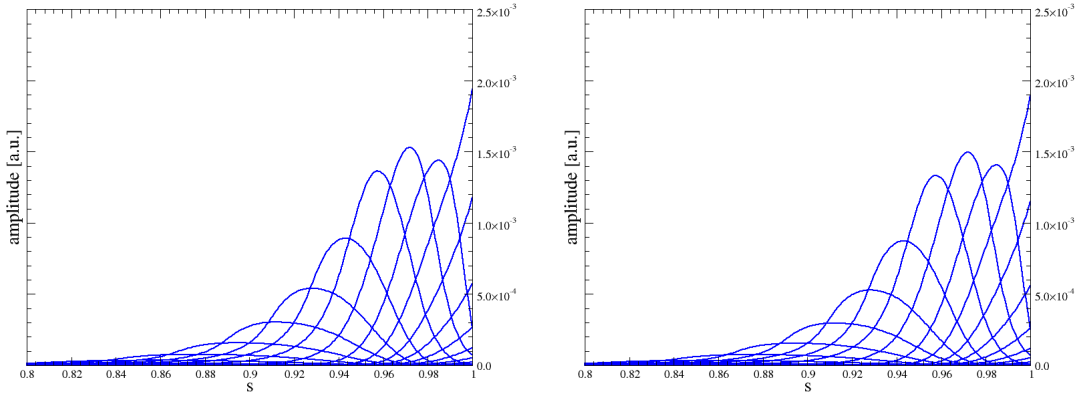

$d_{wp} = 2.50$ $d_{wp} = 1.25$

Figure 6.11: Radial mode structures for the fastest growing modes

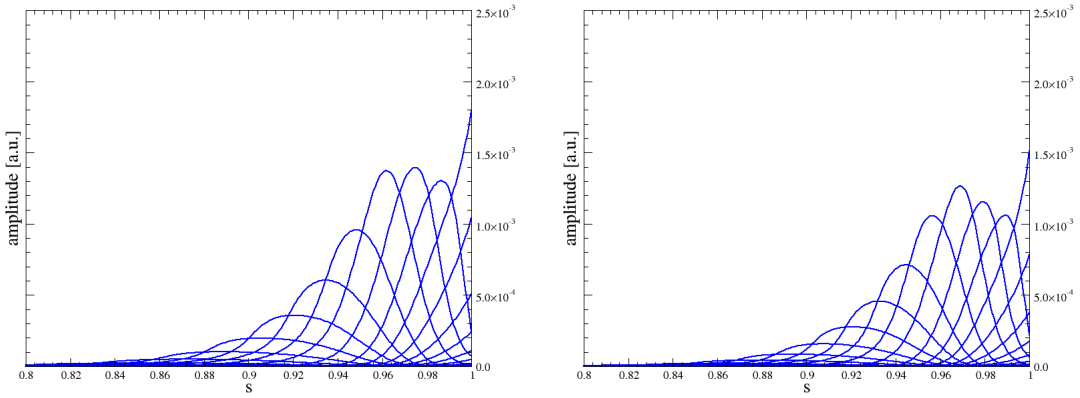

$d_{wp} = 1.10$ $d_{wp} = 1.05$

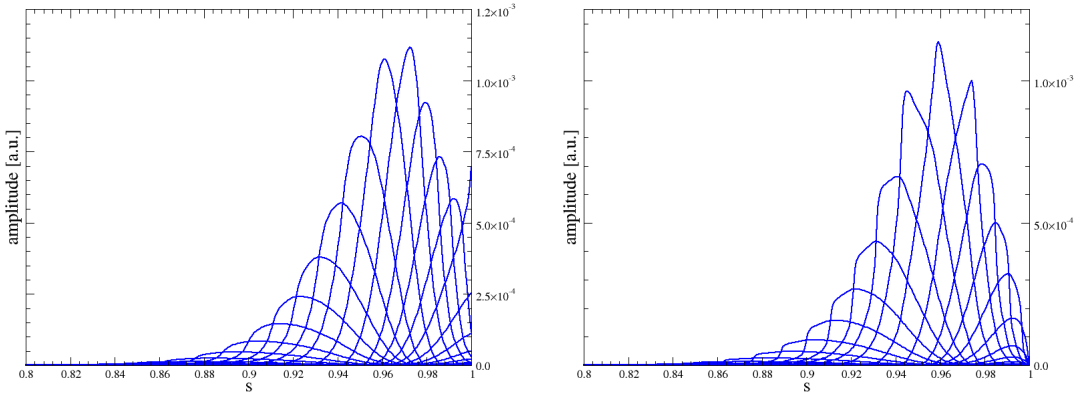

$d_{wp} = 1.01$ $d_{wp} = 1.00$

Figure 6.12: Radial mode structures for the fastest growing modes

6.3 Shaped plasma

Using the boundary description of HELENA in eqs. 6.2, the plasma parameters are

- $R_0 = 1.65$ m
- $a = 0.5$ m
- $B_0 = 2.0$ T
- $\kappa = 1.6$
- $\delta_H = 0.4$.

The triangularity $\delta_H = 0.4$ from the analytical description of the boundary corresponds to a geometric $\delta = 0.39$. The spectra in fig. 6.13 show the strong stabilizing effect of D-shaped plasma cross sections.

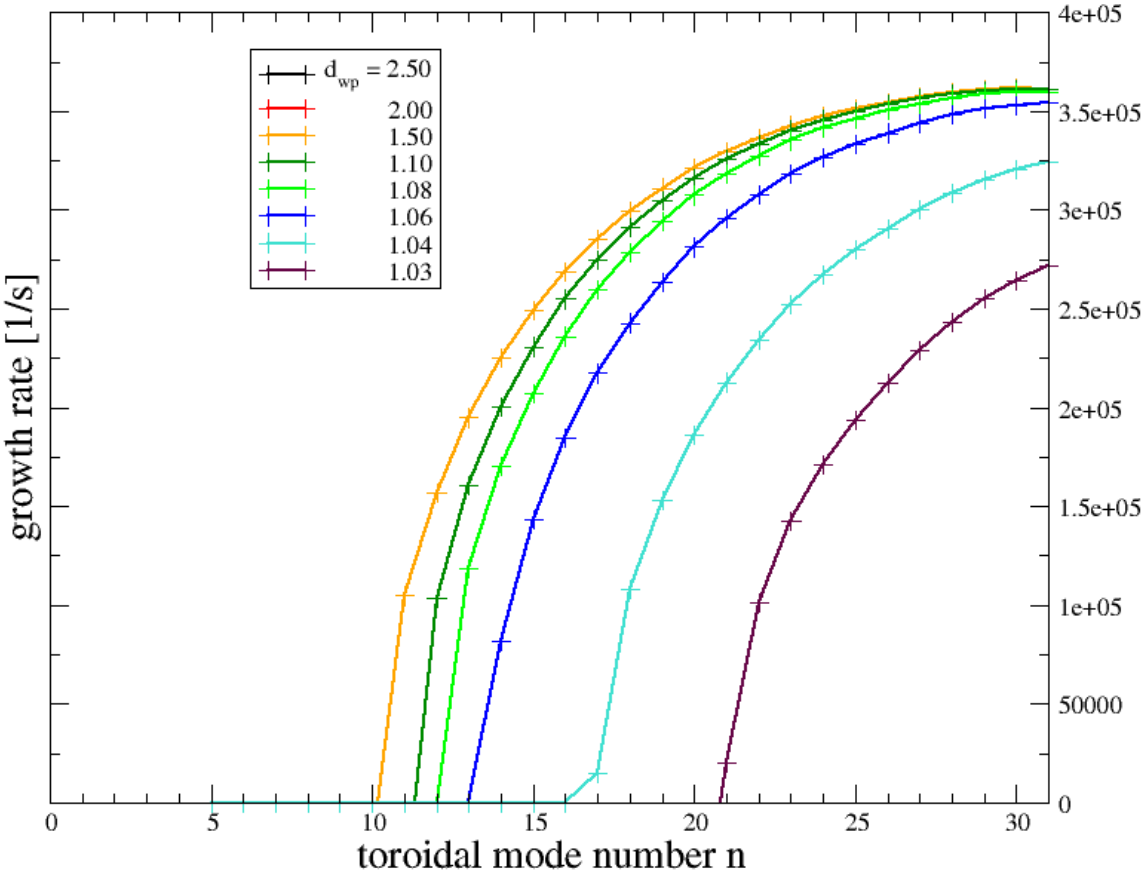

Figure 6.13: Growth rates vs. toroidal mode number n

For our case, this is most prominent for the low-n to intermediate-n modes, which get completely stabilized even with negligible influence from the perfectly conducting wall, $d_{wp} = 2.50$. This is due to lower edge current density drive (with regard to the circular case with high ϵ), fig. 6.3, and shaping effects. In the high-n, ballooning part of the spectra, growth rates are higher by $\approx 10\%$ - 15% compared to the circular, small aspect ratio case. This is a result of the increased maximum pressure gradient $\frac{dp}{d\psi}$, which is larger by $\approx 30\%$.

The plasma-wall distance furthermore effects the high-n modes stronger than observed in the previous chapter 6.2, but as the lower-n part is stable, the difference between the maximum growth rates for $d_{wp} = 2.50$ and $d_{wp} = 1.03$ is much smaller, on our case $\approx 20\%$. For lower $d_{wp} \leq 1.03$, however, the wall provides complete stabilization for all modes in the investigated toroidal mode number interval.

Comparing to the circular case, the radial mode structures inf figs. 6.14 and 6.15 show a smaller amplitude ratio between external and internal modes due to the lower edge current density and shaping effects. As the plasma shaping already provides a stabilizing effect on the lower-n, external modes, a smaller plasma-wall distance has only a small decreasing effect on the external perturbations up to $d_{wp} = 1.03$. For lower d_{wp}, however, the combination of shaping and proximity of the perfectly conducting wall result in stabilization of both the ballooning modes and the external modes with toroidal mode numbers $n \leq 35$.

As the shift of the onset of instability shift to higher n becomes more pronounced with lower d_{wp}, it is possible that very localized ballooning modes with $n > 35$ are still unstable for $d_{wp} \leq 1.03$, but computations for higher n become inreasingly involved and were not pursued further.

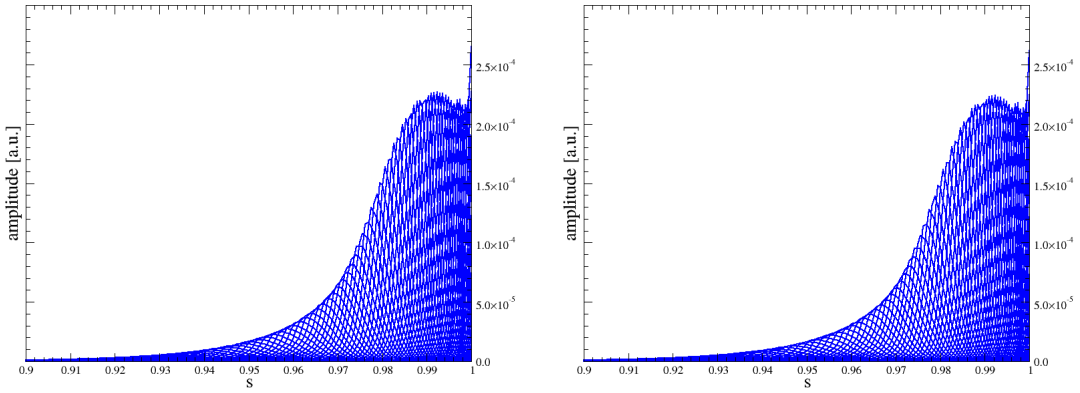

$d_{wp} = 2.50$ $d_{wp} = 1.10$

Figure 6.14: Radial mode structures for the fastest growing modes

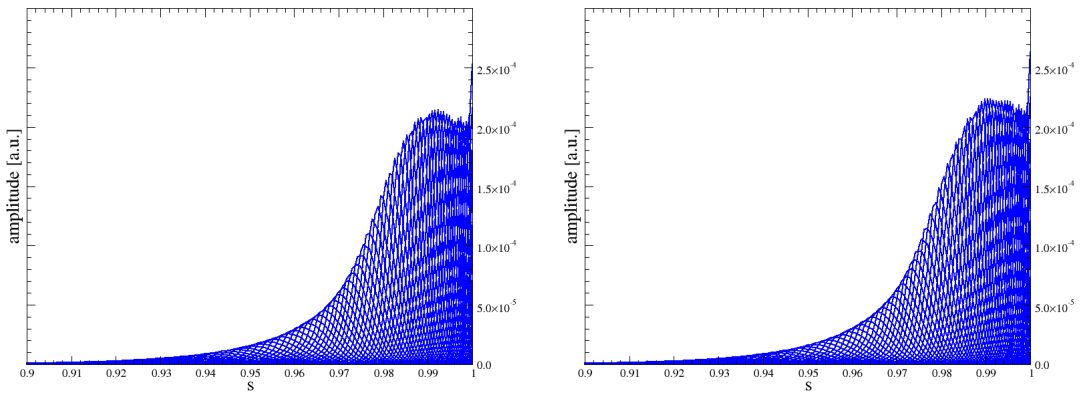

$d_{wp} = 1.08$ $d_{wp} = 1.06$

$d_{wp} = 1.04$ $d_{wp} = 1.03$

Figure 6.15: Radial mode structures for the fastest growing modes, shaped cross section

6.4 Comparison

Both the growth rates and the toroidal mode numbers of the fastest growing modes show a change only for $d_{wp} < 1.10$, compare figs. 6.16 and 6.17. For these plasma-wall distances, the maximum growth rates show large drops for smaller aspect ratios, but remain finite for the circular case for all d_{wp}. Shaping further provides stabilizing effects, so that the corresponding equilibrium is stable against modes with $n \leq 35$ even for $d_{wp} > 1.0$. The large aspect ratio case shows similar behavior as the circular small aspect ratio equilibrium, but the relative growth rate changes are smaller by a factor ≈ 2.
The toroidal mode numbers generally increase for $d_{wp} < 1.10$, as the external low-n modes get damped by the wall. This effect is most pronounced for the circular small aspect ratio case: because shaping effects already cause a stabilizing influence on the low-n modes even for $d_{wp} = 2.50$, the change of n remains small. The large aspect ratio case, however, features a large external contribution due to the small ϵ, and consequently also a small ballooning drive $\sim \kappa \nabla p_0$, therefore the mode numbers of the fastest growing modes remain smaller.

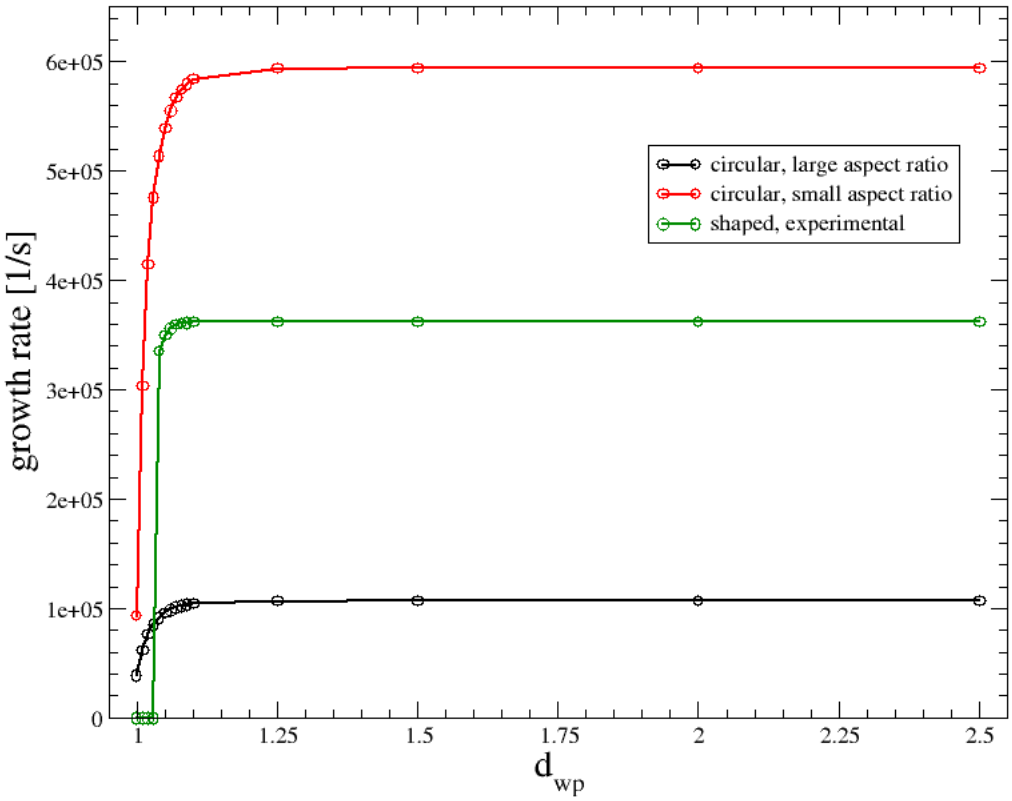

Figure 6.16: Growth rates of the fastest growing modes

For all cases, the proximity of a perfectly conducting wall has the largest effect on the low-n part of the spectra, associated with external modes. The high-n, ballooning part is much less affected, with the exception of $d_{wp} = 1.00$ for the circular, small aspect ratio case. For the

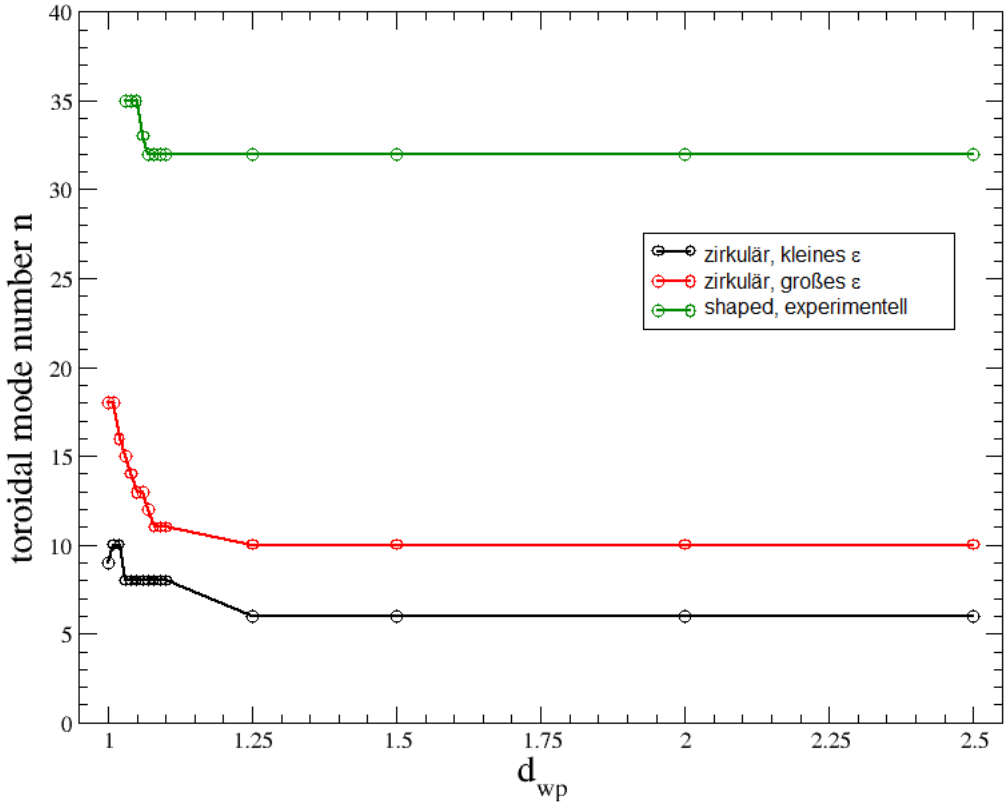

Figure 6.17: Toroidal mode numbers of the fastest growing modes

large aspect ratio, the influence of d_{wp} can even be neglected for large n.

So for an equilibrium featuring an edge ballooning mode and an external kink, both $d_{wp} = 1.01$ and $d_{wp} = 1.00$ give an indication of the pure ballooning contribution to the growth rates. Neither of them, however, gives the exact contribution, as $d_{wp} = 1.01$ still allows external modes and $d_{wp} = 1.00$ can have a strong effect on the internal ballooning mode as well. Furthermore, the coupling between internal and external modes is forced to zero, thus neglecting possible destabilizing effects.

In chapter 5, we stated that we have to exclude external modes from the GEM simulations. This is accomplished by a radial computation domain which does not cover a small region close to the LCFS. Therefore apart from instabilities exclusive to the gyrofluid model (ITGs, drift wave etc.), the GEM computations only consider the internal instabilities caused by the pressure gradient drive. The external modes are not suppressed like in the ILSA analysis, they are simply neglected. Thus a comparison between the ILSA and GEM results for $d_{wp} = 1.01$ and $d_{wp} = 1.00$ give the best comparison for the actual ideal ballooning instability. Opposing GEM and ILSA for $d_{wp} = 2.50$ give an indication of the error due to current driven contributions.

7 Numerical comparison

In this chapter, we present a numerical comparison of ideal linear MHD stability analysis and the nonlinear gyrofluid model GEM. We investigate the properties of model equilibria with regard to the pressure profile pedestal height, pedestal width, aspect ratio of the plasma and shaping effects of the plasma cross section (elongation κ and triangularity δ).

The ideal MHD equilibria are computed with HELENA, using pressure and current density as input profiles. The pressure profiles $p(\psi)$ are described analytically by

$$\begin{aligned} p(\psi) = p_{sep} &+ a_0 \left(\tanh \frac{2(1-\psi_{mid})}{\Delta} - \tanh \frac{2(\psi-\psi_{mid})}{\Delta} \right) \\ &+ a_1 \Theta \left(1 - \frac{\psi}{\psi_{ped}} \right) \cdot \left[1 - \left(\frac{\psi}{\psi_{ped}} \right)^{a_1} \right]^{a_2}, \end{aligned} \tag{7.1}$$

allowing for scans of the pedestal height and pedestal width of the pressure profiles. The coordinate ψ takes is normalized $0 \leq \psi \leq 1$, and Θ is the Heaviside function.
The current density profiles are given simple analytic forms with artificially small current densities and gradients in the edge region, avoiding drive of peeling / external kink modes because of the issues discussed in chapter 5. The exact profiles are given in each following section.

The equilibria are then tested for stability in the framework of ideal linear MHD with ILSA. This yields the growth rates as a function of the toroidal mode number n and the radial mode structure of possible instabilities for each n. We compute the spectra for plasma-wall distances $d_{wp} = 2.50$, $d_{wp} = 1.01$ and with a fixed boundary $d_{wp} = 1.00$ in conformal wall geometry. As we will see in due course, external contributions are often inevitable for the ideal linear MHD computations, but we have to exclude modes located at the LCFS for the gyrofluid computations as discussed in chapter 6. The fixed boundary $d_{wp} = 1.00$ not only completely surpresses external modes, but has also potential effect on ballooning modes located close to the edge, because there is no more coupling of external/internal modes as presented in chapter 5.3.1.

From the equilibria provided by HELENA, the Hamada metric is set up as described in [83],[84] and [36]. Unlike HELENA and ILSA, GEM additionally requires knowledge of the ion and electron temperature profiles. The local values of the temperatures (at the position of the fluxtube) enter the collision frequency $\nu_{e,i}$, defined as the inverse of the Braginskii

collision time[1]

$$\tau_{e,i} = \frac{6\sqrt{2}\pi^{\frac{3}{2}}\epsilon_0^2\sqrt{m_{e,i}}T_{e,i}^{\frac{3}{2}}}{\ln\Lambda e^4 n} \tag{7.2}$$

with the Coulomb logarithm[2]

$$\ln\Lambda \approx 6.6 - 0.5\ln(n) + 1.5\ln(T_e). \tag{7.3}$$

The temperature profile determine the gradient lengths $L_{T_{e,i}}$. For our purposes, we chose a temperature profile as described in chapter 5, yielding edge values of $\frac{T_i}{T_e} = 1.2$ and $L_{T_i} = 0.035$m. The simulation is started by applying a small perturbation to the density, so that possible instabilities can grow.
We use GEM in the local geometry representation, simulating only a single fluxtube with small radial computation domain L_x[3]. The radial background gradients are kept fixed[4], and the radial profiles are approximated by linear functions, i.e. constant gradients over the radial domain.

For all GEM runs, we investigate the fluctuating total energy E_T, the ion heat flux Q_i and their respective growth rates $\gamma_E = \frac{1}{2}\frac{\partial E_T}{\partial t}$ and $\gamma_Q = \frac{1}{2}\frac{\partial Q_i}{\partial t}$, the mode number spectra of n_e, ϕ, T_i and vorticity $\omega = \nabla \times \vec{v}$, and the envelope of the parallel mode structure for n, ϕ, h, T_i and T_e. For convenience, we have dropped the tilde from the fluctuating quantities. The mode number spectra show the squared amplitude of the respective quantities as a function of $k_y\rho_s$ and therefore give the toroidal mode number n of the maximum of the corresponding quantity because of the relation

$$n = \frac{k_y r}{q(r)}. \tag{7.4}$$

For the linear phase, a comparison between the ideal linear MHD stability analysis and the gyrofluid simulation can be done in terms of growth rates and toroidal mode numbers n. Note that at high n, the latter cannot be simply compared because of dissipation at small grid scales (towards the ion gyroradius) and FLR effects included in the gyrofluid model, occurring at high mode numbers $n \geq 100$. The spectra show if the dynamics have already reached the ion gyroradius scale $k_y\rho_s \approx 1$, with the vorticity showing the scale of the actual (fluid-like) plasma motion. During the linear phase, the spectra amplitudes at $k_y\rho_s = 1$ are several orders of magnitude lower than at lower wave numbers $k_y\rho_s \approx 0.1$, while flattening of the amplitude profiles mark the onset of the turbulent phase. In general, higher amplitudes at higher k_y indicate stronger turbulent character of the plasma and dynamics on smaller scales.

[1] in cgs units, except $T_{e,i}$ are given in eV
[2] with n in units of $10^{20}\frac{1}{m^3}$ and $T_{e,i}$ in eV
[3] recall that $L_x \leq L_\perp$ to validate the flux tube treatment, i.e. the profiles do not change significantly over the radial computation domain
[4] enforced by Dirichlet boundary conditions for the fluctuating quantities

7.1 Pedestal height

We consider a circular plasma cross section with nominal parameters

- major radius $R_0 = 1.65\text{m}$
- minor radius $a = 0.5\text{m}$
- vacuum magnetic field $B_0 = 2.5\text{T}$,

i.e. an inverse aspect ratio $\epsilon = 0.303$. We vary the pressure pedestal height, i.e. the pressure gradient in the edge, but leave the pedestal width constant. The pressure profiles in fig. 7.1 were chosen to cover the range from the onset of ideal MHD instability (p_2) to the max. achievable pressure gradient (p_{10}), above which no equilibrium could be found by HELENA.

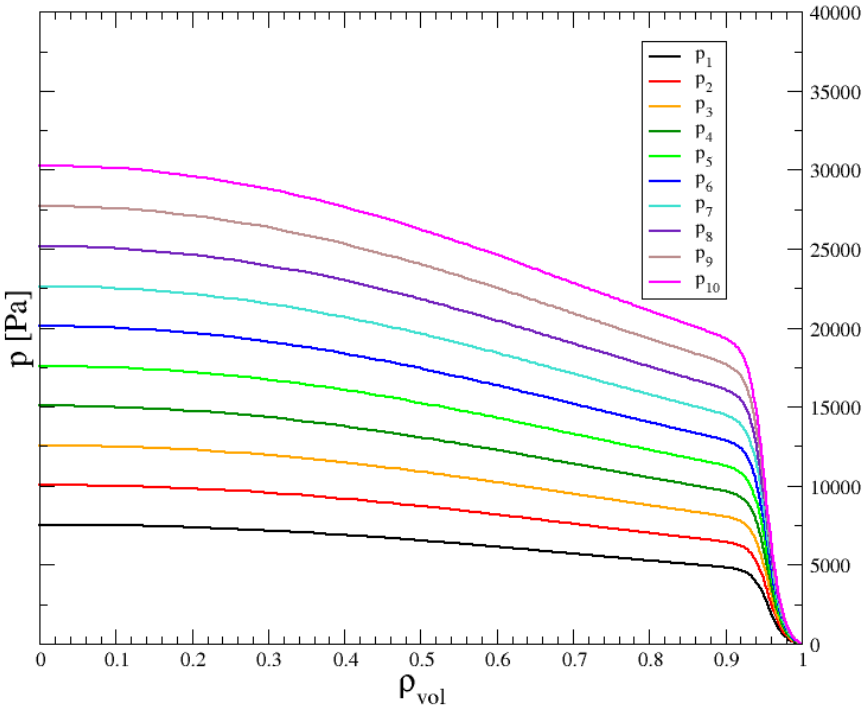

Figure 7.1: Pressure profiles

The flux-surface averaged current density profile shown in fig. 7.2 is given by

$$< j_{tor}(\psi) >= j_0 \left(1 - \psi\right)^2 . \tag{7.5}$$

The current density and the current density gradient at the edge of the plasma were chosen small to avoid drives for peeling modes as discussed in 5.2.

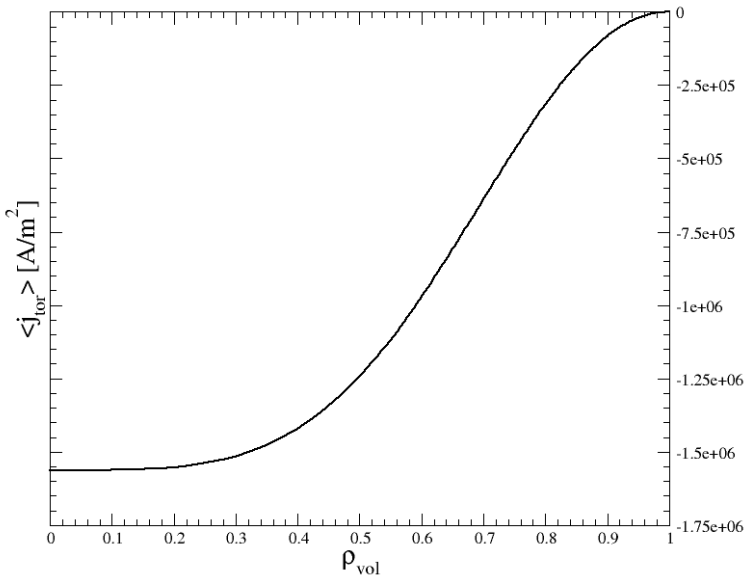

Figure 7.2: Current density profile

This setup yields q profiles with $q_0 \approx 1.5$ and edge values $q_a = 4 \ldots 5$, while the q factor at the positions of maximum pressure gradient is $q \approx 3.5$, fig. 7.3.

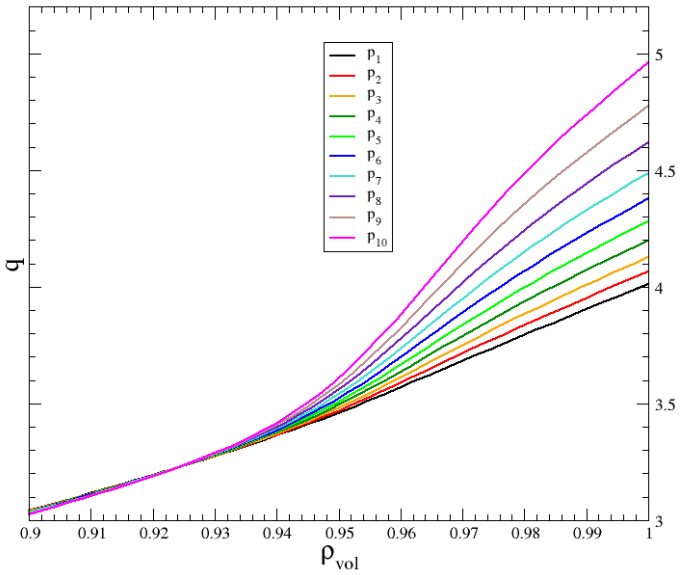

Figure 7.3: q profiles

The pressure gradients vary by a factor of ≈ 4 from the lowest pressure gradient p_1 to the highest one p_{10}, fig. 7.2.

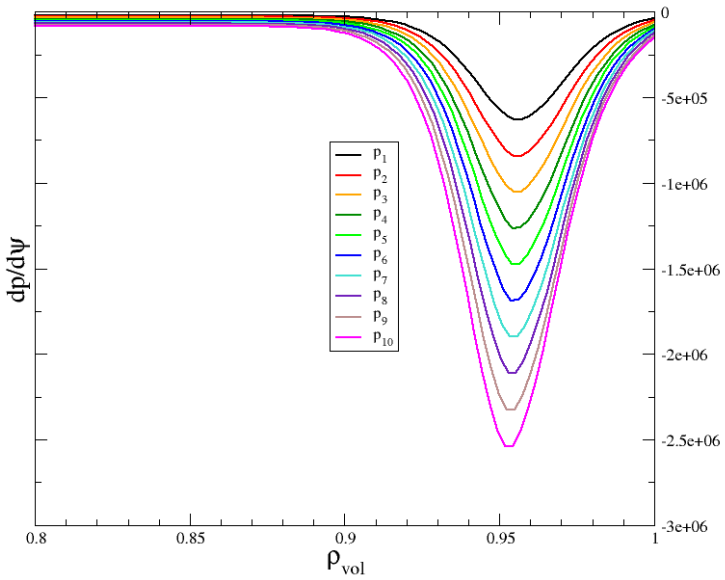

Figure 7.4: Pressure gradients

The global magnetic shear, see fig. 7.5, varies by a factor of ≈ 3 at the position of the maximum pressure gradient.

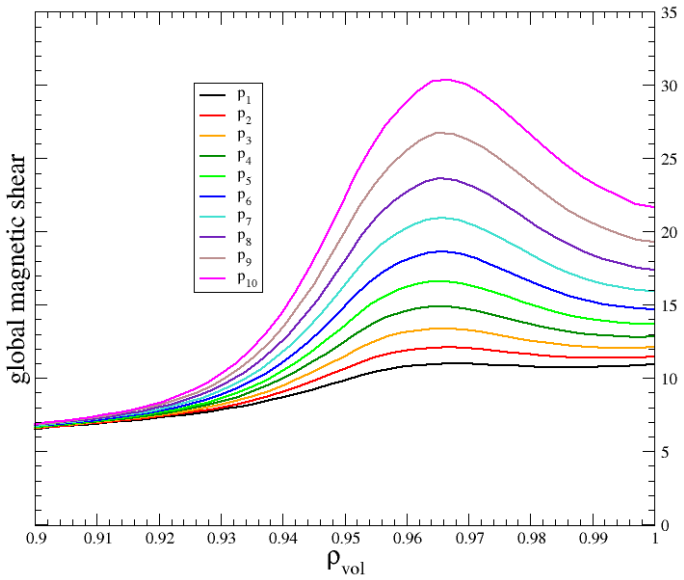

Figure 7.5: Global magnetic shear

7.1.1 Linear ideal MHD stability - ILSA

The spectra computed by ILSA are shown in figs. 7.6 - 7.9. For $d_{wp} = 2.50$, the onset of instability is at $n = 2$ for higher pressure gradients (p_6 - p_{10}) and shifts to higher values of n for lower pressure gradients. This behavior is due to decreasing contributions from external modes (having lower n) for lower pressure gradients, compare the radial mode structures in fig. 7.10, and an increasing radial mode width with increasing pressure gradients. As the pressure gradient exceeds the critical value for ballooning modes over a larger radial region, ballooning modes with lower n and thus less radial localization are destabilized.

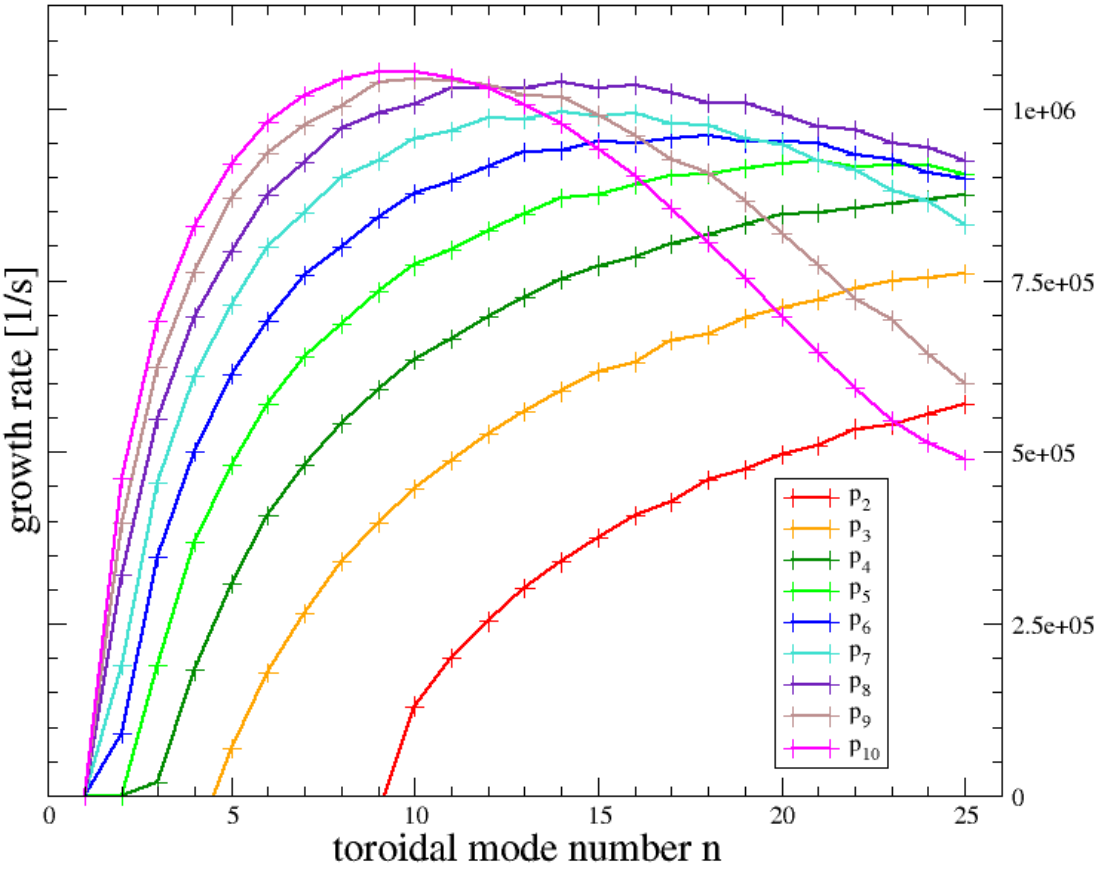

Figure 7.6: ILSA spectra with $d_{wp} = 2.50$

Even though the flux-surfaced current density was explicitly chosen to be small at the plasma edge, the setup gives a large difference of the current density at the inboard and outboard side, and only the average current density is small, fig. 7.7. These currents are the Pfirsch-Schlüter currents j_{PS} [?] [?], which are

$$j_{PS} \sim \frac{r}{R_0} \frac{dp}{dr} \cos\Theta, \tag{7.6}$$

where Θ is the poloidal angle and r the radial coordinate of the plasma cross section. For sufficient pressure gradients, external instabilities caused by j_{PS} cannot be avoided. This has to be taken into account when comparing with the GEM simulations.

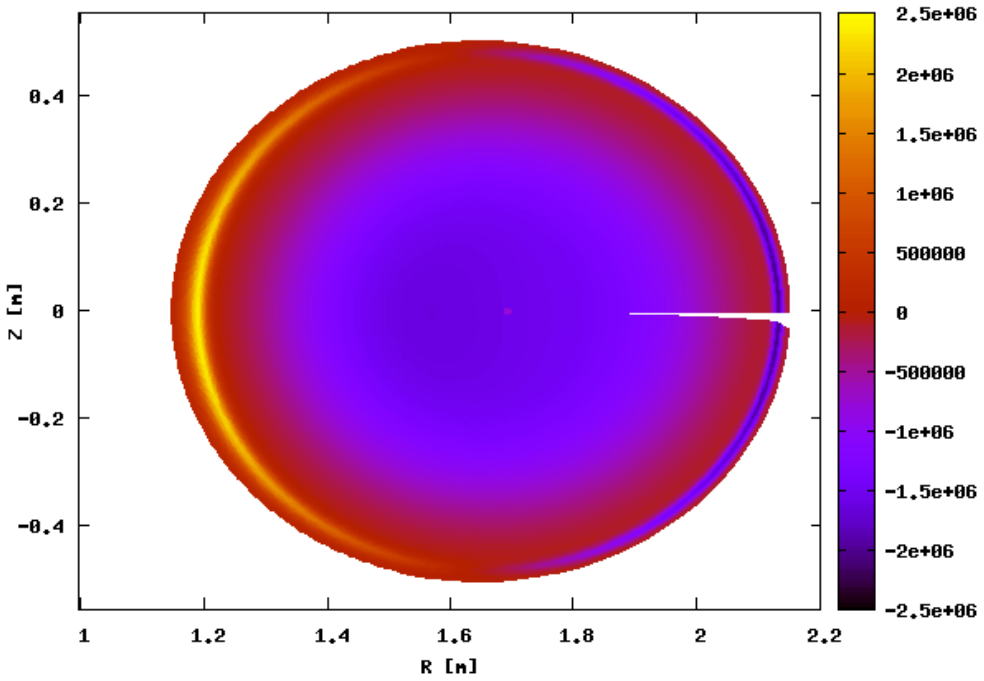

Figure 7.7: Contour plot of $j_{tor}(R, Z)$ in units of $\frac{\mathrm{A}}{\mathrm{m}^2}$, with R being the distance from the tokamak symmetry axis and the cylindrical coordinate Z

For higher pressure gradients, the external part becomes comparable to the internal ballooning part even for $d_{wp} = 1.01$, see fig. 7.10. This effect could not be prevented by altering the pressure profile form and must be taken into account when comparing the linear MHD results to the gyrofluid ones, as the the gyrofluid code radial simulation domain excludes the external contributions as discussed above. For lower pressure gradients, the spectra are more ballooning-like with max. growth rates at high values of $n > 25$. The max. growth rates monotonically grow with increasing pressure gradient, but for the two highest pressure gradients (p_9 and p_{10}), the high-n part of the spectra shows clear stabilizing effects from the high magnetic shear of these configurations. The maximum growth rates differ by a factor of ≈ 1.8, and the increase of the growth rates becomes lower for higher pressure gradient.

This general picture is the same for $d_{wp} = 1.01$ and $d_{wp} = 1.00$, except that the growth

rates do no increase monotonically with increasing pressure gradient. For the cases with pressure profile p_7 and above, the max. growth rates decrease. This is due to the significant contribution from external modes, which get stabilized by a perfectly conducting wall close to the plasma as shown in chapter 6. The latter also causes the shift of the onset of stability to higher n, as the external modes typically have low n.

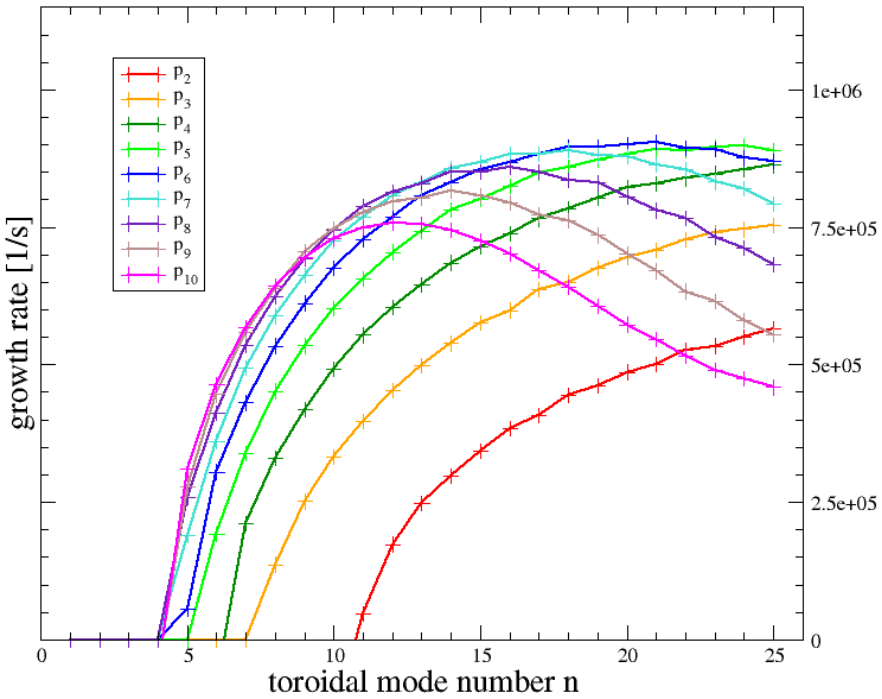

Figure 7.8: ILSA spectra with $d_{wp} = 1.01$

The case with pressure profile p_1 is stable in the framework of linear ideal MHD.

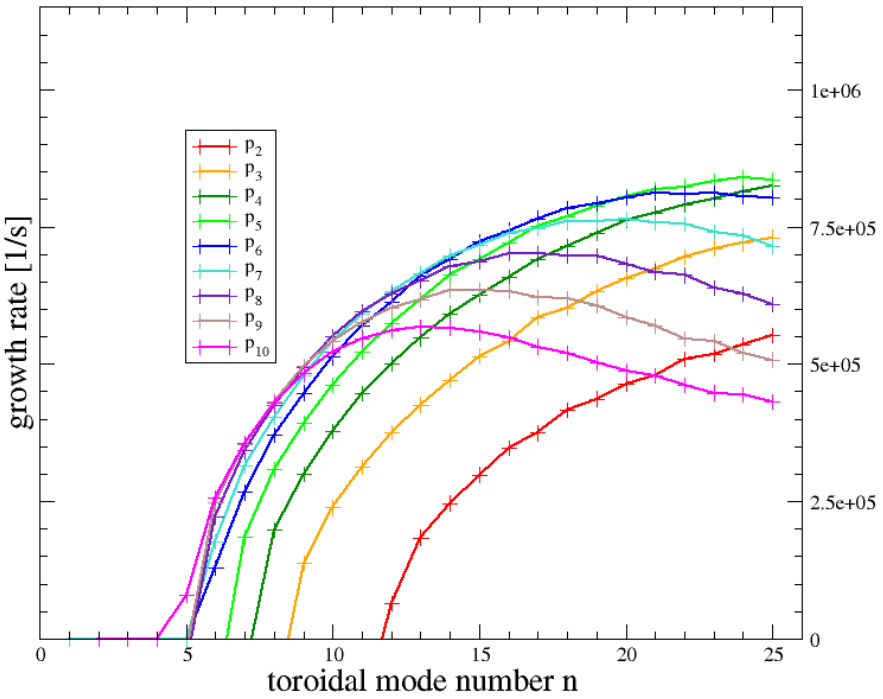

Figure 7.9: ILSA spectra with $d_{wp} = 1.00$

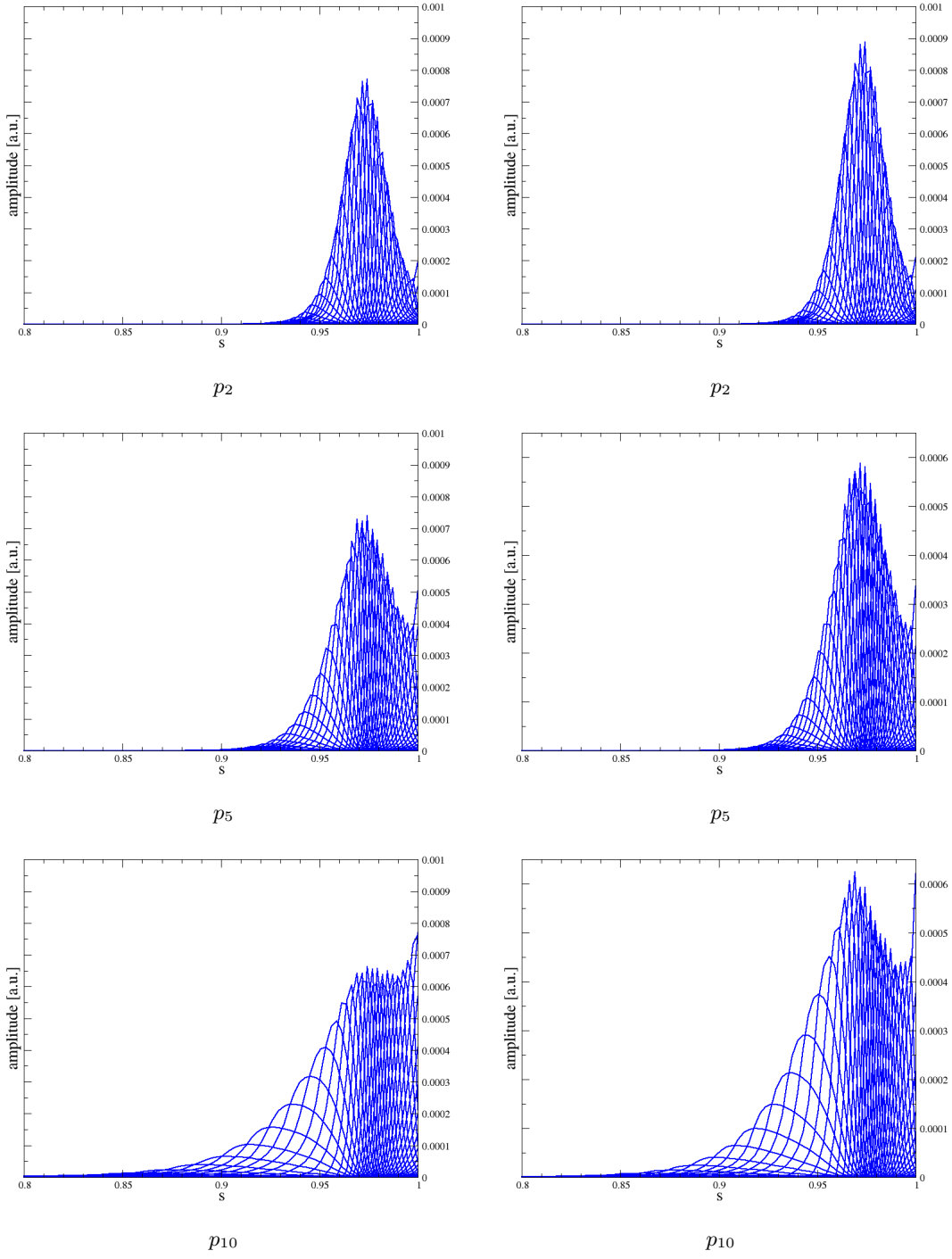

Figure 7.10: Left column: radial mode structures for the fastest growing modes with $d_{wp} = 2.50$ Right column: radial mode structures for the fastest growing modes with $d_{wp} = 1.01$

7.1.2 Gyrofluid - GEM

The fluctuating part of the total energy E_T shows clear initial exponential growth of the total energy , see fig. 7.11, correlated to the linear phase of the instability. The growth rates increase with increasing pressure gradient, and the time point of maximum growth rates γ_E and onset of the nonlinear saturation phase shifts to smaller time values, compare fig. 7.12.The growth rate γ_E is maximal at $t = 16.5\mu$s for p_3 and at $t = 4.7\mu$s for p_{10}. Both the growth rates and the maximum values of E_T increase less with higher pressure gradient, a trend similar to the ILSA results.
Only for the cases with p_4 and higher there is a clear overshoot of E_T, and the saturation level in the nonlinear phase as well as the fluctuations around the average value tend to increase with increasing pressure gradient.
The cases p_1 and p_2 show a short, small increase in growth rate shortly after the begin of the simulation, with no clear ideal ballooning signature. This can be seen in the parallel mode structure of both cases, see fig. 7.19; and at the time point of the initial small burst, the squared amplitude of n_e is much higher than in the following cases.
The case with p_2 can be considered a threshold case, as there is a small increase in the growth rate at $t \approx 17\mu$s. This could still be a mere fluctuation, but the growth rate γ_Q of the ion heat flux Q_i in fig. 7.14 indicate that this is indeed qualitatively different from the case with p_1, which was stable in the linear ideal MHD picture. Else, the ion heat fluxes and their growth rates follow the trend of E_T and γ_E.

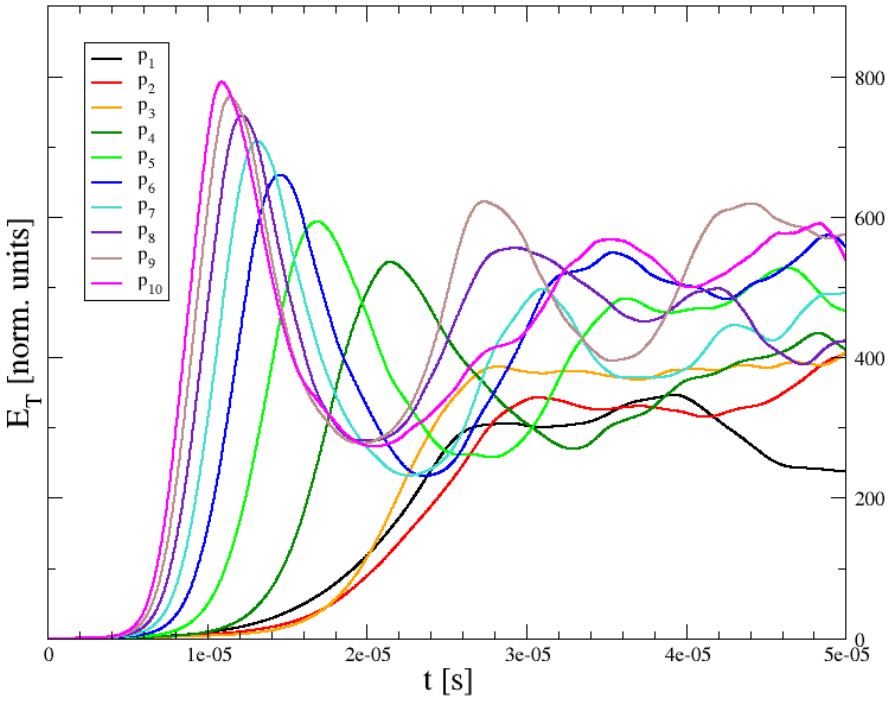

Figure 7.11: Total energy E_T

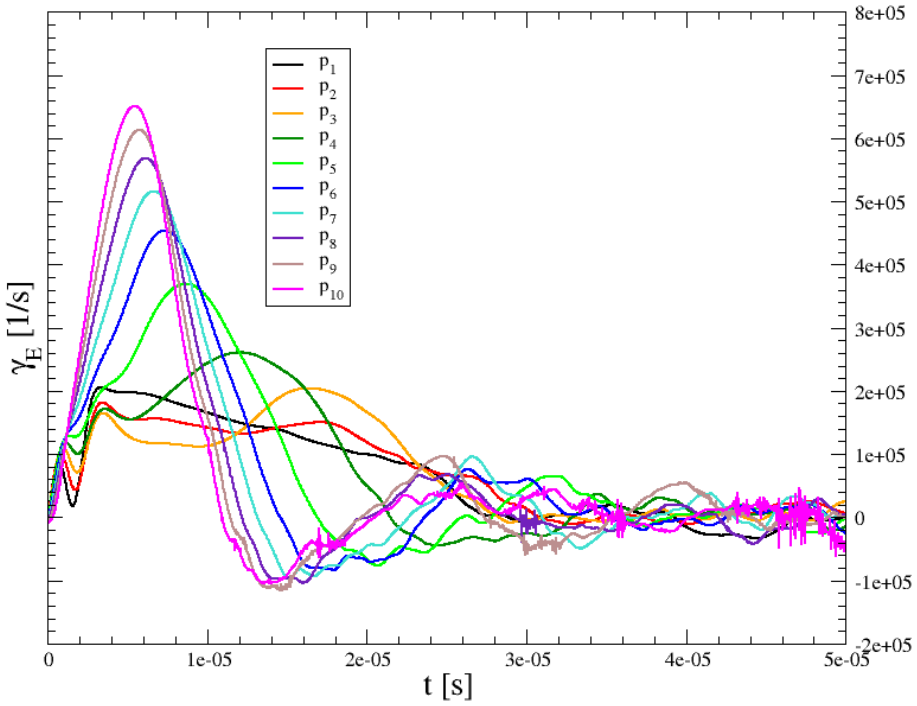

Figure 7.12: Growth rate γ_E

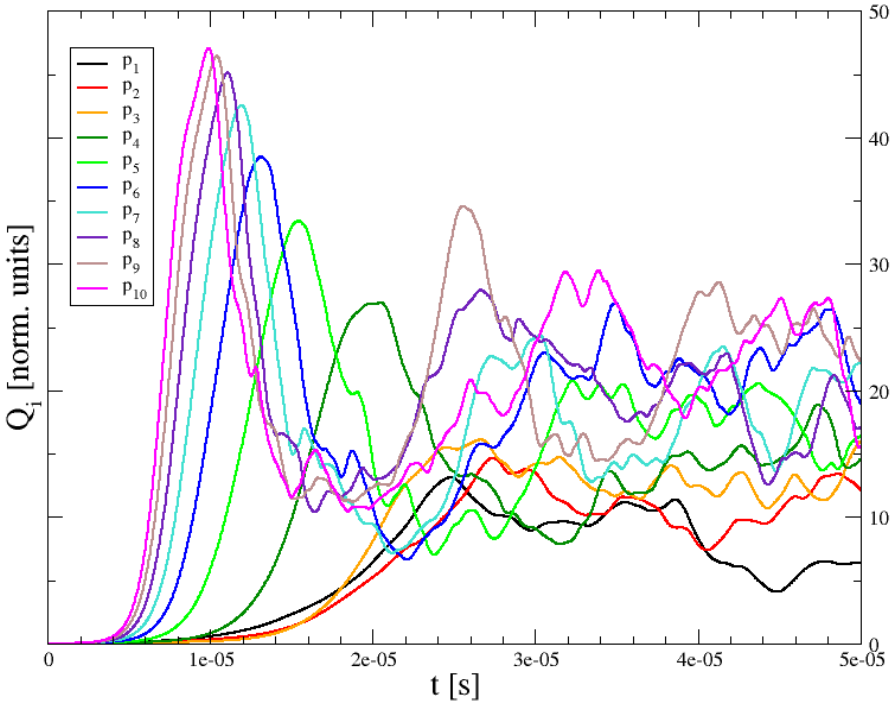

Figure 7.13: Ion heat flux Q_i

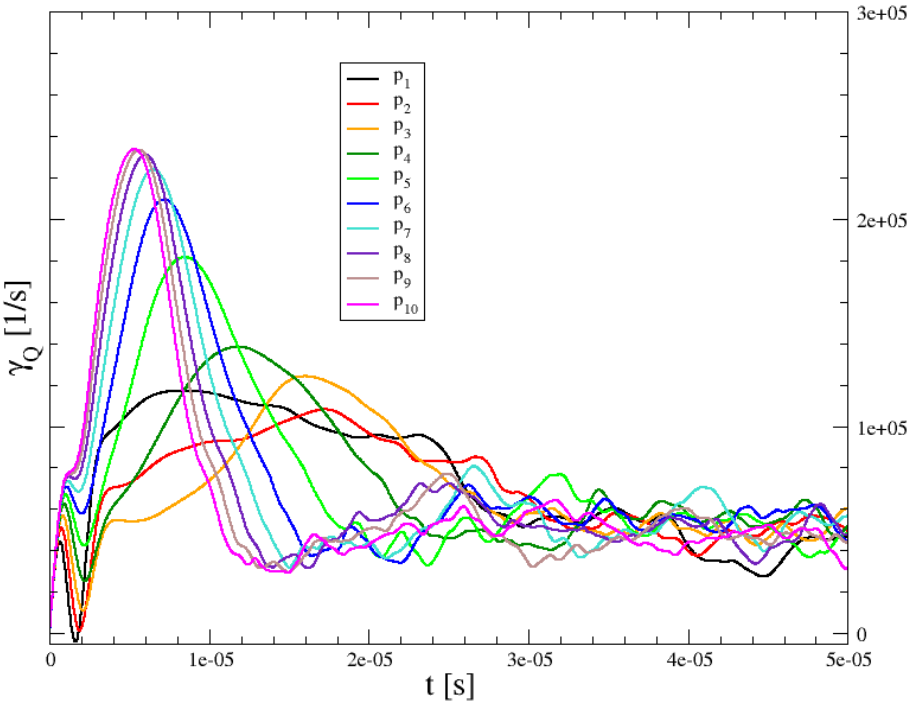

Figure 7.14: Growth rate γ_Q

The spectra of n_e, Q_i, ϕ at the time point of maximum growth rate all have a peak at $k_y\rho_s = 0.1$ for all cases, compare figs. 7.15 - 7.18, except p_1 and p_2. The latter do not show this peak for the spectra of n_e and ϕ, but it is present in the spectra of Q_i. Again, this indicates the threshold character of the case with p_2. Except for p_1 and p_2, the vorticity ω already reaches down to the ion gyroradius scale. The spectra for vorticity and ion heat flux show largest squared amplitudes especially at $k_y\rho_s \gtrsim 1$ for p_3, the first case after the threshold case p_2, and decrease subsequently with increasing pressure gradient.

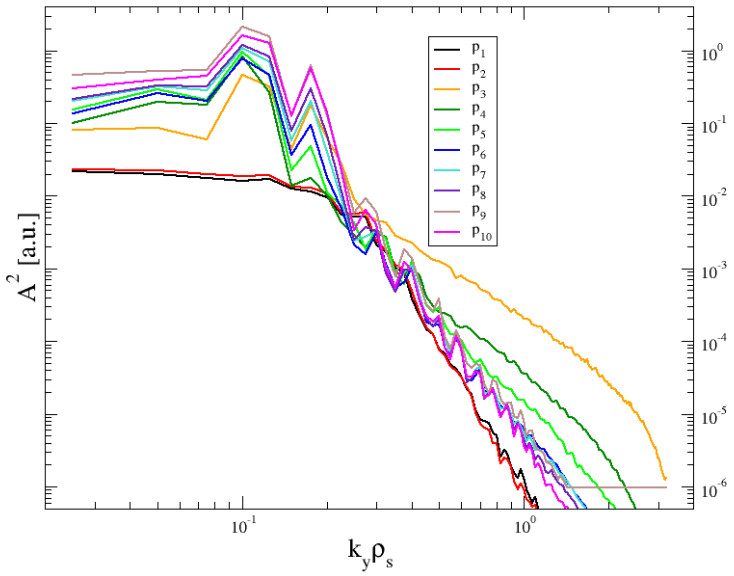

Figure 7.15: Spectra of n_e at the time of max. growth rate

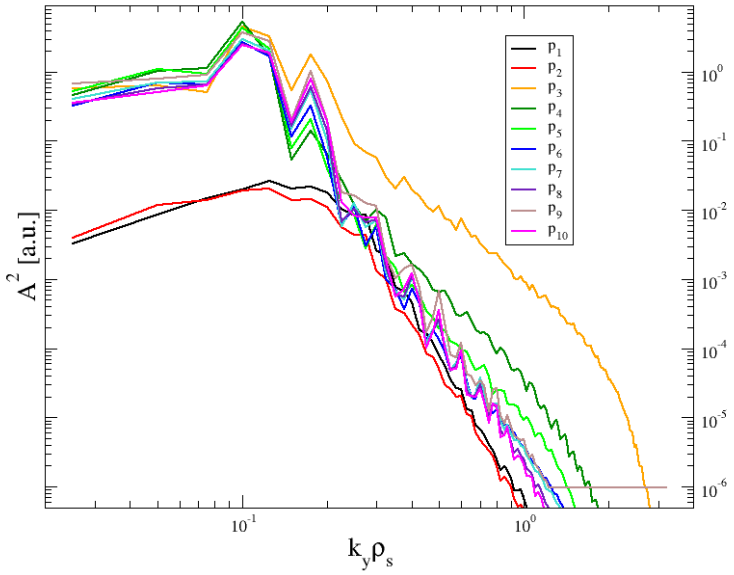

Figure 7.16: Spectra of Q_i at the time of max. growth rate

The parallel mode structures in fig. 7.19 identifies the case p_3 to have a strong ITG-like mode

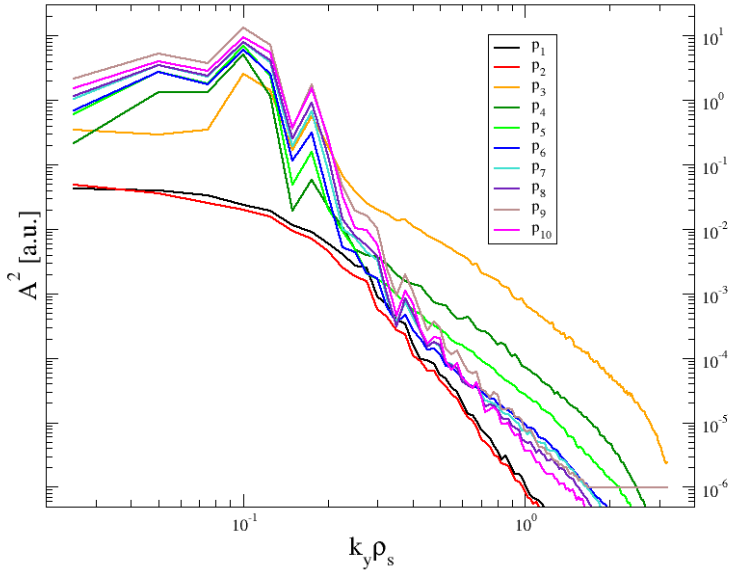

Figure 7.17: Spectra of ϕ at the time of max. growth rate

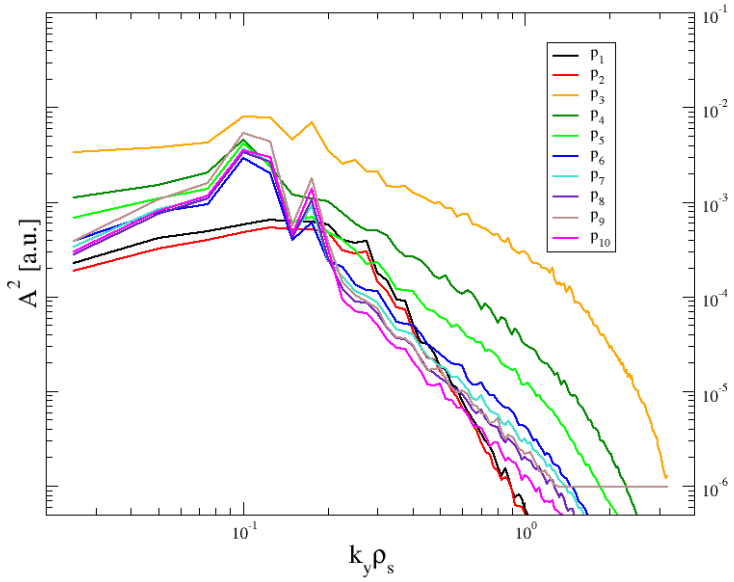

Figure 7.18: Spectra of ω at the time of max. growth rate

structure, with $T_i \gg$ all other quantities. While p_2 is the threshold case for gradient driven instability, for the transition to the ideal MHD ballooning regime, the threshold case is p_4. The non-adiabatic coupling h_e is already larger than all other quantities, but still the squared amplitudes for $T_i \approx \phi$. From p_5 onward, there is clear ideal MHD ballooning regime, with $h_e > \phi \gg$ all others. For higher ∇p, the ideal MHD ballooning character further becomes more pronounced, and the temperature gradient effects dimish with decreasing η_i.

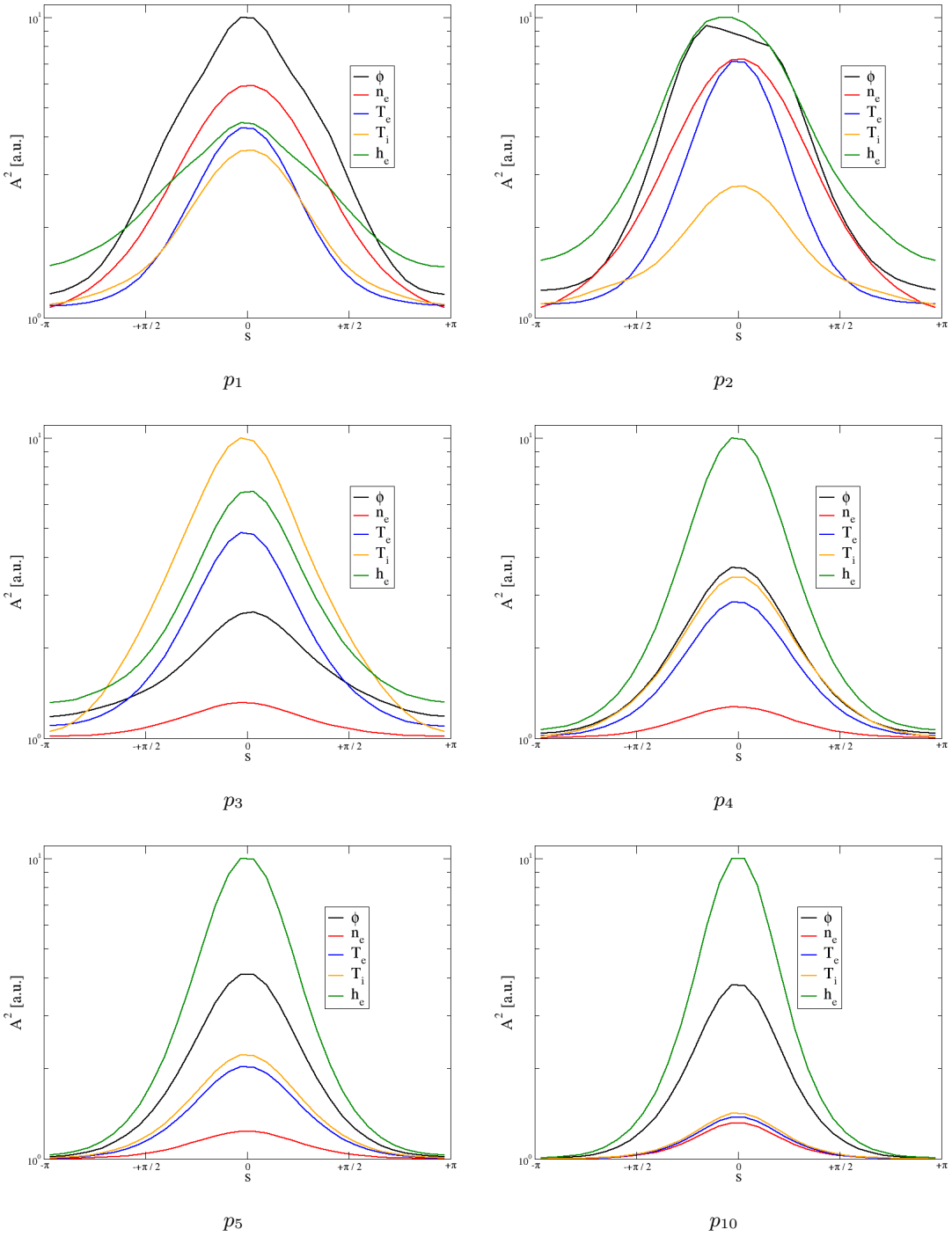

p_1 p_2 p_3 p_4 p_5 p_{10}

Figure 7.19: Parallel mode structures at the time of maximum growth rate

7.1.3 Comparison

The growth rates from ILSA are generally higher by a factor of $\approx 2-3$ compared to the GEM values for $d_{wp} = 2.50$, see fig. 7.20, while the relative difference is smaller for higher pressure gradients. The relative difference has a noticeable drop from the case p_5 onwards, the first case with a clear ideal MHD ballooning regime. There are two trends visible: the growth rates agree better for higher pressure gradients and a consequently clearer ideal ballooning mode structure of the gyrofluid simulations, and a smaller plasma-wall distance d_{wp}. For larger ∇p, the relative difference in growth rates gets smaller even for practically no influence of the perfectly conducting wall $d_{wp} = 2.50$, although the external contributions of the ideal MHD stability analysis grow substantially. Therefore the clearer ballooning character is more important to the gyrofluid results than the neglected external modes. For the steepest pressure pedestal p_{10}, the growth rates are in very good agreement for $d_{wp} = 1.01$ and $d_{wp} = 1.00$. Note that for $d_{wp} = 1.00$, the growth rates obtained from ILSA underestimate the ballooning instability of the underlying equilibrium, as the complete suppression of the external modes also eliminates the destabilization of ballooning modes by means of the internal-external coupling described in chapter 5.3.1 The largest relative difference with regard to the growth rates is for the cases p_2 - p_4, which are all outside the MHD regime.
In general, the growth rates computed with GEM can be regarded as too small, as the radial computation domain does not cover the contributions from the external modes as well as a small part of the actual internal ballooning part, as a region close to the edge is always missing.

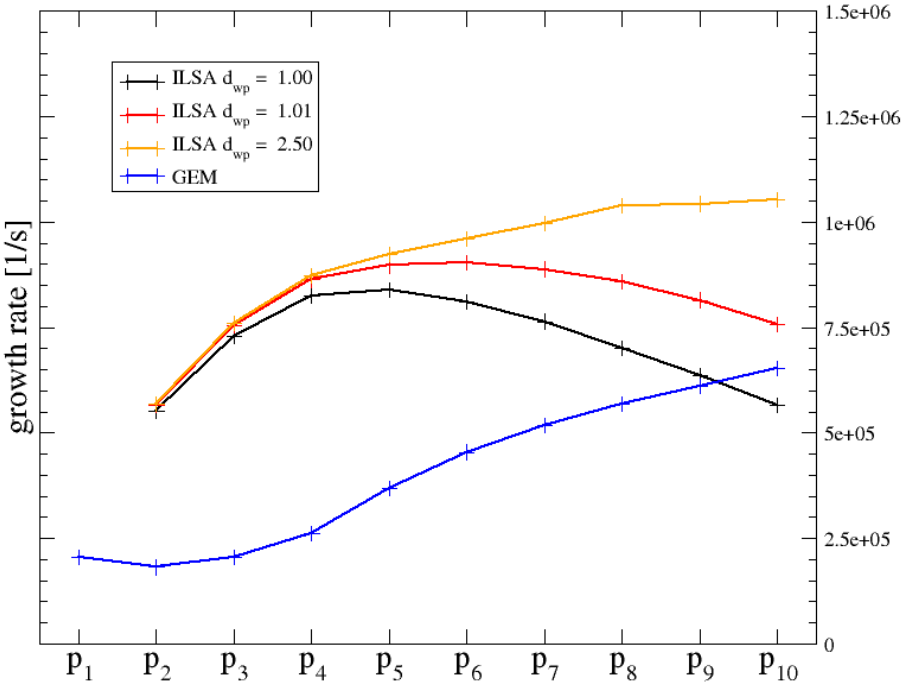

Figure 7.20: Maximum growth rate comparison

The mode numbers obtained by GEM with fixed radial computation domain are nearly insensitive to the pressure gradient, even for the ITG-like case p_3, see fig. 7.21. Only the cases p_1 and p_2 show slightly higher mode numbers expected for more ITG-like setups. The gyrofluid mode numbers are slightly smaller than the MHD ones, except for the cases with higher pressure gradients. As the cases with higher pressure gradients show significant external contributions, this deviation is clearly understandable, as the GEM computations neglect these external contributions and thus experience no shift to smaller mode numbers. Again, the difference is smaller when $d_{wp} = 1.01$ for the same reasons as with the growth rates.

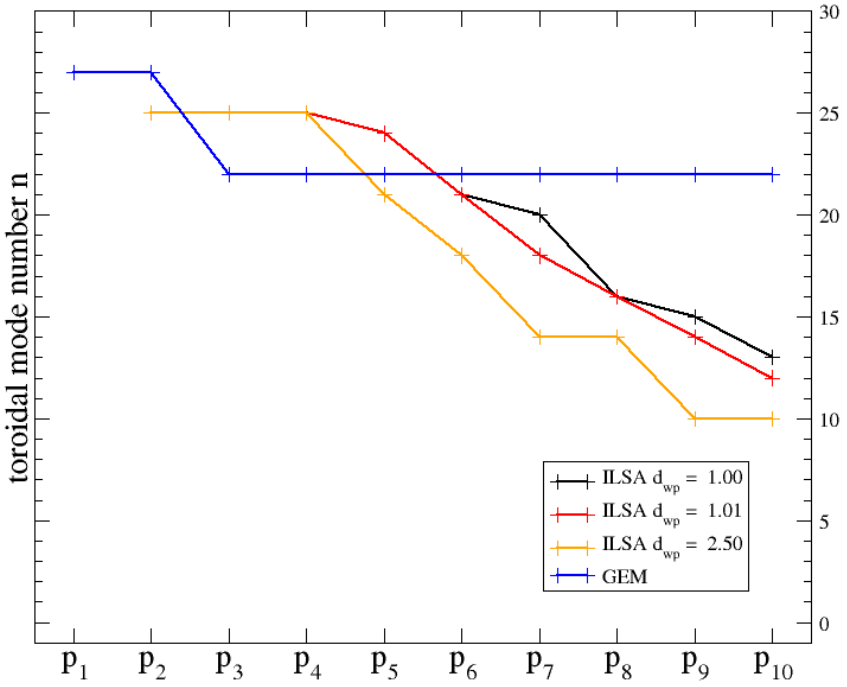

Figure 7.21: Toroidal mode number comparison for the fastest growing modes

In [72], the dynamics of edge ballooning modes has been investigated with GEM using global geometry, i.e. true radial dependence of the profiles and no assumptions of linearized profiles and constant gradients. The underlying equilibrium, however, was not computed with external ideal MHD equilibrium solvers like HELENA. The initial profiles were pre-equilibrated to yield shapes according to experimental observations. The nominal ballooning case in [72] roughly corresponds to our case p_8. The global simulations gives a maximum growth rate of $\approx 7.2 \cdot 10^5 \frac{1}{\mathrm{s}}$, compared to $\gamma \approx 6.0 \cdot 10^5 \frac{1}{\mathrm{s}}$ for our study. Furthermore, the toroidal mode number for the global case is ≈ 10 at the time of maximum growth, which would be in good agreement with the ILSA results in fig. 7.21.

7.2 Pedestal width

We consider a circular plasma cross section with nominal parameters

- major radius $R_0 = 1.65\text{m}$
- minor radius $a = 0.5\text{m}$
- vacuum magnetic field $B_0 = 2.5\text{T}$,

i.e. an inverse aspect ratio $\epsilon = 0.303$. We vary the pedestal by changing the parameter Δ in eq. (7.1), while leaving the pedestal height constant, see figs. 7.22 and 7.23. Furthermore we chose

$$\psi_{ped} = 1 - \Delta \tag{7.7}$$

$$\psi_{mid} = 1 - \frac{\Delta}{2}. \tag{7.8}$$

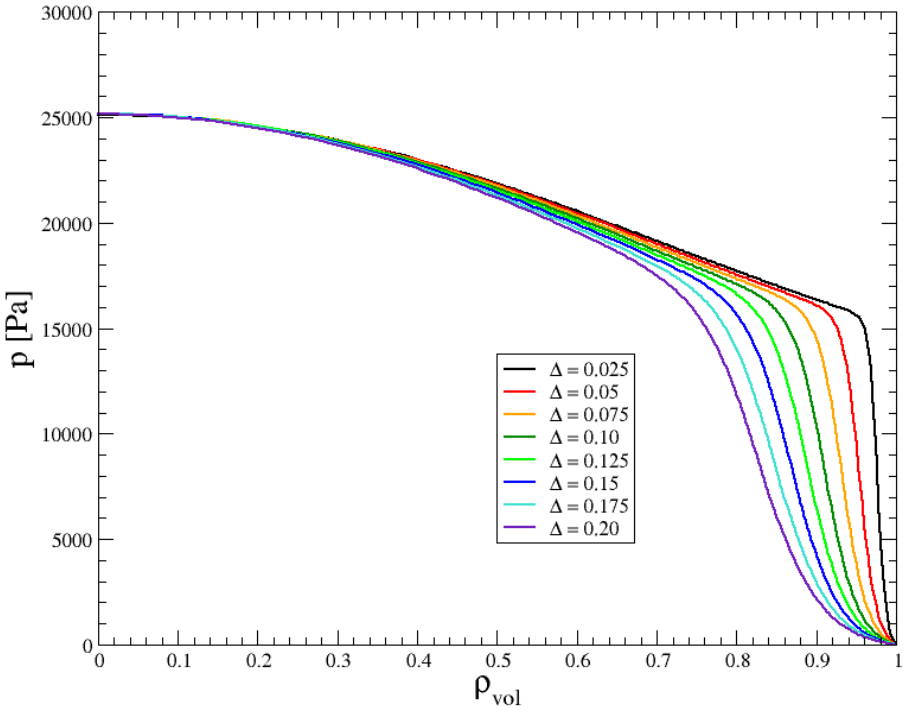

Figure 7.22: Pressure profiles

For higher Δ the pedestal width increases, the pressure gradient decreases and the radial position of the maximum pressure gradient shifts away from the LCFS as shown in fig. 7.24.

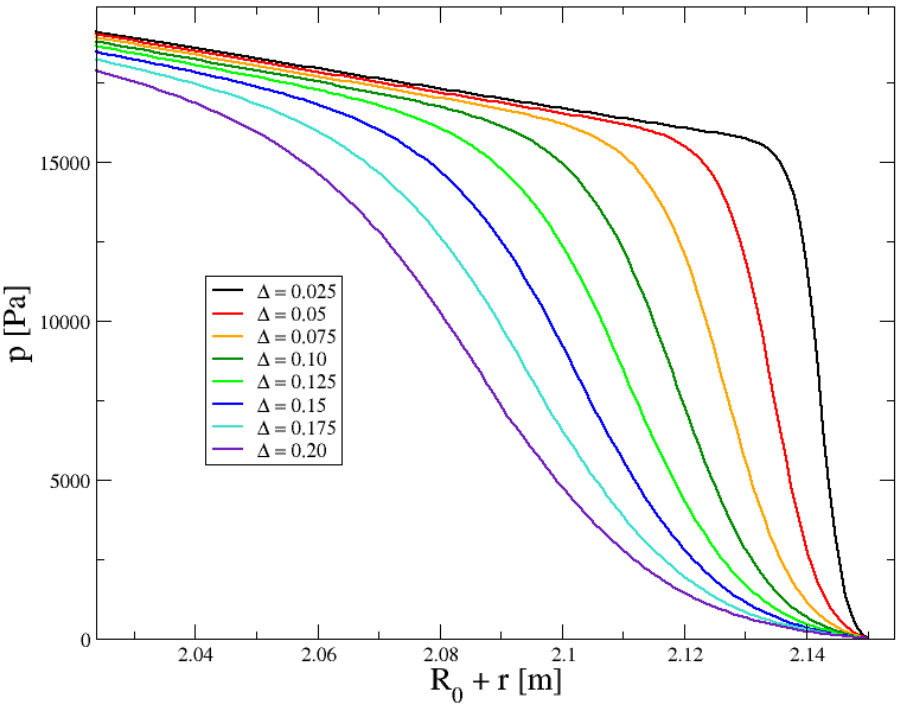

Figure 7.23: Pressure profiles pedestal region. R_0 is the major radius and r the distance from the center of the plasma cross section

The range of Δ covers the onset of linear MHD instability ($\Delta = 0.175$) to the maximum pressure gradient ($\Delta = 0.025$) above which no equilibrium could by found.
The pressure profiles with $\Delta = 0.15$, 0.175 and 0.2 have gradient maxima outside the temperature profile pedestal (towards the axis), where $L_{T_i} \approx 0.1m$. The pressure gradient maximum for $\Delta = 0.025$ is located very close to the edge and was chosen so that the density gradient length is actually smaller than the ion temperature gradient length.

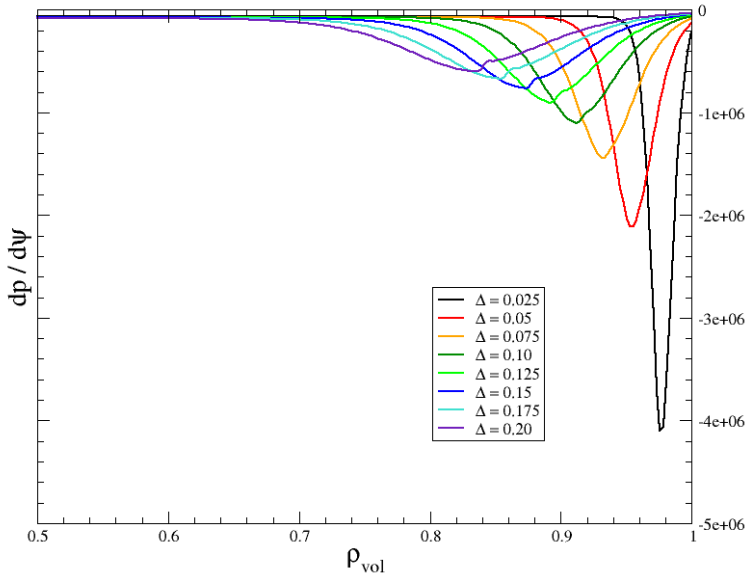

Figure 7.24: Pressure gradients

The fixed flux-surface averaged current density $< j_{tor} >$ is the same as in the previous section analyzing the pedestal height, see fig. 7.2.

This setup gives q profiles shown in fig. 7.25, with $q_0 > 1$ ensuring stability against internal kinks and moderate values of $q_a \approx 4.5$. The q profile for $\Delta = 0.025$ shows a larger increase in the edge region relative to the other q profiles, resulting in a much larger global magnetic shear, fig. 7.26.

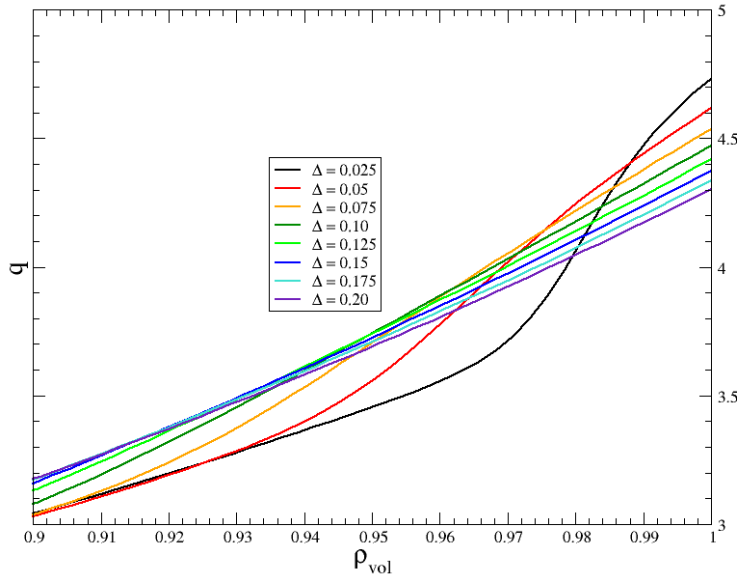

Figure 7.25: q profiles

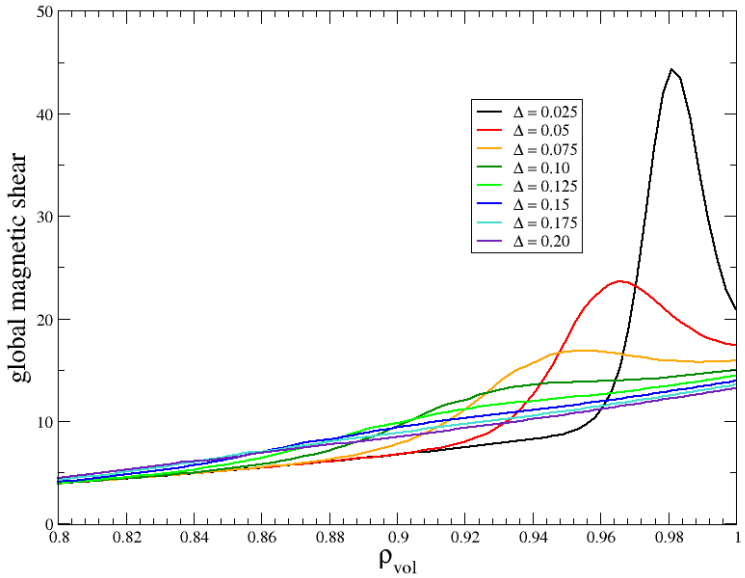

Figure 7.26: Global magnetic shear

7.2.1 Linear ideal MHD stability - ILSA

In the ILSA spectra, figs. 7.27 - 7.29, we see a very strong effect of the wall on the spectrum corresponding to the pressure profile with $\Delta = 0.025$, and a smaller but still noticeable effect on the one with $\Delta = 0.05$. The fastest growing modes for both values of Δ still show a clear external part aside the internal ballooning part even for $d_{wp} = 1.01$, see fig. 7.30. This is due to the Pfirsch-Schlüter currents as in chapter 7.1. For the cases from $\Delta = 0.175$ to 0.075,

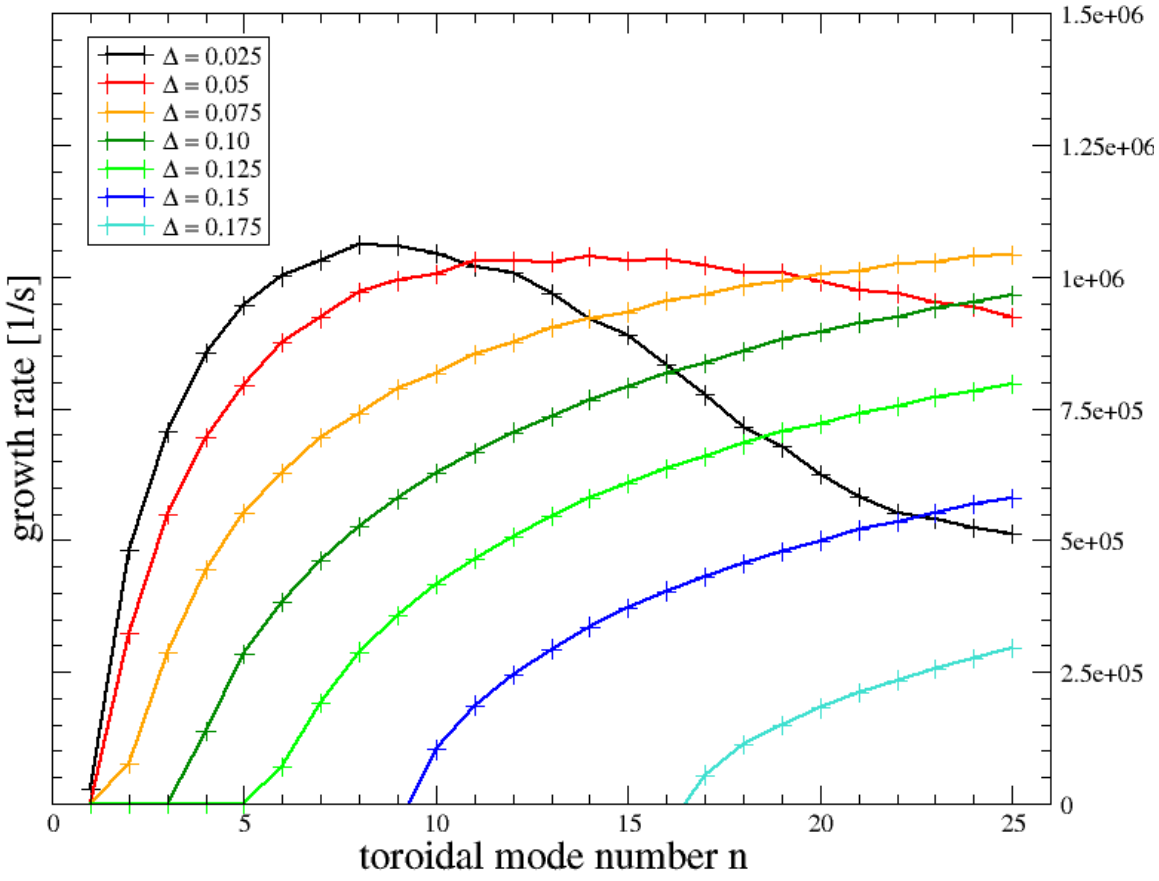

Figure 7.27: ILSA spectra with $d_{wp} = 2.50$

the maximum growth rate increases with smaller pedestal width for all values of d_{wp} and the spectra show a strong ballooning character with max. $n > 25$. The onset of instability is shifted to higher n for larger Δ because the external, low-n part of the perturbations decrease, compare fig. 7.30. The cases with $\Delta = 0.05$ and 0.025 exhibit an external part that is comparable or even larger than the internal ballooning part, despite a close proximity of the conducting wall. This also explains the sharp drop of the growth rate for $\Delta = 0.025$

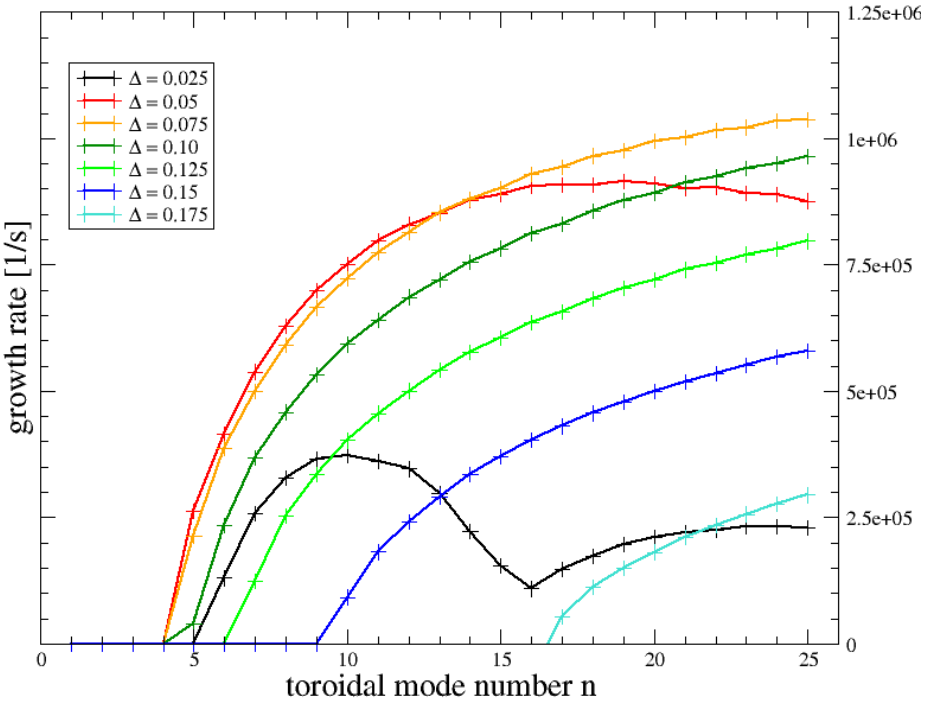

Figure 7.28: ILSA spectra with $d_{wp} = 1.01$

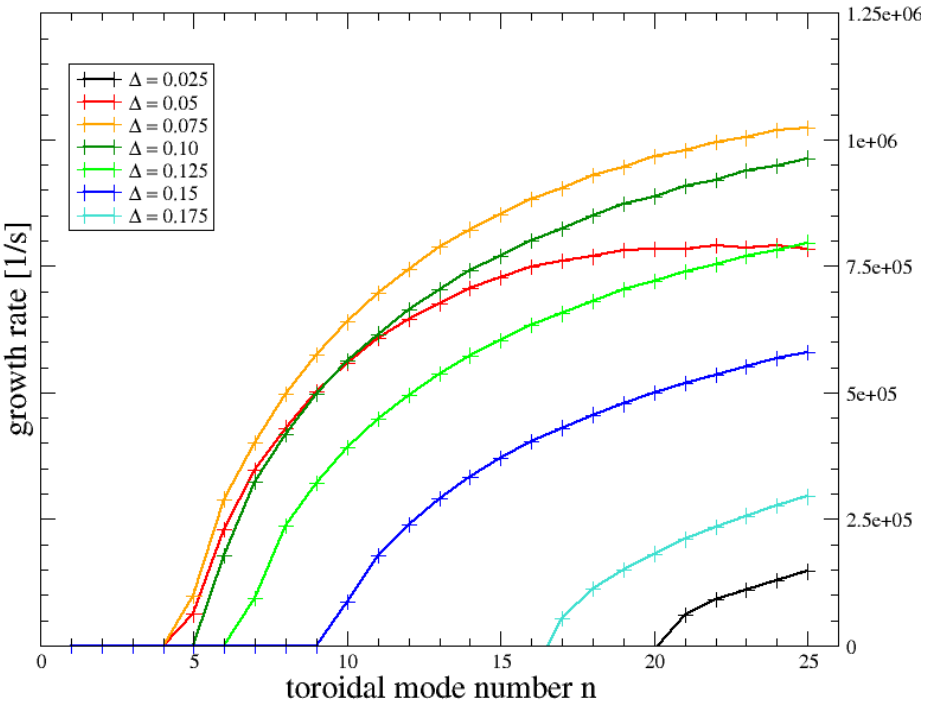

Figure 7.29: ILSA spectra with $d_{wp} = 1.00$

when changing $d_{wp} = 2.50$ to 1.01, with a relative decrease of γ_{max} by $\approx 60\%$. For the perfectly conducting wall placed directly on the plasma surface $d_{wp} = 1.00$, the growth rates for this case even drop below the ones for $\Delta = 0.175$, although the maximum pressure gradient is larger by a factor of ≈ 6.5, reflecting the strong coupling of external and internal modes. This case also shows a radial mode structure concentrated around a narrow interval close to the LCFS, a clear deviation from the Gaussian as expected by theory [52]. For broader pedestal widths and pressure gradient maxima closer to the axis, the mode structure regains its Gaussian shape with smaller / negligible external modes.
The case with $\Delta = 0.20$ is stable in the framework of ideal linear MHD for both plasma-wall distances.

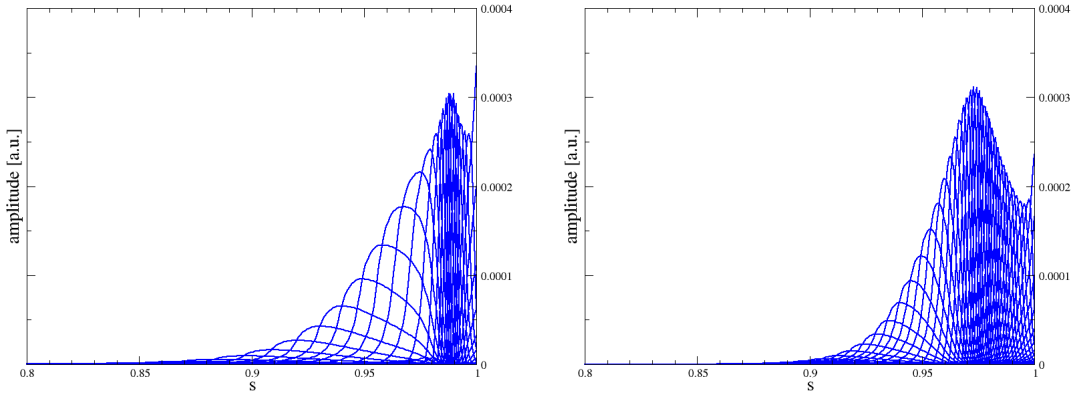

$\Delta = 0.025$

$\Delta = 0.05$

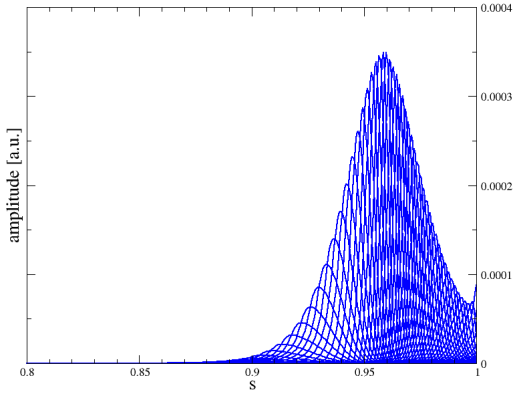

$\Delta = 0.075$

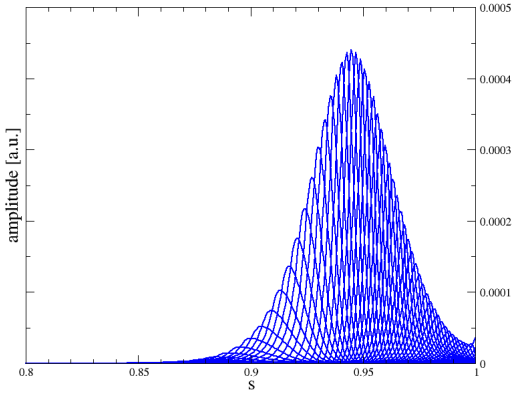

$\Delta = 0.10$

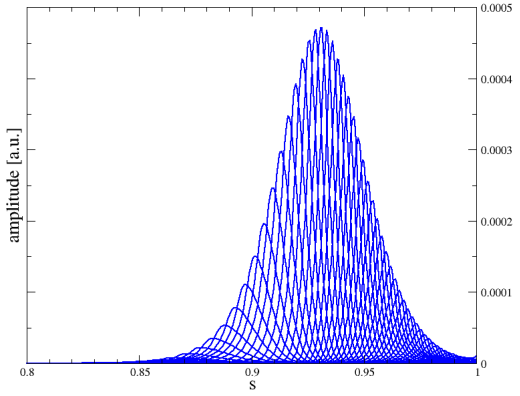

$\Delta = 0.125$

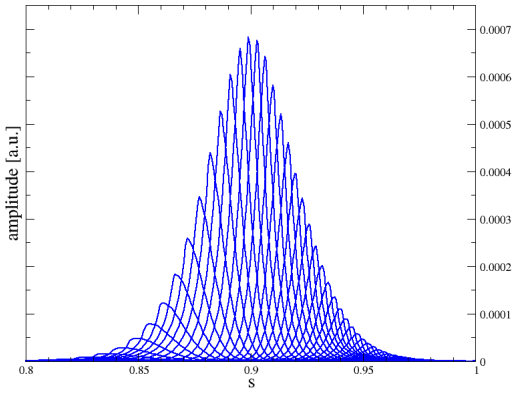

$\Delta = 0.175$

Figure 7.30: Radial mode structures for the fastest growing modes with $d_{wp} = 1.01$

7.2.2 Gyrofluid - GEM

Only the states with $\Delta = 0.025$ - 0.075, i.e. with clearly edge-localized pressure gradient with small L_n, show a clear initial exponential growth of E_T with an overshot and subsequent saturated state. This is also reflected in the growth rates γ_E, compare figs. 7.31 and 7.32. The growth rates decrease with larger Δ resp. smaller pressure gradient, and the time points where γ_E is maximal shift to higher values due to the pressure gradient drive to the instability. This agrees with the parallel mode structure in fig. 7.39, with dominant h_e and ϕ. Also the increasing role of T_i and T_e is visible as the pressure gradients get smaller, i.e. η_i gets larger because of the fixed temperature profiles. That is the general gradual transitional behavior of the ITG mode, compare e.g. the investigations in [41]. As observed in the pressure scan in chapter 7.1, a higher pressure gradient yields more pronounced ideal ballooning signature. The ion heat fluxes and their growth rates concur with this trend, compare figs. 7.33 and 7.34, except for $\Delta = 0.025$: while the growth rate γ_E stagnates compared to $\Delta = 0.05$, the ion heat flux growth rate γ_Q is clearly smaller, and Q_i shows a lower saturation level as the case with $\Delta = 0.05$.

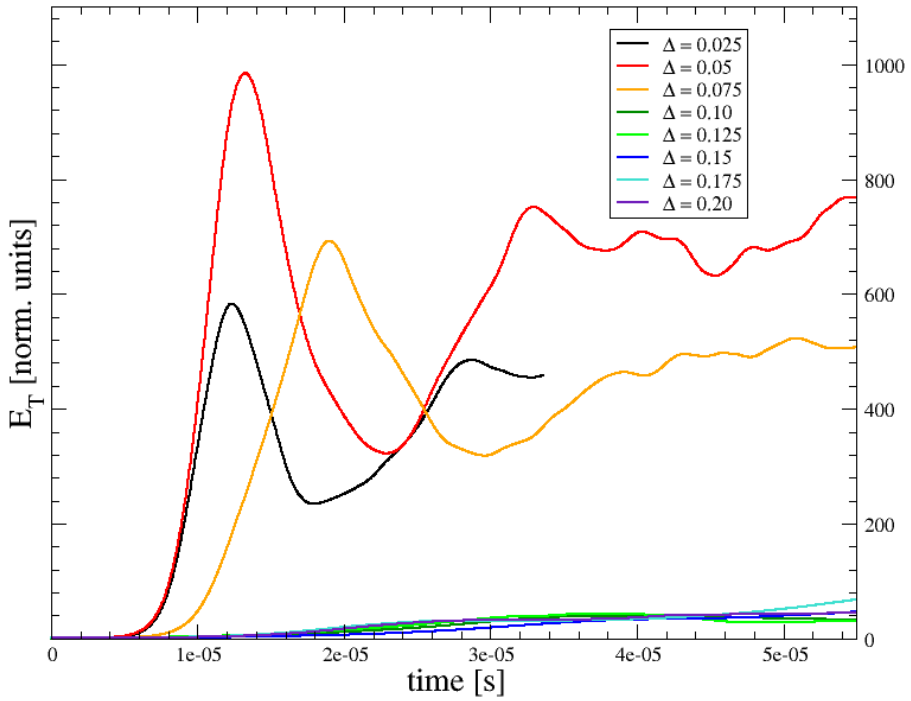

Figure 7.31: Total energy E_T

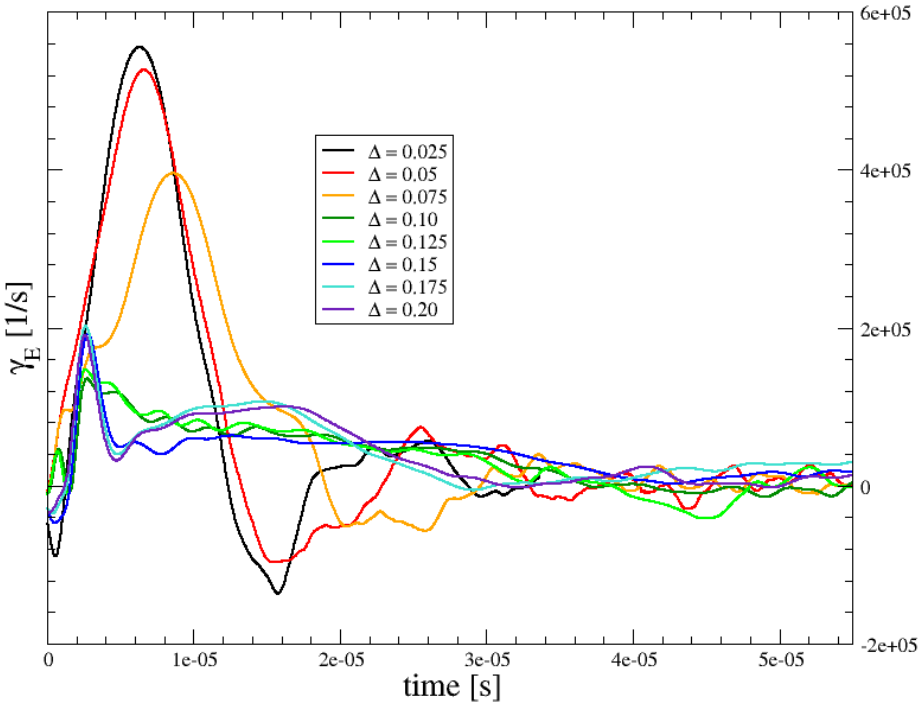

Figure 7.32: Growth rate γ_E

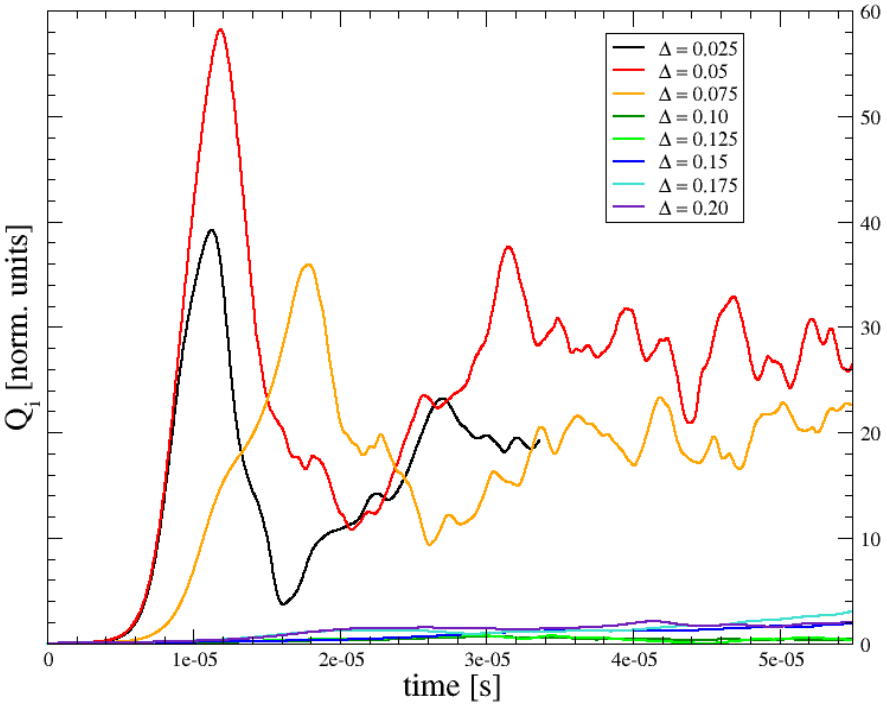

Figure 7.33: Ion heat flux Q_i

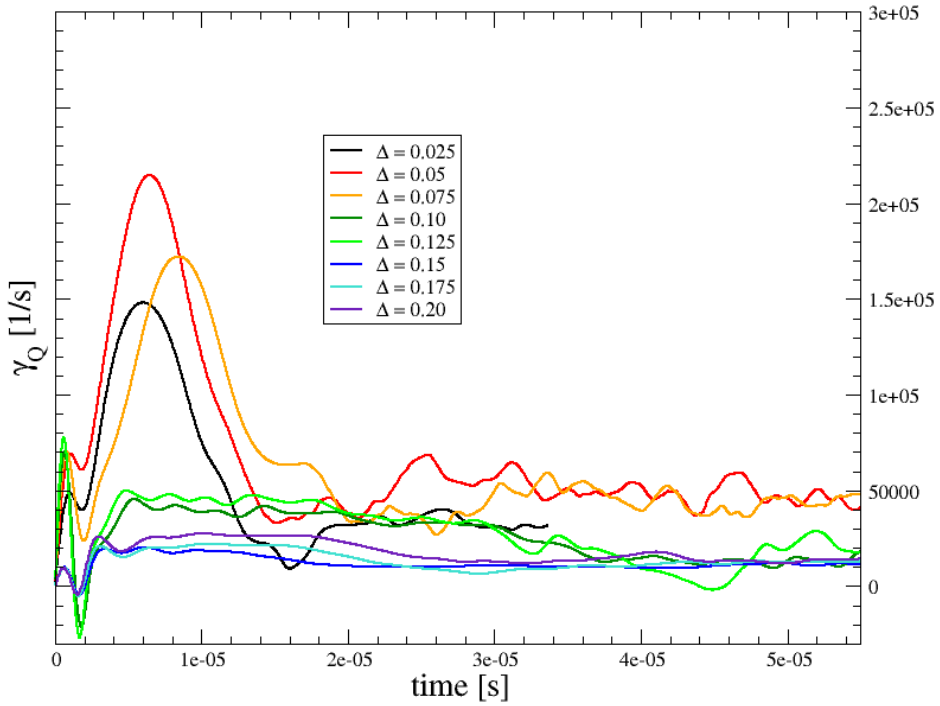

Figure 7.34: Growth rate γ_Q

All the setups with larger pedestal widths feature pressure gradients too small to excite ballooning modes, so E_T and Q_i are more than a magnitude smaller than the previous cases. All of them show some low-amplitude growth rates shortly after the start of the simulations. These cases can further be separated into two different regimes, the first with $\Delta = 0.10, 0.125$ and the second with $\Delta = 0.15, 0.175, 0.20$. This is evident from the parallel mode structures in fig. 7.39 and the spectra in figs. 7.35 - 7.38. The first regime has strongly ballooned n_e and T_e, while for the second regime T_e is significantly smaller. The ion temperature T_i, however, plays no role for either. Moreover the first regime has mode numbers ≈ 24 similar to the cases with the maximum pressure gradient located in the temperature profile pedestal, while the cases with a pressure gradient maximum in the core show a jump to higher mode numbers ≈ 36.

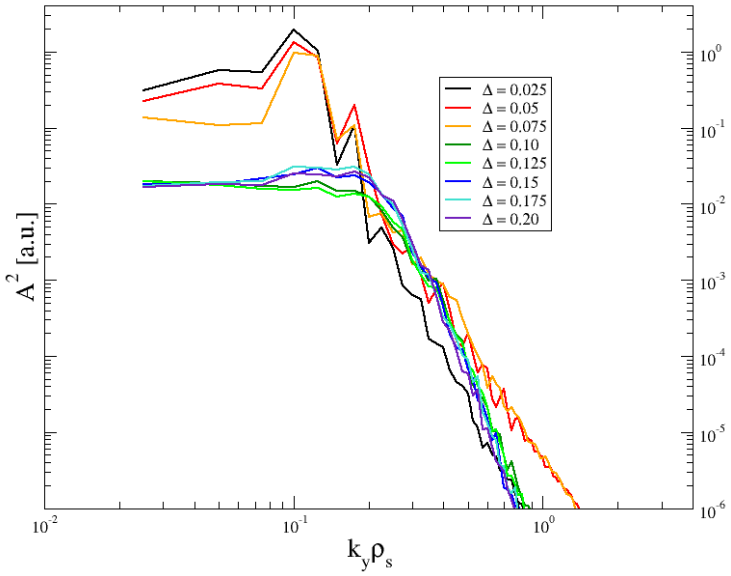

Figure 7.35: Spectra of n_e at the time of max. growth rate

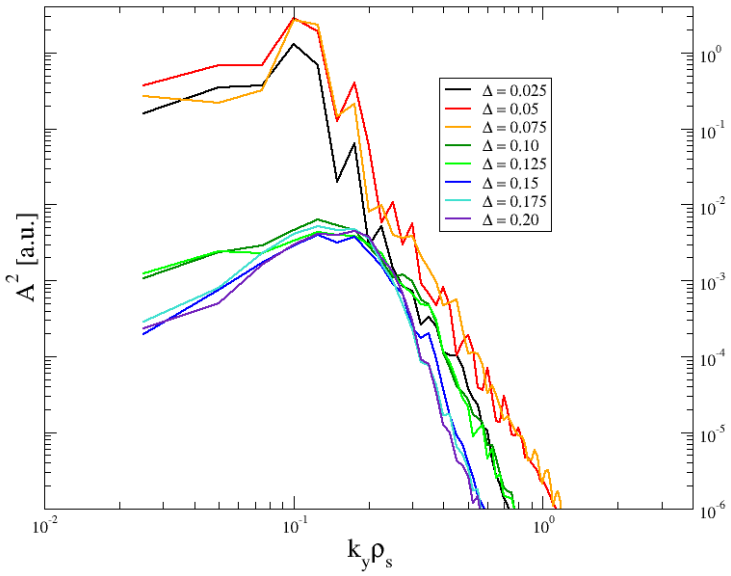

Figure 7.36: Spectra of Q_i at the time of max. growth rate

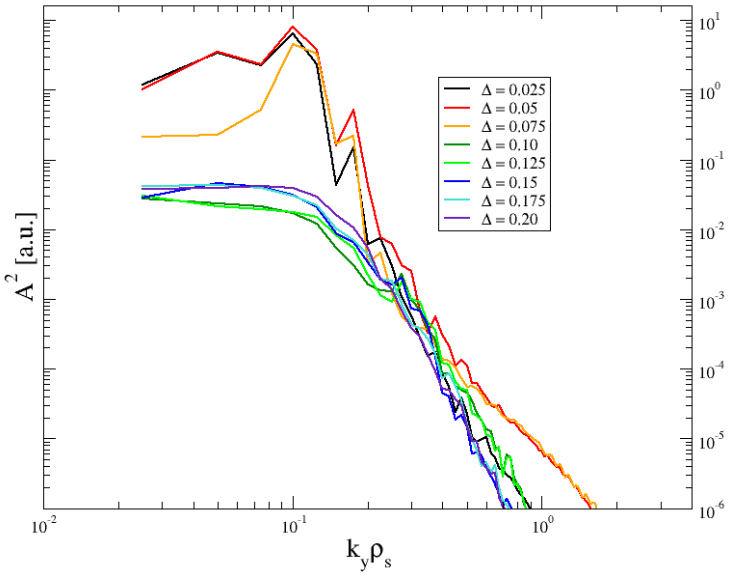

Figure 7.37: Spectra of ϕ at the time of max. growth rate

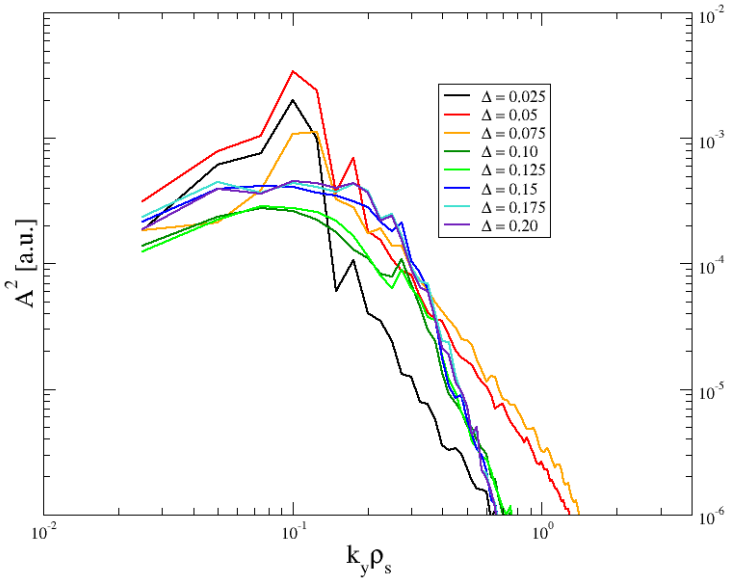

Figure 7.38: Spectra of ω at the time of max. growth rate

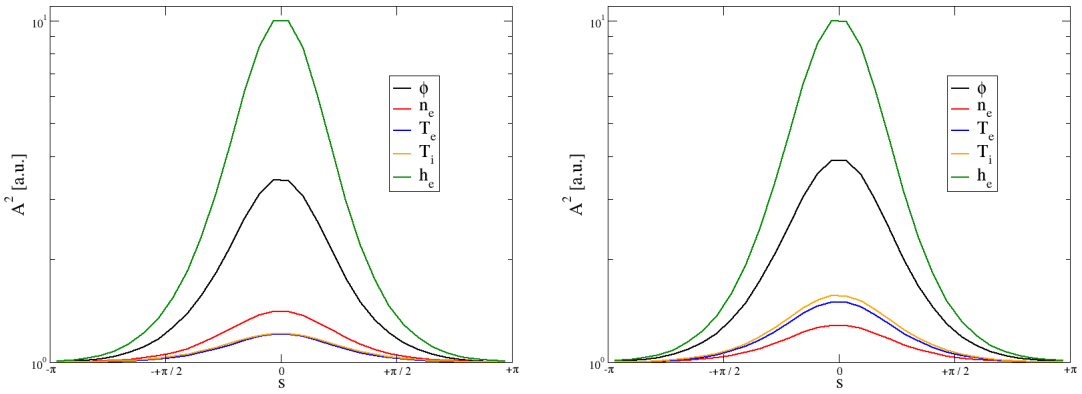

$\Delta = 0.025$

$\Delta = 0.05$

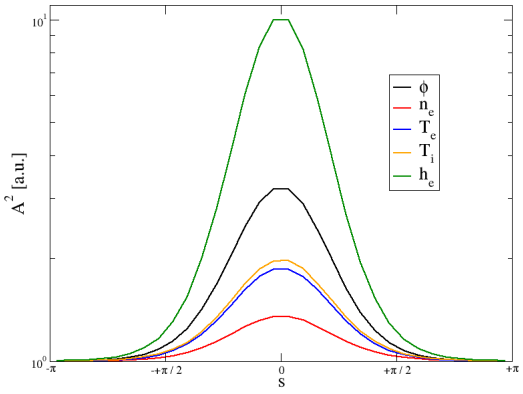

$\Delta = 0.075$

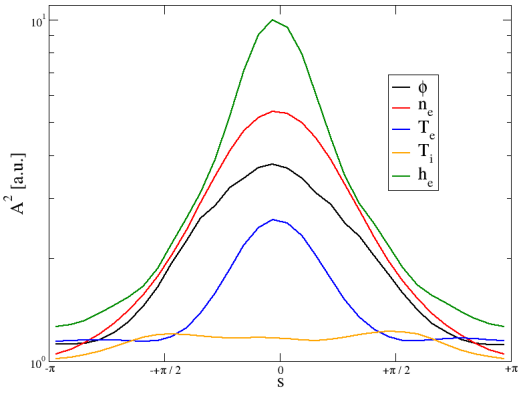

$\Delta = 0.10$

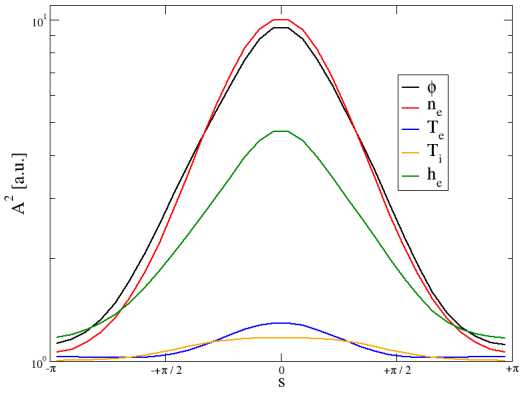

$\Delta = 0.175$

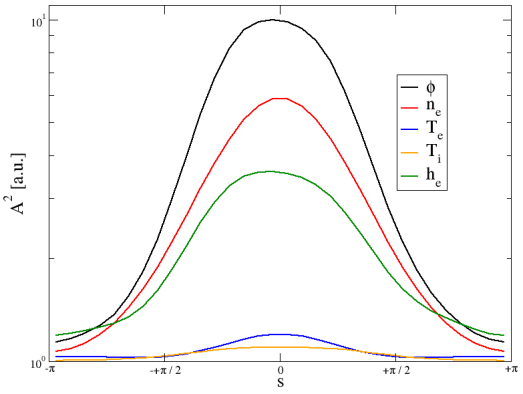

$\Delta = 0.20$

Figure 7.39: Parallel mode structures at the time of maximum growth rate

7.2.3 Comparison

Similar to the investigation of the pedestal height, the GEM growth rates are smaller by a factor 2 compared to ILSA for the cases with $d_{wp} = 2.50$ and $\Delta = 0.025, 0.05, 0.075$, i.e. small pedestal widths with larger pressure gradients and locations of $\frac{dp}{d\psi}$ close to the LCFS, see fig. 7.40. Both models however show the same trend for those 3 values of Δ, with decreasing γ for smaller pressure gradients. The case with $\Delta = 0.025$ can be considered an exception, as the external part of the perturbation is still very large and results in a strong deviation for $d_{wp} = 1.01$ and 1.00. The consequent loss of coupling of the internal and external modes and the suppression of the external perturbations in the linear ideal MHD stability analysis drops the growth rates below the GEM growth rates .
All other cases show a substantial difference between the predictions of ideal linear MHD and the gyrofluid model. The pressure gradients are too small to cause an MHD regime ballooning behavior for the GEM simulations, and the growth rates are accordingly smaller by about 50%.. Only for large Δ, meaning pressure gradients peaked in the core region of the plasma, become the growth rates similar. The type of the instabilities, however, remain different in character.

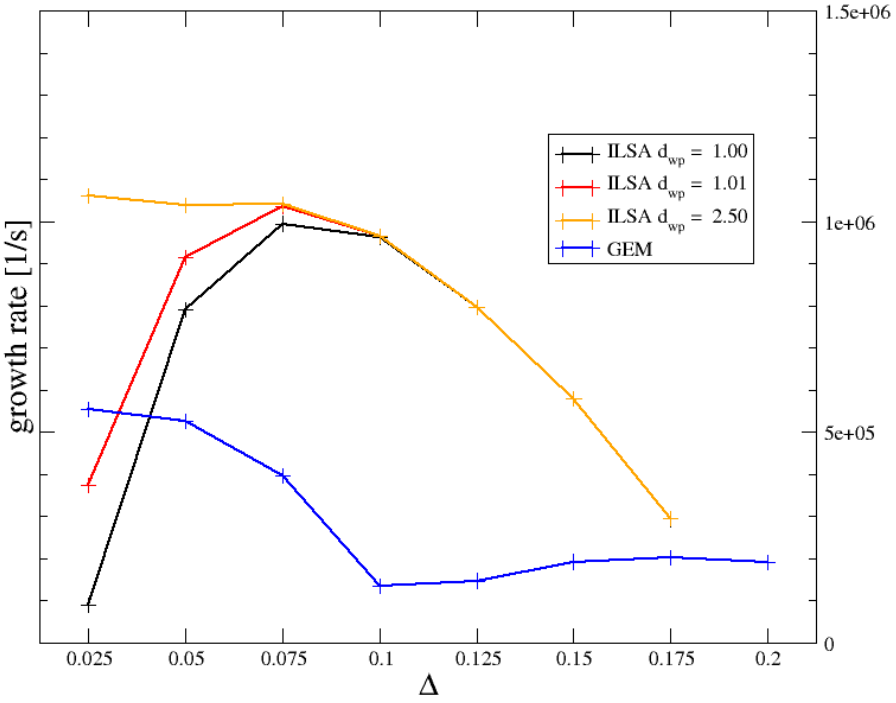

Figure 7.40: Maximum growth rate comparison

The mode numbers in fig. 7.41 further illustrate these characteristics. The mode numbers obtained with GEM and ILSA agree best for $\Delta = 0.05$ and $\Delta = 0.075$, as for this case the external perturbation part (i.e. the part not captured by our GEM simulations) is relatively small and the pressure gradient is still large enough to drive a clear ballooning mode. For

smaller Δ, the external part gets large and thus shifts the ideal MHD mode numbers to smaller values, while for GEM only the internal ballooning part is considered and the mode numbers therefore stay approximately constant. Generally the agreement is better for lower d_{wp}, as the external part gets dimished.
The mode numbers of the intermediate first regime as defined above still agree with the ILSA predictions, but the types of instabilities are not comparable. For the second regime the mode numbers are mutually different, highlighting the additional dynamics of the gyrofluid model.

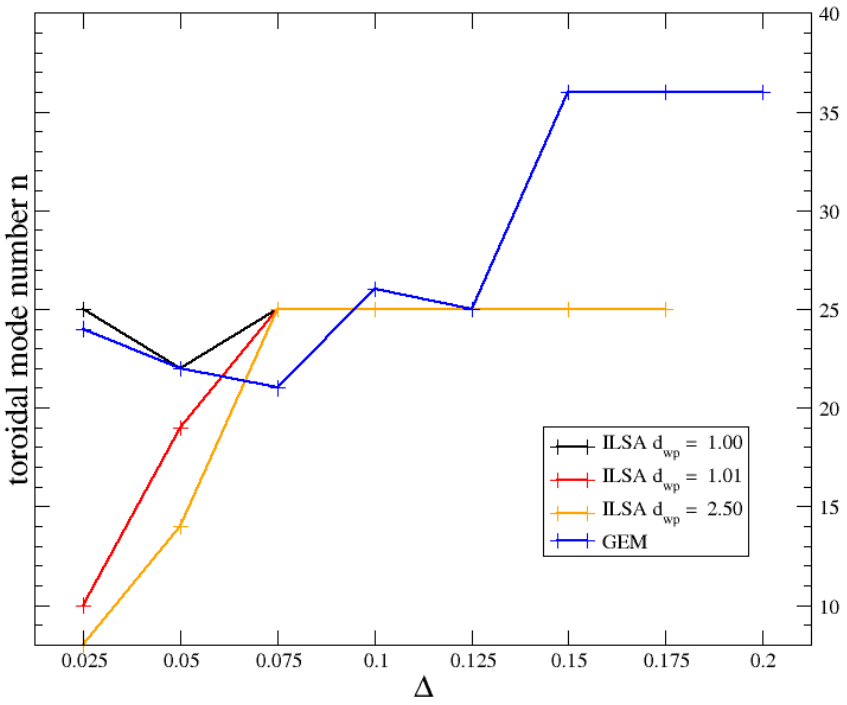

Figure 7.41: Toroidal mode number comparison for the fastest growing modes

7.3 Aspect ratio

We consider a plasma with fixed minor radius $a = 0.5$ and fixed pressure profile, compare fig. 7.42, varying the inverse aspect ratio ϵ (i.e. change the major radius R_0). The vacuum magnetic field is $B_0 = 2.5$T. The pressure gradient consequently remains fixed as well, fig.

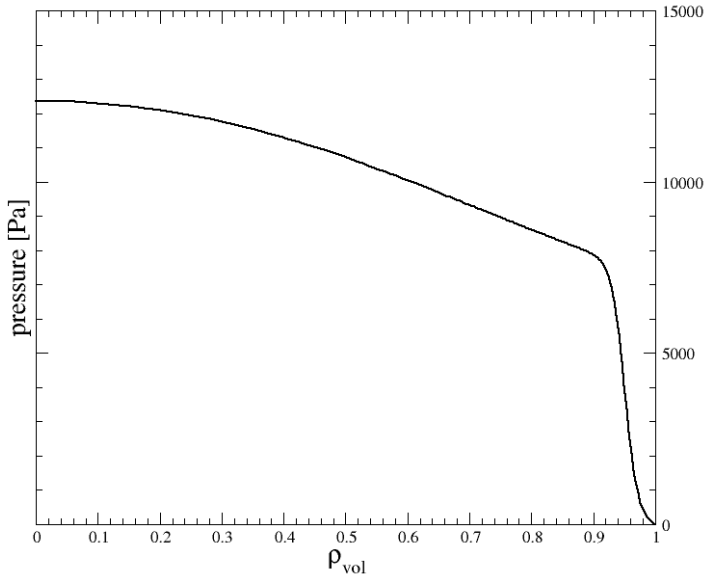

Figure 7.42: Pressure profile

7.43, and corresponds to the case p_3 investigated in chapter 7.1.

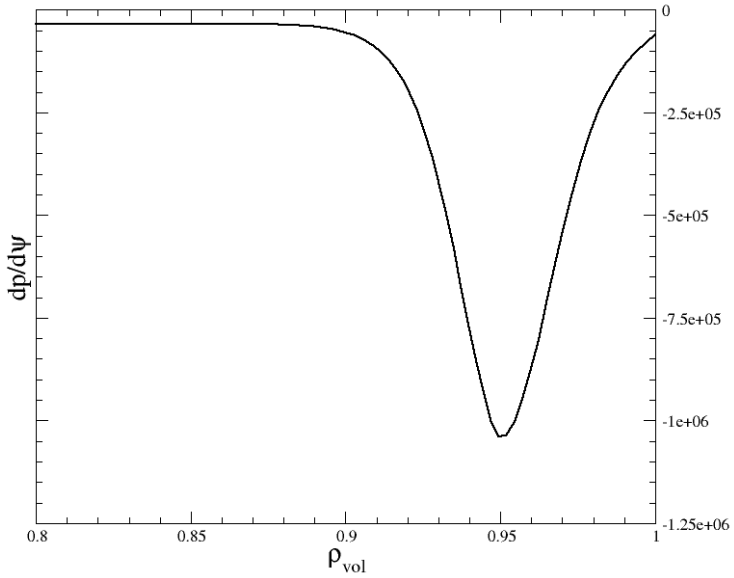

Figure 7.43: Pressure gradient

The current density is increased for smaller aspect ratios, fig. 7.44, primarily in the core region of the plasma. This proved necessary, as for too small current densities, no equilibria could be found with HELENA. The ballooning drive caused by ∇p, however, stays the same.

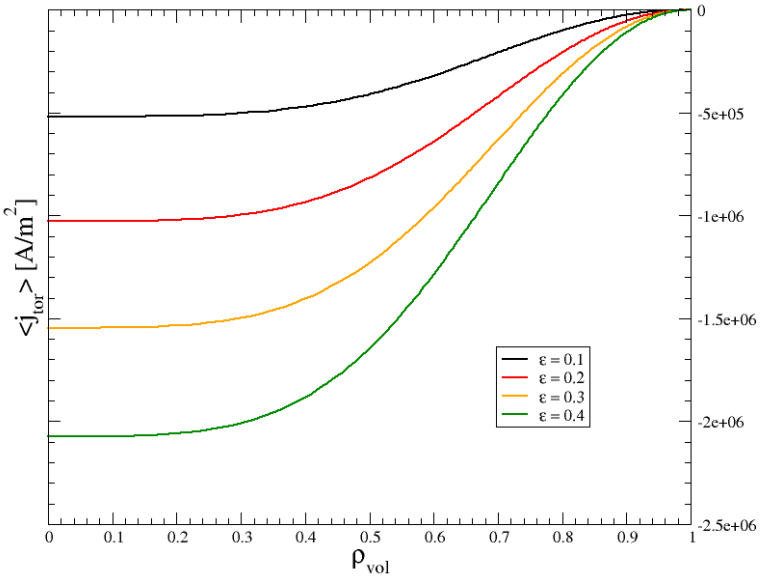

Figure 7.44: Current density profiles

This results in q profiles as shown in fig. 7.45, where higher ϵ yields higher q values but approximately the same relative increase, with the exception of the lowest $\epsilon = 0.1$. The latter case features a steeper increase in the edge region with $\rho_{vol} > 0.95$.

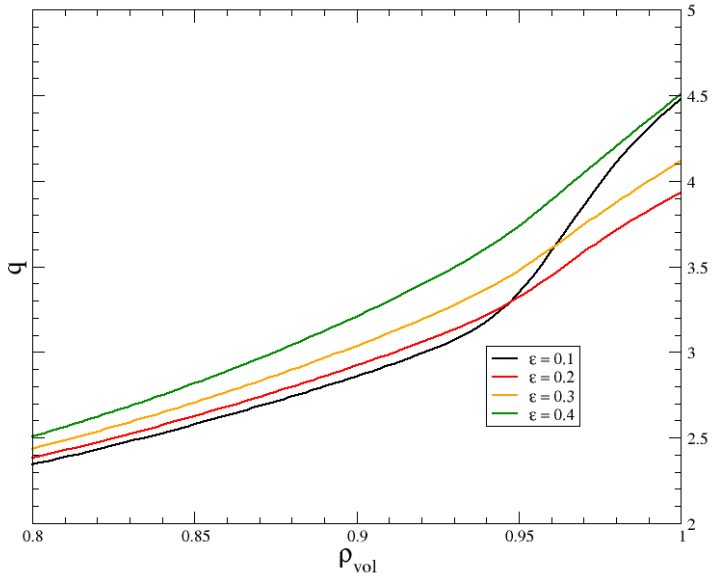

Figure 7.45: q profiles

The behavior of the q profiles is reflected in the global magnetic shear in fig. 7.46, with all

cases except $\epsilon = 0.1$ showing roughly the same shear over the whole radius of the plasma.

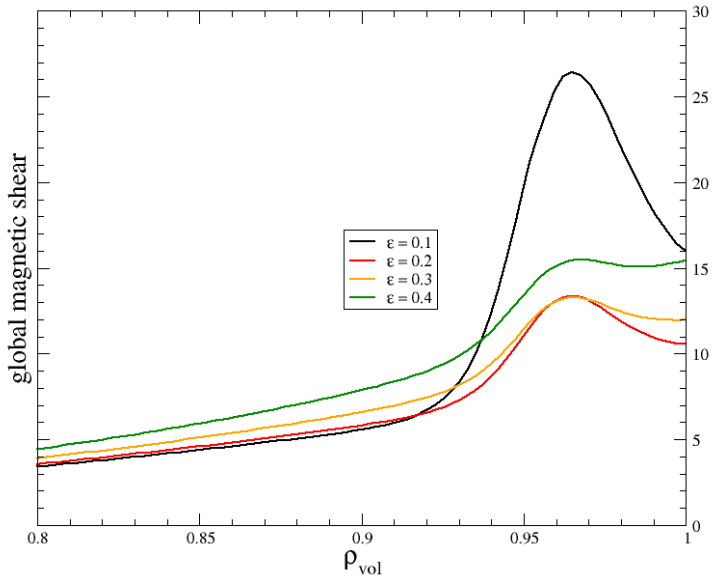

Figure 7.46: Global magnetic shear

7.3.1 Linear ideal MHD stability - ILSA

The ideal linear MHD stability spectra for $d_{wp} = 2.50$, see fig. 7.47, show a gradual stabilization of the lower-n part with increasing ϵ. The onset of instability is shifted to higher toroidal mode numbers n, and the growth rates for lower n generally decrease. The case with $\epsilon = 0.1$ features an unstable mode for $n = 1$ and is characterized by a larger contribution from external, low-n modes compared to the cases with higher ϵ. Moreover, the high-n part shows a stabilizing effect from the higher shear for the smallest inverse aspect ratio.

The growth rates follow no monotonic trend with ϵ, as their is an competition between different effects stemming from the changing curvature. Higher ϵ resp. curvature has a stabilizing effect on the external kink mode (low-n), compare [85], which was already observed in chapter 6.1. Additionally, larger curvature provides an increased drive κp_0 for ballooning modes (high-n) as already discussed, but increases the stabilizing effect of magnetic field line bending for all modes.

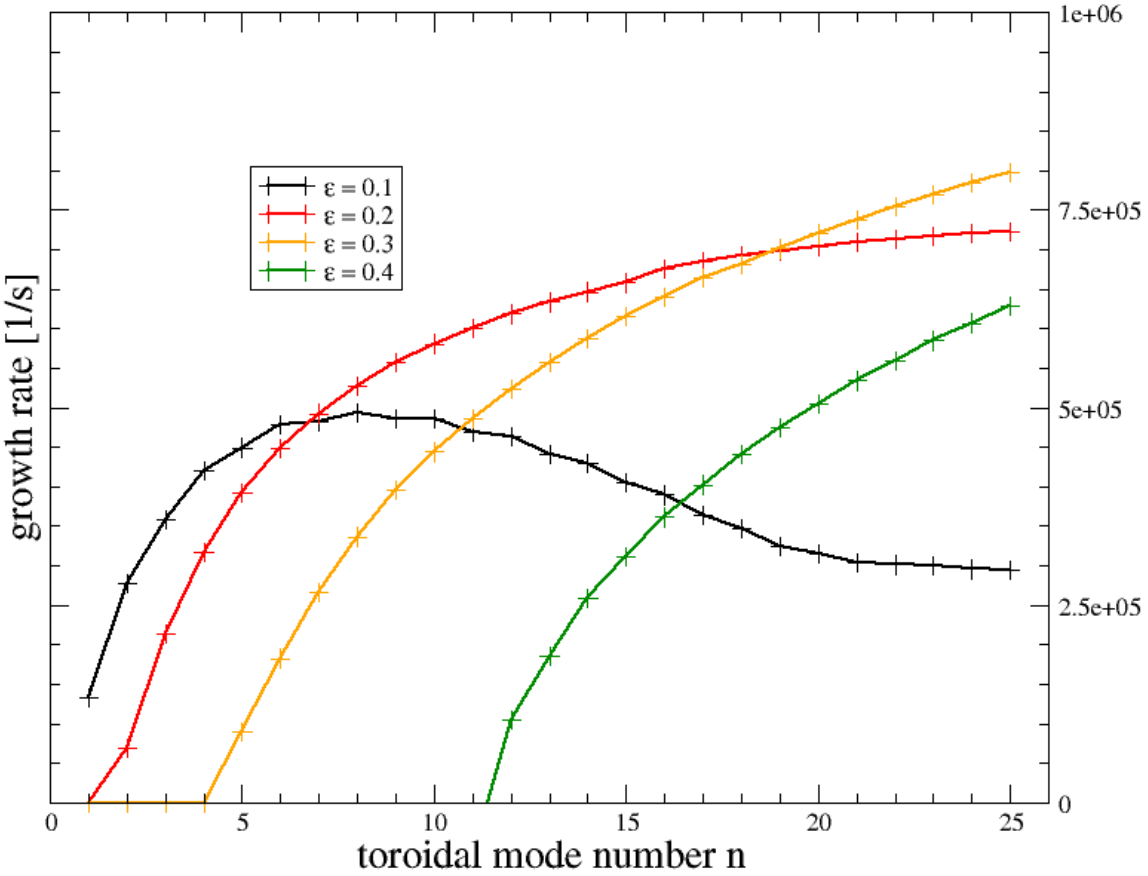

Figure 7.47: ILSA spectra with $d_{wp} = 2.50$

The spectra behavior is clearly represented in the radial mode structures, compare fig. 7.48. Only the case with $\epsilon = 0.1$ exhibits a strong external perturbation, whereas the other cases have a dominating ballooning structure. Consequently, the radial extent of the instability is larger for $\epsilon = 0.1$, as it includes more low-n, less localized modes. Furthermore, the relative amplitude of maximum internal to maximum external perturbation increases with higher ϵ, concurring with stronger ballooning character.

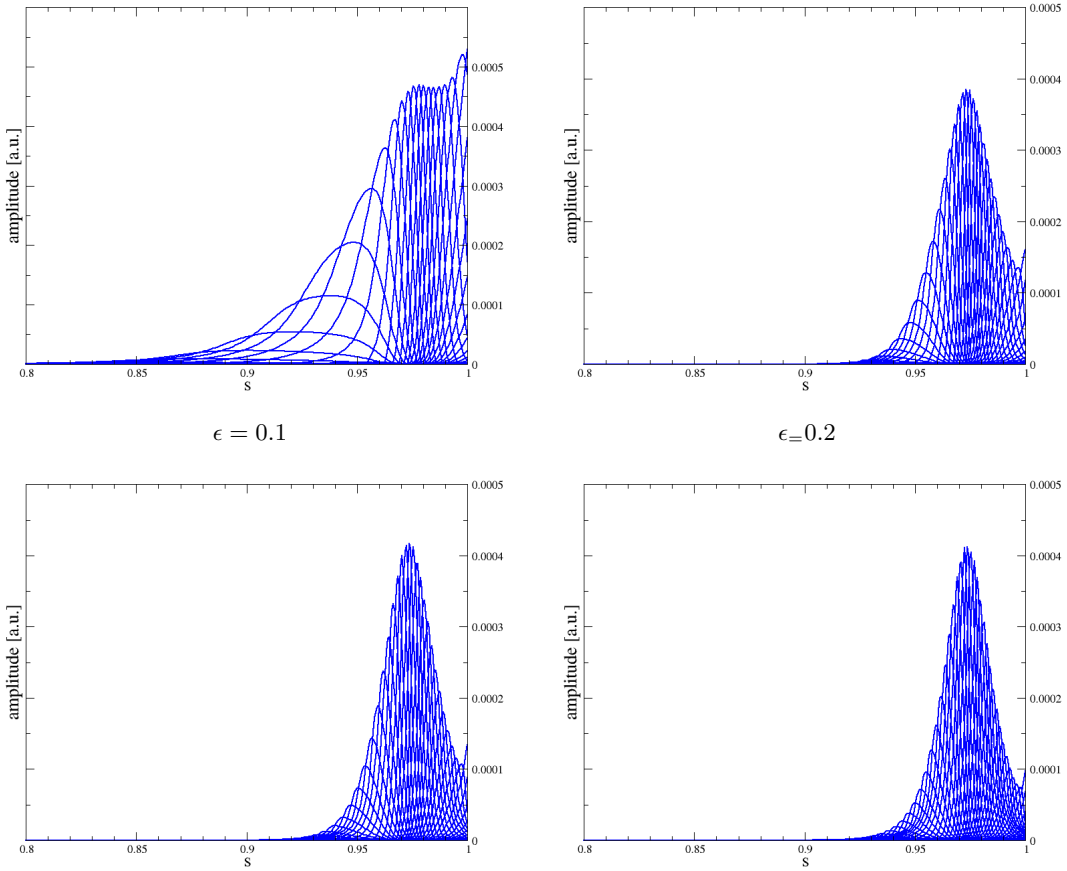

$\epsilon = 0.1$ $\epsilon_{=}0.2$

$\epsilon = 0.3$ $\epsilon = 0.4$

Figure 7.48: radial mode structures for the fastest growing modes with $d_{wp} = 2.50$

The influence of the plasma-wall distance d_{wp} accordingly has the strongest effect on the case $\epsilon = 0.1$, see figs. 7.49 and 7.50. Smaller aspect ratios show a gradual stabilizing effect on the low-n to medium-n part of the spectra ($1 \leq n \leq 15$), but have almost no consequence on the growth rates of the high-n ballooning part. Except the case $\epsilon = 0.1$, also the toroidal mode numbers of the onset of instability only increase slightly with smaller d_{wp}. The growth rate for the smallest aspect ratio, however, drops by $\approx 50\%$ when changing d_{wp} from 2.50 to the wall placed on the plasma surface.

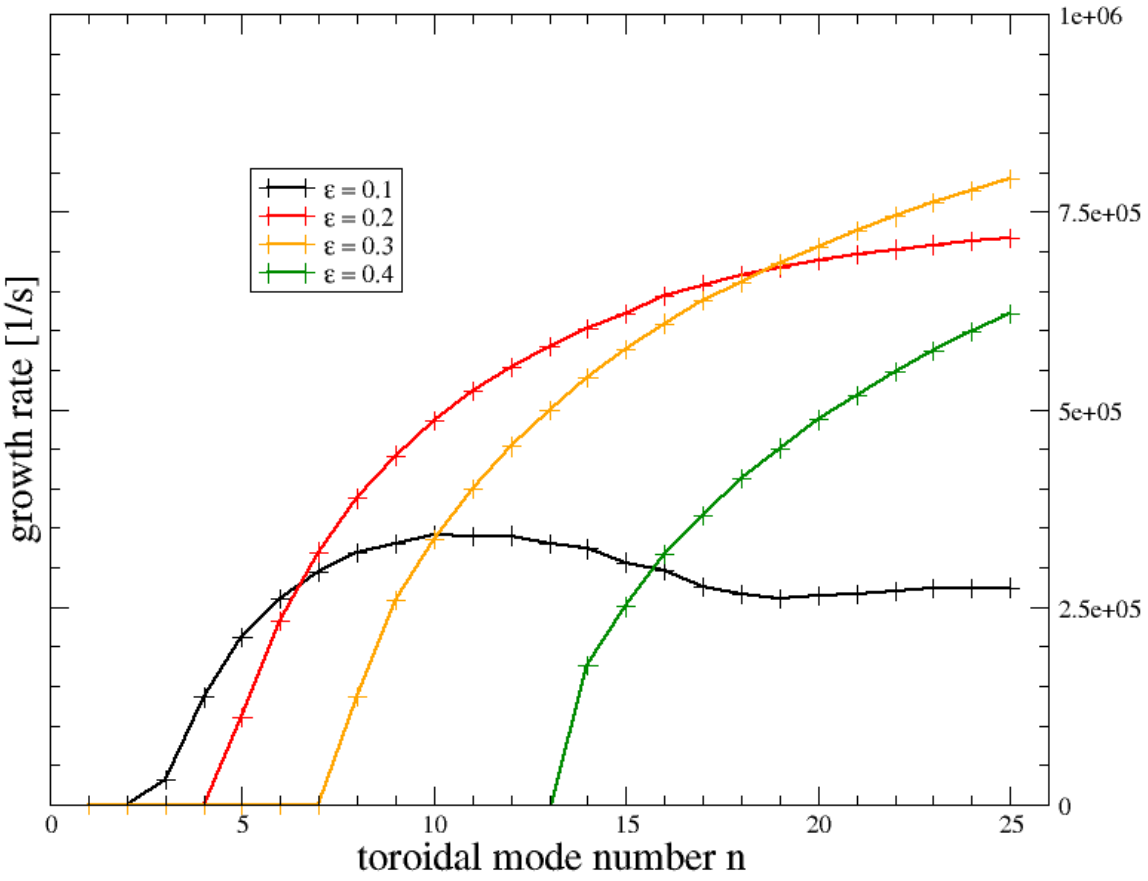

Figure 7.49: ILSA spectra with $d_{wp} = 1.01$

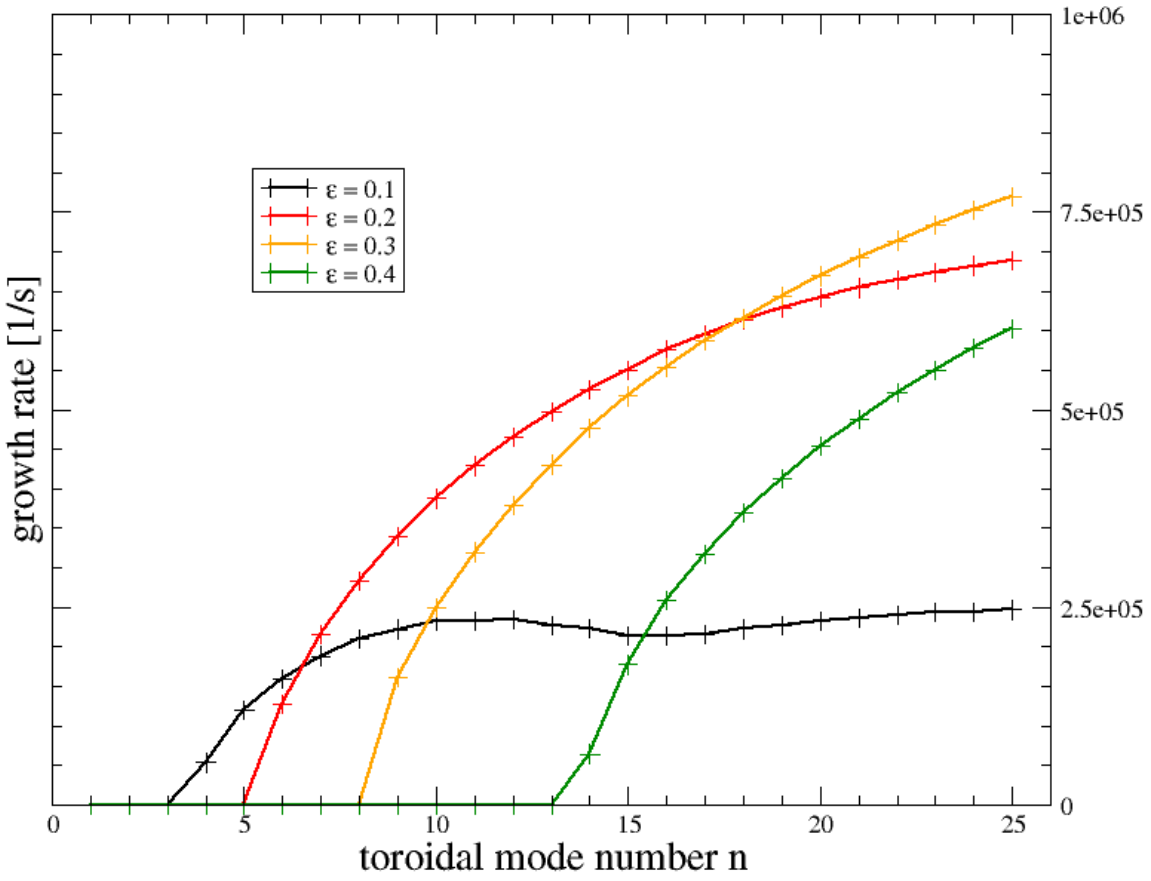

Figure 7.50: ILSA spectra with $d_{wp} = 1.00$

As the cases with inverse aspect ratio $\epsilon = 0.2$ to 0.4 already are ballooning dominated with smaller external contributions, the impact of d_{wp} on the radial mode structure is also small for these cases, compare figs. 7.48 and 7.51. As expected, the mode structure for $\epsilon = 0.1$ shows a clear decrease of the external part and consequently a narrower radial extent of the instability. Moreover, the destabilization of ballooning modes by coupling to the external modes gets damped for $d_{wp} = 2.50 \rightarrow 1.01$, as can be clearly seen in the dip of the mode amplitude around $s \approx 0.99$ for $\epsilon = 0.1$.

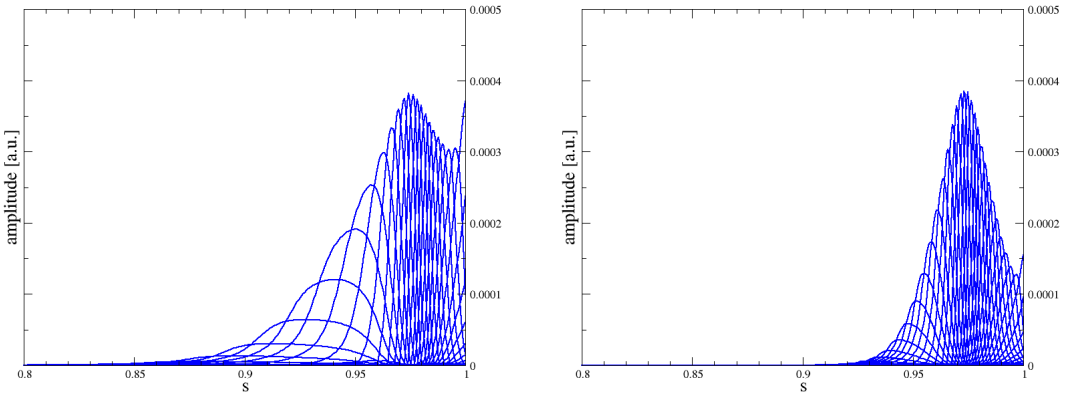

$\epsilon = 0.1$ $\epsilon_{=}0.2$

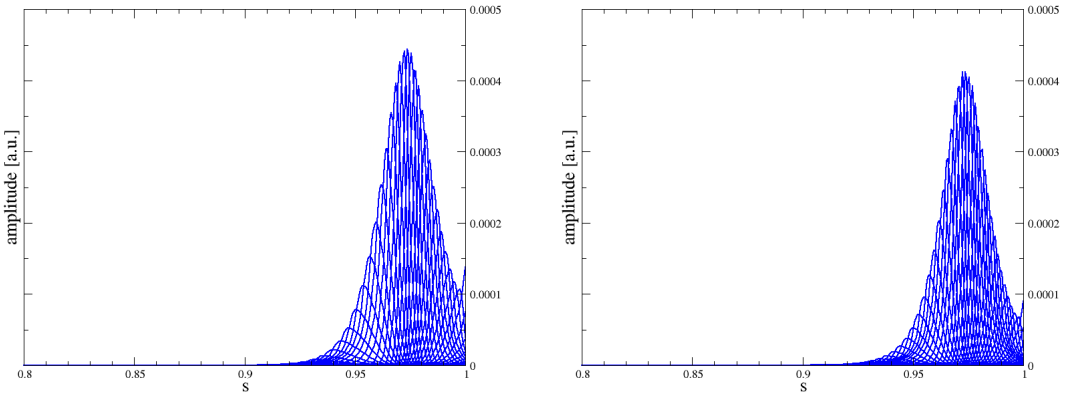

$\epsilon = 0.3$ $\epsilon = 0.4$

Figure 7.51: Radial mode structures for the fastest growing modes with $d_{wp} = 1.01$

7.3.2 Gyrofluid - GEM

In fig. 7.52, the total energy shows only marginal differences for $\epsilon = 0.1$ and 0.2 with regard to the peak of E_T, but the case with $\epsilon = 0.2$ features a slightly shorter linear phase. As a consequence, the maximum growth rate for the higher inverse aspect ratio is larger and moreover has a more pronounced overshoot, compare fig. 7.53. For higher ϵ, the growth rates drop noticeably and the time point of peak E_T shifts to larger values.

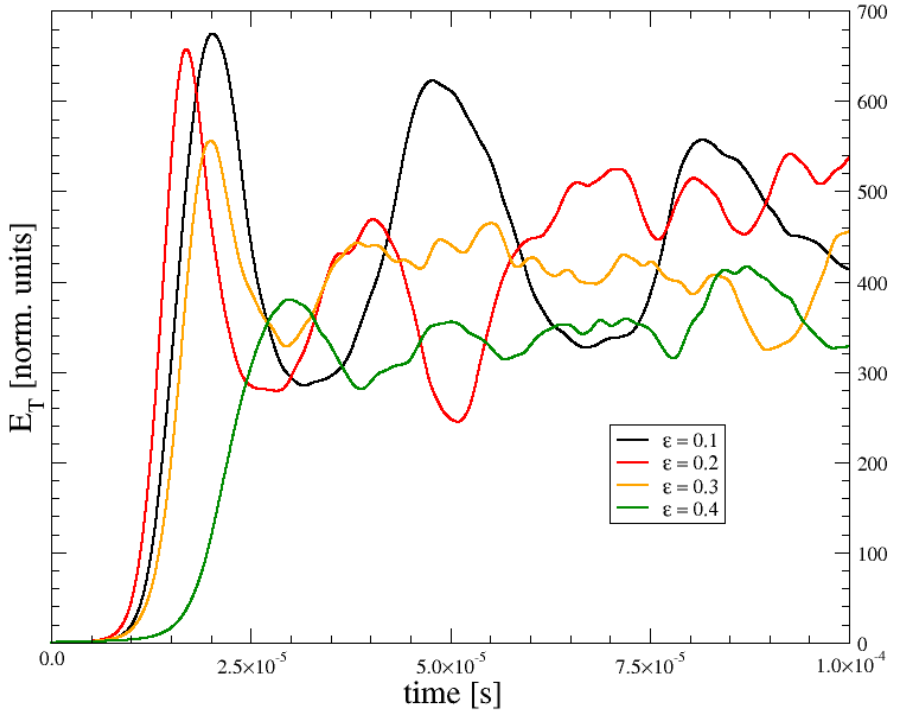

Figure 7.52: Total energy E_T

In contrast, the ion heat flux shown in fig. 7.54 has a qualitatively different behavior. The peak value of Q_i for $\epsilon = 0.2$ is much larger than for $\epsilon = 0.1$, and is reached in a shorter time. With regard to the maximum Q_i, this remains true also for $\epsilon = 0.3$. However, the time of peak Q_i is shifted to a higher value. Consequently, the growth rates for Q_i in fig. 7.55 follow the same pattern as γ_E. The difference of the highest inverse aspect ratio to the other cases is significant and best visible for the ion heat flux. There is no longer an overshoot of Q_i, whereas a weakly pronounced one is still visible for E_T. Both growth rates γ_E and γ_Q are considerably smaller, and the instability grows on a timescale approximately a factor of 2 longer compared to all other cases.

The spectra for ϕ in fig. 7.56 feature two distinct peaks $k_y\rho_s = 0.05$ and 0.1 for $\epsilon = 0.1$ and 0.2, whereas the peak at higher wave number is still slightly larger. For all other quantities, however, there is a prominent single peak at $k_y\rho_s = 0.1$ for all values of ϵ, see figs. 7.57 - 7.59. As a general trend, the turbulent character at the time of maximum growth rate increases with higher inverse aspect ratio. This is most clearly visible for the vorticity ω: at $k_y\rho_s = 1$,

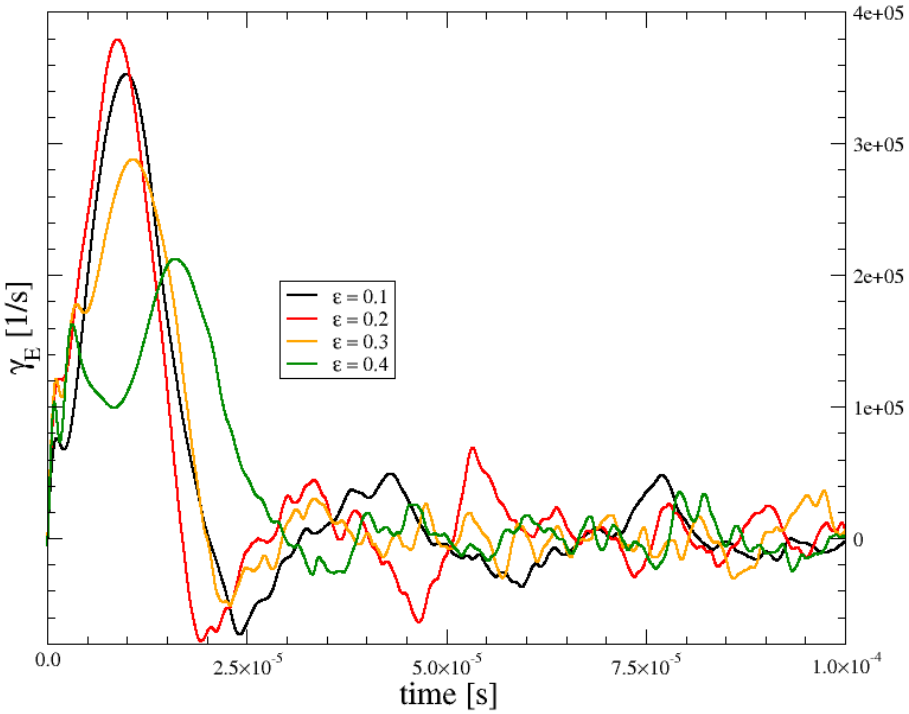

Figure 7.53: Growth rate γ_E

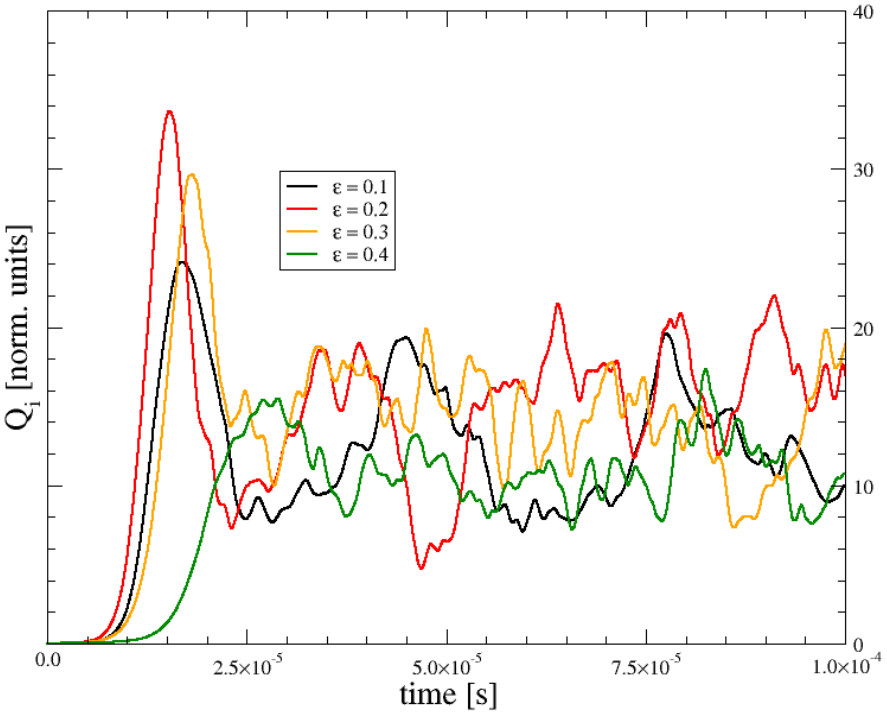

Figure 7.54: Ion heat flux Q_i

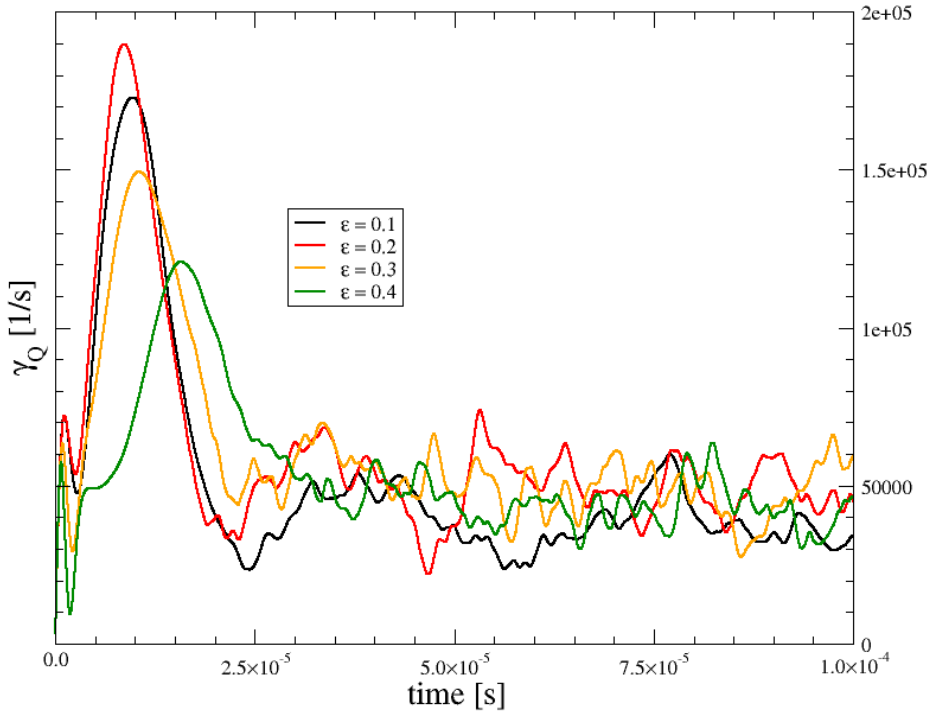

Figure 7.55: Growth rate γ_Q

the squared amplitude increases by approximately a factor of 10 with subsequently higher ϵ.

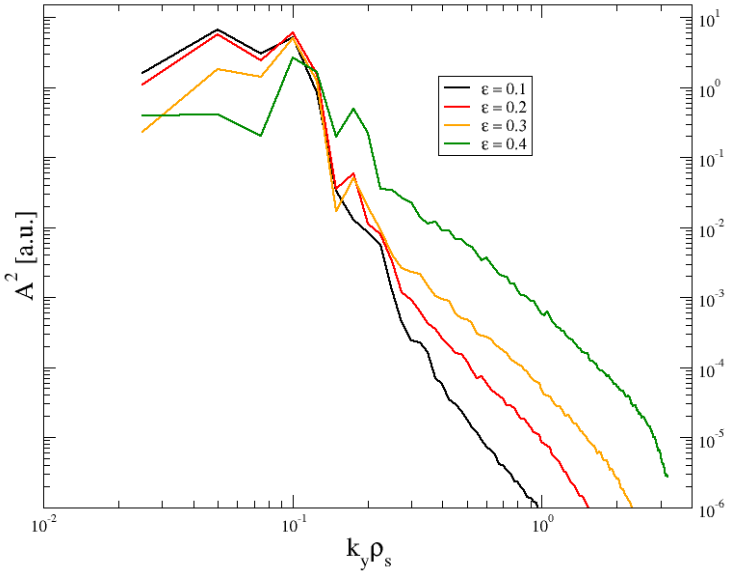

Figure 7.56: Mode number spectra ϕ

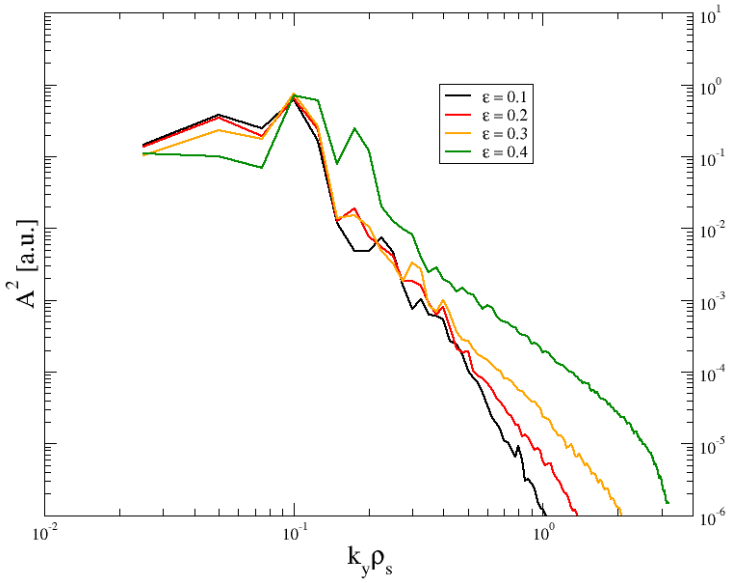

Figure 7.57: Mode number spectra n_e

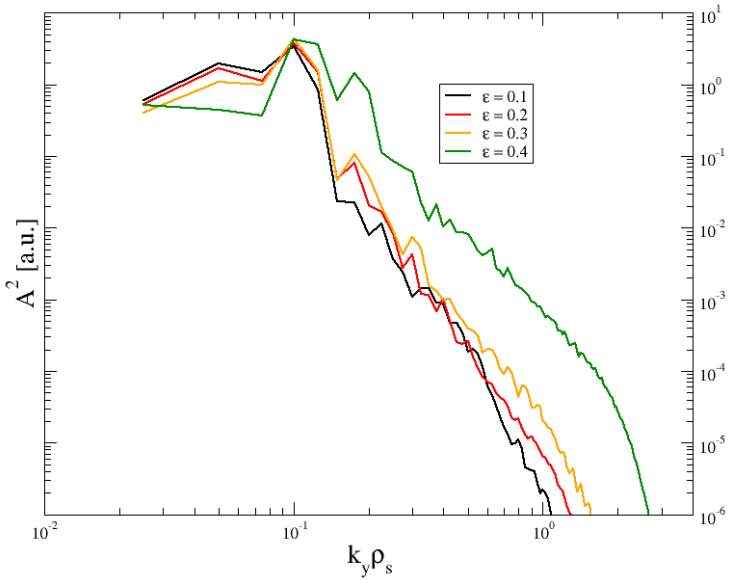

Figure 7.58: Mode number spectra Q_i

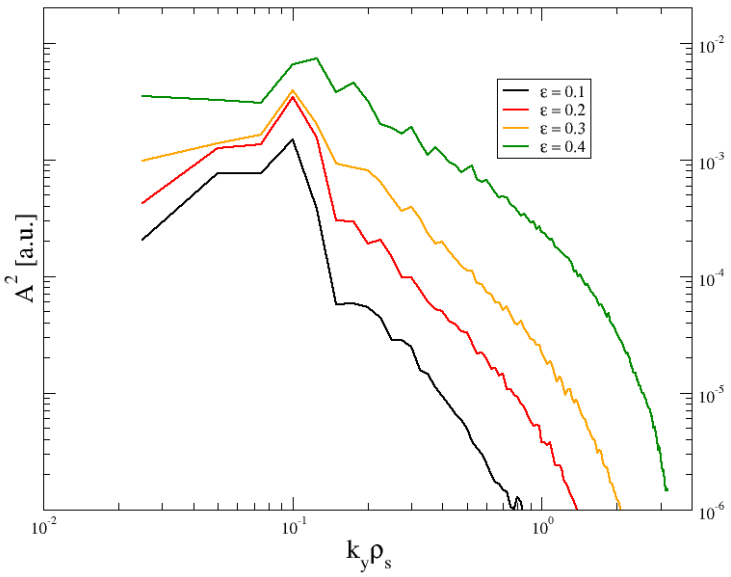

Figure 7.59: Mode number spectra ω

The parallel mode structures in fig. 7.60 show an increasing amplitude of the temperatures T_i, T_i with smaller aspect ratio. This behavior reflects the theoretical predictions that temperature gradient driven modes in toroidal systems are enhanced by curvature [86]. The ballooning character for the GEM simulations is most prominent for $\epsilon = 0.1$ and 0.2, i.e. smaller curvature, as the drive for the ITG mode is weak. This highlights the observed similar characteristics of the energetics for these two cases. For higher inverse aspect ratio, the ideal ballooning character gets dimished, as the amplitude of ϕ decreases. For $\epsilon = 0.3$, the temperature amplitudes are already comparable to ϕ, and for the highest inverse aspect ratio, the T_i amplitude clearly dominates ϕ.

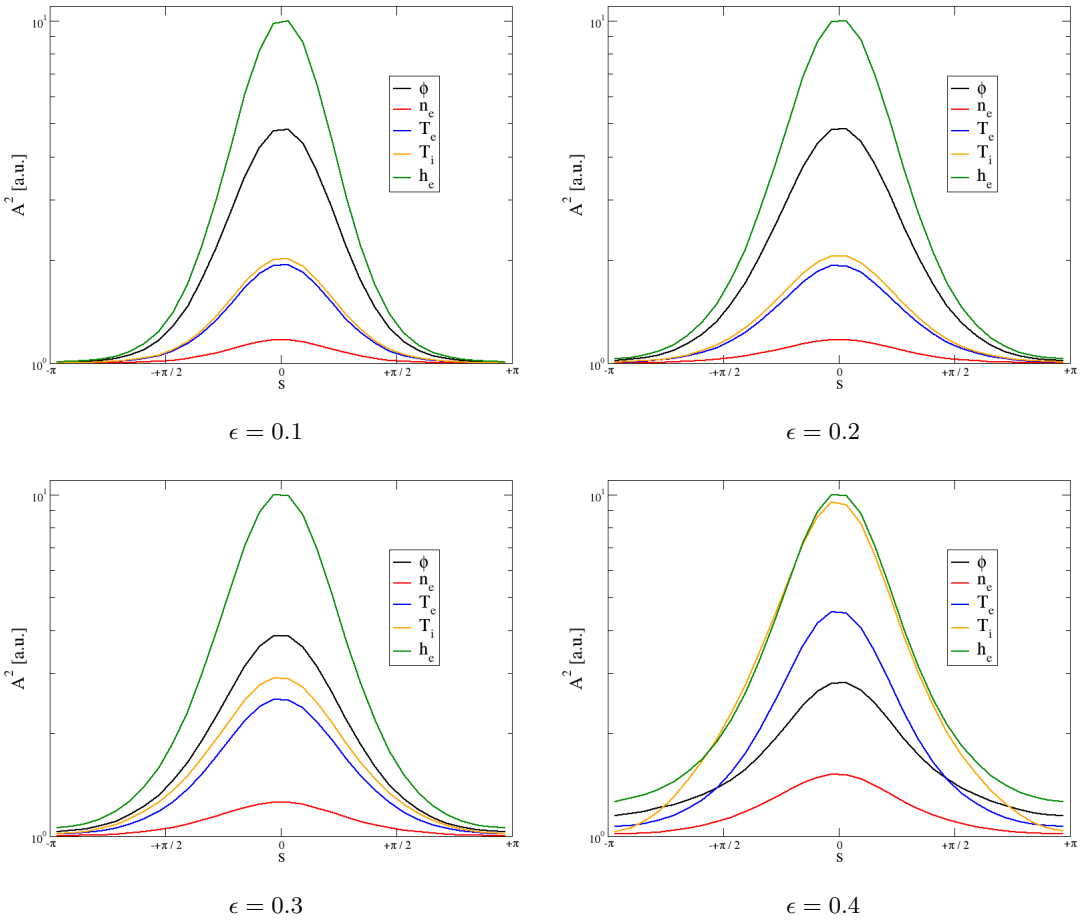

$\epsilon = 0.1$ $\epsilon = 0.2$

$\epsilon = 0.3$ $\epsilon = 0.4$

Figure 7.60: Parallel mode structures at the time of maximum growth rate

7.3.3 Comparison

In agreement with the observations in the previous sections, the relative difference of the maximum growth rates is smallest for the most pronounced ballooning character of the GEM simulations. This is the case for the smallest inverse aspect ratio $\epsilon = 0.1$, see fig. 7.61, where in agreement with theory the temperature dynamics show the weakest amplitude for the gyrofluid model.

For $d_{wp} = 2.50$ and $\epsilon = 0.1$, the relative difference of the max. growth rates is $\approx 30\%$, as there is a larger contribution from external modes in the ideal linear MHD stability analysis. As these contributions get suppressed for $d_{wp} = 1.01$, the growth rates match, although the radial mode structure from ILSA still shows an external mode (which is not covered in the GEM simulations) comparable to the internal mode amplitude. For $d_{wp} = 1.00$, however, the complete suppression of the external modes also cancel all couplings (i.e. destabilizing effects) to the ballooning modes, dropping the ILSA growth rate below the GEM value.

For our selected case, the relative difference in growth rates increases with higher ϵ and consequently deteriorating ideal ballooning signature of the GEM results. Except $\epsilon = 0.3$, the trend of both the ideal linear MHD and the gyrofluid results as a function of ϵ are roughly comparable, but this is not due to the same physical dynamics.

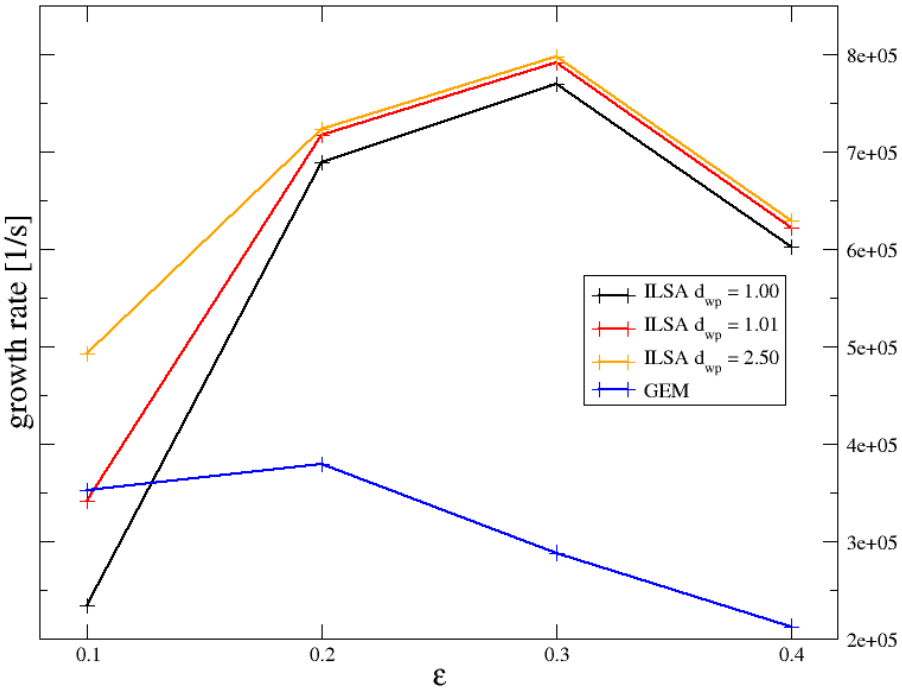

Figure 7.61: Maximum growth rate comparison

For $\epsilon = 0.3$ and 0.4, the temperature amplitudes in the parallel mode structures of the GEM runs become comparable / dominant to the ideal ballooning signature. These temperature profile effects are outside the scope of ideal linear MHD, but the stabilizing effect of curvature on the external kinks present in the ILSA runs has no counterpart in the GEM simulations, as external modes have been excluded from the latter.

The toroidal mode numbers show the best agreement for $\epsilon = 0.1$, compare fig. 7.62 in accordance to the growth rate observations, but with $d_{wp} = 1.00$. This is due to the fact that the perfectly conducting wall in direct contact with the plasma suppresses the external, low-n modes as already discussed and therefore leaves the high-n ballooning modes as dominant instabilities. For this inverse aspect ratio and $d_{wp} = 1.00$, despite the match of the maximum growth rates, the mode numbers differ significantly, as there is still a large external mode in the ILSA stability analysis. For $\epsilon = 0.2$, the mode numbers agree well, as the radial mode structure computed with ILSA show a dominant internal ballooning mode. Note that for larger ϵ, the ILSA mode numbers in fig. 7.62 are $n = 25$, because the simulations only extend to this toroidal mode number. We limited the range of n, because the spectra showed a strong ideal ballooning behavior, differing from the GEM observations, so modes with higher n obtained with ILSA would not provide any further insight. From figs. 7.47 - 7.50, however, they can be expected to be much higher. Consequently the difference to the GEM mode numbers, which are almost insensitive to the aspect ratio, increases with higher ϵ.

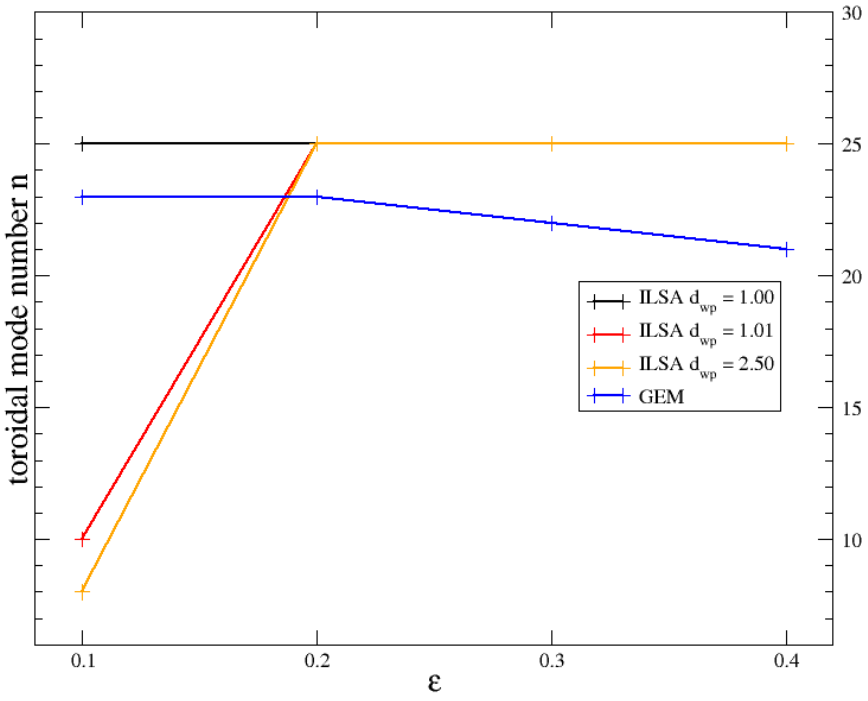

Figure 7.62: Toroidal mode number comparison for the fastest growing modes

7.4 Shaping effects

We use a fixed pressure profile $p(\psi)$, and current density profile was chosen as in eq. 7.5. Note that the radial coordinate is ψ instead of ρ as in the previous sections. The plasma cross section shape is varied with respect to elongation κ and triangularity δ as described in eqs. (6.3) and (6.4). The upper limit of the shaping parameters corresponds to experimental values of ASDEX Upgrade $\kappa = 1.6, \delta = 0.4$ [7]. For this range of triangularities, there is no large difference between the code parameter δ_H and the experimental δ, so we use them interchangeably.

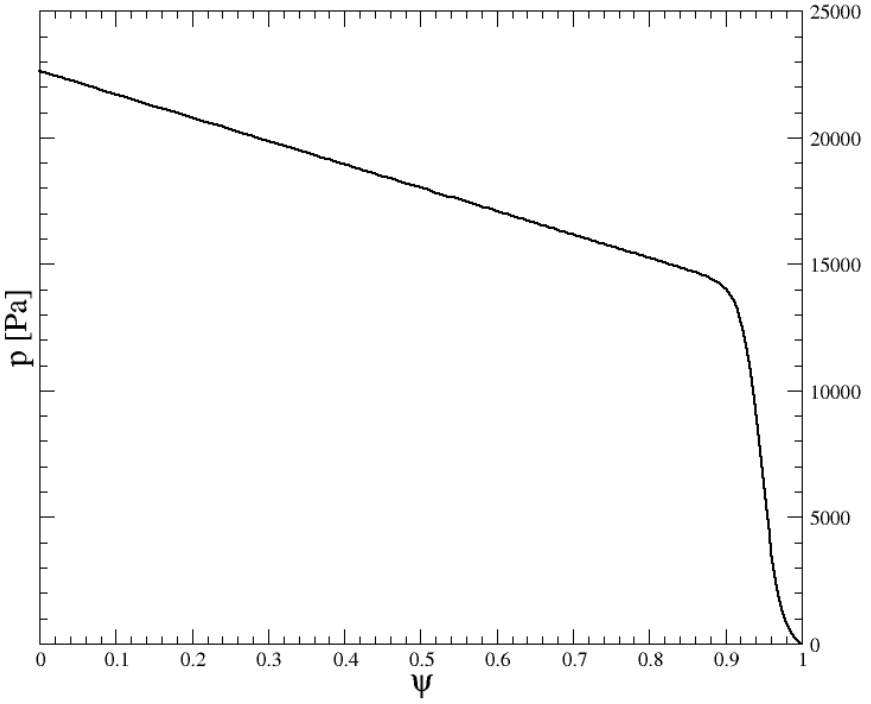

Figure 7.63: Pressure profile vs. normalized ψ

As the HELENA parametrization of the poloidal boundary surface does not conserve the volume, the position of the maximum pressure gradient shifts slightly to the magnetic axis for higher κ and δ, see fig. 7.64. The change however is very small and can be neglected.

For higher κ and δ, the q profile shows overall larger values, with the largest absolute differences close to the edge, compare fig. 7.65. This is understandable from geometric considerations, as basically the length in poloidal direction increases when following a magnetic field line. The q value can be approximated as [6]

$$q = \frac{2AB_t}{\mu_0 R_0 I}, \tag{7.9}$$

where A is the area of the poloidal cross section. For a circular plasma, $A = a^2\pi$, where a is the minor radius of the circle. For a plasma with elongation κ and $\delta = 0$, we have $A = \pi a^2 \kappa$,

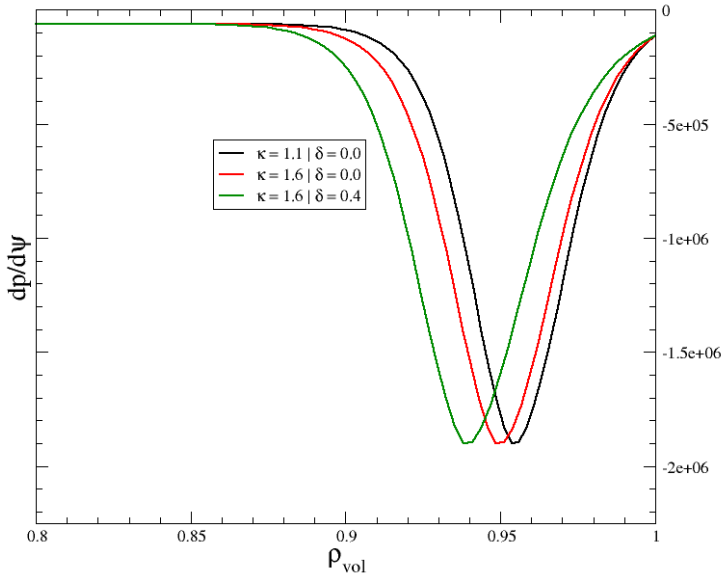

Figure 7.64: Pressure gradients with $\kappa = 1.1, \delta = 0.0$ and $\kappa = 1.6, \delta = 0.4$

so for fixed current I the relation is

$$q(\kappa) = \kappa q_{circular}. \tag{7.10}$$

This relative increase in the q values then results in a higher global magnetic shear, compare fig. 7.66. Elongation by itself has a weaker increasing effect on both q and the shear, whereas triangularity features large changes.

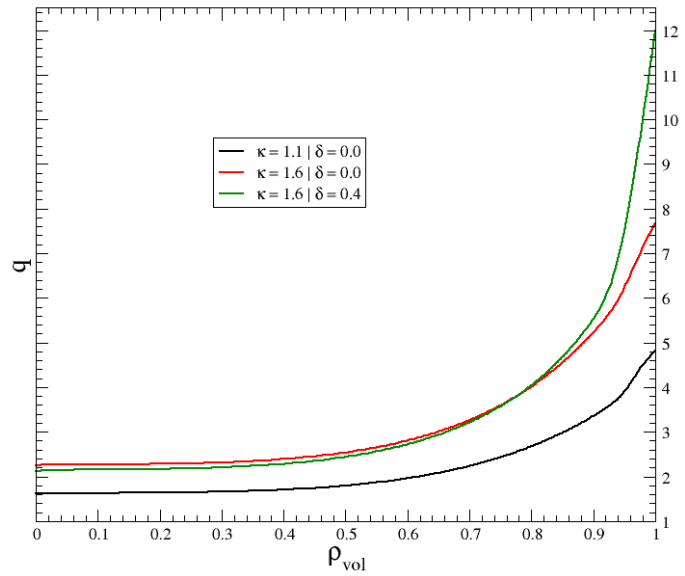

Figure 7.65: q profiles with $\kappa = 1.1, \delta = 0.0$ and $\kappa = 1.6, \delta = 0.4$

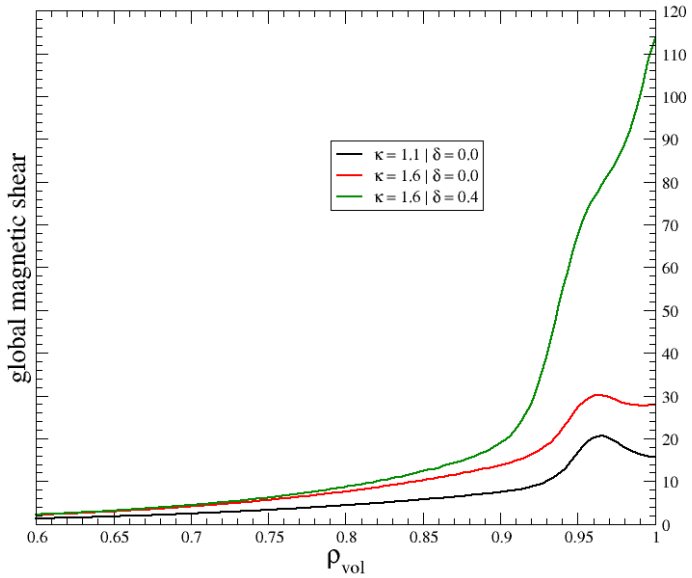

Figure 7.66: Global magnetic shear profiles with $\kappa = 1.1, \delta = 0.0$ and $\kappa = 1.6, \delta = 0.4$

7.4.1 Linear ideal MHD stability - ILSA

We first investigate the effects of varying elongation κ at zero triangularity $\delta = 0.0$ and negligible effect of the wall $d_{wp} = 2.50$, see fig. 7.67. Comparing to the circular case with $\kappa = 1.0$ and $\delta = 0.0$, higher elongation has a destabilizing effect on the low-n part of the spectra ($n \lesssim 5$), where $\kappa \geq 1.2$ features an unstable $n = 1$ mode. This mode, is an unstable kink-ballooning mode, see fig. 7.68, and higher κ increases the ratio of internal to external amplitude.

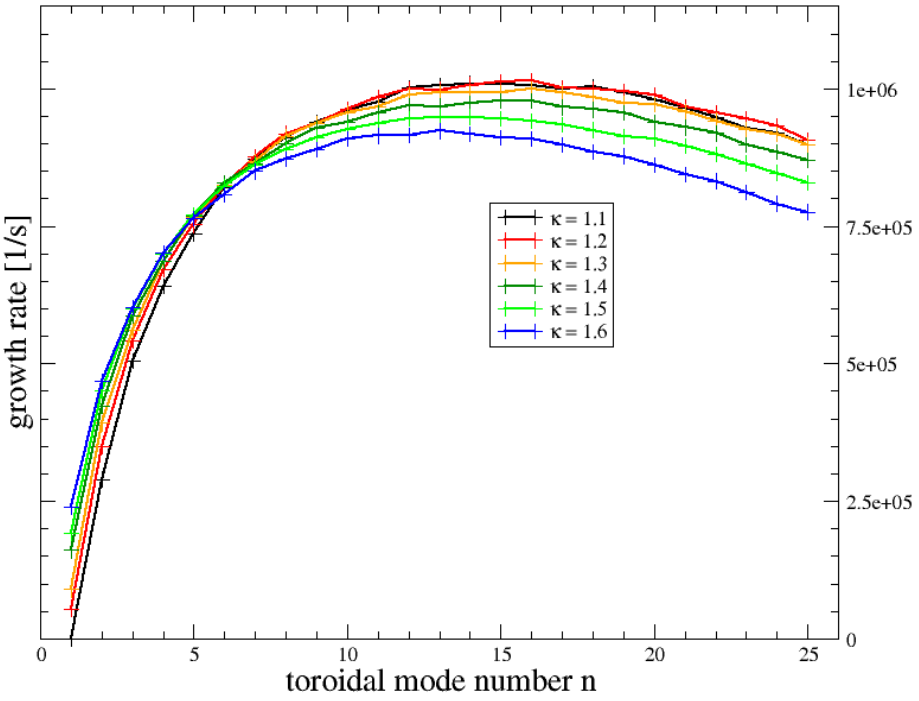

Figure 7.67: ILSA spectra with $d_{wp} = 2.50$, elongation scan with $\delta = 0.0$

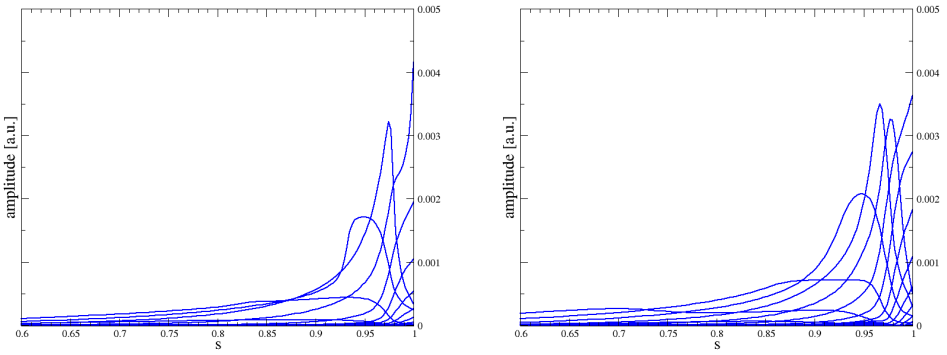

$\kappa = 1.2$ $\kappa = 1.6$

Figure 7.68: Radial mode structures for the $n = 1$ modes with $d_{wp} = 2.50$ and triangularity $\delta = 0.0$

Modes with high n also show slightly larger growth rates for $\kappa \leq 1.4$, therefore the elongation rather has overall influence on the internal modes and less on the external pertubations. Higher elongation, however, decreases the corresponding growth rates, indicating a stabilizing effect from the higher shear of the equilibria.

For fixed low elongation $\kappa = 1.1$, a stabilizing effect of increasing triangularity is visible for $\delta \geq 1.2$, see fig. 7.69. Furthermore, only the intermediate to high n modes are affected ($n \gtrsim 10$, with the strongest effect on modes with the highest n. Comparing $\delta = 0.0$ and $\delta = 0.4$, the maximum growth rate drops by $\approx 10\%$, while the growth rates for $n = 25$ decrease by more than 40%.

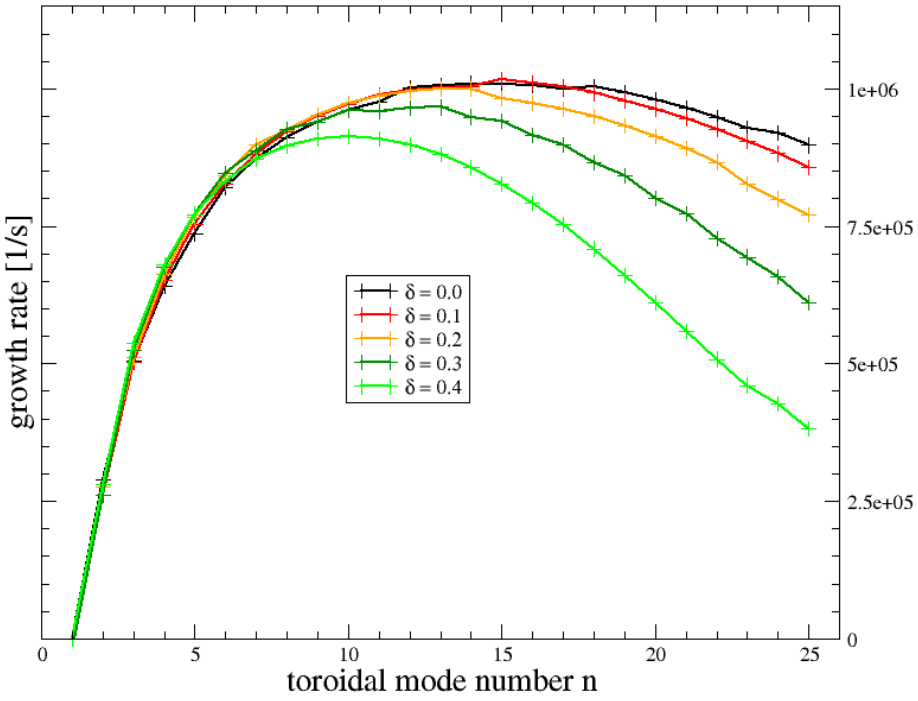

Figure 7.69: ILSA spectra with $d_{wp} = 2.50$, triangularity scan with low elongation $\kappa = 1.1$

With fixed high elongation $\kappa = 1.6$, triangularity shows an even stronger stabilizing effect, even for low-n modes, compare fig. 7.70. When comparing zero triangularity to $\delta = 0.4$, the growth rate of the fastest growing mode decreases by $\approx \frac{1}{3}$. For high $\delta = 0.3, 0.4$, the spectra exhibit complete stabilization of modes with $n \gtrsim 20 - 25$.

The strong effect of triangularity on modes with higher n, i.e. modes with stronger ballooning character, can be understood with the changing plasma geometry. For $\delta \geq 0$, the length of a poloidal flux surface boundary on the high-field side relative to the magnetic axis increases, while the length on the low-field side decreases. Higher elongation enhances this even further. Now following a magnetic field line, the field line resides longer in the region of favorable curvature, therefore showing a stabilizing effect on ballooning modes associated with higher n.

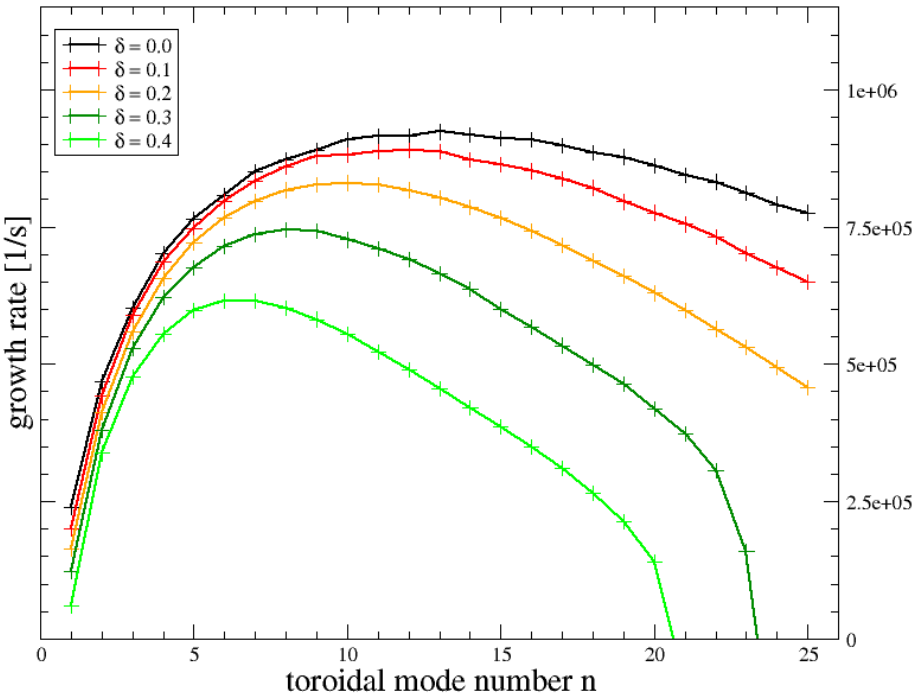

Figure 7.70: ILSA spectra with $d_{wp} = 2.50$, triangularity scan with high elongation $\kappa = 1.6$

The overall higher stabilizing influence of δ on the ballooning part of the spectra causes a shift of the toroidal mode numbers of the fastest growing modes to lower values. Changing elongation, however, has only marginal impact on the mode numbers, with a slight shift to lower n.

The radial mode structures only experience slight changes with fixed κ and varying δ, see fig. 7.71, and generally an increased ratio of max. amplitude of internal to external modes with fixed δ and varying κ. This ratio increase is more pronounced for higher δ, because higher elongation shows mostly a destabilizing effect on the ballooning part and the destabilization is stronger for lower n. Higher triangularity, however, is linked to lower n, thus the stronger effect.
The increased external-internal mode amplitude ratio for fixed κ and increasing δ stems from the stabilizing effect of triangularity on ballooning modes and the shift of the fastest growing mode to lower n, which is also associated with stronger external perturbations.

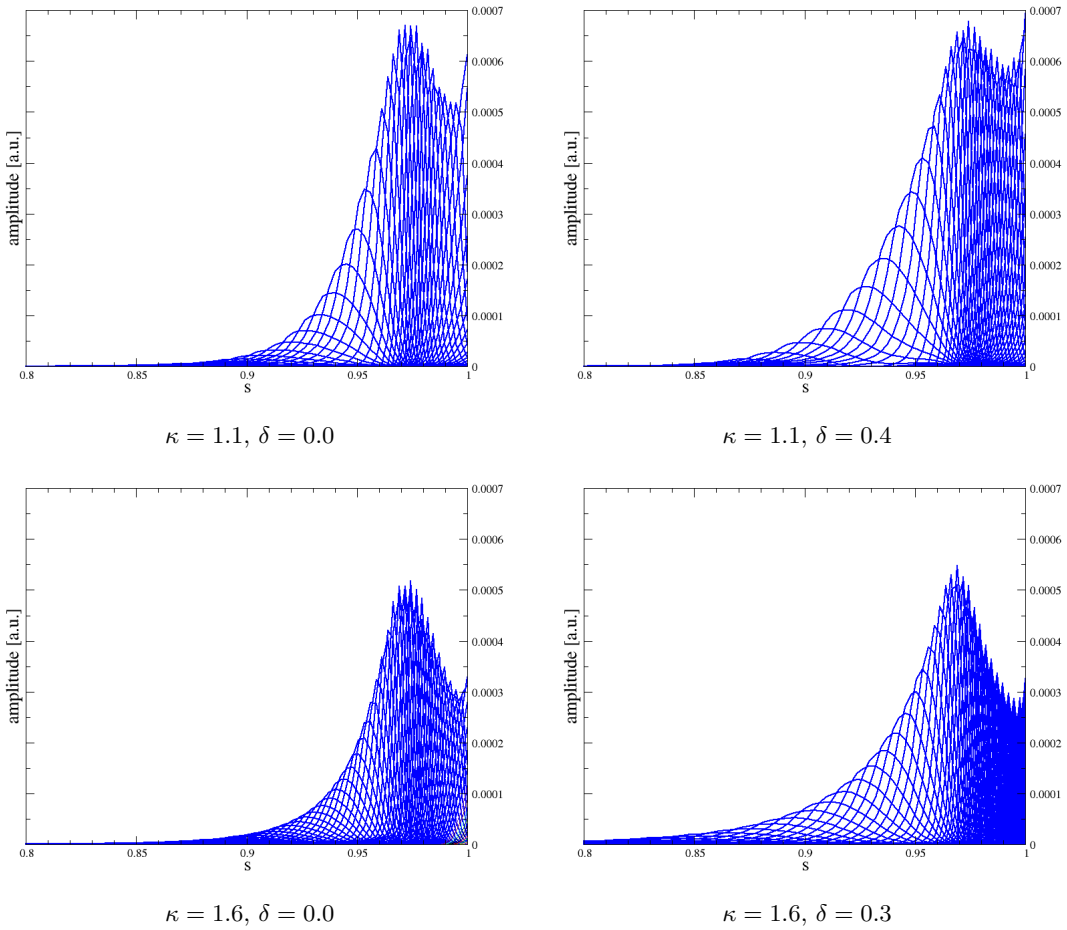

$\kappa = 1.1$, $\delta = 0.0$ $\kappa = 1.1$, $\delta = 0.4$

$\kappa = 1.6$, $\delta = 0.0$ $\kappa = 1.6$, $\delta = 0.3$

Figure 7.71: Radial mode structures for the fastest growing modes with $d_{wp} = 2.50$

The effect of a close proximity $d_{wp} = 1.01$ of the perfectly conducting wall to the plasma surface for zero triangularity and changing elongation is commensurate with the findings in the previous sections, with the spectra shown in figs. 7.72 - 7.74. As higher κ destabilizes the low-n modes, low d_{wp} results in a wider spread of the toroidal mode numbers for the onset of instability with varying κ, as the external parts of the low-n modes get dampened. The maximum growth rates are marginally lower as for $d_{wp} = 2.50$, and the difference is negligible for high n, as these modes already feature a strong ballooning character and are therefore not affected.

The shift of the onset of instability gets smaller for higher elongation, where for $\kappa = 1.6$ only the $n = 1$ mode gets completely stabilized with the relative plasma-wall distance $d_{wp} = 1.01$. This is because for higher κ, the radial mode structures already show a more dominating ballooning character, compare the previous fig. 7.71 and the radial mode structures for $d_{wp} = 1.01$ in figs. 7.75 and 7.75, so consequently the impact of d_{wp} also dimishes with increasing elongation.

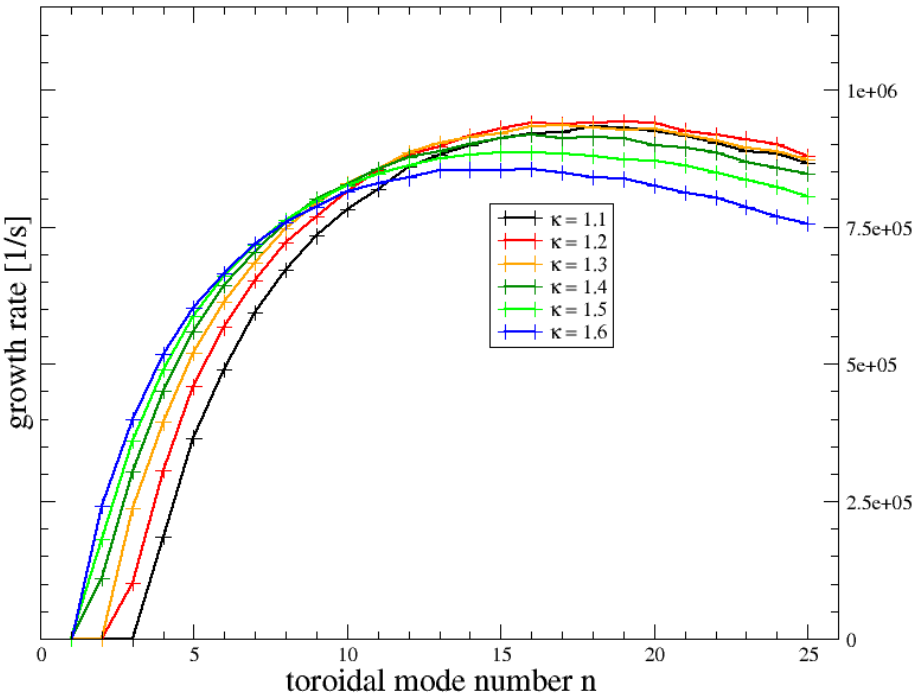

Figure 7.72: ILSA spectra with $d_{wp} = 1.01$, pure elongation scan with $\delta = 0.0$

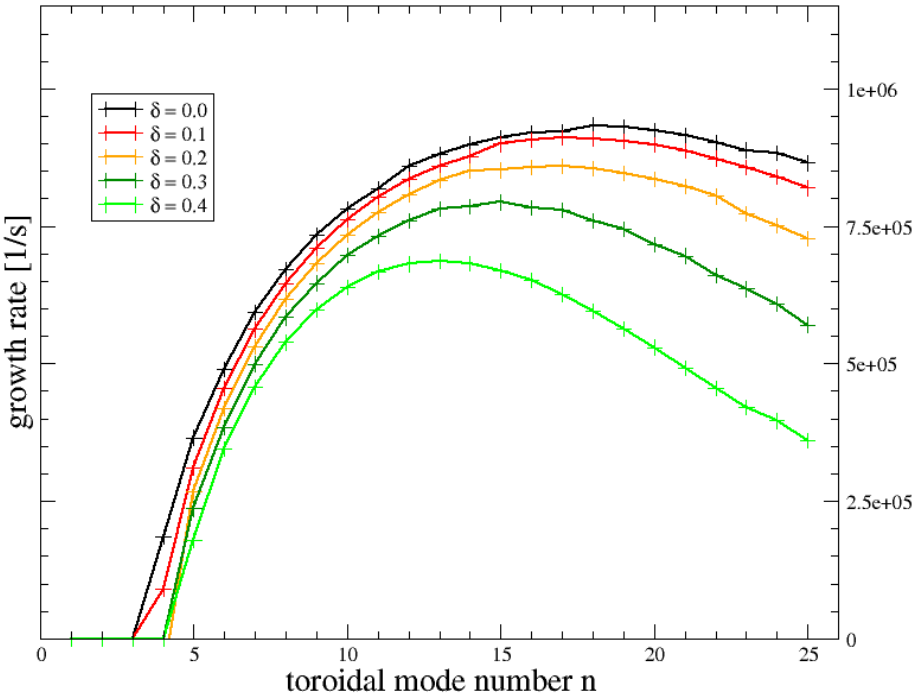

Figure 7.73: ILSA spectra with $d_{wp} = 1.01$, triangulation scan with low elongation $\kappa = 1.1$

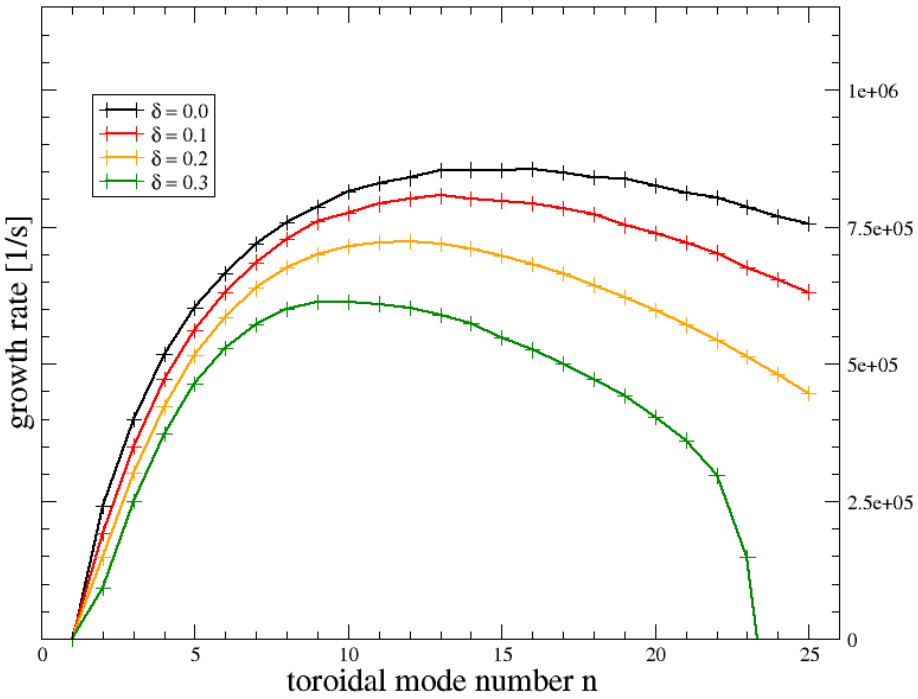

Figure 7.74: ILSA spectra with $d_{wp} = 1.01$, triangulation scan with high elongation $\kappa = 1.6$

Placing the perfectly conducting wall on the plasma surface, $d_{wp} = 1.00$, does not yield any qualitative and only slightly quantitative changes of the toroidal mode number spectra compared to $d_{wp} = 1.01$, so we just refer to the results cumulated in the comparison with GEM, figs. 7.94 - 7.99.

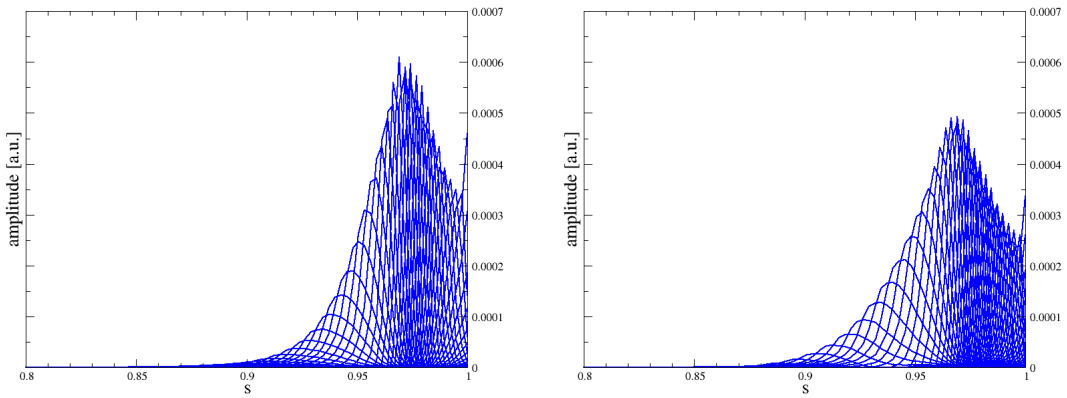

$\kappa = 1.1$, $\delta = 0.0$ $\kappa = 1.1$, $\delta = 0.4$

Figure 7.75: Radial mode structures for the fastest growing modes with $d_{wp} = 1.01$

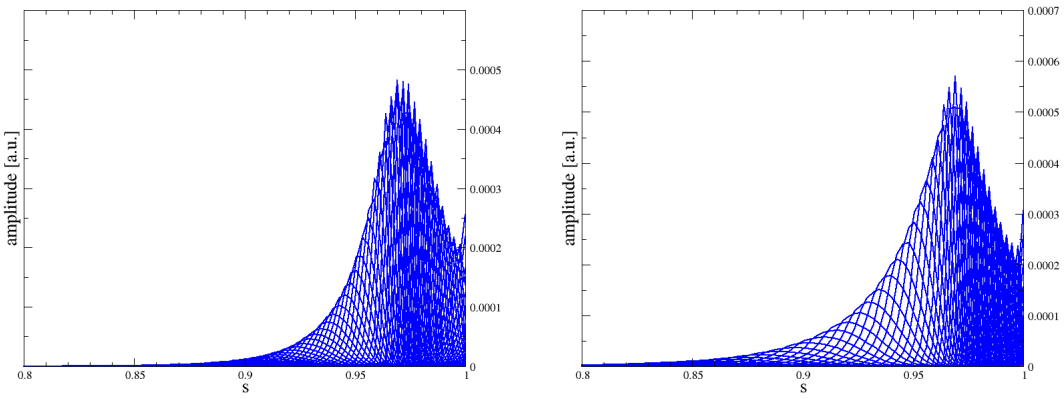

$\kappa = 1.6,\ \delta = 0.0$ $\kappa = 1.6,\ \delta = 0.3$

Figure 7.76: Radial mode structures for the fastest growing modes with $d_{wp} = 1.01$

7.4.2 Gyrofluid - GEM

For strong shaping, the GEM simulations showed violent dynamics during the turbulent saturated phase due to the high pressure gradient. A high ∇p, however, was necessary to obtain a clear ballooning signature. As gyrofluid studies of $\kappa - \delta$ effects of the turbulent particle transport and ion heat flux in flux-surface geometry with low pressure gradient an in an ITG-regime have already been done with GEM in ref. [84], we did not pursue this further and focused solely on the initial linear phase. The simulations were performed until the dynamics reached the ion gyroradius range $k_y \rho_s \approx 1$, i.e. the spectra flattened.
The fluctuating total energy and its associated growth rate in figs. 7.77 and 7.78 for a scan of the elongation with $\delta = 0.0$ show similar behavior as the previous ILSA analysis. Increasing κ from 1.1 to 1.2 yields only a marginal change in the peak of E_T, but the maximum value is taken in a shorter time, resulting in a slightly higher growth rate. For higher κ, the time with maximum G_T increases and the peak E_T as well as the highest growth rate for each case decreases. For $\kappa = 1.5$ and 1.6, there is a competition between ITG and ballooning mode at the beginning $t \approx 4\mu$s, but eventually the ballooning instability dominates. The ion heat flux and its growth rate concur with the behavior of E_T and G_T, compare figs. 7.79 and 7.80. The relative change in the peak values and the maximum growth rate is approximately the same as for the energetics.

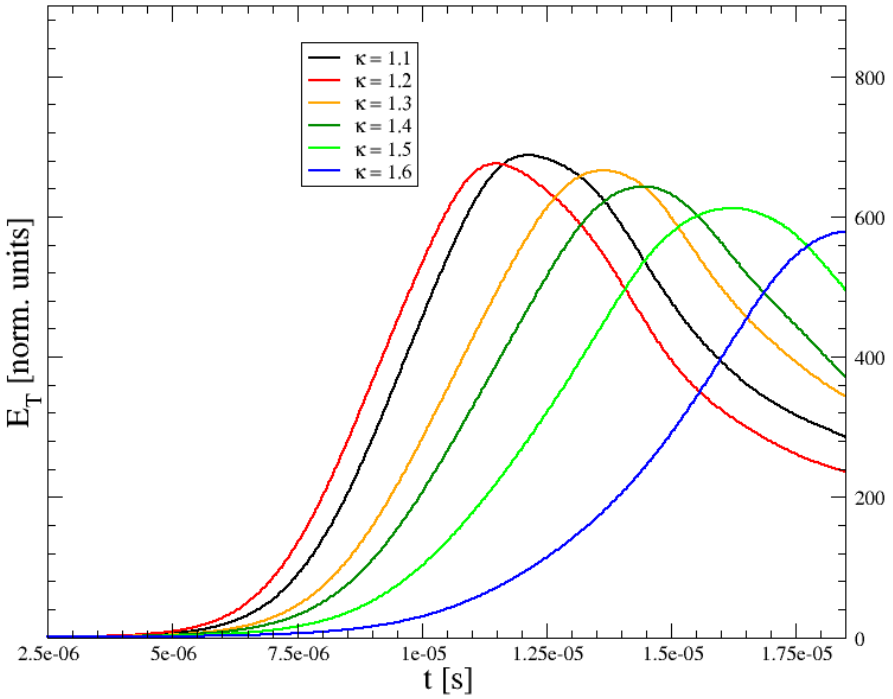

Figure 7.77: Total energy E_T, elongation scan with $\delta = 0.0$

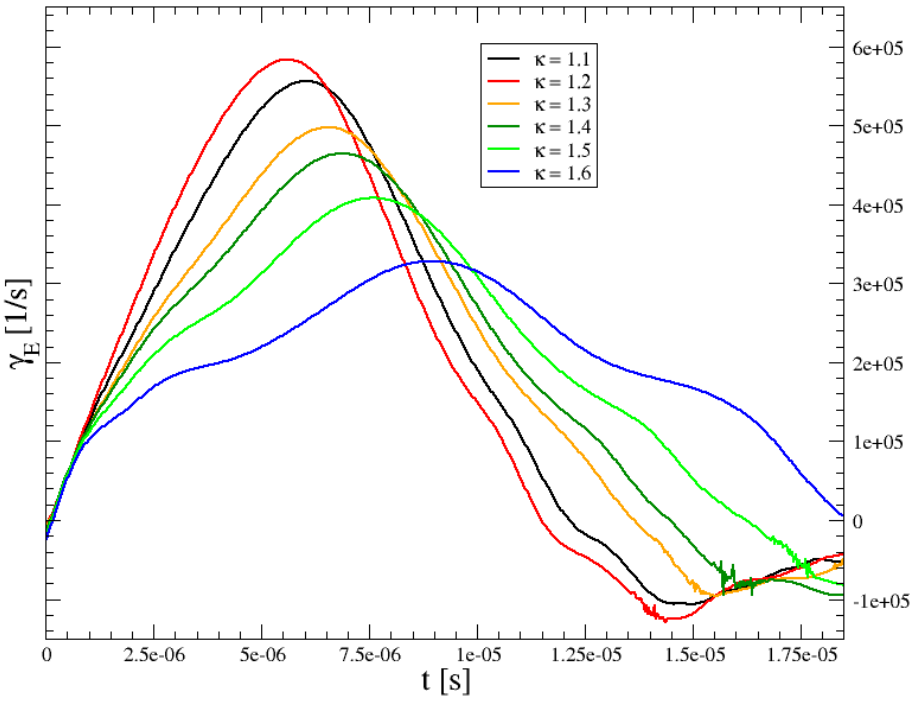

Figure 7.78: Growth rate γ_E, elongation scan with $\delta = 0.0$

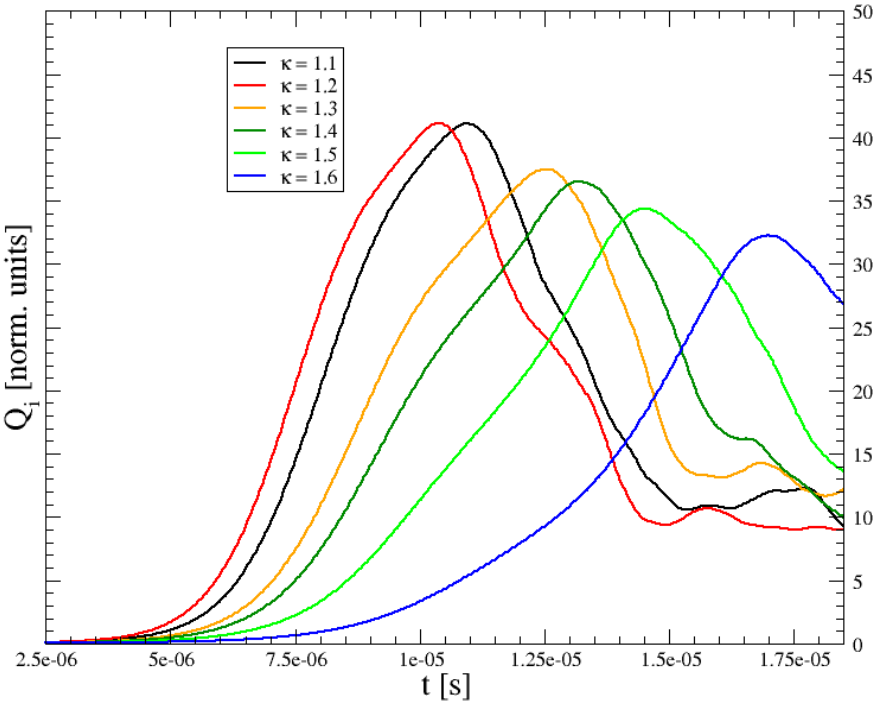

Figure 7.79: Ion heat flux Q_i, elongation scan with $\delta = 0.0$

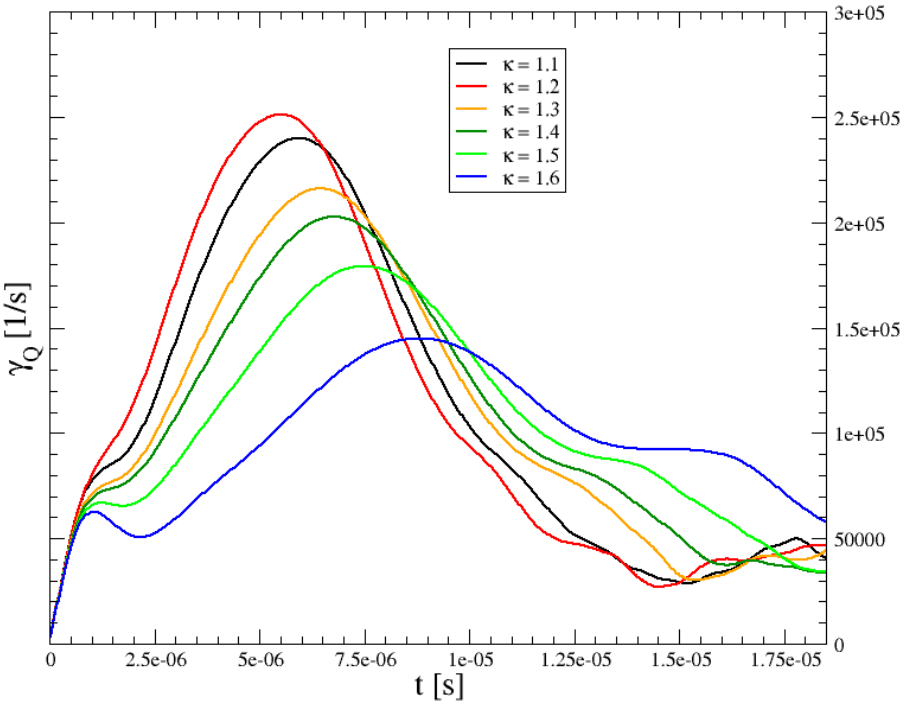

Figure 7.80: Growth rate γ_Q, elongation scan with $\delta = 0.0$

The parallel mode structures reflect the differences for $\kappa = 1.5$ and 1.6, see fig. 7.81. Only for these cases, a decrease of the squared amplitude of ϕ is clearly visible. For the other elongation values, the decrease of ϕ with higher κ is weak.

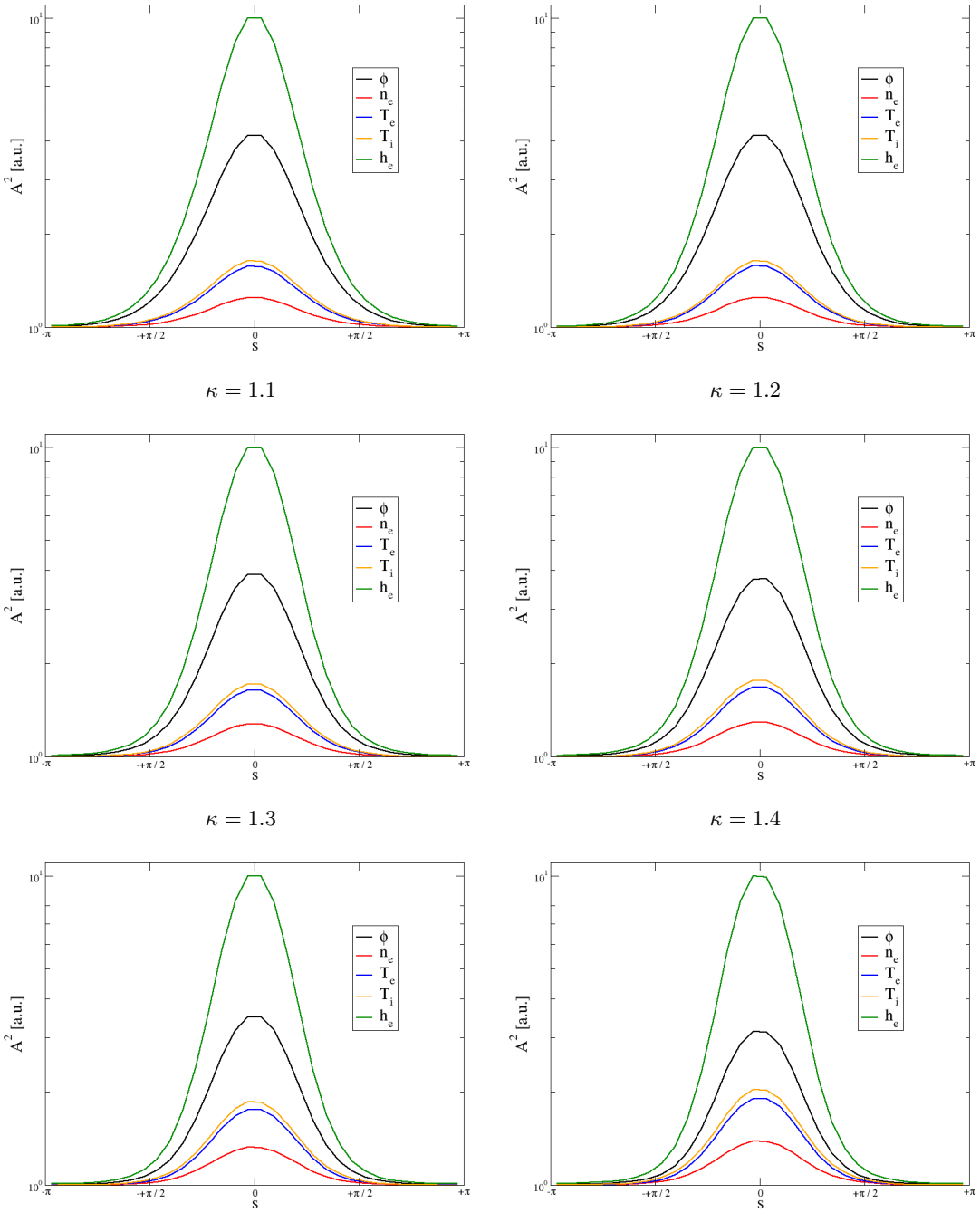

$\kappa = 1.1$ $\kappa = 1.2$

$\kappa = 1.3$ $\kappa = 1.4$

$\kappa = 1.5$ $\kappa = 1.6$

Figure 7.81: Parallel mode structures at the time of maximum growth rate, elongation scan with $\delta = 0.0$

The spectra in figs. 7.82 - 7.85, however, show not much variation at the time of maximum γ_E. There is a dominant peak at $k_y\rho_s = 0.1$ for all cases, with a second, less pronounced peak at $k_y\rho_s = 0.175$. As with E_T and Q_i, the squared amplitude for all cases increases with $\kappa = 1.1 \rightarrow 1.2$, and subsequently decreases for higher elongations.

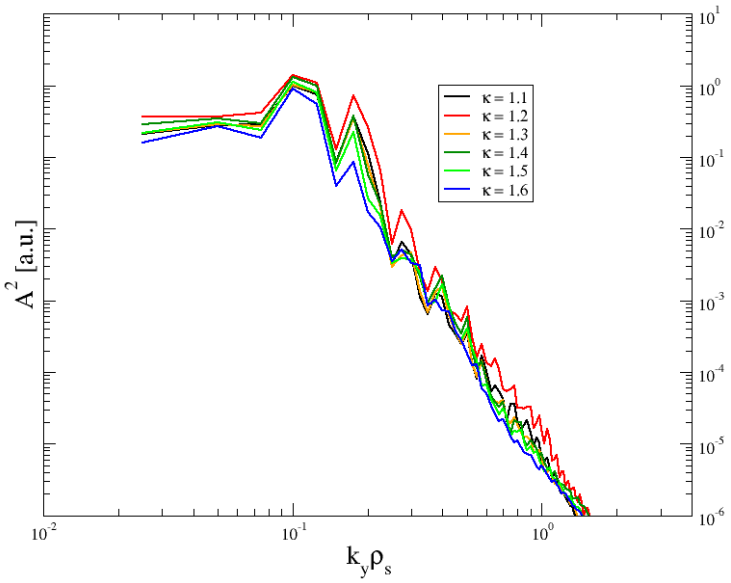

Figure 7.82: Spectra of n_e at the time of maximum growth rate

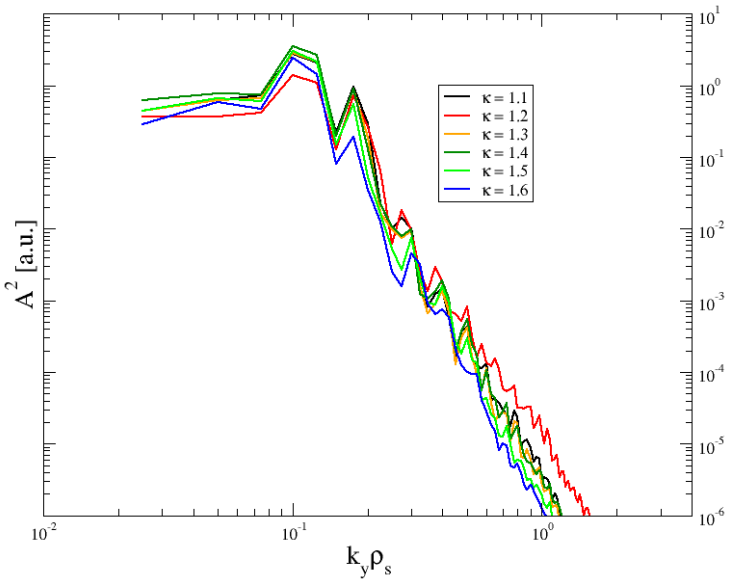

Figure 7.83: Spectra of Q_i at the time of maximum growth rate

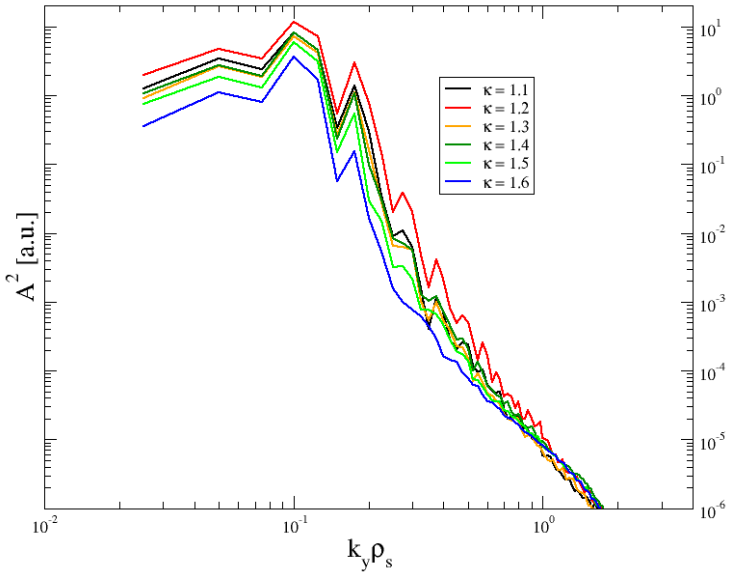

Figure 7.84: Spectra of ϕ at the time of maximum growth rate

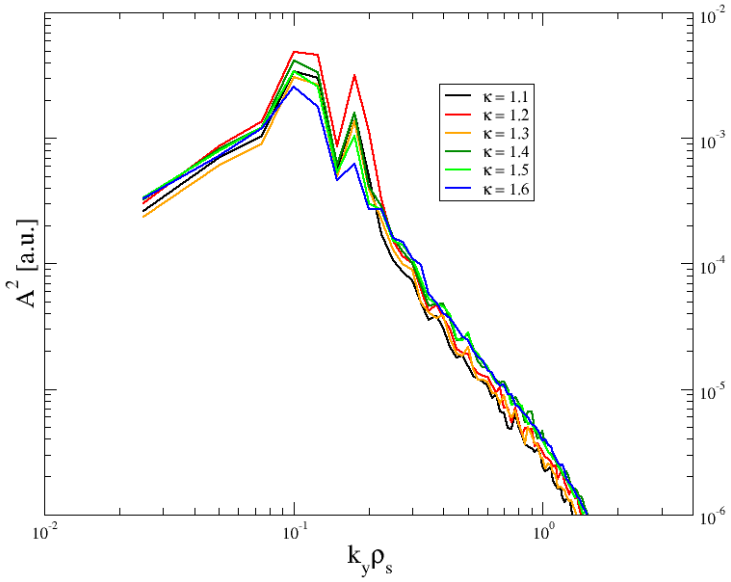

Figure 7.85: Spectra of ω at the time of maximum growth rate

For constant low elongation $\kappa = 1.1$ and varying triangularity, however, the GEM results showed only marginal changes. Neither the energetics in figs. 7.86 and 7.87 nor the ion heat flux and its associated growth rate in figs. 7.88 and 7.89 feature significant evolution with δ. Alongside, the spectra and parallel mode structure were almost completely insensitive to δ as well[5].

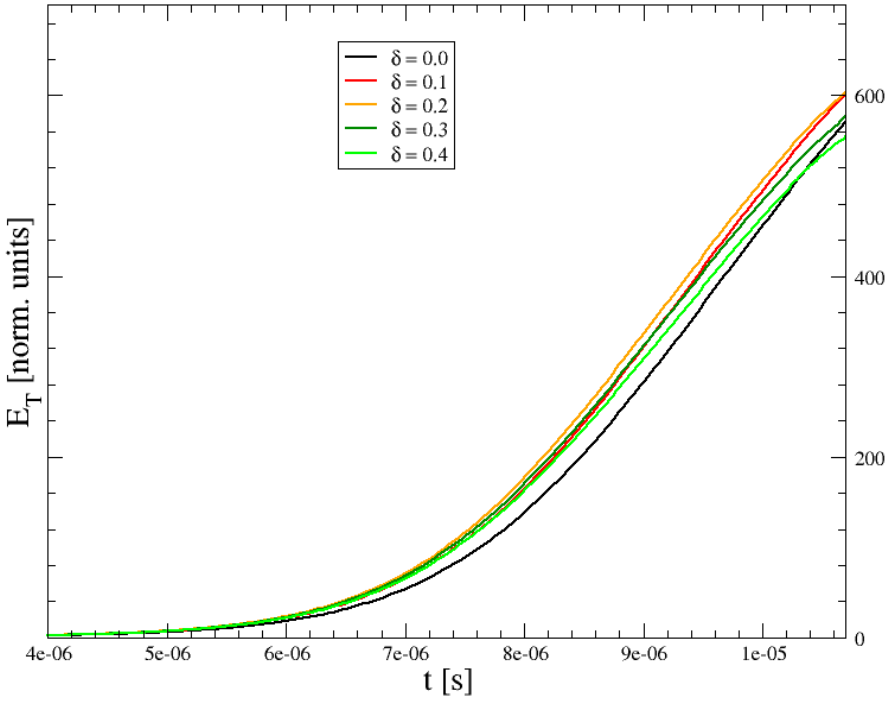

Figure 7.86: Total energy E_T, triangularity scan for low elongation $\kappa = 1.1$

[5]Not explicitly shown here, for the spectra and parallel mode structures see figs. 7.81 - 7.85 for triangularity $\delta = 0.0$

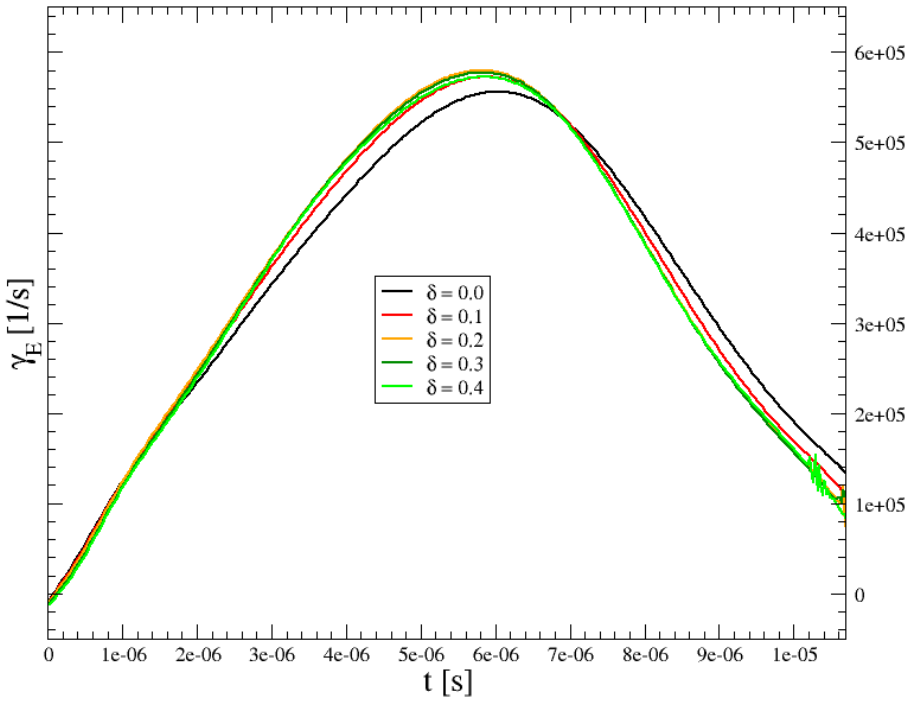

Figure 7.87: Growth rate γ_E, triangularity scan for low elongation $\kappa = 1.1$

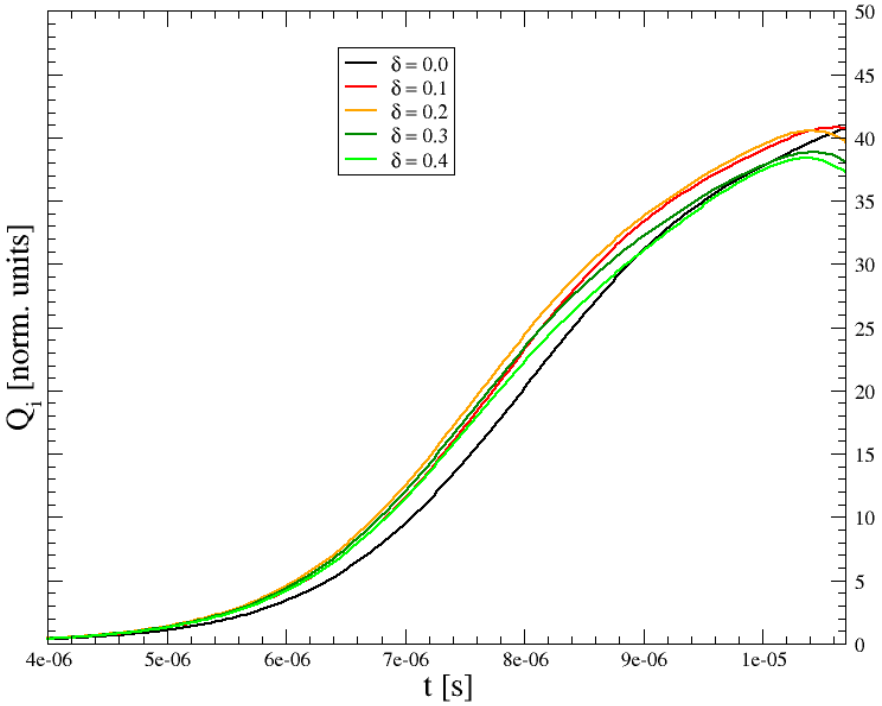

Figure 7.88: Ion heat flux Q_i, triangularity scan for low elongation $\kappa = 1.1$

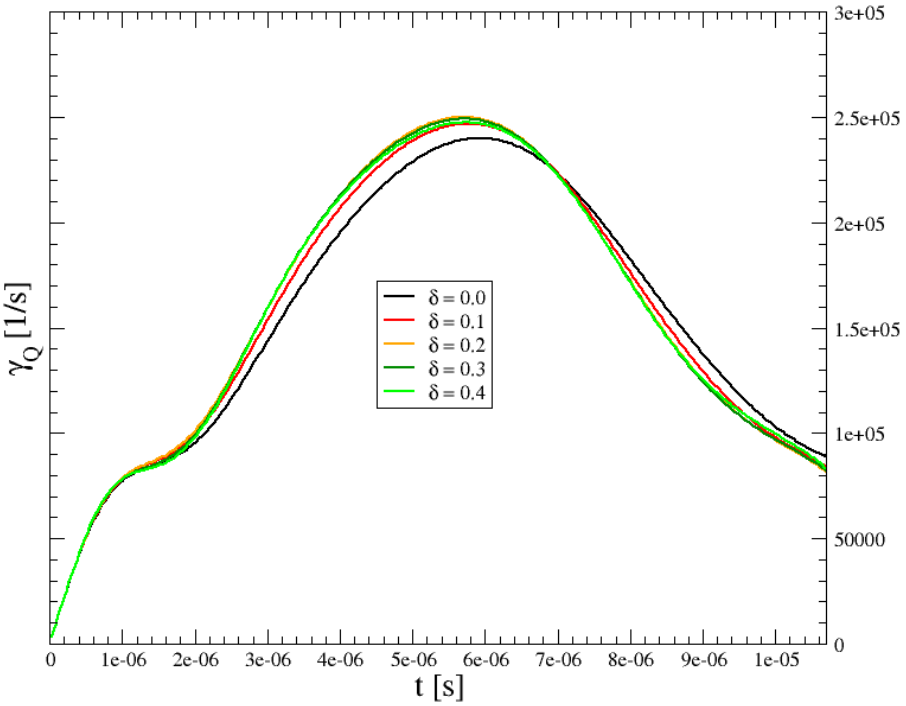

Figure 7.89: Growth rate γ_Q, triangularity scan for low elongation $\kappa = 1.1$

Increasing δ at higher elongation $\kappa = 1.6$ shows almost the same picture for both the energetics and the ion heat flux, compare figs. 7.90 - 7.93. A more triangular plasma cross section decreases the peak values of both E_T and Q_i slightly, but the maximum growth rates are unaffected. For the strongest shaping with $\kappa = 1.6$ and $\delta = 0.4$, however, there is a clearly visible drop in the growth rates for both the fluctuating total energy and the ion heat flux. Moreover, the time point of the peak growth rate shifts to slightly higher values as the instability becomes weaker. The spectra and parallel mode structures nevertheless do not show noticeable differences compared to vanishing triangularity $\delta = 0.0$.

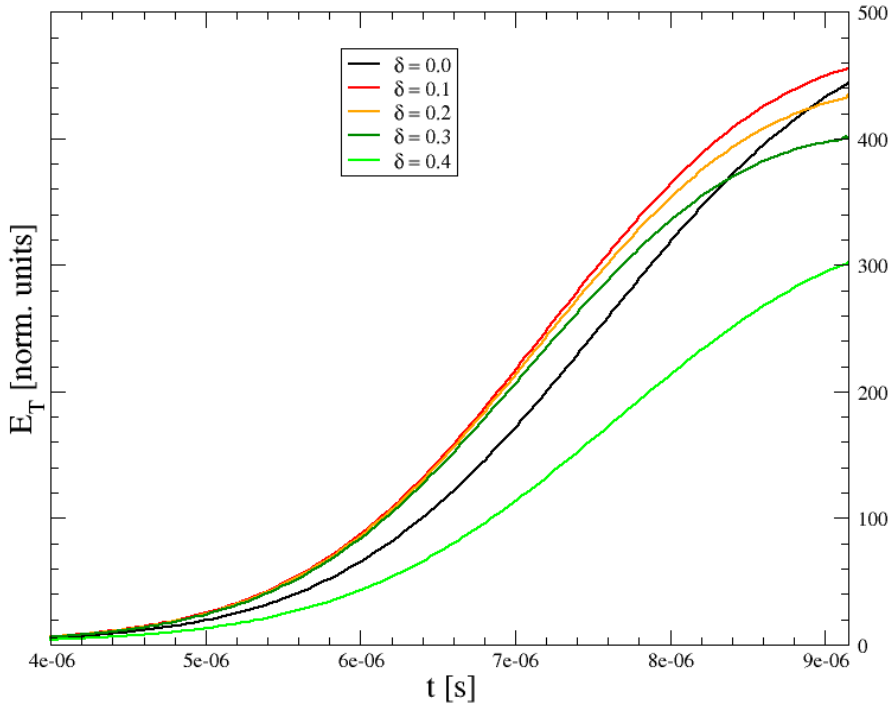

Figure 7.90: Total energy E_{total}, triangularity scan for high elongation $\kappa = 1.6$

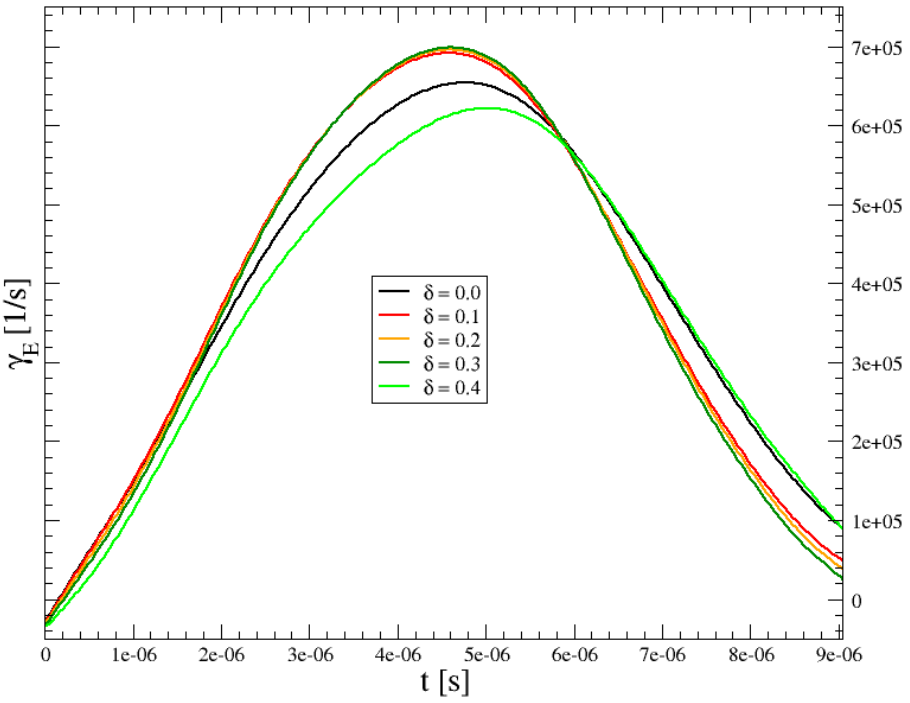

Figure 7.91: Growth rate γ_E, triangularity scan for high elongation $\kappa = 1.6$

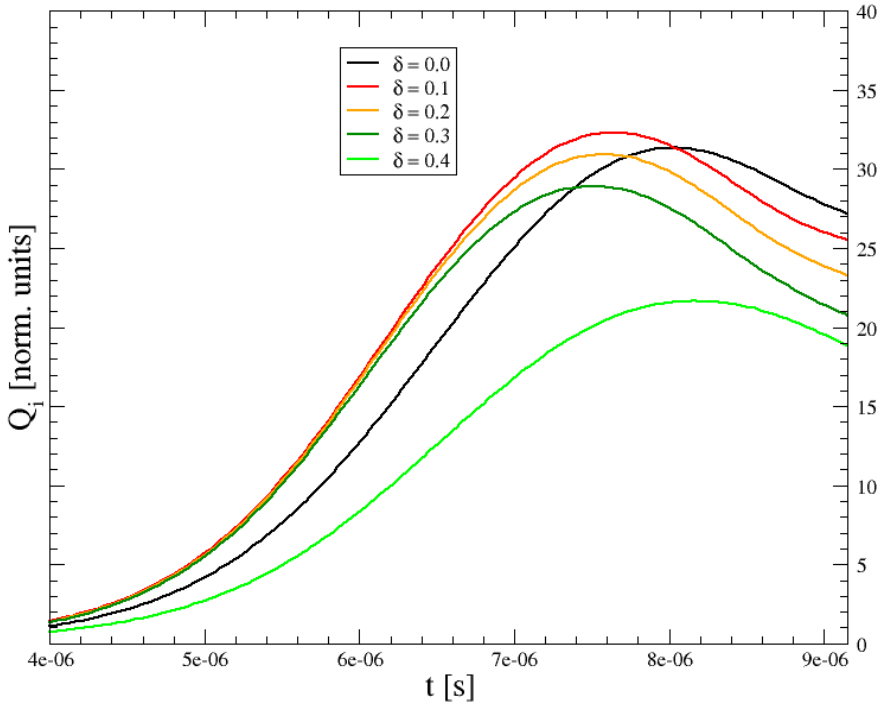

Figure 7.92: Ion heat flux Q_i, triangularity scan for high elongation $\kappa = 1.6$

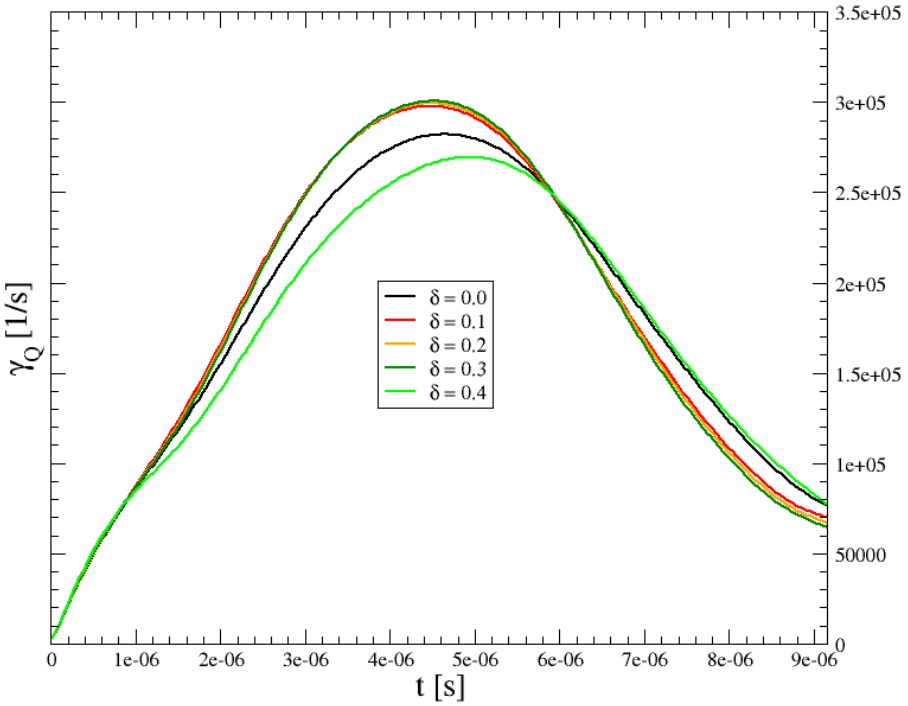

Figure 7.93: Growth rate γ_Q, triangularity scan for high elongation $\kappa = 1.6$

7.4.3 Comparison

For vanishing triangularity and varying elongation, the growth rates in fig. 7.94 show similar scaling with κ, slightly rising for $\kappa = 1.1 \rightarrow 1.2$ and decreasing for higher κ. For higher elongation, however, the relative growth rate drop is larger for GEM than for the ILSA spectra, as the squared amplitude of ϕ and thus the ballooning signature of the parallel mode structures decreases. The toroidal mode numbers of the fastest growing modes for GEM and ILSA roughly follow the same trend for all d_{wp} and are also comparable with regard to their absolute values. The agreement is slightly worse for larger κ, concurring with the change in the parallel mode structures.

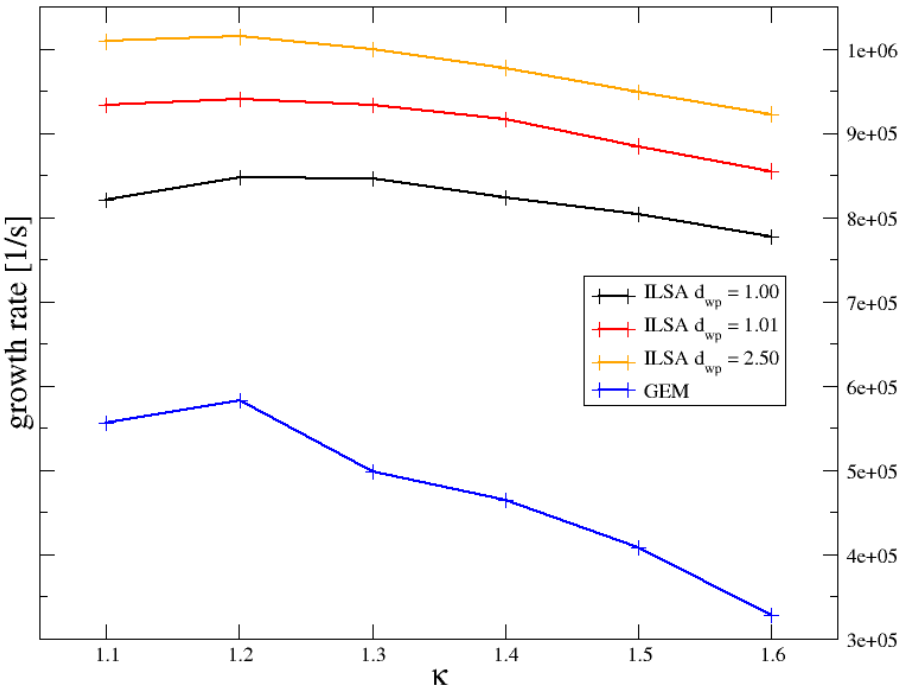

Figure 7.94: Maximum growth rate comparison, elongation scan with $\delta = 0.0$

As the GEM dynamics were only marginally affected by triangularity at fixed elongation, the ILSA and GEM mode numbers and growth rates show very different scalings with δ, see figs. 7.96 - 7.99. At high δ, the difference between the growth rates becomes small, but this is due to the strong stabilizing effect of triangularity in the framework of linear ideal MHD stability analysis and not reflected in the GEM simulations. Only for the strongest shaping, $\kappa = 1.6$ and $\delta = 0.4$, a clear decrease of γ computed with GEM can be observed. The mode numbers, however, show no significant change even for this case.

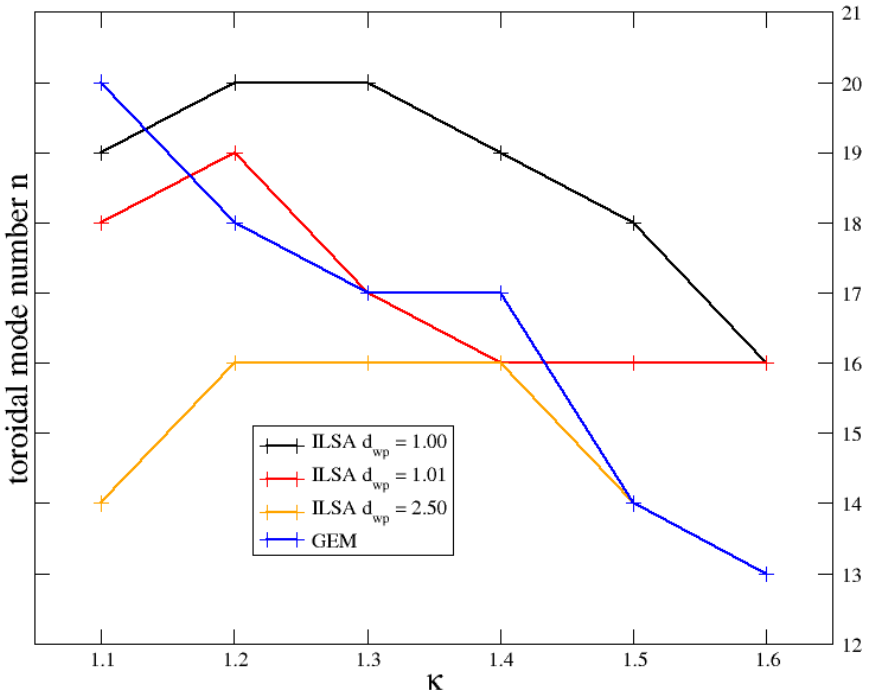

Figure 7.95: Toroidal mode number comparison for the fastest growing modes, elongation scan with $\delta = 0.0$

Shaping effects on turbulent particle transport and ion heat flux in flux-surface geometry have been studied in the context of GEM gyrofluid simulations based on HELENA equilibria in reference [84], and equally found barely any effect of triangularity. The scaling with elongation nevertheless agreed well with experimental observation. It is possible that excluding a small region close to the plasma surface from the GEM radial computation domain is the cause for the lack of impact of δ. Advancements in the numerical treatment of this small region could clarify that issue, see e.g. the ongoing studies of conformal coordinates in [47] and the references therein.

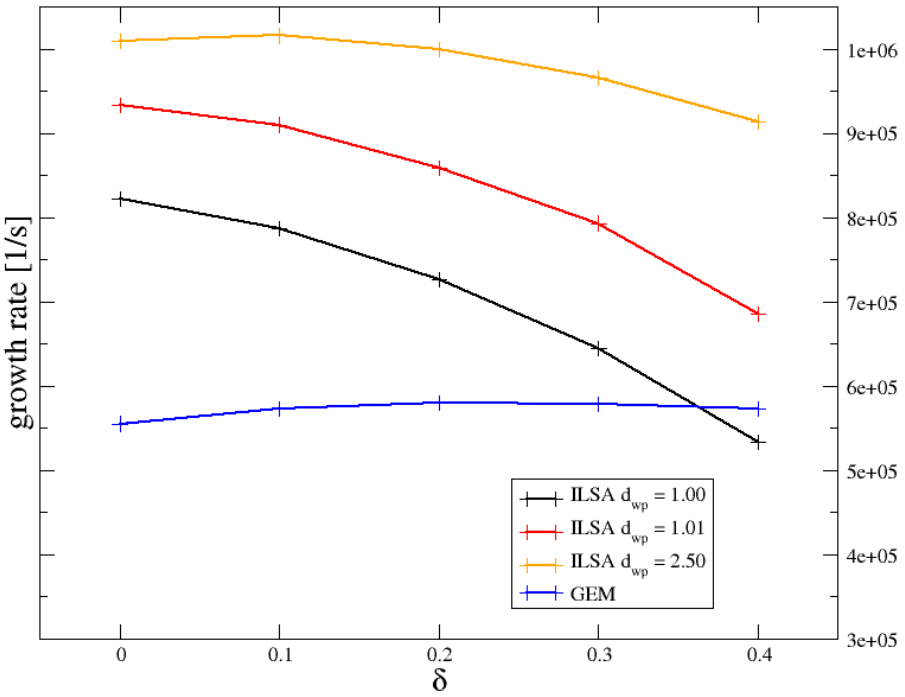

Figure 7.96: Maximum growth rate comparison, triangularity scan for low elongation $\kappa = 1.1$

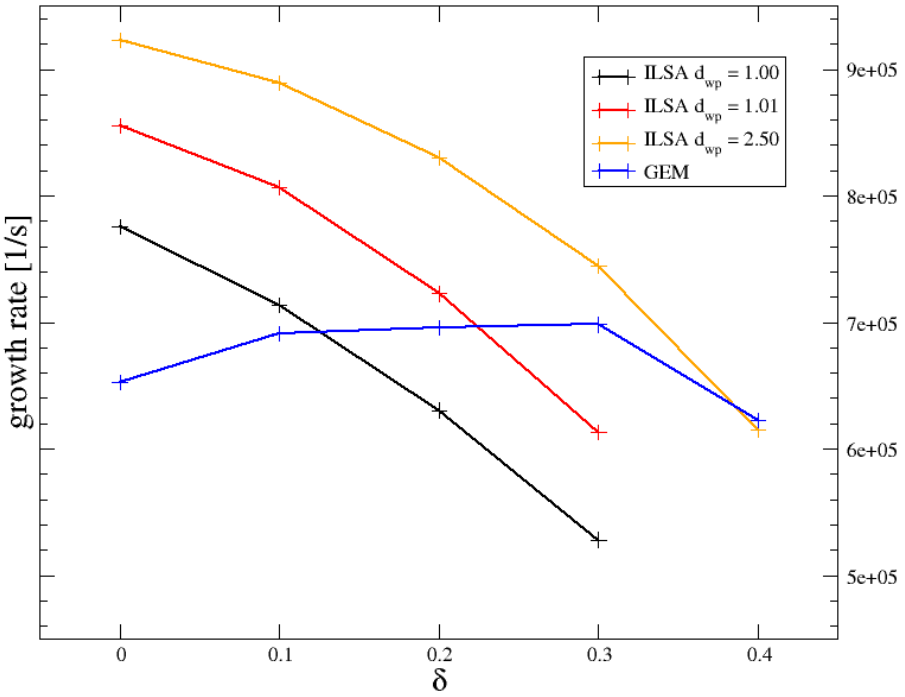

Figure 7.97: Maximum growth rate comparison, triangularity scan for high elongation $\kappa = 1.6$

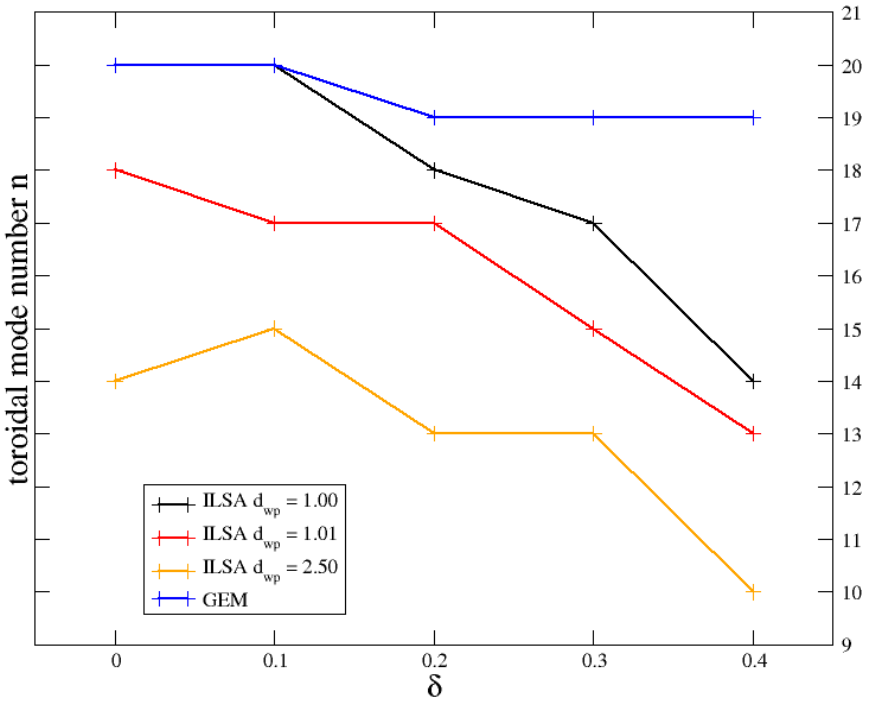

Figure 7.98: Toroidal mode number comparison for the fastest growing modes, triangularity scan for low elongation $\kappa = 1.1$

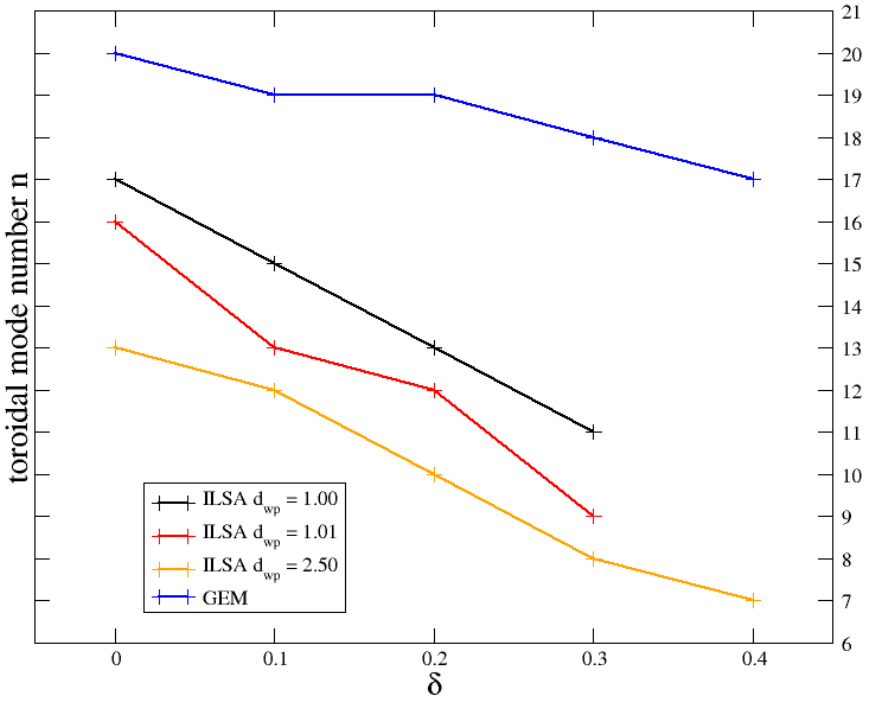

Figure 7.99: Toroidal mode number comparison for the fastest growing modes, triangularity scan for high elongation $\kappa = 1.6$

7.5 Core ballooning

As we have observed in the chapter 7.1, the relative difference in growth rates when comparing linear ideal MHD and the gyrofluid model was smallest for high pressure gradients, resulting in a strong ideal ballooning signature of the parallel mode structures, and smaller contributions from external modes in the MHD stability analysis. So we consider an equilibrium with the profiles shown in figs. 7.100 - 7.104. The pressure gradients peak in the core region at $\rho_{vol} \approx 0.8$, therefore we can avoid edge physics in the gyrofluid runs and the pressure does not provide any drive to external modes.

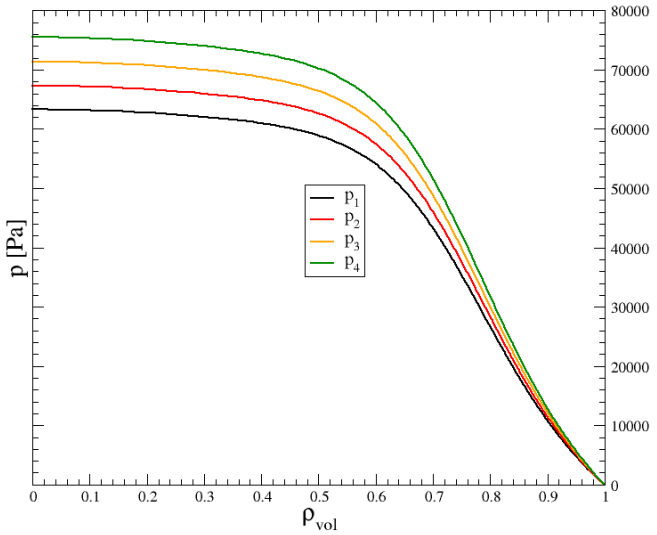

Figure 7.100: Pressure profiles

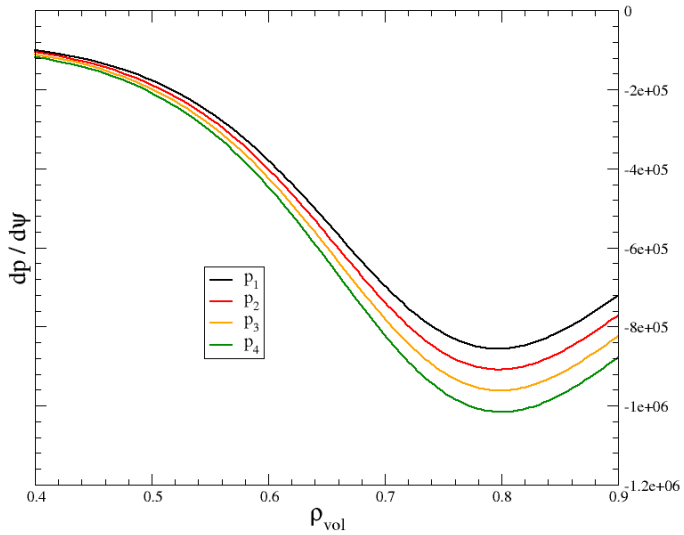

Figure 7.101: Pressure gradients

The flux-surface averaged current density was chosen to be

$$< j_{tor} > (\psi) = j_0 \, (1 - \psi) \exp(-\psi) \tag{7.11}$$

as this choice yields quasi-parabolic q profiles, on that matter c.f. [93]. The shear at the position of the maximum pressure gradient is always small, so there are no detrimental distortions of the grid elements on the GEM simulations. The nominal plasma parameters are

- major radius $R_0 = 1.65\text{m}$
- minor radius $a = 0.5\text{m}$
- vacuum magnetic field $B_0 = 2.5\text{T}$,

and the plasma cross section is circular.

This section is not supposed to be a comprehensive study of core ballooning, for detailed studies of kinetic core ballooning, see e.g. [87]. It is merely meant to briefly test the remaining differences between gyrofluid and ideal linear MHD stability when other dynamics such as peeling modes, ITGs, shear deformation of the computation grid etc. can be considered small, and the ballooning character is very dominant. As this study is similar to the pedestal height investigations in chapter 7.1, we only show the essential characteristics.

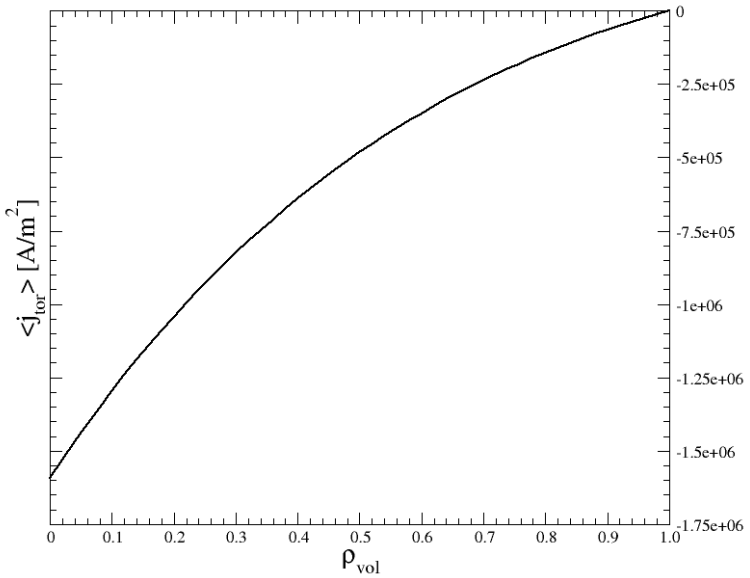

Figure 7.102: Current density profile

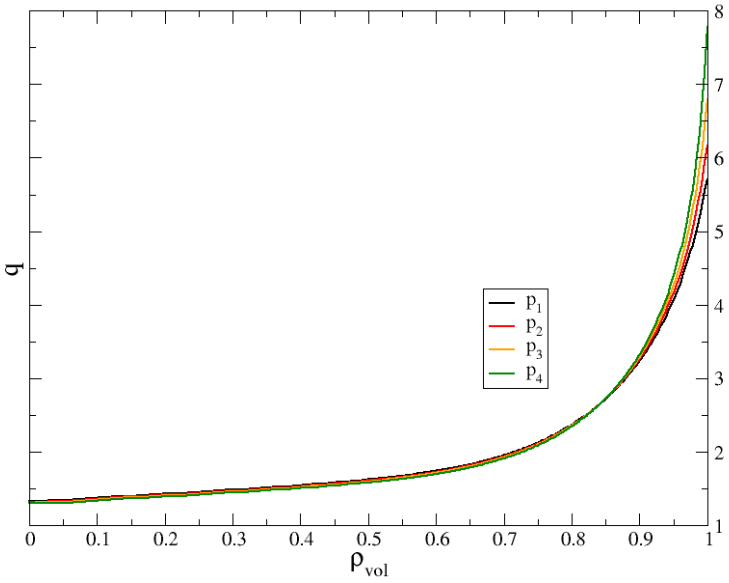

Figure 7.103: q profiles

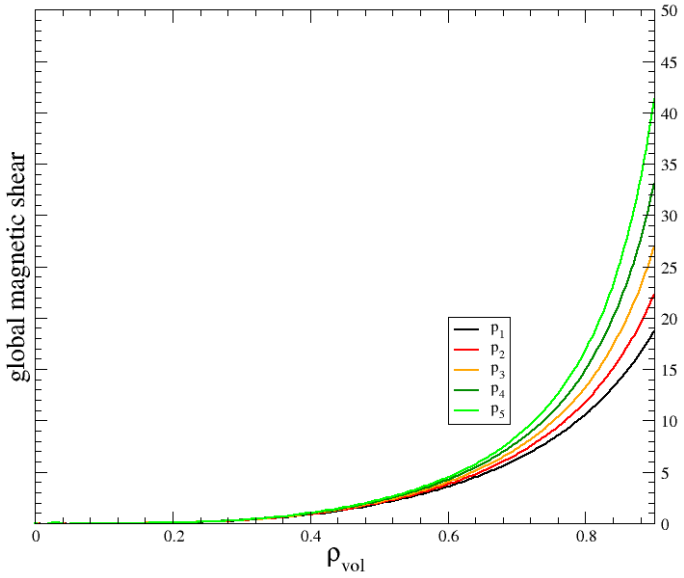

Figure 7.104: Global magnetic shear

7.5.1 Linear ideal MHD stability - ILSA

The ILSA spectra in fig. 7.105 clearly show an increasing maximum growth rate with higher ballooning drive from the pressure gradient ∇p. As the radial mode structure only exhibits an internal ballooning mode, compare the example in fig. 7.106, the toroidal mode number of the onset of instability remains almost unchanged, as there are no low-n external modes. The small shift of $\delta n = 1$ for higher pressure gradients results from pressure gradients which exceed the critical ∇p over a larger radial intervall, therefore causing slightly less localized modes with lower n.
The plasma-wall distance d_{wp} has no effect on the (maximum) growth rates and the mode numbers, as the ballooning mode is sufficiently away from the edge region and there are no external modes, so we only consider $d_{wp} = 2.50$.

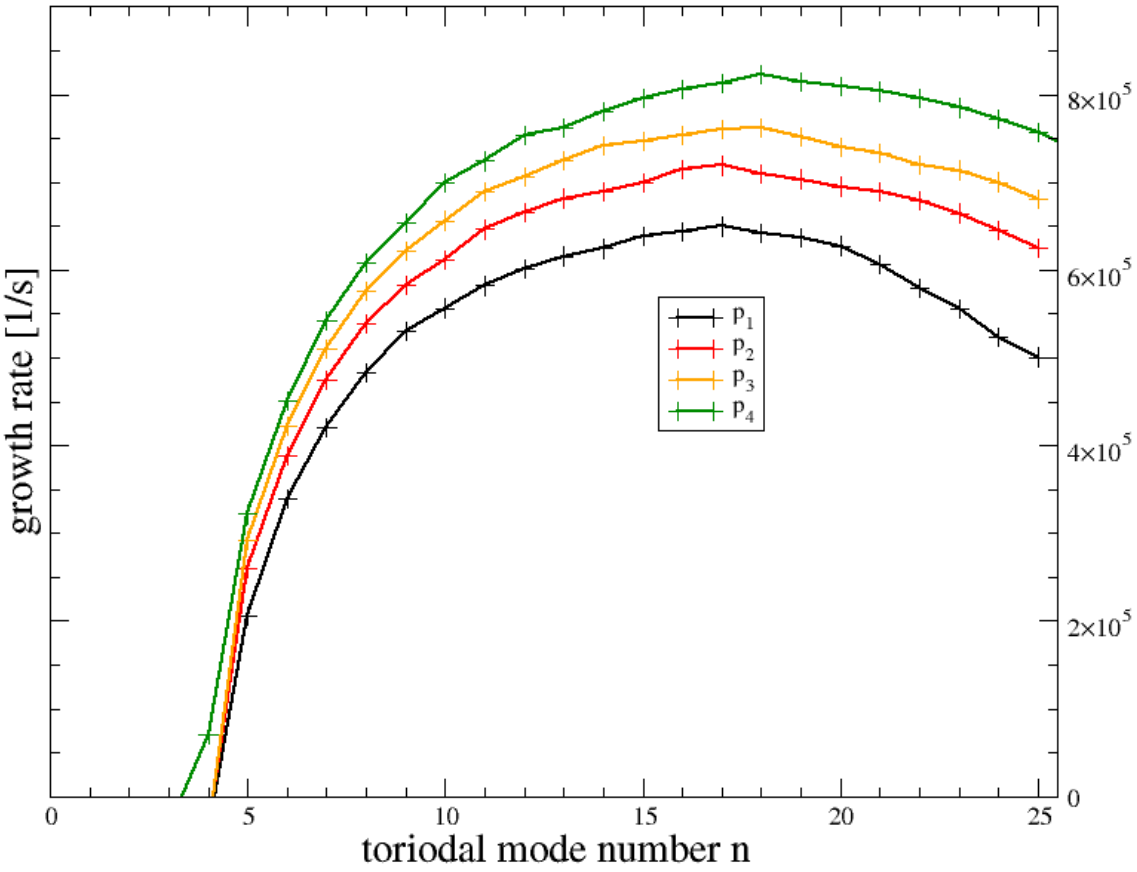

Figure 7.105: ILSA spectra with $d_{wp} = 2.50$

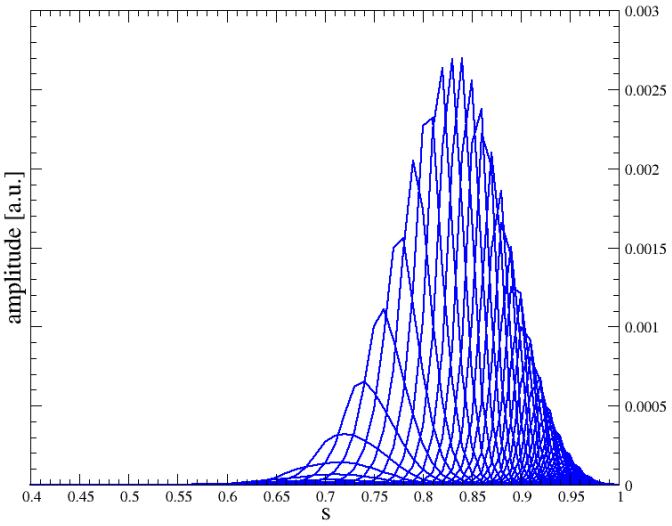

Figure 7.106: Radial mode structure for the fastest growing modes for p_4

7.5.2 Gyrofluid - GEM

As in the study of the pedestal height, increasing pressure gradients lead to a higher peak of the fluctuating total energy E_T, and the linear phase occurs on a subsequently shorter timescale, see fig. 7.107. The spectra, here exemplary for ϕ shown in fig. 7.108, show a dominant peak which shifts to higher $k_y\rho_s$ (i.e. higher n) for larger ∇p, commensurate with the ILSA bevahior.

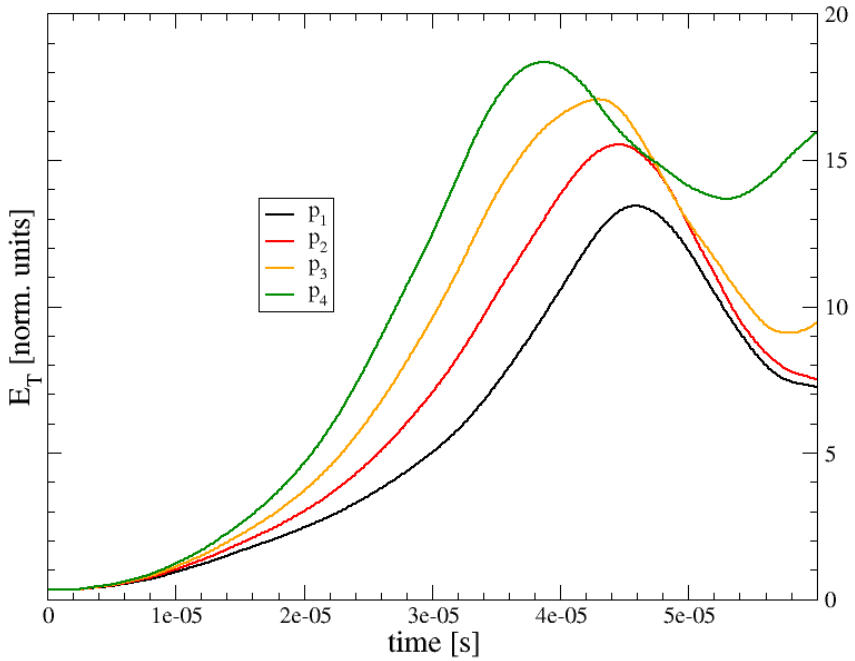

Figure 7.107: Total energy E_T

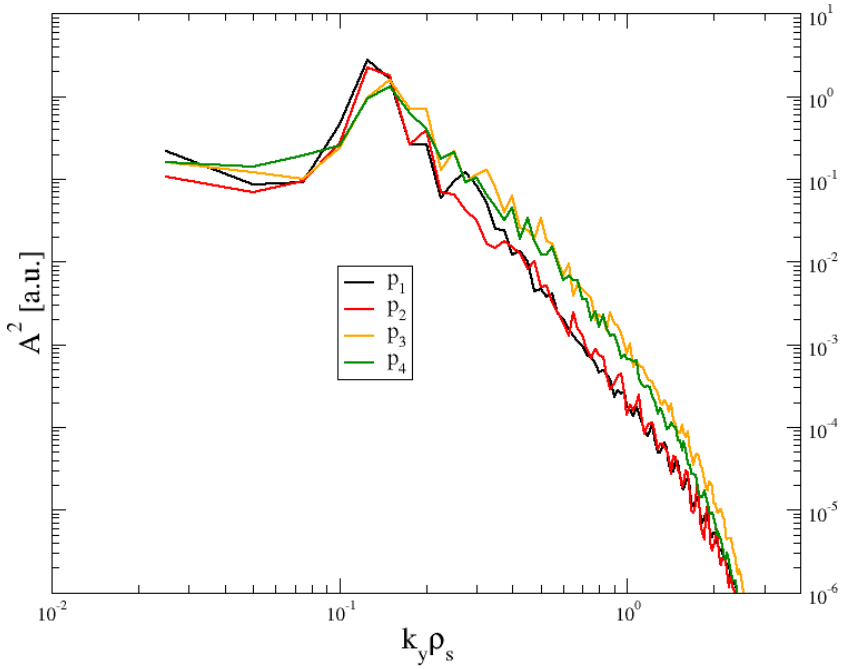

Figure 7.108: Spectra of ϕ at the time of maximum growth rate

7.5.3 Comparison

As can be seen in figs. 7.109 and 7.110, the growth rates and mode numbers of ILSA and GEM are in good agreement. The growth rates are within 5% of each other, while the GEM mode numbers are slighty higher, but follow the same trend as ILSA. One should note, however, that the equilibrium setups are very artificial, specifically designed to suppress instabilities exclusive to only one of the models, ideal linear MHD and gyrofluid theory with the restriction of no surface-located modes.

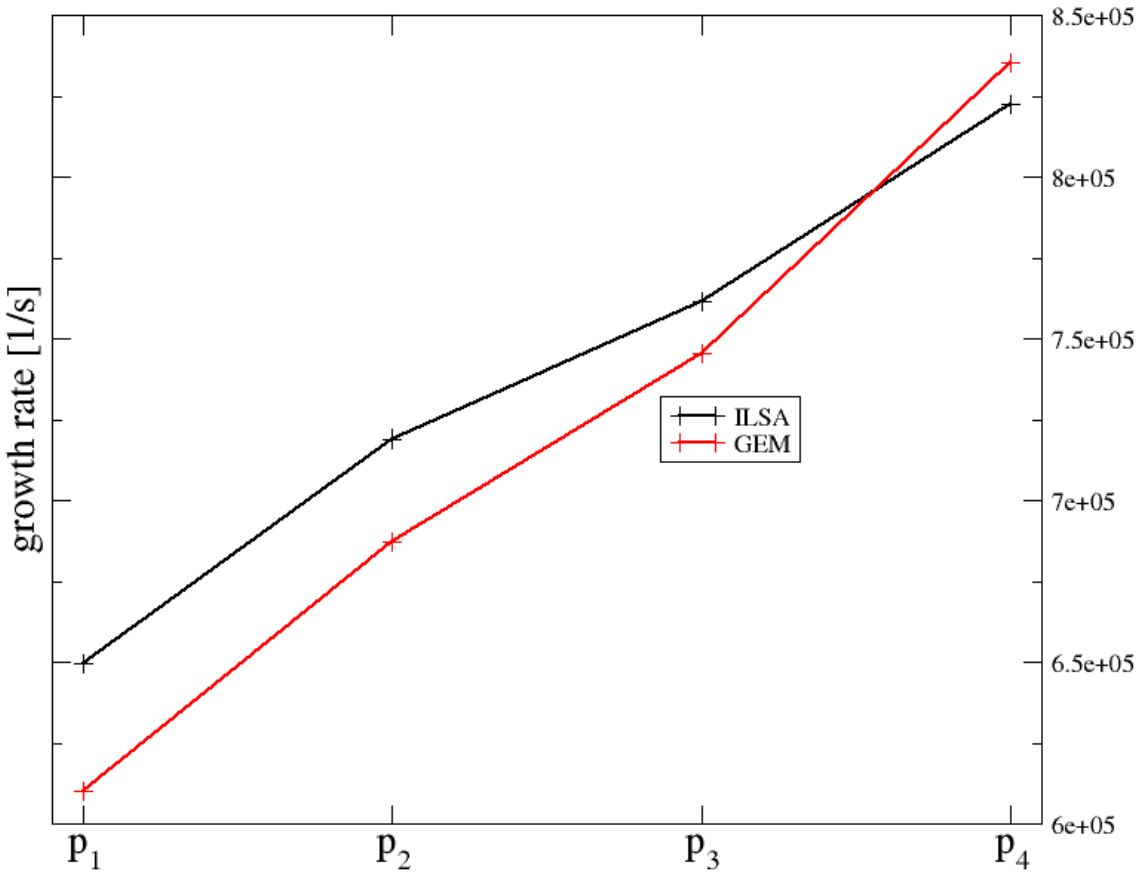

Figure 7.109: Maximum growth rate comparison

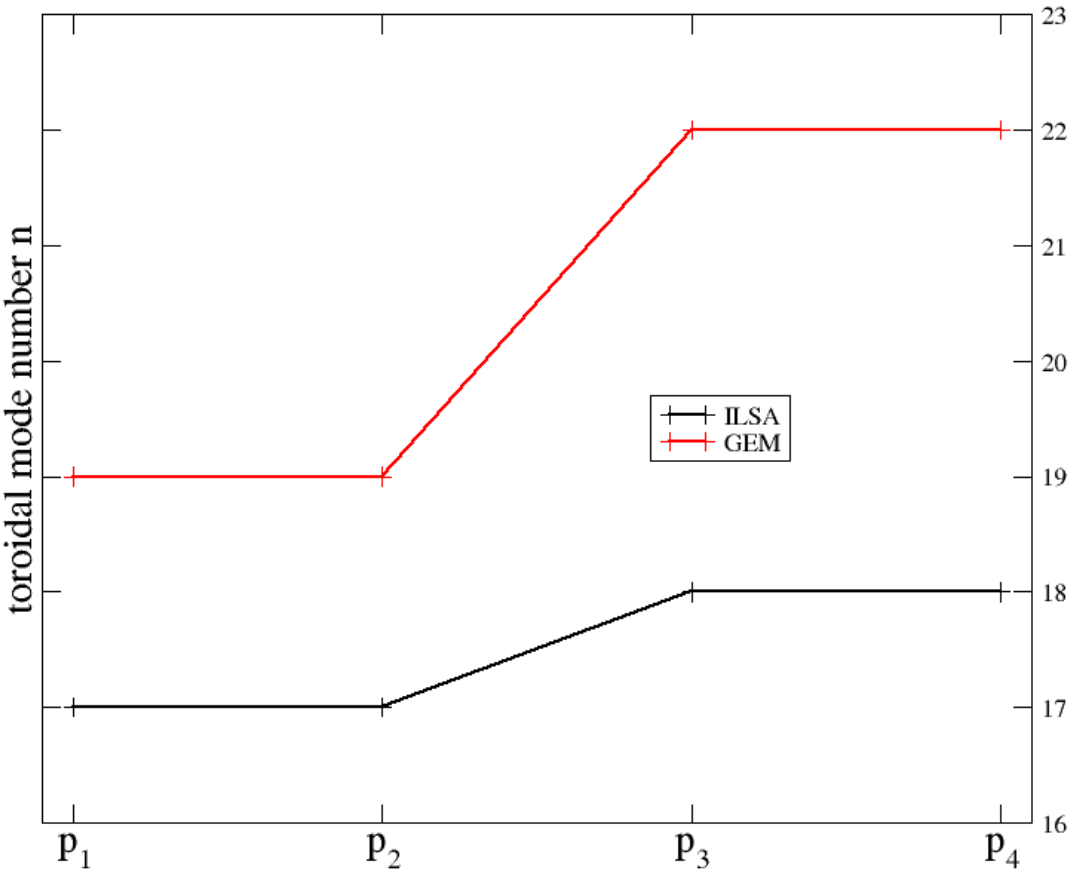

Figure 7.110: Toroidal mode number comparison for the fastest growing modes

8 Conclusions and outlook

8.1 Conclusions

We give a brief overview of the main results of this thesis, highlighting the comparison between ideal linear MHD stability analysis and gyrofluid simulation predictions.
The general steps for the comparison can be summarized as follows:

(i) Prescribing analytical profiles for the pressure p and the flux-surface averaged current density $< j_{tor} >$, we computed the corresponding equilibria with the HELENA code. The current density lacked any bootstrap current to avoid drive for external kink / peeling instabilities. The latter could however never be completely avoided, as large pressure gradients close to the LCFS caused large differences of the current density at the inboard and outboard side, resulting in moderate to severe external modes nonetheless.

(ii) The equilibria were then investigated for instability with the linear MHD stability code ILSA in MISHKA mode, giving growth rates γ as function of the toroidal mode number n and the radial mode structures.

(iii) The equilibria provided the initial setup, from which the time-dependent GEM equations were computed with the gyrofluid code GEM using local geometry (flux tube representation). This additionally required local values of the temperature profiles for the electron and ion temperatures, T_e and T_i, which were chosen from experimental observations of the H-mode ASDEX Upgrade shot #17151. From the time evolution of the fluctuating part of the total energy E_T, a growth rate for the initial linear instability phase could be calculated. The amplitude spectra as function of $k_y \rho_s$ yielded toroidal mode numbers for the initial phase.

Perfectly conducting wall

As the GEM code run with local geometry uses a dampening layer with width Δ at the boundary of the radial computation box, fluctuating quantities are dimishing, ensuring Dirichlet boundary conditions to hold the background equilibrium gradients constant over the radial domain. For the edge region of the plasma, this resembles the effect of a perfectly conducting wall close to the plasma surface to an extent, as the wall suppresses perturbations of the plasma surface as well. Furthermore, because the large shear close to the plasma boundary causes severe distorsions to the computational grid elements of GEM in this region, simulations had to exclude a small radial layer close to the plasma surface, i.e. surface-located and external instabilities could not be resolved. The latter instabilities, however, occurred

in most cases analyzed in the framework of linear ideal MHD. Therefore we investigated the influence of the relative distance d_{wp} between the plasma surface and a perfectly conducting wall on the linear ideal MHD stability of specific equilibria. These equilibria were prepared to feature an edge ballooning mode and an external kink / peeling mode, but otherwise to be stable with regard to other ideal MHD instabilities. We investigated three equilibrium setups: circular plasma cross sections with large and small aspect ratio $\frac{R_0}{a}$, and a shaped plasma with elongation $\kappa = 1.6$ and triangularity $\delta = 0.4$ with small aspect ratio.
For all cases, $d_{wp} = 1.10$ was the threshold, below which the growth rates of the fastest growing modes started to drop, at an increased rate for smaller d_{wp}. The same threshold character was seen for the toroidal mode numbers n of the most virulent modes, although to a lesser extent. The proximity of the wall had the most pronounced stabilizing impact on the lower-n part of the spectra and the external kink instabilities. For the shaped plasma cross section, however, the shaping itself showed a strong stabilizing effect and masked the influence of the wall until d_{wp} reached low values. Choosing Δ to correspond to the distance between plasma surface and perfectly conducting wall, for equilibria with an edge ballooning instability we have $d_{wp} \approx 1.01$, providing a strong stabilizing effect on the external modes (excluded from the GEM simulations) and a lesser but not negligible effect on the ballooning modes. Thus, this gives an estimate on the pure ballooning contribution to the plasma instability within the linear ideal MHD framework and allows for better comparison with GEM results. However, because internal and external modes are coupled, the dampening of the kink / peeling modes also cause a lower ballooning contribution.

Pedestal height

Considering a circular plasma cross section and an aspect ratio of 3.3, the first part of the comparison varied the pressure pedestal height with fixed pedestal width. With regard to the maximum growth rates, two trends could be observed: the difference between ILSA and GEM results decreased with higher pressure gradient ∇p, i.e. larger pedestal height, and a smaller d_{wp}. For the highest ∇p and $d_{wp} = 1.01$, the growth differ by merely $\approx 10\%$. Alongside, the parallel mode structure from the GEM simulations showed a more pronounced ideal ballooning signature with increasing ∇p. For lower pressure gradients, however, the relative difference of the growth rates grew up to a factor of 2. The mode numbers share the better agreement for lower d_{wp}, but the difference becomes larger for the higher pressure gradients.

Pedestal width

Instead varying the pedestal width and leaving the pedestal height approximately constant changes both ∇p and the location of the pressure gradient maximum. Only for high pressure gradients and smaller pedestal widths do the growth rates obtained with GEM follow the behavior of the ILSA spectra, with a relative difference of γ commensurate with the pedestal height scan. For low ∇p and broad pedestal widths however, the GEM parallel mode structures showed no ideal ballooning signature, and the growth rates dropped abruptly, in contrast to the gradual decrease of γ for lower pressure gradient in the ILSA simulations. Again, lower d_{wp} yielded better agreement. The mode numbers are in good agreement for narrow and intermediate pedestal widths, but the physics differ for the latter. For broad pedestals, the mode numbers differ by a large amount, concurring with the growth rate characteristics.

Aspect ratio

With fixed plasma minor radius, lower inverse aspect ratio ϵ and lower d_{wp} yielded better agreement of the growth rates, as high ϵ tended to increase temperature dynamics in the gyrofluid computations and consequently dimished the ideal ballooning character. The mode numbers showed overall good agreement with the exception of the lowest ϵ and $d_{wp} \neq 1.0$, as low inverse aspect ratio showed a strong external mode with lower n, an instability which was never captured in the GEM simulations as mentioned above.

Shaping effects

For a fixed triangularity δ and varying the elongation κ of the plasma cross section, the growth rates trend is the same for GEM and ILSA, with the absolute differences comparable with the previous studies. At large κ, the γ difference increases slightly, as the ideal ballooning signature of the GEM simulations deteriorates. The mode numbers agree well for dampened external kinks $d_{wp} = 1.01$, with slight differences for higher elongation as observed for the growth rates. Keeping κ constant and changing δ, however, has only marginal effects on the GEM dynamics (γ and n), in stark contrast to the strong stabilizing effect of triangularity on the linear ideal MHD framework. Previous gyrofluid studies of turbulent particle transport and heat flux in shaped flux-surface geometry [84] equally showed negligible influence of triangularity, but elongation scalings in agreement with experimental observations.

Core ballooning

The overall observation that growth rates differed the least with high pressure gradient and otherwise small contributions from instabilities exclusive to only of the codes (external kink /peeling for ILSA and temperature effects for GEM) agreed with the stability analysis of an equilibrium setup which featured only a strong core ballooning mode. No external mode was unstable for all toroidal mode numbers n, and ITG modes were very weak. This equilibrium setup, however, was specifically tuned to yield these characteristics, and the plasma parameters of the simulations vastly differed from experimental values.

8.2 Outlook

Global geometry

Using a global geometry lifts the restrictions of the flux tube treatment, the latter only featuring a small radial computation domain. The profiles can be given experimental shapes with radial dependencies instead of simple linearized functions with constant gradient, yielding a much more realistic description of the plasma dynamics. First studies of edge localized ideal ballooning mode (linear and turbulent phase) and the blowout due to the instability have been performed in [72]. However, the initial profiles need further pre-equilibration to give a

consistent initial state for the GEMR simulations. Moreover, the magnetic field line geometry cannot simply be obtained by e.g. HELENA equilibria and must be computed separately.

Conformal coordinates

As the high shear in the edge region of the plasma and the consequent severe deformation of the grid elements prevented simulations of surface-located instabilities with GEM, the external kink / peeling modes occurring in the linear ideal MHD stability analysis limited the comparison of mode numbers and growth rates between GEM and ILSA. Conformal coordinates, however, may allow for resolving even the regions close to the plasma surface. For results on this topic, see e.g. [47]. If the implementation of conformal coordinates is successful, one could study the differences of gyrofluid and ideal linear MHD that stem solely from the additional dynamics of the gyrofluid model. Furthermore, it could shed light on the insensitivity of the GEM simulations on the triangularity δ, i.e. if the lack of scaling with δ is only a problem of extending the radial computation domain further towards the surface.

Bibliography

[1] R. D. Atkinson and F. G. Houtermans. Zur Frage der Aufbaumöglichkeit der Elemente in Sternen. *Z. Phys.*, 54:656, 1929.

[2] H. A. Bethe. Energy production in stars. *Phys. Rev.*, 55(5):434, 1939.

[3] C. F. von Weizsäcker. Über Elementumwandlungen im Innern der Sterne. *Z. Phys.*, 38:176, 1937.

[4] C. F. von Weizsäcker. Über Elementumwandlungen im Innern der Sterne. *Z. Phys.*, 39:633, 1938.

[5] NRL Plasma formulary. http://wwwppd.nrl.navy.mil/nrlformulary/NRL_FORMULARY_09.pdf, 2009.

[6] J. Wesson. *Tokamaks*. Clarendon Press - Oxford, 3rd edition, 2004.

[7] IPP Garching Homepage. http://www.ipp.mpg.de.

[8] ITER. http://www.iter.org/.

[9] J. P. Freidberg. *Ideal Magnetohydrodynamics (Modern Perspectives in Energy)*. Springer, 1st edition, 1987.

[10] H. Goedbloed and S. Poedts. *Principles of Magnetohydrodynamics*. Cambridge University Press, 2004.

[11] M. Kaufmann. *Plasmaphysik und Fusionsforschung*. Vieweg+Teubner, 2003.

[12] R. Dux. Plasmaphysik und Fusionsforschung - Teil I: Plasmaphysik. Lecture script, 2001/2002. Universtität Augsburg.

[13] H. Grad and H. Rubin. Hydromagnetic equilibria and force-free fields. *Proc. of the 2nd UN Conf. on the peaceful uses of atomic energy*, 31:190, 1958.

[14] V. D. Shafranov. Plasma equilibrium in a magnetic field. *Reviews of plasma physics*, 2:103, 1966.

[15] T. Boyd and J. Sanderson. *The Physics of Plasmas*. Cambridge University Press, 2003.

[16] G. Laval, C. Mercier, and R. M. Pellat. Necessity of the energy principles for magnetostatic stability. *Nucl. Fusion*, 5:156, 1965.

[17] J. P. Goedbloed. Lecture notes on ideal magnetohydrodynamics. Fom-Instituut voor Plasmafysica, Nieuwegein, Netherlands, 1979.

[18] J. M. Greene and J.L Johnson. Interchange instabilities in ideeal hydromagnetic theory. *Plasma Phys.*, 8:729, 1968.

[19] H. P. Furth et. al. Necessity of the energy principles for magnetostatic stability. *Plasma Physics and Controlled Nuclear Fusion Research, IAEA, Vienna*, Vol. I, 1964.

[20] U. Stroth. Materialien zu Vorlesungen der Plasmaphysik. http://www.ipf.uni-stuttgart.de/lehre/plasmaphys/plasma.html.

[21] J. W. Connor, R. J. Hastie, and R. J. Taylor. High mode number stability of an axisymmetric toroidal plasma. *Proc. R. Soc. London A*, 365:1720, 1979.

[22] J. W. Connor, R. J. Hastie, H. R. Wilson, and R. L. Miller. Magnetohydrodynamic stability of tokamak edge plasmas. *Physics of Plasmas*, 5(7), 1998.

[23] D. Lortz and J. Nuhrenberg. Comparison between necessary and sufficient stability criteria for axially symmetric equilibria. *Nucl. Fusion*, 13:821, 1973.

[24] Grimm et. al. MHD stability properties of bean-shaped tokamaks. *PPPL report*, page 2090, 1984.

[25] J. P. Freidberg. MHD theory of fusion systems - Lecture. http://ocw.mit.edu/courses/nuclear-engineering/22-615-mhd-theory-of-fusion-systems-spring-2007/lecture-notes/, 2007.

[26] S. Cowley. Introduction to kink modes - the Kruskal-Shafranov limit. http://home.physics.ucla.edu/calendar/conferences/cmpd/talks/cowley.pdf.

[27] T. S. Hahm. Nonlinear gyrokinetic equations for tokamak microturbulence. *Phys. Fluids*, 31(9), 1988.

[28] W. W. Lee. Gyrokinetic approach in particle simulation. *Phys. Fluids*, 26:556, 1983.

[29] W. Dorland and G. W. Hammet. Gyrofluid turbulence models with kinetic effects. *Phys. Fluids B*, 5(3), 1993.

[30] M. A. Beer and G. W. Hammet. Toroidal gyrofluid equations for simulations of tokamak turbulence. *Phys. Plasmas*, 3:4046, 1996.

[31] B. D. Scott. Free-energy conservation in local gyrofluid models. *Physics of Plasmas*, 12(102307), 2005.

[32] B. D. Scott. Shifted metric procedure for flux tube treatments of toroidal geometry: Avoiding grid deformation. *Phys. Plasmas*, 8:447, 2001.

[33] A. J. Brizard and T. S. Hahm. Foundations of nonlinear gyrokinetic theory. *Reviews of modern Physics*, 79, 2007.

[34] B. D. Scott. Lectures in gyrokinetic theory and computation. EFDA Goal Orientated Training in Theory program, 2008.

[35] R. G. Littlejohn. Hamiltonian perturbation theory in noncanonical coordinates. *J. Math. Phys.*, 23:742, 1982.

[36] Tiago Miguel Tamissa Madeira da Costa Ribeiro. *Turbulence studies in the scrape-off layer of tokamak plasmas by three-dimensional gyrofluid simulations.* PhD thesis, Universidade técnica de lisboa - Instituto superior técnico, 2005.

[37] S. I. Braginskii. Transport properties in a plasma. *Rev. Plasma Phys.*, 1:205, 1965.

[38] A. B. Hassam. Higher-order Chapman-Enskog theory for electrons. *Phys. Fluids*, 23:38, 1980.

[39] E. C. Bowers and M. G. Haines. Application of finite larmor radius equations for collisionless plasmas to a theta pinch. *Phys. Fluids.*, 14:165, 1971.

[40] B. D. Scott. Low frequency fluid drift turbulence in magnetised plasmas. *IPP report - habilitation thesis*, 2000.

[41] B. D. Scott. The nonlinear drift wave instability and its role in tokamak edge turbulence. *New J. Phys.*, 4(52), 2002.

[42] F. Wagner et. al. Regime of improved confinement and high beta in neutral-beam-heated divertor discharges of the ASDEX tokamak. *Phys. Rev. Lett.*, 49(19), 1982.

[43] D. Biskamp. *Nonlinear Magnetohydrodynamics.* Cambridge University Press, 1997.

[44] J. W. Connor and H.R. Wilson. A review of theories of the L-H transition. *Plasma Phys. Control. Fusion*, 42, 2000.

[45] L. D. Horton and A. V. Chankin et. al. Characterization of the H-mode edge barrier at ASDEX upgrade. *Nucl. Fusion*, 45, 2005.

[46] O. Sauter et. al. Neoclassical conductivity and bootstrap current formulas for general

axisymmetric equilibria and arbitrary collisionality regime. *Phys. Plasmas*, 6(7):2834, 1999.

[47] T. T. Ribeiro and B. D. Scott. Conformal tokamak geometry for turbulence computations. *IEEE Transactions on plasma science*, 38(9), 2010.

[48] J. W. Connor, A. Kirk, and H. R. Wilson. Edge localised modes (ELMs): Experiments and theory. *AIP Conf. Proc.*, page 1013, 2008.

[49] H. Zohm. Edge localized modes (ELMs). *Plasma Phys. Control. Fusion*, 38(2), 1996.

[50] JAEA. JAEA Research and Development Review. http://jolisfukyu.tokai-sc.jaea.go.jp/fukyu/mirai-en/2007/index.html/.

[51] N. Ben Ayed and A. Kirk et. al. Inter-ELM filaments and turbulent transport in the Mega-Amp spherical tokamak. *Plasma Phys. Contro. Fusion*, 51(035016), 2009.

[52] C. C. Hegna, J. W. Connor, R. J. Hastie, and H. R Wilson. Toroidal coupling of ideal magnetohydrodynamic instabilities in tokamak plasmas. *Phys. Plasmas*, 3(2), 1996.

[53] J. W. Connor, R. J. Hastie, H. R. Wilson, and R.L. Miller. Magnetohydrodynamic stability of tokamak edge plasmas. *Physics of Plasmas*, 5(7), 1998.

[54] H. R. Wilson, S. C. Cowley, A. Kirk, and P. B. Snyder. Magnetohydrodynamic stability of the H-mode transport barrier as a model for edge localized modes: an overview. *Plasma Phys. Control. Fusion*, 48, 2006.

[55] C. Konz, L. D. Horton, E. Strumberger, S. Günter, P. J. Mc Carthy, G. T. A Huysmans, P. B. Snyder, and the ASDEX Upgrade Team. The peeling-ballooning model revisited. *34th EPS Conference on Plasma Phys. Warsaw, 2 - 6 July 2007 ECA Vol.*, 31F, 2007.

[56] P. B. Snyder et. al. ELMs and constraints on the H-mode pedestal: peeling-ballooning stability calculation and comparison with experiment. *Nucl. Fusion*, 44:320, 2004.

[57] EFDA. http://www.jet.efda.org/focus-on/edge-localised-modes/elm-model/.

[58] M. Becoulet et. al. Edge localized modes control: experiment and theory. *Journal of Nuclear Materials*, page 337, 2005.

[59] C. Konz and R. Zille. HELENA manual, 2007. IPP Garching.

[60] E. Strumberger, C. Konz, V. Igochine, and C. Tichmann. ILSA manual, 2005. IPP Garching.

[61] S. Günter. Einführung in die Plasmaphysik. Lecture script. TU Munich.

[62] S. Günter. Plasmaphysik und Fusionsforschung. Lecture script. TU Munich.

[63] B. J. Burke, S. E. Kruger, C. C. Hegna, P. Zhu, P. B. Snyder, C. R. Sovinec, and E. C. Howell. Edge localized linear ideal magnetohydrodynamic instability studies in an extended-magnetohydrodynamic code. *Physics of Plasmas*, 17(032103), 2010.

[64] B. D. Scott. GEM - an energy conserving electromagnetic gyrofluid model. arxiv.org/PS_cache/physics/pdf/0501/0501124v1.pdf, 2008.

[65] B. D. Scott. Drift wave versus interchange turbulence in tokamak geometry: Linear versus nonlinear mode structure. *Physics of Plasmas*, 12(062314), 2005.

[66] B. D. Scott. Basics of turbulence computation for magnetically confined plasmas. ITER school Aix-en-Provence, 2007.

[67] L. J. Zheng, M. T. Kotschenreuther, and J. W. Van Dam. Revisiting linear gyrokinetics to recover ideal magnetohydrodynamics and missing finite larmor radius effects. *Physics of Plasmas*, 14(072505), 2007.

[68] B. D. Scott. Introduction to turbulence in magnetised plasmas. ITER school Aix-en-Provence, 2007.

[69] A. Kendl and B. D. Scott. Flux surface shaping effects on tokamak turbulence and flows. *Physics of Plasmas*, 13(012504), 2006.

[70] B. D. Scott. $E \times B$ shear flows and electromagnetic gyrofluid turbulence. *Physics of Plasmas*, 7(5), 2000.

[71] B. D. Scott. Three-dimensional computation of collisional drift wave turbulence and transport in tokamak geometry. *Plasma Phys. Control. Fusion*, 39, 1997.

[72] A. Kendl, B. D. Scott, and T. T. Ribeiro. Nonlinear gyrofluid computation of edge localised ideal ballooning modes. *Physics of Plasmas*, 17(072302), 2010.

[73] B. D. Scott, A. Kendl, and T. T. Ribeiro. Nonlinear dynamics in the tokamak edge. *Contrib. Plasma Physics*, 50:228, 2010.

[74] S. Saarelma, S. Günter, T. Kurki-Suonio, and H-P. Zehrfeld. ELM phenomenon as an interaction between bootstrap-current driven peeling modes and pressure-driven ballooning modes. *Plasma Phys. Control. Fusion*, 42, 2000.

[75] P. B. Snyder and H. R. Wilson et. al. Edge localized modes and the pedestal: A model based on coupled peeling-ball ooning modes. *Physics of Plasmas*, 9(5), 2002.

[76] H. R. Wilson et. al. Ideal magnetohydrodynamic stability of tokamak high-confinement mode edge region. *Physics of Plasmas*, 6(5), 1999.

[77] H. R. Wilson, P. B. Snyder, G. T. A. Huysmans, and R. L. Miller. Numerical studies of edge localized instabilities in tokamaks. *Physics of Plasmas*, 9(4), 2002.

[78] H. R. Wilson et. al. Influence of the plasma edge on tokamak performance. *Nucl. Fusion*, 40(3Y), 2000.

[79] M. Kaufmann et. al. Edge operational regimes in tokamaks. *Czech. J. Phys*, 48(S2), 1998.

[80] MPI für Plasmaphysik. Ein neues Betriebsszenario für das Fusionskraftwerk. http://www.mpg.de/print/399622.

[81] D. Lortz. The general peeling instability. *Nucl. Fusion*, 15, 1975.

[82] B. D. Scott. Three-dimensional computation of collisional drift wave turbulence and transport in tokamak geometry. *Plasma Phys. Control. Fusion*, 39, 1997.

[83] B. D. Scott. $E \times B$ shear flows and electromagnetic gyrofluid turbulence. *Physics of Plasmas*, 7(5), 2000.

[84] A. Kendl and B. D. Scott. Flux-surface shaping effects on tokamak edge turbulence and flows. *Plasma Phys. Control. Fusion*, 39, 1997.

[85] Aiba Noboyuki et. al. The effect of the aspect ratio on the external kink-ballooning instability in high-beta tokamaks. *J. Plasma Fusion Res. Series*, 6:241, 2004.

[86] B. Coppi and F. Pegoraro. Theory of the ubiquitous mode. *Nucl. Fusion*, 17(5).

[87] M. Püschel. *Electromagnetic effects in gyrokinetic simulations of plasma turbulence*. PhD thesis, Universität Münster, 2009.

[88] T. Görler. *Multiscale Effects in plasma microturbulence*. PhD thesis, Universität Ulm, 2009.

[89] T. Hauff. *Transport of energetic particles in turbulent plasmas*. PhD thesis, Universität Ulm, 2009.

[90] G. T. A. Huysmans, J. P. Goedbloed, and W. Kerner. Theory of the ubiquitous mode. *CP90 Conference on Comp. Physics*, page 371.

[91] G. T. A. et. al. A. *Phys. Plasmas*, 5:371, 1991.

[92] E. Strumberger et. al. B. *Nucl. Fusion*, 45:1156, 2005.

[93] B. D. Scott. The shifted-circle case. http://www.ipp.mpg.de/~bds/write-ups/tokamak/shafranov.ps.

Danksagung

Zuallererst möchte ich mich bei meinem Betreuer Dr. Christian Konz herzlich bedanken, der mich in die Plasmaphysik, speziell die MHD-Theorie sowie die Codes HELENA und ILSA eingearbeit hat hat und immer für Fragen und Hilfestellung bereit stand, sowie für das sehr hilfreiche und umfassende Korrekturlesen meiner Doktorarbeit.

Dr. Bruce Scott sei vielmals für die private Einführung in die Gyrokinetik, die Gyrofluid-Theorie und der Hilfe mit GEM gedankt, ebenso für seine extrem interessanten Kommentare zu einer großen Bandbreite von Themen: von Hunter S. Thompson über Sport zu Geschichte bis hin zur Politik.

Dank gebührt auch Dr. Tiago Ribeiro für die vielen praktischen Tipps im alltäglichen Umgang mit GEM.

Vielen Dank an Prof. Dr. Sibylle Günter für die wichtigen Hilfen bei den physikalischen Hintergründen und Zusammenhängen.

Zusätzlich müssen auch noch Dr. David Coster, Dr. Hajo Klingshirn, Dr. Philipp Lauber, Dr. Andreas Bergmann, Dr. Alex Chenkin und Dr. Timothy Stoltzfus-Dueck genannt werden, die zu den oben genannten Personen unsere Kaffee-Runden immer zu einem absoluten Highlight gemacht haben.

Daneben wünsche ich meinen Kollegen Hauke Doerk, Vittoria Belmondo, Angelo Limone, Mirjam Schneller und Nitya Hariharan noch alles Gute für die weitere Arbeit am IPP und bedanke mich für unsere Dinner-/Grill-/Movie-Night-/Party-Abende.

Ein besonderer Dank an Dr. Alessandro Biancalani für unseren kleinen Fightclub nach der Arbeit.